The Development of $Ni_{1-x-y}Cu_xMg_yO$-SDC Anode for Intermediate Temperature Solid Oxide Fuel Cells (IT-SOFCs)

by

Monrudee Phongaksorn

A thesis
presented to the University of Waterloo
in fulfillment of the
thesis requirement for the degree of
Doctor of Philosophy
in
Chemical Engineering

Waterloo, Ontario, Canada, 2010

AUTHOR'S DECLARATION

I hereby declare that I am the sole author of this thesis. This is a true copy of the thesis, including any required final revisions, as accepted by my examiners.

I understand that my thesis may be made electronically available to the public.

Abstract

Solid oxide fuel cells (SOFCs) conventionally operate between 800 and 1000°C. The barriers for full-scale commercialization of SOFCs are the high cost and relatively poor long-term stability due to the high temperatures used in current state-of-the-art SOFCs. One solution is to decrease the operating temperature, e.g. to 550-750°C but this requires developing new electrolytes and electrode materials. Also, to increase efficiency and practicality, the anode should be able to internally reform hydrocarbon fuels especially methane because it is the most common hydrocarbon in natural gas.

The overall goal of this research is to develop a coke-tolerant $Ni_{1-x-y}Cu_xMg_yO$-SDC anode for methane fuelled IT-SOFCs. The Ni-Cu-Mg-O-SDC anode has been chosen based on the premises that doped-ceria is suitable for intermediate operating temperatures (550-800°C), Ni is known as an active metal and good electronic conductor, Cu increases resistance to coking, MgO helps prevent agglomeration of Ni during reduction, and finally SDC improves oxide ion transport to the cell at this intermediate temperature range. In this work, these materials were characterized in three primary ways: material physical and chemical properties, methane steam reforming activity and electrochemical performance.

Two different methods have been used to add Cu to $Ni_{1-y}Mg_yO$: a one-step co-precipitation method and a two-step co-precipitation/impregnation method. For the first method, $Ni_{1-x-y}Cu_xMg_yO$ was synthesized via co-precipitation of Ni, Mg and Cu. In the two-step method, $Ni_{0.9}Mg_{0.1}O$ was first prepared by co-precipitation, followed by addition of copper to $Ni_{0.9}Mg_{0.1}O$ by impregnation. However, co-precipitation of all metal in one step limits the sintering temperature of the anode in the cell fabrication due to the low boiling point of CuO. Therefore, co-precipitation of Cu is not a practical method and only Cu impregnation should be considered for practical SOFC applications.

It was found that the addition of Mg ($Ni_{0.9}Mg_{0.1}O$) lowers the reducibility of NiO. Addition of Cu to $Ni_{0.9}Mg_{0.1}O$ up to 5% shows similar reducibility as $Ni_{0.9}Mg_{0.1}O$. The reducibility of $Ni_{1-x-y}Cu_xMg_yO$ becomes lower when the Cu content is increased to 10%. Nonetheless, all materials are fully reduced at 750ºC. The XRD patterns of pure NiO, $Ni_{0.9}Mg_{0.1}O$, and the Cu-containing material when Cu is less than 10 mol% are similar. The lower reducibility of Ni-Mg-O and Ni-Cu-Mg-O compared to NiO indicates that they form a solid solution with NiO as the matrix.

Addition of Mg also lowers the BET specific surface area from 11.5 m^2/g for NiO:SDC to 10.4 m^2/g for $Ni_{0.9}Mg_{0.1}O$. The surface area is further reduced when Cu is added; for example, at 10% Cu, the surface area is 8.2 m^2/g.

The activity of 50wt% $Ni_{1-x-y}Cu_xMg_yO$/50wt% SDC samples for methane steam reforming (SMR) and water-gas-shift reaction (WGS) was evaluated in a fully automated catalytic fixed-bed reactor where the exiting gases were analyzed online by a gas chromatograph (GC). The tests were performed at steam-to-carbon ratios (S/C) of 3, 2 and 1, and at temperatures of 750°C and 650°C for twenty hours. Higher methane conversions were obtained at the higher temperature and higher S/C ratio.

Higher methane conversion are obtained using NiO:SDC and $Ni_{0.9}Mg_{0.1}O$:SDC than Ni-Cu-Mg-O. The conversion decreases with increasing Cu content. Over NiO:SDC and $Ni_{0.9}Mg_{0.1}O$:SDC the methane conversions are the same; for example 85% at 750°C for S/C of 3. At the same conditions, impregnation of 5%Cu and 10%Cu yields lower conversions: 62% and 48%, respectively.

The activity for the WGS reaction was determined by mornitoring $CO_2/(CO+CO_2)$ ratio. As expected because WGS is a moderately exothermic reaction, this ratio decreases when increasing the temperature. However, the $CO_2/(CO+CO_2)$ ratio increases with higher S/C. The results indicate that adding Mg does not affect the WGS activity of NiO. The WGS activity of $Ni_{0.9}Mg_{0.1}O$:SDC is higher when Cu is added. The effect of additional Cu is more pronounced at 650ºC. At 750°C, changing the amount of Cu does not change the WGS activity because the WGS reaction rapidly reaches equilibrium at this high temperature.

At 750°C for S/C of 1, carbon filaments were found in all samples. At 650ºC, different types of deposited carbon were observed: carbon fibers and thin graphite layers. Spent NiO:SDC had the longest carbon fibers. Addition of Mg significantly reduced the formation of carbon fibers. Impregnating 5% Cu on $Ni_{0.9}Mg_{0.1}O$:SDC did not change the type of deposited carbon. Monitoring the amount of deposited carbon on $Ni_{0.9}Mg_{0.1}O$:SDC, 3%Cu and 5%Cu impregnated on $Ni_{0.9}Mg_{0.1}O$:SDC for S/C of 0 at 750ºC showed that Cu addition deactivated methane cracking causing a reduction in the amount of carbon deposited.

Electrochemical performance in the presence of dry and humidified hydrogen was determined at 600, 650, 700 and 750ºC. Electrolyte-supported cells constructed with four different anodes were tested using polarization curve and electrochemical impedance spectra. The four anodes were NiO:SDC, $Ni_{0.9}Mg_{0.1}O$:SDC, 3%Cu and 5%Cu on $Ni_{0.9}Mg_{0.1}O$:SDC. Adding Mg improved the maximum power density from 356 $mW.cm^{-2}$ with NiO:SDC to 369 $mW.cm^{-2}$ with $Ni_{0.9}Mg_{0.1}O$:SDC at 750ºC in dry

hydrogen. Addition of Cu, on the other hand, lowered the maximum power density to 325 $mW.cm^{-2}$ with 3%Cu impregnated and to 303 $mW.cm^{-2}$ with 5% Cu impregnated.

The cell with $Ni_{0.9}Mg_{0.1}O$:SDC was also tested under dry methane. To minimize methane cracking under this extreme condition, a current density of 0.10 $A.cm^{-2}$ was always drawn when methane was present in the feed. The voltage decreased during the first hour from 0.8 to 0.5 V, then remained stable for 10 hours, and then started to drop again. Many small cracks were observed on the anode after completion of the electrochemical test, but there was no evidence of much carbon being deposited. In addition to dry methane, tests were also carried out, using the same material, with a H_2O/CH_4 mixture of 1/6 in order to generate a polarization curve at 750°C. Under these conditions, the maximum power density was 226 $mW.cm^{-2}$. This is lower than the maximum power density obtained with humidified hydrogen, which was 362 $mW.cm^{-2}$.

Acknowledgements

First and foremost, I would like to express my sincere gratitude to my supervisors, Dr. Eric Croiset and Dr. Stephen F. Corbin, for their constant support, patience, motivation and their guidance. Without their help, this thesis would not be possible. I would like to extend thanks to my review committee for their insightful suggestions/comments. They were: Dr. François Gitzhofer (Université de Sherbrooke), Dr. Linda Nazar (Department of Chemistry), Dr. Michael Fowler (Department of Chemical Engineering) and Dr. Mark Pritzker (Department of Chemical Engineering).

Special thanks are extended to Energy Policy and Planning Office (EPPO), Ministry of Energy, Thailand; King Mongkut's University of Technology North Bangkok (KMUTNB) and SOFC Canada NSERC Strategic Network for the financial support.

I would like to also thank Mr. Yeong Yoo for offering me the internship opportunity in ICPET, NRC. I have gained useful knowledge of cell fabrication techniques from the project I was involved. My thanks also go to Dr. Naoki Oishi, Dr. Anne C. Co and Mr. Nuong Lim who have been my very good friends since that time.

My sincere thanks go to the Department of Chemical Engineering staff who were very helpful. You all gave me hand in all time. You all helped me went through many experimental techniques and paper work processes.

I wish to thank my research group including Dr. Bill Epling's group. Dr. Bill Epling, Dr. Luke Coleman and Dr. Ryan Clemmer, I appreciate your stimulating discussion. I thank all co-op students who worked with me and become my friends afterward. You all, thank you again for useful discussion, valuable effort and your friendship.

I also wish to give many thanks to my friends who make my Ph.D. study time be wonderful. Dr. Sabaithip, Rungsima ,Tussanee, Dr. Suwadee, Dr. Wongpaka, Sirikanya, Watcharapong, Anuchart, and others, you showed me the meaning of friend.

Finally, I dedicate this thesis to my mother Sopa, my father Monrit, my stepfather Kanuang, my sister Supawadee, and my nephew Suparit. Mom, everything I have achieved, it comes from your love that you have been giving to me. My family member, thank you very much for standing by me.

Table of Contents

Author's Declaration ii
Abstract iii
Acknowledgement vi
Table of Contents vii
List of Figures x
List of Tables xiv
Chapter 1 Introduction and Motivation 1
Chapter 2 Background and Literature 5
2.1 Fuel Cell Fundamentals 5
2.2 Principle of SOFC Operation 8
2.3 Thermodynamic Principle 9
2.3.1 Fuel Cell Performance 11
2.3.2 Overpotentials 12
2.4 Material Properties 13
2.4.1 Electrolyte Materials 14
2.4.2 Cathode Materials 16
2.4.3 Anode Materials 18
2.5 Advantages and Disadvantages of SOFCs 19
2.6 SOFC Designs 19
2.6.1 Sealless Tubular Designs 20
2.6.2 Planar Designs 20
2.7 Literature Review on Anode Materials 21
2.7.1 Ni-based/YSZ cermet 21
2.7.2 Anode for IT-SOFCs (focusing on metal-doped ceria) 27
2.7.3 Interesting properties of Ni-Cu-MgO 36
Chapter 3 Experimental 37
3.1 Methane Steam Reforming and Water Gas Shift Reaction 37
3.2 Electrochemical Measurements 42
3.2.1 Button Cell 44
3.2.2 Test Rig 45
3.2.3 Control System 47
3.2.4 Gas Conditioning System and Fuel Humidifier 48
3.2.5 Furnace 50

3.2.6 Measurement Equipments 50
3.3 Material Characterization Techniques 54
3.3.1 Temperature Programmed Analysis (TPO and TPR) 54
3.3.2 Phase Identification 56
3.3.3 Surface Area Analysis 56
3.3.4 Scanning electron microscopy (SEM) 57
3.3.5 Conductivity test equipment 57
Chapter 4 Material Preparation and Properties 60
4.1 Material Preparation 60
4.1.1 One-Step Co-precipitation Method 60
4.1.2 Two-Step Co-precipitation/Impregnation Method 60
4.2 Material Properties 62
4.2.1 Calcination Temperatures 62
4.2.2 Reduction Temperatures 63
4.2.3 Material Phase 67
4.2.4 Surface Area 70
4.3 Button Cell Fabrication using Alternative Anode Material 70
4.4 Conductivity 74
Chapter 5 Methane Steam Reforming Activity over $Ni_{0.9-x}Cu_xMg_{0.1}O$/SDC 78
5.1 Experimental Procedure 78
5.2 Thermodynamic Simulation Results: Effect of Temperature and S/C on Methane Conversion, Carbon Yield, Hydrogen Yield and CO_2/(CO+ CO_2) Ratio 79
5.3 No Cu Addition: NiO:SDC and $Ni_{0.9}Mg_{0.1}O$:SDC 82
5.4 Cu Addition 89
5.4.1 Addition of Copper via One-step Co-precipitation Method 89
5.4.2 Addition of Copper via Two-step Co-precipitation/Impregnation Method 94
5.4.3 Summary for Effect of Material Preparation on SMR Activity 98
5.5 Carbon Deposition Analysis 101
5.5.1 Type of Carbon Deposited 101
5.5.2 Amount of Carbon Deposition on Methane Cracking Using Copper-Free Material and Copper-Containing Material Prepared via Two-step Co-precipitation/Impregnation Method 106
Chapter 6 Electrochemical Test 109
6.1 Evaluation of Cell Performance with Hydrogen Fuel 109
6.1.1 Polarization Test 112

6.1.2 Electrical Impedance Spectra (EIS) 123
6.2 Preliminary Test with Methane 127
6.2.1 Dry Methane 127
6.2.2 Humidified Methane (H_2O/CH_4= 1/6) 131
Chapter 7 Conclusions and Recommendations 134
7.1 Conclusions 134
7.1.1 Material Preparation and Properties 134
7.1.2 Button Cell Fabrication 134
7.1.3 Material Activity on SMR 135
7.1.4 Electrochemical Performance 137
7.2 Recommendations for Future Work 138
7.2.1 Button Cell Fabrication 138
7.2.2 Material Activity on SMR 139
7.2.3 Electrochemical Performance 140
Appendix A: Mass Flow Control Calibration 141
Appendix B: Calculations for Control Evaporator and Mixer (CEM) 144
Appendix C: Phase diagrams for systems involved in the thesis 146
Bibliography 149

List of Figures

Figure 2-1 Operating principle of a SOFC.....8
Figure 2-2 Overall effects of various polarizations on the performance curve (curves for illustration purpose only, not from actual data).....12
Figure 2-3 Atomic structure and oxygen travelling in the conducting perovskite $ABO_{3-\delta}$ (adapted from Adler (2004)).....17
Figure 2-4 Sealless tubular SOFC design (a) Schematic illustration of a Siemens Westinghouse tubular SOFC. (b) The cell operation and current path.....20
Figure 2-5 Planar SOFC design.....21
Figure 3-1 Experimental setup for SMR-WGS.....40
Figure 3-2 Quartz tube reactor.....41
Figure 3-3 The SOFC button cell setup a) Schematic diagram b) Overall feature c) Fuel conditioning system and d) SOFC located in the furnace and the measurement equipment.....44
Figure 3-4 Schematic of the button cell.....44
Figure 3-5 Schematic of the rig design.....46
Figure 3-6 Control panel of LabVIEW program.....47
Figure 3-7 Field-point used as an interface of the electronic devices and LabVIEW program.....48
Figure 3-8 Flow controllers placed next to the computer in the real set up.....48
Figure 3-9 Three options of fuel conditioning system.....49
Figure 3-10 The connection between the SOFC setup and the measurement equipment.....51
Figure 3-11 Idealization of the impedance spectra in the Nyquist plot.....53
Figure 3-12 Schematic of Cahn TG-2151 thermobalance.....55
Figure 3-13 Principle's scheme of XRD.....56
Figure 3-14 The setup designed for conductivity measurement a) Actual setup b) Schematic view and the flow of current.....58
Figure 4-1 Procedure for preparing $Ni_{1-x-y}Cu_xMg_yO$ powder by one-step co-precipitation.....61
Figure 4-2 Process of wet impregnation of Cu on Ni-based catalyst (two-step method).....61
Figure 4-3 Rate of weight loss in TPO test for different $Ni_{1-x-y}Cu_xMg_yO$ materials.
a) Materials fabricated using one-step co-precipitation,
b) materials prepared using two-step method (Cu impregnation).....64
Figure 4-4 Rate of weight loss in TPR test for different $Ni_{1-x-y}Cu_xMg_yO$ materials.
a) Materials fabricated using one-step co-precipitation,
b) materials prepared using two-step method (Cu impregnation).....65

Figure 4-5 XRD patterns of $Ni_{0.45}Cu_{0.45}Mg_{0.1}O$ from the one-step method at the initial state and after calcination at 550ºC and 750ºC for 4h. 68
Figure 4-6 XRD patterns of $Ni_{1-y}Mg_yO$ calcined at 750ºC for 4h. 68
Figure 4-7 XRD patterns of $Ni_{1-x-y}Cu_xMg_yO$ from the one-step method after calcination at 750ºC for 4h. 69
Figure 4-8 XRD patterns of 3, 5 and 10 mol% Cu impregnated on $Ni_{0.9}Mg_{0.1}O$ made from the two-step method after calcination at 750ºC for 4h compared with $Ni_{0.85}Cu_{0.05}Mg_{0.10}O$ and $Ni_{0.80}Cu_{0.10}Mg_{0.10}O$ made from the one-step method. 69
Figure 4-9 Process of button cell preparation. 71
Figure 4-10 Button cell a) actual feature b) SEM backscattered electron micrograph of the anode/electrolyte interface (after sintering) c) SEM backscattered electron micrograph of the anode surface (after reduction). 72
Figure 4-11 SEM-EDX image and elemental distribution of a 50wt% $Ni_{0.9}Mg_{0.1}O$: 50wt% SDC impregnated with Cu to make 50wt% 5%Cu on $Ni_{0.9}Mg_{0.1}O$: 50wt% SDC a) SEM backscattered electron image for overall determination b) cerium c) samarium d) nickel and e) copper. 73
Figure 4-12 Procedure of sample preparation for the conductivity measurement. 74
Figure 4-13 $Ni_{0.9}Mg_{0.1}O$ sample after sintering. 74
Figure 4-14 SEM backscattered electron micrographs of a) Ni:SDC and b) $Ni_{0.9}(MgO)_{0.1}$:SDC c) 5%Cu impregnated on $Ni_{0.9}(MgO)_{0.1}$:SDC. 76
Figure 5-1 Procedure of SMR test. 79
Figure 5-2 Effect of temperature and S/C on equilibrium CH_4 conversion and C yield. 80
Figure 5-3 Effect of temperature and S/C on equilibrium H_2 yield and $CO_2/(CO+ CO_2)$ ratio. 80
Figure 5-4 Results for NiO:SDC and $Ni_{0.9}Mg_{0.1}O$:SDC for S/C of 1, 2 and 3 at 750°C over 1200 min a) CH_4 conversion, b) H_2 yield, and c) $CO_2/(CO+ CO_2)$ ratio. 84
Figure 5-5 CH_4 conversion for S/C of 1 2 and 3 at 750°C and 650°C over 1200 min for a) NiO:SDC, b) $Ni_{0.9}Mg_{0.1}O$:SDC. 85
Figure 5-6 H_2 yield for S/C of 1 2 and 3 at 750°C and 650°C over 1200 min for a) NiO:SDC, b) $Ni_{0.9}Mg_{0.1}O$:SDC. 87
Figure 5-7 CO2/(CO+CO2) ratio for S/C of 1 2 and 3 at 750°C and 650°C over 1200 min for a) NiO:SDC, b) $Ni_{0.9}Mg_{0.1}O$:SDC. 88
Figure 5-8 Results for $Ni_{0.85}Cu_{0.05}Mg_{0.1}O$:SDC for S/C of 1, 2 and 3 at 750°C and 650°C over 1200 min a) CH_4 conversion, b) H_2 yield, and c) $CO_2/(CO+ CO_2)$ ratio. 91
Figure 5-9 Results for $Ni_{0.85}Cu_{0.05}Mg_{0.1}O$:SDC and $Ni_{0.8}Cu_{0.1}Mg_{0.1}O$:SDC for S/C of 1, 2 and 3

at 750°C over 1200 min a) CH_4 conversion, b) H_2 yield, and c) $CO_2/(CO+ CO_2)$ ratio. 93
Figure 5-10 Results for 5%Cu impregnated on $Ni_{0.9}Mg_{0.1}O$:SDC for S/C of 1, 2 and 3 at 750°C and 650°C over 1200 min a) CH_4 conversion, b) H_2 yield, and c) $CO_2/(CO+ CO_2)$ ratio. 96
Figure 5-11 Average results for 3% 5% and 10% Cu impregnated on $Ni_{0.9}Mg_{0.1}O$:SDC for S/C of 1, 2 and 3 at 750°C (average data for time-on-steam between 10 and 20 h) 98
Figure 5-12 Average results for Ni0.9Mg0.1O:SDC (no_Cu), $Ni_{0.85}Cu_{0.05}Mg_{0.1}O$:SDC (5%_one-step), 5% Cu on $Ni_{0.9}Mg_{0.1}O$:SDC (5%_two-step), and 10% Cu on $Ni_{0.9}Mg_{0.1}O$:SDC (10%_two-step) for S/C of 2 and 3 at 650 and 750°C (average data for time-on-stream between 10 and 20 hrs) a) CH_4 conversion and b) $CO_2/(CO+ CO_2)$ ratio. 100
Figure 5-13 a) SEM micrograph of $Ni_{0.9}Mg_{0.1}O$:SDC after S/C=1 at 750°C b) TEM image of $Ni_{0.9}Mg_{0.1}O$:SDC after S/C=2 at 750°C..... 101
Figure 5-14 SEM backscattered electron micrographs of $Ni_{0.9}Mg_{0.1}O$:SDC a) freshly reduced, b) spent, S/C=1 at 750°C and c) spent, S/C=1 at 650°C. 103
Figure 5-15 SEM backscattered electron micrographs of NiO:SDC a) freshly reduced, b) spent, S/C=1 at 750°C and c) spent, S/C=1 at 650°C. 104
Figure 5-16 SEM backscattered electron micrographs of $Ni_{0.85}Cu_{0.05}Mg_{0.1}O$:SDC a) freshly reduced, b) spent, S/C=1 at 750°C and c) spent, S/C=1 at 650°C. 105
Figure 5-17 SEM backscattered electron micrographs of 5%Cu on $Ni_{0.9}Mg_{0.1}O$:SDC a) freshly reduced, b) spent, S/C=1 at 750°C and c) spent, S/C=1 at 650°C. 106
Figure 5-18 Percentage weight gain for $Ni_{0.9}Mg_{0.1}$OSDC, 3%Cu on $Ni_{0.9}Mg_{0.1}O$:SDC, and 5%Cu on $Ni_{0.9}Mg_{0.1}O$:SDC at 750°C. 107
Figure 6-1 Procedure for fuel cell testing with hydrogen. 111
Figure 6-2 Voltage and power density vs. current density with dry H_2 on $Ni_{0.9}Mg_{0.1}O$:SDC/SDC/SSC:SDC 112
Figure 6-3 Voltage and power density vs. current density at different flow rates of dry H_2 on $Ni_{0.9}Mg_{0.1}O$:SDC/SDC/SSC:SDC at 700°C. 113
Figure 6-4 Voltage and power density vs. current density with dry H_2 on NiO:SDC, $Ni_{0.9}Mg_{0.1}O$:SDC, 3%Cu on $Ni_{0.9}Mg_{0.1}O$:SDC, and 5%Cu on $Ni_{0.9}Mg_{0.1}O$:SDC anodes at a)750°C, b) 700°C, c) 650°C, and d) 600°C. 117
Figure 6-5 Voltage and power density vs. current density with 3%humidified H_2 on NiO:SDC, $Ni_{0.9}Mg_{0.1}O$:SDC, 3%Cu on $Ni_{0.9}Mg_{0.1}O$:SDC, and 5%Cu on Ni0.9$Mg_{0.1}O$:SDC anodes at a)750°C, b) 700°C, c) 650°C, and d) 600°C. 119
Figure 6-6 Average maximum power density vs. temperature to NiO:SDC, $Ni_{0.9}Mg_{0.1}O$:SDC,

3%Cu on $Ni_{0.9}Mg_{0.1}O$:SDC, and 5%Cu on $Ni_{0.9}Mg_{0.1}O$:SDC anodes with a) dry H_2 b) 3% humidified H_2.....121
Figure 6-7 Average limiting current density vs. temperature to NiO:SDC, $Ni_{0.9}Mg_{0.1}O$:SDC, 3%Cu on $Ni_{0.9}Mg_{0.1}O$:SDC, and 5%Cu on $Ni_{0.9}Mg_{0.1}O$:SDC anodes with a) dry H_2 b) 3% humidified H_2. 122
Figure 6-8 EIS spectra with dry H_2 (dotted lines) and 3% humidified H_2 (solid lines) on NiO:SDC, $Ni_{0.9}Mg_{0.1}O$:SDC, 3%Cu on $Ni_{0.9}Mg_{0.1}O$:SDC, and 5%Cu on $Ni_{0.9}Mg_{0.1}O$:SDC anodes at a) 750°C, b) 700°C, c) 650°C, and d) 600°C.....125
Figure 6-9 Procedure of fuel cell test with pure methane.....128
Figure 6-10 Voltage and power density vs. current density with humidified H_2 on $Ni_{0.9}Mg_{0.1}O$:SDC anode. Thick anode: 180μm; thin anode: 20μm. 129
Figure 6-11 EIS spectra with humidified H_2 to $Ni_{0.9}Mg_{0.1}O$:SDC anode cell. Thick anode: 180μm; thin anode: 20μm. 130
Figure 6-12 Cell voltage vs. time at constant current density of 0.10A/cm^2 to $Ni_{0.9}Mg_{0.1}O$:SDC anode cell operated in dry methane at 750°C 131
Figure 6-13 Procedure of fuel cell test with H_2O/CH_4=1/6.....132
Figure 6-14 Voltage and power density vs. current density with H_2O/CH_4=1/6 on $Ni_{0.9}Mg_{0.1}O$:SDC anodes at 750°C, 700°C, 650°C and 600°C.....133
Figure 7-1 Schematic of a) two electrodes b) three electrodes.....140

List of Tables

Table 2-1 Types of Fuel Cells including anode and cathode reactions of the fuel cells (EG&G Technical Service (2002) and Aguiar (2002)). 7
Table 2-2 Material Requirements (Minh and Takahashi (1995)) 14
Table 2-3 Ionic conductivities of ceria-rare earth oxide systems at 800°C (Eguchi (1997)) 15
Table 2-4 Ionic conductivity data for selected electrolyte compositions (Steele (2000)) 15
Table 2-5 Ionic conductivity data for CeO_2-Ln_2O_3 (Singhal and Kendal (2003)) 16
Table 2-6 Maximum power densities of some SOFC single cells for IT-SOFCs. 31
Table 3-1 Properties and the corresponding material characterization techniques used in this work 54
Table 4-1 Results for TPO analysis. 66
Table 4-2 Results for TPR analysis 66
Table 4-3 Single point and BET surface areas of $Ni_{1-x-y}Cu_xMg_yO$. 70
Table 4-4 Percentage of reduction and conductivity 77
Table 6-1 Maximum power densities and limiting current density with dry H_2 and 3% humidified H_2 on NiO:SDC, $Ni_{0.9}Mg_{0.1}O$:SDC, 3%Cu on $Ni_{0.9}Mg_{0.1}O$:SDC, and 5%Cu on $Ni_{0.9}Mg_{0.1}O$:SDC 110
Table 6-2 Polarization resistance with dry H2 and 3% humidified H_2 on NiO:SDC, $Ni_{0.9}Mg_{0.1}O$:SDC, 3%Cu on $Ni_{0.9}Mg_{0.1}O$:SDC, and 5%Cu on $Ni_{0.9}Mg_{0.1}O$:SDC 126

Chapter 1
Introduction and Motivation

Fuel cells have received a great deal of interest as alternative high performance and environmentally friendly power generation system. Low temperature fuel cells or polymer electrolyte membrane fuel cells (PEMFCs), alkali fuel cells (AFCs) and phosphoric acid fuel cells (PAFCs) are appropriate for small-scale applications, such as laptops, cellular phones, and automobiles. In contrast, high temperature fuel cells, such as molten carbonate fuel cells (MCFCs) and solid oxide fuel cells (SOFCs), are better suited for large-scale power plants and distributed power because of their higher efficiencies, greater fuel flexibility, and the possibility of combined heat and power generation. Among several types of fuel cells, SOFCs are considered to be the most desirable fuel cell for generating electricity in stationary applications because of their simplicity, fuel flexibility, high performance, solid state material (easy to handle), and possibility for hydrocarbon internal reforming.

A solid oxide fuel cell, conventionally operating at 800 to 1000°C, consists of three important solid components: an electrolyte located between a cathode and an anode. Oxygen molecules fed on the cathode side are reduced to oxide ions at the cathode/electrolyte interface, which are then transported to the other side of the electrolyte. At the electrolyte/anode interface, the oxide ions react with H_2 and CO in the fuel producing H_2O and CO_2, respectively. Due to the high operating temperatures, H_2 or CO could be either directly supplied or produced from catalytic reforming reactions of the fuel at the anode layer before reaching the active area for an electrochemical reaction, the latter known as the three phase boundary (TPB). Currently, the barriers for full-scale commercialization of SOFCs are their high cost and relatively poor long-term stability. These two barriers are essentially due to the high temperature used in current state-of-the-art SOFCs. An obvious solution is to decrease the operating temperature from the conventional 800-1000°C to 550-800°C. At these lower temperatures, cheaper materials can be used. To further reduce the costs, the number of fuel pre-processing steps must be reduced. Consequently, the use of hydrocarbon fuel (e.g. natural gas) as the feed to the SOFC is highly desirable. Temperature limitations and fuel conditions, however, significantly affect material options. While the ohmic overpotential increases rapidly as the operating temperature is decreased, the anode deactivation is usually associated with carbon formation when hydrocarbons are fed to the cell. Therefore, the development of an anode cermet for intermediate temperature SOFCs (IT-SOFCs) fed directly by hydrocarbon fuel becomes an important goal.

State-of-the-art anodes have been developed based on Ni-YSZ cermets because of their high electrical conductivity and catalytic activity for operation in the 800-1000°C range. Unfortunately, many studies have shown that such SOFCs are neither stable for long-term operation nor possess suitable ionic conductivity for operation in the intermediate temperature range. Therefore, to increase the ionic conductivity at lower temperatures, stabilized zirconia has been replaced by doped-ceria because of its higher ionic conductivity, especially that of SDC ($Ce_{0.8}Sm_{0.2}O_{1.9}$).

Nickel oxide in a cermet anode becomes electrochemically active after reduction but, at the same time it is also strongly active toward carbon deposition. Although Ni is reasonably priced and has a high activity for catalytic reforming, coking either takes place on the active sites or blocks access to the TPB. Several methods reported in the literature to develop-carbon tolerant anodes using additives, adding functional layers, combining precious metal oxides with NiO, Ni-alloys, etc. has been reported in the literature. Two interesting low-cost methods used to reduce carbon deposition with the possibility of stable performance are the addition of an alkali or alkali earth oxide and the replacement of Ni by a metal alloy.

Tests with NiO-alkali earth oxide catalysts for oxidative methane-to-syngas conversion have shown that NiO-MgO has high activity and low reducibility. Addition of MgO prevents coarsening and agglomeration of Ni because NiO forms a solid solution in MgO and only Ni at the surface is reduced to Ni^0 which has a high activity for methane oxidation (Choudhary et al., 1998). For methane CO_2 reforming, NiO-MgO also provides higher activity than NiO (Moon and Ryu, 2003). The performance of a LSM/YSZ/NiO-MgO PEN (positive/electrolyte/negative) SOFC cell was investigated at 800°C with a mixture of CH_4 and CO_2. The performance of NiO-MgO anodes was stable because the surface area remained unchanged. On the other hand, the performance for NiO only decreased because of the loss of the surface area. Although Ni obtained by reduction of NiO agglomerates and sinters rapidly, Shiratori et al. (2006) showed that the interaction between NiO and MgO to form a stable solid solution decreases the reduction rate and consequently, slows down the agglomeration and sintering of Ni. Thus, MgO can be used as a promoter to avoid Ni coarsening and to achieve higher Ni dispersion. Moreover, Shiratori et al. (2006) revealed that Ni with MgO or (Ni,Mg)O solid solution provides higher catalytic activity for reforming.

Another possibility to sustain SOFC performance using hydrocarbon fuels is to replace Ni by a metal alloy. Ni-Cu/YSZ was found to be an effective coke resistant anode, especially at low Ni content (Lee et al., 2004). Among the different anodes (Cu/YSZ, Co/YSZ, Ni/YSZ, Cu-Co/YSZ and Cu-Ni/YSZ) exposed to dry n-butane at 500°C, the bimetallic anodes perform better than Cu/YSZ and also

reduced carbon formation compared to Ni/YSZ or Co/YSZ. The reforming activity of Cu/YSZ is very low, but it is improved by using CeO_2 as a composite support of CeO_2-YSZ because CeO_2 is catalytically active and provides mixed conductivity to increase the TPB at the interface between the anode and electrolyte (Ye et al., 2007; Park et al., 2000). Cu-CeO_2 is also considered to be a sulphur-tolerant anode for SOFCs (He et al., 2005) because it can be used with H_2 containing as high as 450 ppm H_2S when operated at 800°C. Based on density functional theory (DFT) calculations, alloying Ni with Cu improves sulphur tolerance (Choi et al., 2007). Lu et al. (2003) investigated the use of Cu-CeO_2-SDC anodes in butane-fuelled SOFCs. The performances were not high because the cell was operated at temperatures as low as 600°C.

The main objective of the research work described in this thesis is to develop a $Ni_{1-x-y}Cu_xMg_yO$-SDC anode. This anode has been chosen based on the assumption that doped-ceria is suitable for intermediate temperature operation (550-750°C), Ni-Cu alloys play a vital role in increasing resistance to coking (as well as raising sulphur tolerance), MgO reduces the likelihood of agglomeration during reduction and increases Ni-Cu alloy activity and finally, SDC improves oxide ion transport to the three phase boundary. This research focuses on evaluating the physical and chemical properties, methane steam reforming and water gas shift activities, and electrochemical performance of $Ni_{1-x-y}Cu_xMg_yO$-SDC anodes.

In this thesis, chapter 2 introduces the principle of operation of SOFC, as well as its main components. It also contains a comprehensive literature review on anode materials with a focus on IT-SOFC materials and materials for internal reforming. This chapter ends with a presentation of some interesting properties of the Ni-Cu-Mg-O system.

Chapter 3 describes the experimental setup used in this work which is essentially a fixed-bed reactor system used for methane steam reforming, and a SOFC button cell test station. This chapter also describes techniques used for material characterization.

Chapter 4 begins with a description of two material preparation methods for $Ni_{1-x-y}Cu_xMg_yO$ followed by a presentation of the properties of the materials fabricated. Here, calcination-reduction properties, material phase, and surface area of the anode are reported. Then, the procedure for fabricating the button cell is also presented. Conductivities of $Ni_{1-x-y}Cu_xMg_yO$-SDC were measured at room temperature in ambient air because conductivity measurement at high temperature in controlled atmosphere was not available in our laboratory at the time of this research work.

Chapter 5 discusses the activity of $Ni_{1-x-y}Cu_xMg_yO$-SDC for methane steam reforming and water gas shift reactions. In this chapter, the effect of temperature, steam-to-carbon ratio, copper content and material preparation method on activities as well as carbon deposition are presented in detail.

Chapter 6 reports on the electrochemical performance of electrolyte-supported cells tested with dry and humidified hydrogen. These cells are fabricated with four different anodes: NiO:SDC, $Ni_{0.9}Mg_{0.1}O$:SDC, and $Ni_{0.9}Mg_{0.1}O$:SDC impregnated with 3 and 5 mol% Cu. Electrochemical impedance spectroscopy is also applied to determine the electrochemical properties of the cells. Finally, at the end of chapter 6, electrochemical behaviours of a $Ni_{0.9}Mg_{0.1}O$:SDC cell operating in dry methane is presented and discussed.

Chapter 7 gives the conclusions of this thesis and present recommendations for future work.

Chapter 2
Background and Literature

This chapter can be categorized into two parts. The first part briefly presents some basic concepts about fuel cells and, then, gives a general overview of some principles and materials related to solid oxide fuel cells (SOFCs). Because an objective of this thesis is to develop an alternative Ni-based anode for IT-SOFCs fuelled by hydrogen and/or methane, the second part summarizes the literature pertaining to the development of state-of-the-art Ni-based anodes during the past two decades. The last part contains information about research efforts to develop Ni-based catalysts for methane steam reforming. However, the literature on methane steam reforming has been screened for materials related to the materials considered in the present thesis.

2.1 Fuel Cell Fundamentals

Like a battery, a fuel cell is an electricity generator which transforms electrochemical reactions directly into electrical power without the Carnot limitation. Nonetheless, it differs from the battery in terms of limitations in electrical generation. The total charge from a battery is limited by the amount of stored reactant within the battery itself; therefore, it has to be recharged after running out of the reactant. A fuel cell, in contrast, can continuously generate electricity as long as fuels are supplied. A single fuel cell includes three important components: a positive electrode, a negative electrode and an ionic conductor, called cathode, anode, and electrolyte, respectively. Fuels, normally hydrogen, supplied at the anode are oxidized to cations while oxygen molecules (or the source of oxygen such as air) fed into the cathode are reduced to oxide ions. Either cations or anions diffuse through the electrolyte from one electrode to the other and react at the electrode/electrolyte interface, a.k.a triple phase boundary (TPB). Overall electrochemical hydrogen and carbon monoxide oxidation reactions are written:

$$H_{2(g)} + \frac{1}{2} O_{2(g)} \leftrightarrow H_2O_{(g)} \tag{2-1}$$

$$CO_{(g)} + \frac{1}{2} O_{2(g)} \leftrightarrow CO_{2(g)} \tag{2-2}$$

Although all types of fuel cells operate with similar overall reactions, occur in all types of fuel cells, they can be classified into the following five types, depending on the electrolyte: alkali fuel cells (AFCs), molten carbonate fuel cells (MCFCs), phosphoric acid fuel cells (PAFCs), proton exchange

membrane fuel cells (PEMFCs) and solid oxide fuel cells (SOFCs). The differences in each type are summarized in Table 2-1.

PEMFCs, AFCs and PAFCs must be fed with hydrogen or methanol because they operate at temperatures too low to promote internal reforming of carbonaceous fuels to produce hydrogen and carbon monoxide, active reductants of an anode. Consequently, they are appropriate for small-scale applications such as notebooks, cell phones and automobiles. In addition, a main problem is that carbon monoxide is a poison for catalysts employed in these low-temperature fuel cells, causing rapid deactivation of the electro-catalyst.

Conversely, high temperature MCFCs and SOFCs are able to reform natural gas within the cell (i.e., internal reforming) at the anode not only because of the high operating temperature but also because of the properties of the active metal loaded on the anode. For example, nickel, a high temperature catalyst for reforming reactions, is also the most common active anode metal for SOFCs (Bolman and Mugerwa, (1993); EG&G Technical Service (2002)). Principles of SOFC operation, including thermodynamics, materials used, and cell designs are discussed below.

Table 2-1 Types of Fuel Cells including anode and cathode reactions of the fuel cells (EG&G Technical Service (2002) and Aguiar (2002)).

Item	Type of fuel cell				
	Polymer Electrolyte Membrane (PEMFCs)	**Alkaline (AFCs)**	**Phosphoric Acid (PAFCs)**	**Molten Carbonate (MCFCs)**	**Solid Oxide (SOFCs)**
Electrolyte	Ion exchange membrane	Alkaline	Phosphoric acid	Alkali Carbonate mixtures	Stabilized zirconia and ceria
Operating Temp. (^oC)	50-85	50-250	160-220	630-650	800-1000
Charge Carrier	H^+	OH^-	H^+	CO_3^{2-}	O^{2-}
Electrolyte State	Solid	Liquid	Immobilized Liquid	Immobilized Liquid	Solid
Corrosiveness	None	High	High	High	None
Fuel	H_2	H_2	H_2	Synthesis gas, CH_4	Synthesis gas, CH_4
Anode Reaction	$H_2 \rightarrow 2H^+ + 2e^-$	$H_2 + 2OH^- \rightarrow 2H_2O + 2e^-$	$H_2 \rightarrow 2H^+ + 2e^-$	$H_2 + CO_3^{2-} \rightarrow H_2O + CO_2 + 2e^-$ $CO + CO_3^{2-} \rightarrow 2CO_2 + 2e^-$	$H_2 + O^{2-} \rightarrow H_2O + 2e^-$ $CO + O^{2-} \rightarrow CO_2 + 2e^-$
Cathode Reaction	$O_2 + 4H^+ + 4e^- \rightarrow H_2O$	$O_2 + 2H_2O + 4e^- \rightarrow 4OH^-$	$O_2 + 4H^+ + 4e^- \rightarrow H_2O$	$O_2 + 2CO_2 + 4e^- \rightarrow 2CO_3^{2-}$	$O_2 + 4e^- \rightarrow 2O^{2-}$
Catalyst	Cathode: Pt, Pt/Ru Anode: Pt	Pt/Au, Pt, Ag for cathode and anode	Cathode: Pt/Cr/Co, Pt/Ni Anode: Pt	Cathode: Li/NiO Anode: Ni, Ni/Cr	Cathode: $LaSrMnO_3$ Anode: Ni/ZrO_2
Cogeneration Heat	None	None	Low quality	High	High
Size (MW)	0.25	Very small	11	2	1-2
Application	Transport, small appliances	Small power in aerospace	Power generation, CHP	Power generation, CHP	Power generation, CHP
Efficiency (%)	<40	>60	40-45	50-60	50-60

2.2 Principle of SOFC Operation

A solid oxide fuel cell (SOFC), conventionally operating at 800 to 1000ºC, consists of three solid components: two porous electrodes (an anode and a cathode) and a dense electrolyte (Figure 2-1). It operates by passing air through the porous cathode and fuel through the anode. Oxygen molecules receive electrons at the cathode/electrolyte interface and are reduced to oxide ions. The oxide ions are conducted through the electrolyte between the two electrodes from the cathode side to the anode side. Then, the oxide ions interact with the fuel at the anode/electrolyte interface where the gaseous fuel, active metal and electrolyte meet known as the three phase boundary (TPB) (Singhal and Kendal 2003).

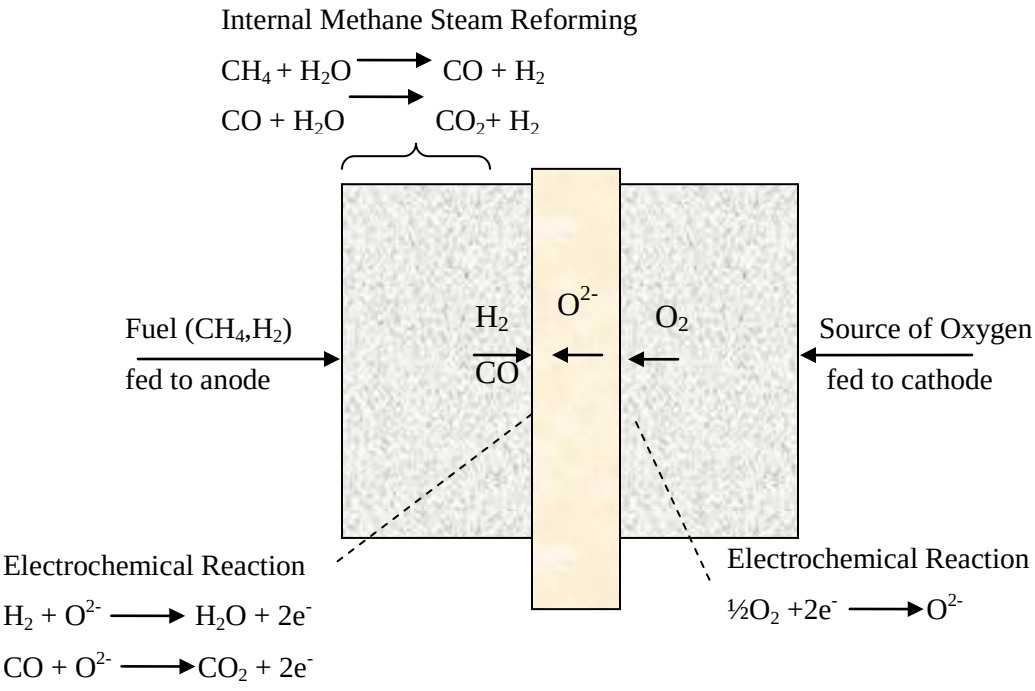

Figure 2-1 Operating principle of a SOFC

According to the thermodynamics of the system, many possible reactions can occur when hydrogen or methane is used as a fuel. The reactions that are most likely to occur under direct internal reforming of methane are showed as follows (Sfeir (2002)):

$$H_{2(g)} + \frac{1}{2}O_{2(g)} \leftrightarrow H_2O_{(g)} \tag{2-1}$$

$$CO_{(g)} + \frac{1}{2}O_{2(g)} \leftrightarrow CO_{2(g)} \tag{2-2}$$

$$CH_{4(g)} + 2O_{2(g)} \leftrightarrow CO_{2(g)} + 2H_2O_{(g)} \quad (CH_4 \text{ oxidation}) \tag{2-3}$$

$$CH_{4(g)} + H_2O_{(g)} \leftrightarrow CO_{(g)} + 3H_{2(g)} \quad (CH_4 \text{ steam reforming}) \tag{2-4}$$

$$CH_{4(g)} + CO_{2(g)} \leftrightarrow 2CO_{(g)} + 2H_{2(g)} \quad (CH_4 \text{ dry reforming}) \tag{2-5}$$

$$CO_{(g)} + H_2O_{(g)} \leftrightarrow CO_{2(g)} + H_{2(g)} \quad \text{(water-gas shift)} \tag{2-6}$$

$$2CO_{(g)} \leftrightarrow C_{(s)} + CO_{2(g)} \quad \text{(CO disproportionation)} \tag{2-7}$$

$$CH_{4(g)} \leftrightarrow C_{(s)} + 2H_{2(g)} \quad (CH_4 \text{ pyrolysis}) \tag{2-8}$$

$$CO_{(g)} + H_{2(g)} \leftrightarrow C_{(s)} + H_2O_{(g)} \quad \text{(CO hydrogenation)} \tag{2-9}$$

Equations (2-1), (2-2) and (2-3) are direct electrochemical oxidations. The reforming reactions (2-4) and (2-5) are the steam and dry reforming reactions, respectively. When a mixture of methane and steam is used as a fuel, equation (2-4) is normally followed by the water-gas shift reaction (equation (2-6)). If the amount of steam is not high enough, reactions (2-7) and (2-8) are more favoured. Consequently, carbon may deposit on the active site or clog gas flow channels, causing loss of TPB.

2.3 Thermodynamic Principles

The electrical work done by a fuel cell is the work produced from transferring a charge Q (per mole of reactant) along a distance L in the presence of a potential difference E. The charge Q can be written as a function of electron (equation 2-10). The electrical work is expressed according to equation (2-11).

$$Q = nF \tag{2-10}$$

$$W_{elec} = nEF \tag{2-11}$$

where n is the number of electrons transferred in the reaction and F is the Faraday's constant.

The variation of Gibbs free energy is given by

$$dG = dU - TdS - SdT + pdV + Vdp \tag{2-12}$$

Equation (2-12) shows that G is a function of internal energy (U), temperature (T), entropy (S), pressure (p), and volume (V). Writing dU in term of mechanical work and electrical work (equation 2-13), it contains some similar terms as in equation (2-12):

$$dU = TdS - pdV + dW_{elec} \tag{2-13}$$

Substitution of equation (2-13) into (2-12) for constant temperature and pressure (dT, dp =0) yields

$$dG = -dW_{elec} \tag{2-14}$$

Combining equation (2-11) and (2-14) and integrating from the start to end of a process resulting in

$$\Delta G = -nEF \tag{2-15}$$

In addition, the Gibbs free energy at any condition also depends on the Gibbs free energy at the standard condition (superscript 0) and activity (a) of the chemical substances involved in the reaction:

$$\Delta G = \Delta G^{O} + RT \ln\left(\frac{\prod a_{products}^{\nu_i}}{\prod a_{reac\,tants}^{\nu_i}}\right) \tag{2-16}$$

where R is the gas constant.

Replacing Gibbs free energy in equation (2-16) with equation (2-15) gives

$$E = E^{O} - \frac{RT}{nF} \ln\left(\frac{\prod a_{products}^{\nu_i}}{\prod a_{reac\,tants}^{\nu_i}}\right) \tag{2-17}$$

In principle, two different electrochemical reactions are taking place at the anode and the cathode. Oxygen molecules are reduced at the cathode, as in the reaction below:

$$O_{2c(g)} + 4e^{-} \leftrightarrow 2O_{e}^{2-} \tag{2-18}$$

where the subscripts c and e refer to states at the cathode and the electrolyte, respectively. The oxide ions are transported to the other side of the electrolyte and are oxidized at the anode (2-19), the reverse reaction of (2-18)

$$2O_{e}^{2-} \rightarrow O_{2a} + 4e^{-} \tag{2-19}$$

where the subscript a refers to state at the anode. The overall reaction is then written by equation (2-20), corresponding to an oxygen concentration cell. The reversible voltage of this cell can be given by equation (2-21).

$$O_{2c} \rightarrow O_{2a} \tag{2-20}$$

$$E = -\frac{RT}{4F}\ln\left(\frac{p_{O_{2a}}}{p_{O_{2c}}}\right) \tag{2-21}$$

where $p_{O_{2c}}$ and $p_{O_{2a}}$ represent the oxygen partial pressures at the cathode and anode, respectively. $p_{O_{2c}}$ is usually known or measurable, whereas $p_{O_{2a}}$ can be calculated depending on the fuel composition. For example, in the case of hydrogen fuel, the oxidation reaction taking place at the anode is represented by equation (2-1) or (2-2), assuming that they are at equilibrium. In this way, $p_{O_{2a}}$ can be expressed as in equation (2-22) and (2-23), respectively:

$$p_{O_{2a}} = \left(\frac{p_{H_2O_a}}{p_{H_{2a}} K_{eq2-1}}\right)^2 \tag{2-22}$$

$$p_{O_{2a}} = \left(\frac{p_{CO_{2a}}}{p_{CO_a} K_{eq2-2}}\right)^2 \tag{2-23}$$

Consequently, equation (2-21) can be rewritten as equation (2-24) for H_2 fuel cell and equation (2-25) for CO fuel cell:

$$E = E^0_{H_2} + \frac{RT}{4F}\ln\left(p_{O_{2c}}\right) + \frac{RT}{2F}\ln\left(\frac{p_{H_{2a}}}{p_{H_2O_a}}\right) \tag{2-24}$$

$$E = E^0_{CO} + \frac{RT}{4F}\ln\left(p_{O_{2c}}\right) + \frac{RT}{2F}\ln\left(\frac{p_{CO_a}}{p_{CO_{2a}}}\right) \tag{2-25}$$

Equations (2-24) and (2-25) are known as the Nernst equations. Fuel cells always operate at lower cell voltage than the thermodynamic voltage (Nernst potential). It is consequently important to indicate the performance of fuel cell.

2.3.1 Fuel Cell Performance

As long as the fuel is being fed, the fuel cell should ideally maintain a constant voltage. This ideal voltage (the reversible voltage) can be determined using the Nernst equation such as equation (2-24). In the case of hydrogen/air fuel cell, the reversible voltages are 1.16V and 1.11V at 100ºC and 900 ºC, respectively. In contrast, the voltage output of a real fuel cell decreases as the current load

increases due to the irreversible voltage losses. These losses (or overpotentials) are attributed to three causes: activation, ohmic and concentration polarizations, discussed in next section. Thus, the net cell voltage E_{cell} can be expressed as in equation (2-26):

$$E_{cell} = E - \eta \tag{2-26}$$

where η is the overpotential which can be expanded as the following equation:

$$\eta = \eta_{act} + \eta_{ohm} + \eta_{conc} \tag{2-27}$$

where η_{act}, η_{ohm} and η_{conc} are the activation, ohmic and concentration overpotentials, respectively. The overall effects of these overpotentials as a function of current density are indicated on the performance curve shown in Figure 2-2 .

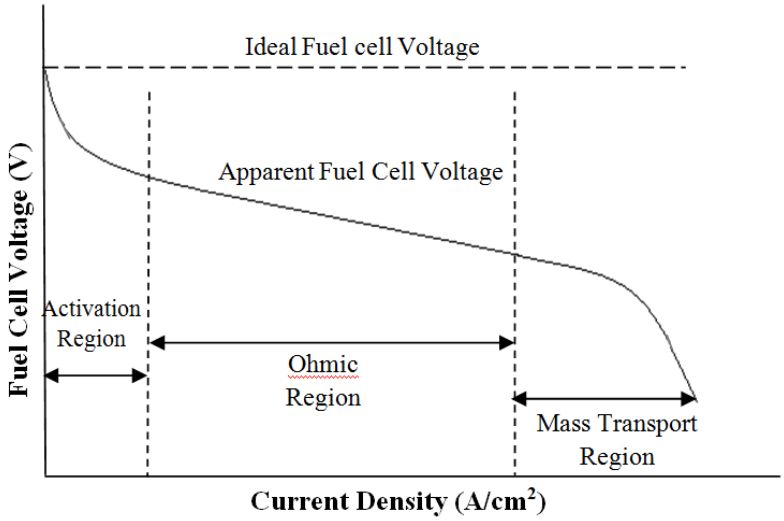

Figure 2-2 Overall effects of various polarizations on the performance curve (curves for illustration purpose only, not from actual data)

2.3.2 Overpotentials

Reactions must overcome an activation energy barrier to proceed at a given rate. This energy must be overcome by the interaction of reactants resulting in the activation (charge transfer) polarization. This loss is the most important loss in the low current density region and it is usually caused primarily by the cathode. The activation polarization is usually related to the current density i by the Butler-Volmer equation:

$$i = i_0 \left[exp\left(\frac{\alpha n F \eta_{act}}{RT} \right) - exp\left(\frac{-(1-\alpha) n F \eta_{act}}{RT} \right) \right] \tag{2-28}$$

where i_0 is the exchange current density and α is the charge transfer coefficient. The exchange current density is equivalent to the balanced partial current densities for the forward and reverse electrode reactions at equilibrium. When the activation polarization becomes important, for a cathodic reaction, the first term on the right hand side becomes much larger than the second term. Thus, the last term in equation (2-28) can be ignored and therefore, the activation overpotential is given by:

$$\eta_{act} = \frac{RT}{\alpha nF} \ln\left(\frac{i}{i_0}\right) \tag{2-29}$$

The effect of activation polarization is decreased by either doping the electrode with a more effective catalyst or increasing the temperature (>800°C).

The ohmic polarization is caused by the resistance of the electrolyte and the interconnect. Figure 2-2 depicts in that the cell voltage varies linearly with current density in the intermediate region. This is where ohmic effects are dominant (equation (2-30)).

$$\eta_{ohm} = ir \tag{2-30}$$

where r is the area specific resistance (ASR). Methods to reduce the ohmic polarization include the use of high conductivity electrodes, low polarization interconnects and thin electrolyte layers.

The concentration polarization dominates at high current density. It becomes prominent when the supply of reactants and the removal of products by diffusion to or from the electrode are slower than that corresponding to the charging/discharging current. The equation would be

$$\eta_{conc} = \frac{RT}{nF} \ln\left(1 - \frac{i}{i_L}\right) \tag{2-31}$$

where i_L is the limiting current density defined as the maximum current density that the cell can achieved. It occurs because the reactant concentration at the reaction site is approaching zero (Hirschenhofer (1998)).

The most important key for commercial success are the materials used. Not only the composition but also the microstructure plays a vital role in the cell performance.

2.4 Material Properties

It is a major challenge to pick materials for each SOFC component because each component has individual material requirements. As shown in Table 2-2, a match between thermal expansion

coefficients of the various components is also a necessity to prevent cracks and delamination in the cell.

Table 2-2 Material Requirements (Minh and Takahashi (1995))

Component	Requirements				
	Conductivity		Stability	Porosity	Thermal Expansion
	Ionic	Electronic			
Electrolyte	High	Nil	In reducing and oxidizing environment	Fully Dense	Matches Others
Cathode	Low	High	In oxidizing environment	Porous	Matches Others
Anode	Low	High	In reducing environment	Porous	Matches Others

2.4.1 Electrolyte Materials

Oxygen ions produced from the reduction reaction of oxygen molecules at the cathode/electrolyte interface must diffuse through the electrolyte and react with the fuel at the TPB. Therefore, the electrolyte material must possess high ionic conductivity without electronic conductivity to provide a high diffusion rate of oxide ions, but must inhibit the transfer of electrons. The electrolyte must also be stable in reducing and oxidizing atmospheres. Moreover, to minimize resistive losses and to prevent the short circuiting of reacting gases within the cell, electrolyte materials must be formed as a fully dense thin film with no gas leaks. Furthermore, the electrolyte has to be chemically and thermally compatible with the other cell components. To date, two predominant types of electrolytes have been used: doped zirconia and doped ceria.

The most common fluorite structure for an electrolyte is stabilized zirconia. Yttria-stabilized zirconia (ZrO_2-Y_2O_3; YSZ) and scandia-stabilized zirconia (ZrO_2-Sc_2O_3; SSZ or ScSZ) have shown high ionic conductivity with a reasonable cost and processing time; however, degradation of ScSZ has been reported at high temperatures (1000°C). Stabilized zirconia materials possess inappropriately low ionic conductivity at temperatures below 750°C. Therefore, they are replaced by doped-ceria materials for IT-SOFCs because ceria-based electrolytes provide much higher ionic conductivity at intermediate temperatures. Doped ceria, the other preferred structure, has higher oxygen ion conductivity compared to doped zirconia at intermediate temperatures, especially samaria-doped ceria (CeO_2-Sm_2O_3; SDC) and gadolinia-doped ceria (CeO_2-Gb_2O_3; GDC or CGO).

To meet the conductivity requirement of 10^{-1} S cm^{-1} at 600°C, doped ceria substances are the most promising materials (Steele (1996); Perednis and Gauckler (2004)). Ionic conductivities of doped

ceria electrolytes have been compared with those of YSZ by Eguchi (1997) as shown in Table 2-3. The ion conductivities of doped ceria especially SDC are higher than that of YSZ. Eguchi (1997) reported that Ni-ceria cermets also exhibited higher fuel electrode performance.

Table 2-3 Ionic conductivities of ceria-rare earth oxide systems at 800°C (Eguchi (1997))

Sample	$\sigma \times 10^{-2}$ (S.cm^{-1})
$(CeO_2)_{0.80}(SmO_{1.5})_{0.20}$	9.45
$(CeO_2)_{0.80}(DyO_{1.5})_{0.20}$	7.74
$(CeO_2)_{0.80}(HoO_{1.5})_{0.20}$	6.39
$(CeO_2)_{0.80}(NdO_{1.5})_{0.20}$	5.93
$(CeO_2)_{0.80}(ErO_{1.5})_{0.20}$	5.74
$(CeO_2)_{0.80}(YdO_{1.5})_{0.20}$	5.59
$(CeO_2)_{0.80}(TmO_{1.5})_{0.20}$	5.59
$(CeO_2)_{0.80}(GdO_{1.5})_{0.20}$	5.53
$(CeO_2)_{0.80}(LaO_{1.5})_{0.20}$	4.16
$(CeO_2)_{0.80}(CaO_{1.5})_{0.20}$	4.28
CeO_2	0.03
$(ZrO_2)_{0.80}(Y_2O_3)_{0.20}$	3.01

Another study supporting that doped ceria is a very promising electrolyte for IT-SOFCs was reported by Steele (2000).

Table 2-4 Ionic conductivity data for selected electrolyte compositions (Steele (2000))

Composition	Dopant	ΔE (eV)	σ_0	σ, 500°C (S.cm^{-1})	σ, 600°C (S.cm^{-1})	σ, 700°C (S.cm^{-1})
$Ce_{0.9}Gd_{0.1}O_{1.95}$	Gd^{3+}	0.64	1.09×10^5	0.0095	0.0253	0.0544
$Ce_{0.9}Sm_{0.1}O_{1.95}$	Sm^{3+}	0.66	5.08×10^4	0.0033	0.0090	0.0200
$Ce_{0.887}Y_{0.113}O_{1.9435}$	Y^{3+}	0.87	3.16×10^6	0.0087	0.0344	0.1015

Likewise, ionic conductivities of those three doped ceria were presented by Singhal and Kendal (2003), as given in Table 2-5. SDC and GDC not only have high ionic conductivities but also maintain the ohmic loss as low as 0.2 Ω.cm^{-2}. Accordingly, SDC and GDC are attractive for relatively

low temperature SOFCs. However, these materials are not suitable for high operating temperature and they have lower mechanical strength than doped zirconia.

Table 2-5 Ionic conductivity data for CeO_2-Ln_2O_3 (Singhal and Kendal (2003))

Composition	Dopant	ΔE(kJ/mol)	σ, 500°C ($S.cm^{-1}$)	σ, 700°C ($S.cm^{-1}$)
$Ce_{0.9}Gd_{0.1}O_{1.95}$	Gd^{3+}	70	0.0038	0.036
$Ce_{0.9}Sm_{0.1}O_{1.95}$	Sm^{3+}	75	0.0050	0.040
$Ce_{0.9}Y_{0.1}O_{1.95}$	Y^{3+}	95	0.00021	0.01

Below are some works aimed at improving the conductivity of doped ceria:

- A composite of calcium-doped ceria (CCO) and carbonate has been synthesized (Zhu et al. (2003)). For this material, Ca^{2+} was used instead of Gd^{3+} or Sm^{3+} and the calcium-doped ceria was mixed with $66Li_2CO_3$:$34Na_2CO_3$. The conductivity of the composite was approximately two orders of magnitude higher than that of pure CCO. The use of the CCO-composite electrolyte in the SOFC demonstrated a performance as high as 600 $mW.cm^{-2}$ at 600°C.
- When small amounts of alkali elements or alkali-earth elements are dissolved in SDC, the ionic conductivity increased, as shown by Mori and Yamamura (1998). They also found that the addition of alkali or alkali-earth elements can inhibit large volume expansion.
- Yan et al. (2005) fabricated $La_{0.9}Sr_{0.1}Ga_{0.8}Mg_{0.2}O_{3-d}$ (LSGM)/$Ce_{0.8}Sm_{0.2}O_{2-d}$ (SDC) composite films. The SDC was deposited on the anode substrate to form a 400 nm thin layer. The 5 μm of LSGM was then deposited on top of the SDC film.

2.4.2 Cathode Materials

The properties of the cathode must cover all requirements described in Table 2-2. Platinum was the first cathode material used but it is too expensive for commercial application. Perovskite oxides are low-cost alternative cathodes. Since 1965 many perovskite cathodes have been studied; for example, $La_{1-x}Sr_xCoO_{3-\delta}$ (LSC) was one of the earliest studied. This research led to studies of other perovskites: $La_{1-x}Ca_xCoO_{3-\delta}$ and $La_{1-x}Sr_xMO_{3\pm\delta}$ (M= Cr, Mn (LSM), Fe (LSF), Co). Besides electrochemical performance, chemical compatibility of the cathode material with the electrolyte is also critical. Interactions between the cathode/electrolyte can limit electrochemical reactions at the cathode side (Adler (2004)).

The perovskite structure can be represented by $ABO_{3-\delta}$, the large cations are located at the corner of a cube, while the small cation located at the centre of the cube. The oxide ions occupy the face-centred positions. δ is the number of oxygen ion vacancies. In the case where a transition metal (such as Mn or Fe) occupies a B-site, whereas the A-site is a mixture, the materials yield high electronic conductivity because the mixture can introduce a charge imbalance and the transition metal has a vacancy d-orbital. For example, LSM: Mn atoms occupy B-sites while La and Sr are placed at A-sites. Figure 2-3 depicts the general structure of a perovskite crystal and the transport mechanism.

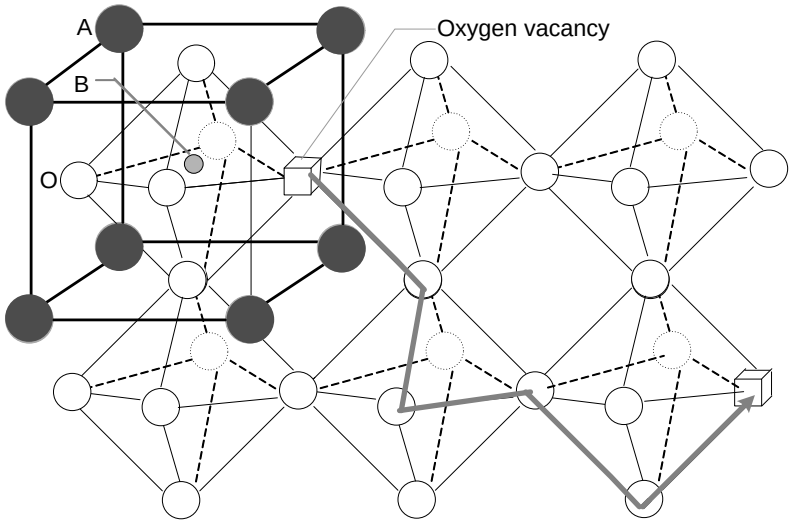

Figure 2-3 Atomic structure and oxygen travelling in the conducting perovskite $ABO_{3-\delta}$ (adapted from Adler (2004)).

To date, LSM has been the most common cathode because of its high electronic conductivity, relatively low cost and thermal expansion match with YSZ. Although many transition metals could be located at B-sites, Mn has the lowest reducibility that prevents large expansion during operation. In addition, LSM is the most thermodynamically stable of the mixed conductors containing cobalt or iron (Adler (2004); Singhal and Kendal (2003)).

Even though LSM is one of the most promising cathode materials for conventional SOFCs, its performance decreases when the operating temperature decreases. Although LSM has been modified by adding doped ceria such as GDC, the oxygen surface exchange coefficient and oxygen diffusion coefficient values of LSM are relative low for intermediate temperatures. Certain alternative materials have been used as cathodes:

- $La_{0.6}Sr_{0.4}Co_{0.2}Fe_{0.8}O_3$-$Ce_{0.7}Bi_{0.3}O_{0.2}$ (LSCF-CBO) composite shows very low specific resistivity at about 700°C (Zhao et al. (2004)).

- Composite cathodes consisting of $Sm_{0.5}Sr_{0.5}CoO_3$ (SSC) and SDC cathode and a dense SDC electrolyte resulted in a significant reduction in the interfacial resistance to 0.18 $V.cm^2$ at 600°C under open circuit condition (Xia et al. (2002)).
- At 700°C, in humidified H_2, a maximum power density of 250 $mW.cm^{-2}$ was obtained when Ni-YSZ, YSZ, and $La_{0.75}Sr_{0.25}CuO_{2.5-\delta}$ (LSCu) were used as an anode, electrolyte, and cathode (Ni-YSZ//YSZ//LSCu), respectively (Yu et al. (2005)).
- Zheng et al. (2005) used similar materials as Yu et al. (2005) but LSCu was replaced by $La_{0.6}Sr_{0.4}CoO_{3-\delta}$ (LSC) resulting in a maximum power density of 100 $mW.cm^{-2}$ at 700°C.
- $Ln_{0.6}Sr_{0.4}Co_{0.2}Fe_{0.8}O_{3-\delta}$ (Ln = Ce, Sm, Gd, Dy) compounds were prepared by glycine-nitrate-process. All compounds had a good chemical compatibility with SDC. The highest catalytic activity was obtained with $Dy_{0.6}Sr_{0.4}Co_{0.2}Fe_{0.8}O_{3-\delta}$ (Dy-SCF). A good cathode material for IT-SOFCs would then be Dy-SCF (Gao et al. (2003)).

2.4.3 Anode Materials

Requirements for the anode material include stability under operating conditions, high electrical conductivity, minimum chemical reactivity and diffusivity with other cell components, thermal expansion similar to that of the electrolyte, stable pore structure, stable reactivity for steam reforming and electrocatalysis (Brown et al. (2000)). The porosity of the electrodes not only provides the transport of fuel and products, but also increases the number of active sites.

Originally, platinum and certain transition metals were tested as anodes. However, no pure metal meets all requirements of an anode. For example, platinum tends to delaminate from the cell over long operating times, while nickel also agglomerates at high temperatures. Nonetheless, nickel has been considered as an active metal species because of its electrical conductivity, catalytic activity and cost. Furthermore, the addition of YSZ lowers its agglomeration tendency and the adjustment of thermal expansion between Ni anode and YSZ electrolyte (Minh and Takahashi (1995)).

To improve the performance or stability of Ni/YSZ, the Ni-based anode can be modified or changed using the following methods:

- Addition of some transition metals (Ti, Cr, Mn and Pd), a small amount of some precious metals, or some alkali oxides to prevent carbon deposition and/or to promote reforming reaction
- Replacement of Ni by Ni alloys or other alloys to limit carbon deposition

- Addition of a functional layer to reduce electrode interface resistance and/or to inhibit carbon deposition
- Replacement of YSZ by ScSZ to achieve higher ionic conductivity
- Replacement of YSZ by doped ceria for IT-SOFCs to achieve acceptable ionic conductivity at intermediate temperatures
- Use of new materials such as Cu-based anode or perovskites to improve fuel cell performance and stability

Details about these different methods to improve the anode are given in section 2.7.

2.5 Advantages and Disadvantages of SOFCs

There are four distinct benefits to using SOFCs when producing electricity.

- Clean conversion of chemical energy to electricity
- Fuel flexibility because they operate at temperatures where CO is not a catalyst poison, thus allowing for internal reforming of hydrocarbon to take place at the anode
- High efficiency of electricity production in comparison to other systems
- High quality of exhausted heat

However, two drawbacks exist with the use of SOFCs, slowing its widespread application in the production of electricity:

- Limitation in the number of candidate materials and high cost of cell fabrication due to the high operating temperature
- Difficulty of scaling up SOFC because of material brittleness

2.6 SOFC Designs

Currently, the most promising cell configurations are the sealless tubular and planar designs. Because a leak is a major problem in an SOFC, the tubular design has an important advantage as sealing is not as much of an issue. However, despite sealing challenges, the planar design is the most common structure because it is simpler to manufacture and because its performance should theoretically be higher than that of the tubular design. A brief description of those two designs is given in the following sections.

2.6.1 Sealless Tubular Designs

This design was first proposed in 1980 and has been developed primarily by Siemens Westinghouse Power Corperation (SWPC). The cell is built up in layers on a closed end support tube made of the cathode materials such as $LaMnO_3$. An interconnect plate is placed directly onto the support tube and then the electrolyte is deposited, followed by deposition of the anode layer (Figure 2-4). The most important advantage is that this design eliminates the need of seals while the other SOFC designs require perfect seals (Singhal and Kendal (2003)). For cell operation, air is supplied via an injector tube located inside the support tube, whereas the fuel flows over the outside surface. This design is suitable for stationary power generation applications ranging from kW to MW size.

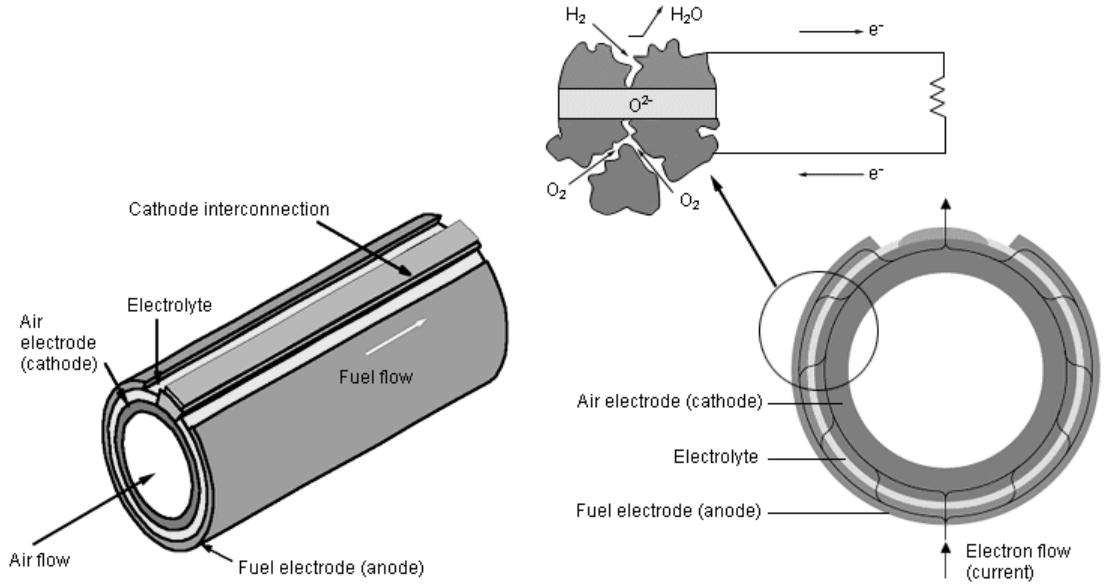

(a) (b)

Figure 2-4 Sealless tubular SOFC design (a) Schematic illustration of a Siemens Westinghouse tubular SOFC. (b) The cell operation and current path.

(Source: http://www.powergeneration.siemens.com/en/fuelcells/technology/tubular/index.cfm)

2.6.2 Planar Designs

In the planar single cell, the simplest geometry (Badwel and Foger (1996)) is composed of layers of each component (Figure 2-5). Cell configuration can be square or circular. The cell support can be cathode-supported, electrolyte-supported, or anode-supported types. However, many researchers have reported that the best performance was obtained from the anode-supported cell (Chan et al. (2001); Ivers-Tiffée et al. (2001)). Because of the simple geometry, the internal resistance can be minimized by forming a thin film for each layer. Therefore, the planar design provides higher performance and

power density than those of the tubular design. As mentioned before, nevertheless, this design requires a perfect seal at high temperature to separate the fuel, oxidant and outside environment.

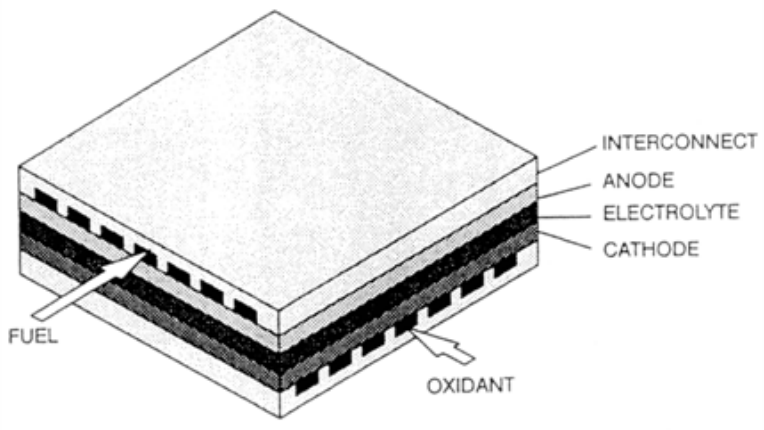

Figure 2-5 Planar SOFC design

(Source: Minh and Takahashi (1995)).

2.7 Literature Review on Anode Materials

As mentioned in the previous sections, several aspects are considered when materials are being developed for used an SOFC anode with internal reforming capability: stability under operating conditions, stable high electrical conductivity over the operating period, minimum chemical reactivity and diffusion of anode material into nearly component with other components, similar thermal expansion coefficients to that of other cell components, stable pore structure, and stable reactivity for electrocatalysis and internal reforming (Clarke et al. (1997)). This section first summarizes the efforts during the past two decades on developing state-of-the-art Ni-YSZ based anodes for high temperature operation (section 2.7.1). Then, it describes anode cermets being developed for IT-SOFCs, with a particular focus on ceria-based materials, which are the materials of interest in this thesis (section 2.7.2). Finally, work in other fields that used Ni-Cu-Mg composites is discussed, especially with respect to properties of this material (section 2.7.3).

2.7.1 Ni-based/YSZ cermet

Ni/YSZ is a good starting point for SOFC anode cermets because of their high electrical conductivity and catalytic activity for operation in the 800-1000°C range. However, many studies have shown that the structure of such Ni/YSZ is not stable for long-term operation due to changes in its structure.

Some materials have been developed and tested as alternative modified Ni/YSZ anode cermets. Details are given below.

A convenient method used to fabricate Ni/YSZ cermets is to blend commercial NiO and YSZ powders by mechanical mixing or ball milling. The mixture is then sintered at high temperature resulting in a NiO/YSZ anode cermet. The cermet is activated by reducing NiO to Ni, which is also accompanied by a volume reduction of ~25% and an increase in porosity due to changes in density (theoretical density is 8.9 $g.cm^{-3}$ for Ni and 6.96 $g.cm^{-3}$ for NiO). Properties of anode cermets are also related to the sintering temperature. Kawada et al. (1990) observed the lowest ohmic polarization resistance for Ni/8YSZ cermet anodes sintered at 1400°C. Jiang (2003) explained that this behaviour corresponds to the good formation of YSZ-to-YSZ network at 1400°C. Therefore, this high sintering temperature creates a good bonding of YSZ (anode)-to-YSZ(anode) and YSZ (anode)-to-YSZ (electrolyte), causing the formation of a grid YSZ structure to support the Ni phase and the formation of a good Ni-to-Ni electronic contact network after reduction. However, the effect of sintering temperature also depends strongly on the fabrication methods. For example, spray pyrolysis, which involves very fine powder, can lower the sintering temperature. With this technique, Fukui et al. (2002) obtained the highest electrical performance using an anode sintered at 1350°C. Other published methods include vapour-deposition (Ogumi et al. (1995)), wet powder spraying (Sammes et al. (1994)) and mechanical milling and plasma spray (Iwasawa et al. (1995)). Gorte and his group have had some success with tape casting combined with an impregnation technique (Gorte and Vohs (2003); Park et al. (2000)).

In addition to the conventional ceramic mixing methods, Ni/YSZ has also been prepared by other chemical techniques such as co-precipitation (Grgicak et al. (2006); Li et al. (2003)), modified Pechini-type methods (Razpotnik and Maček (2007)), and solution combustion of nitrate salt (Aruna et al. (1998)). These methods lead to fine powders with improved homogeneity (uniform concentration) and more uniform particle size. Grgicak et al. (2006) prepared the anode materials by a co-precipitation method and found that the pH of the solution was an important indicator of the product and the smaller the metal particle size-to-YSZ particle size ratio, the higher the performance. However, the particle size can be smaller only if it can still provide sufficient pore size to allow fuel to be transmitted. Therefore, the initial powder also affects the performance of fuel cell.

Electrical conductivity of Ni/YSZ materials is based on the Ni content, particle size and the particle size distribution. More specifically, it rises dramatically when the volume fraction of Ni increases to about 30% at 1000°C (Dees et al. (1987)). Huebner et al. (1995) reported that higher electrical conductivity was observed when the YSZ particles become larger, but decrease when Ni particles

become larger. Later, Huebner et al. (1999) found that the heat treatment and sintering temperatures also have an effect on the conductivity of the Ni/YSZ cermet anode. For 50 vol% Ni/ YSZ anode cermets sintered at 1300°C, the electrical conductivity of the anode was only about 4 $S.cm^{-1}$ at 1000°C but increased approximately to 800 $S.cm^{-1}$ when sintered at 1500°C.

Because state-of-the-art SOFCs operate at high temperatures (800-1000°C), the structure of the anode cermet is not stable for long-term operation causing cell degradation. The main reasons for the changes of the Ni/YSZ cermet are sintering (Iwata (1996); Tsogo (1996)), coarsening of Ni phase (Simwonis, (2000)), transformation of nickel into nickel hydroxide species (Gubner et al. (1997)), and, loss of active sites due to carbon deposition when hydrocarbon are involved (Kim et al. (2006); Lee et al. (2004); Irvinea et al. (1997)). Tsogo et al. (1996) found that the Ni in Ni/YSZ cermet becomes agglomerated owing to the poor wettability and the poor interaction between Ni and YSZ. However, this undesirable effect can be prevented by adding some transition metals, such as Ti, Cr, Mn and Pd (Naoumidis et al. (1995)) and/or applying effective milling and de-agglomeration to powders (Wilkenböner et al. (1997)). The last method yields very fine particles which leads to smaller resistance. For example, Primdahl and Mogensen (1997) and Brown et al. (2000) measured the electrochemical impedance loops for four different anodes at 1000°C in 97%H_2/3%H_2O. Those four different anodes were prepared with different ranges of powder sizes. The smallest overall electrode polarization of $0.19\,\Omega.\,cm^2$ was obtained with a very fine powder from 0.5 to 3 μm and the overall electrode polarization increased with increasing Ni size. It increased to Ω7.8 $.cm^2$ for 50 μm diameter Ni powder.

As discussed previously, an important advantage of SOFC is the possibility of direct internal reforming occurring simultaneously. Lin et al. (2005) examined the proper procedure for direct CH_4-fuelled SOFC. As expected, they suggested that the cell should be checked with hydrogen fuel before switching to methane fuel. The important information given in this work is the procedure when switching to dry methane. Operation must be maintained at constant current density near the level at maximum power density using hydrogen most of the time with a short interruption (~5 s). A period of 30-45 min is needed for the system to adjust to dry methane and a stable voltage should be gained within 2 h. A stable cell voltage was maintained for 168 h at a current density of 0.8 $A.cm^{-2}$ at 700ºC. Finnerty and Ormerod (2000) compared 50%vol and 90%vol Ni/YSZ tested with methane/steam mixture fuel. They obtained not only the operating condition including fuel composition but also optimum choice of anode formula that enhances performance and cell durability. Unfortunately, although Ni is very active for hydrocarbon reforming, it is also very active for catalyzing carbon formation. Many researchers have observed carbon deposition on Ni/YSZ anode cermets, e.g., He and

Hill (2007), He et al. (2005), Kim et al. (2002b), Takeguchi et al. (2002), and so on. Baker and Metcalfe (1995) showed that directly feeding dry CH_4 to a SOFC promoted more carbon deposition than humidified CH_4. They also measured the extent of deposited carbon using temperature-programmed and isothermal experiments. Carbon deposition can be reduced by adding alkali to the nickel catalyst, by adding precious metals such as ruthenium or rhodium (also good catalyst for reforming reactions), or by using higher steam-to-carbon ratio in the fuel stream. However, the use of precious metals is not feasible for commercial applications and the addition of water reduces the efficiency of the cell. Consequently, researchers have attempted to develop modified Ni/YSZ anodes or alternative anode materials in order to achieve long term stability with higher activity. Up to now, many efforts have been put into modifying the conventional Ni/YSZ anode cermet to improve its performance and stability, for example by adding an additive, by introducing a functional layer and/or by using Ni-based alloys or other metals instead of pure Ni. The efforts put into modifying Ni/YSZ anode cermets and the works on alternative materials are described in the following sections.

Additive

The activation energy for the methane/steam reforming reaction in the range of 75.5 to 98.4 kJ mol^{-1} on Ni/YSZ has been reported (Lee et al. (1990); Achenbach and Riensche et al. (1994); Odegard et al. (1995)). A higher activation energy of 118–294 kJ mol^{-1} was obtained when Ce was added into Ni/YSZ cermet. In addition, Ahmed and Foger (2000) proposed a rate expression for methane/steam reforming catalyzed by Ni/YSZ and Ni-based (Mg, Ca, Al, Sr, Ce and Ba)/YSZ as seen in equation (2-32). Ni/YSZ with these additives has much lower activation energy (208±10 kJ mol^{-1}) and higher pre-exponential factor for the reforming rates. In addition, the required steam-to-carbon ratio to prevent carbon deposition is lower from 3.0-5.0 down to 1.4-3.0.

$$-r_{CH_4} = k p_{CH_4}^{1.4\pm0.01} p_{H_2O}^{-0.8\pm0.02} \exp\left(\frac{-E_a}{RT}\right) \qquad 2\text{-}32$$

Takeguchi et al. (2002) found that among alkali earth oxides (MgO, CaO, SrO) and ceria, only the addition of CaO to Ni/YSZ by physical mixing was effective in reducing carbon deposition without deteriorating the reforming activity; however, addition of CaO slightly worsened the cell performance. Moon and Ryu (2003) have examined NiO-MgO and NiO catalysts for methane CO_2 reforming, as well as the performance of NiO-MgO/YSZ/LSM at 800°C operating with CH_4+CO_2. It was found that the activity of NiO-MgO catalyst was higher than that of NiO catalyst and the surface area of NiO-MgO catalyst increased after reaction while that of NiO decreased. Doping with a small amount of precious metals such as ruthenium, rhodium, or platinum is also catalytically active for

steam reforming and inhibits carbonaceous product formation (Takeguchi et al. (2003)). Molybdenum also acted as a good dopant to reduce carbon deposition on Ni/YSZ anode during methane reforming (Finnerty et al. (1998)).

Functional layer

Zhan and Barnett (2006) have tested an additional Ru/CeO_2 catalyst layer placed between the fuel stream and the anode for the internal partial oxidation reforming of iso-octane in SOFC operations. A constant output power density, as a result, has been found without coking on the anode cermet. Zr doped-ceria has been tested as an additional layer in humidified methane and humidified $CO+H_2$ (He and Hill (2007)). It appeared that this Zr doped-ceria functional layer was effective because less carbon was deposited and the deposited carbon was easier to remove. Another approach followed by Lin et al. (2006) was to place an inert porous layer between the anode and the fuel stream. This method decreased the critical current density, e.g. from 1.8 $A.cm^{-2}$ to less than 0.6 $A.cm^{-2}$ at 800°C. The critical current density is the lowest current density that provides stable cell voltage. This increased stable operating range was attributed to mass transport through the barrier layer. Murry et al. (1999), furthermore, reported the effect of an additional YDC (yttria doped-ceria) between the Ni/YSZ cermet anode and YSZ electrolyte. It resulted in a lower electrode interface resistance for methane oxidation due to the larger number of reaction sites.

Ni alloy and other stabilized zirconia

Among Ni-Co/YSZ, Ni-Cu/YSZ and Ni-Fe/YSZ (wet hydrogen), Ni-Co/YSZ has shown the lowest electrode polarization (Ringuedé et al. (2004)) for H_2 (wet) oxidation. Co in Ni-Co/YSZ prepared by co-precipitation and fired at 1100°C improved the cell performance for a methane-fuelled SOFC when compared to Ni/YSZ. The best composition was found to be $Ni_{0.5}Co_{0.5}$/YSZ (Sato et al. (2003)). However, Ni-Cu/YSZ was still considered as a good anode for preventing carbon deposition especially at low Ni content (Lee et al. (2004)). This study compared Cu/YSZ, Co/YSZ, Ni/YSZ, Cu-Co/YSZ and Cu-Ni/YSZ in terms of carbon formation by exposing them to dry n-butane at 500°C and in terms of power density at 500°C in dry H_2. The bimetallic anodes showed improved performance compared to Cu/YSZ and reduced carbon formation compared to Ni/YSZ or Co/YSZ. The Cu-Co/YSZ appeared to be more tolerant to carbon formation. Park et al. (2000) reported that the Cu/YSZ was close to inactive; however, the performance was improved after adding CeO_2 as a dopant. Cu-CeO_2 was also considered as a sulphur tolerant anode for SOFC (He et al. (2005b)) because it can be used with H_2 containing H_2S as high as 450 ppm when operating at 800°C. The use of Ru/YSZ cermet anode is also catalytically active for steam reforming and yielded a very high power density of 1550 $mW.cm^{-2}$ using hydrogen fuel (Sasaki et al. (1992)). However, some important

drawbacks, such as high cost and volatility above 1200°C (Vernoux et al. (1997)) still make the use of precious metals impractical. Boder and Dittmeyer (2006) introduced an anode that can reduce the cooling rate when methane is used as a fuel because methane reforming is a strongly endothermic reaction, by coating copper on Ni/YSZ via an impregnation technique.

It was reported that scandia-stabilized zirconia (ScSZ) has the highest electrical conductivity among zirconia based materials (Badwal (1983)). Mizutani et al. (1994) confirmed that the electrical conductivities of ScSZ are about double that of YSZ at 1000°C. The performance of SOFCs with a Ni/ScSZ anode and a Ni/YSZ anode have been examined in humidified H_2 and humidified CH_4 (Sumi et al. (2004)). In 3% H_2O–CH_4 at 1000°C, the Ni/ScSZ anode provided a power density of 850 $mW.cm^{-2}$ without any drop over 250 h. At the same condition, in contrast, a cell with Ni/YSZ anode showed an initial power density of 800 $mW.cm^{-2}$ that degraded to 600 $mW.cm^{-2}$ after 250 h. Gunji et al. (2004) investigated internal reforming of CH_4 on Ni/ScSZ in SOFC operating at 800°C and 900°C. The stability of the cell voltage and the amount of carbon suggested that carbon deposition is hindered more effectively at higher temperature under operation at high current density. For ethane fuel at a low steam/carbon (S/C) ratio of 1.2 mol%H_2O–98.8 mol% C_2H_6, Yamaji et al. (2006) observed that the amount of carbon at 600°C was smaller than that at 700°C. They also reported that too low of a utilization factor (e.g. below 46% at 550°C) leads to unstable operation due to carbon deposition. CeO_2 must also be added to Cu/ScSZ (Ye et al. (2007)). Another interesting composite anode is $Ni_{1-x-y}Mg_xAl_yO$/ScSZ; Mg can lower the reducing rate to prevent Ni agglomeration and also can promote the reforming reaction on Ni (Shiratori et al. (2006)). Later, Shiratori and Sasaki (2008) studied the stability of NiO/ ScSZ and $Ni_{0.9}Mg_{0.1}O$/ScSZ anode under dry reforming of simulated biogas mixtures ($CH_4/CO_2/N_2$). Although the activity of methane reforming was better in $Ni_{0.9}Mg_{0.1}O$/ScSZ anode, it was less stable than that of NiO/ScSZ due to a higher ohmic loss in $Ni_{0.9}Mg_{0.1}O$/ScSZ. It should be noted that ScSZ is more expensive than YSZ.

At this time, IT-SOFCs (intermediate temperature solid oxide fuel cells) operating in the temperature range from 500°C to 800°C have been increasingly researched due to the combination of cost effectiveness with high efficiency, multi-fuel functions and a wider range of available materials. However, the ionic conductivity of the conventional electrolyte YSZ is too low because a basic requirement for conductivity at 600°C is about 10^{-1} S cm^{-1}, whereas YSZ reaches this conductivity only at 1000°C. To meet this requirement, stabilized zirconia has been replaced by doped-ceria, as described in detail in the next section.

2.7.2 Anode for IT-SOFCs (focusing on metal-doped ceria)

The conventional state-of-the-art SOFC (Ni-YSZ//YSZ//LSM-YSZ) produces in small maximum power densities when operated as an IT-SOFC (Koh et al. (2002)). At 700°C, in humidified H_2, Ni-YSZ//YSZ//cathode provided a maximum power density of 100 $mW.cm^{-2}$ and 250 $mW.cm^{-2}$ with LSCu and LSC, respectively (Yu et al. (2005); Zheng et al. (2005)). Zhang et al. (2006) tested a conventional SOFC using screen-printing technology to fabricate a thin electrolyte film resulting in a considerably higher maximum power density; unfortunately, it cannot be used when the operating temperature is lower than 600°C. Murray et al. (1999) disclosed that an additional YDC layer between electrode and electrolyte can improve the performance of the conventional material at low temperature so as to be useful for IT-SOFCs.

As shown in Table 2-3, Table 2-4 and Table 2-5, SDC and GDC have a high ionic conductivity. Besides, Ni-ceria cermet also exhibited higher fuel electrode performance (Eguchi (1997)). Therefore, Ni-doped ceria anode cermets are more attractive for IT-SOFCs due to the performance of the cell at low temperature. Ni/SDC, for example, is a better anodic electrocatalyst for SOFCs than Ni/YSZ because of the higher OCV and the lower degree of polarization. A 60wt% Ni/SDC anode sustained high activity and stability when fed with diluted methane even though coking occurred to a certain extent (Wang et al. (2003)). Wang concluded that this was the result of a good Ni-Ni, SDC-SDC and Ni-SDC network. Xia et al. (2001) showed the possibility of operating IT-SOFCs at temperatures as low as 450°C and at a power density of 192 $mW.cm^{-2}$ in humidified CH_4. Zhang et al. (1999), nonetheless, recommended a sintering temperature of Ni/SDC on LSGM electrolyte of 1300°C to avoid interface diffusion and to help grain growth. Ni/SDC coated with SDC using vacuum impregnation exhibited very high performance and OCV without significant degradation. A 600°C, Zhu et al. (2006) obtained a maximum power density of 400-500 $mW.cm^{-2}$ and a power density as high as 571 and 353 $mW.cm^{-2}$ when exposed to humidified hydrogen and methane, respectively. It was even higher in some anode-supported cells containing thin electrolytes (Shao and Haile (2004); Leng et al. (2004); Zha et al. (2004)). Tomita et al. (2006) tried to increase the performance of a cell not only by using a thin electrolyte layer but also by adding an ionically conducting layer. With addition of an ion conductor layer, the maximum power increased about 20% from the results obtained with a thin electrolyte layer. Ni/GDC was also tested as a anode cermet; however, the maximum power densities were lower than Ni/SDC anode (Meng et al. (2002)). Chen et al. (2009) frabicated NiO/SDC via a urea combustion technique and fabricated this anode on YSZ by a slurry spin method. This procedure increased the maximum power density by 66.2 $mW.cm^{-2}$ at 800°C in $40\%H_2/N_2$.

Asamoto et al. (2008) used electrophoretic deposition (EPD) technique to fabricate Ni/SDC onto ScCSZ ($(ScO_{1.5})_{0.18}(CeO_2)_{0.01}(ZrO_2)_{0.18}$) electrolyte and reported that this technique can produce a cell that showed higher performing cell with dry methane than using a slurry coating. Later, this group studied the effect of additional alkaline earth oxide. Asamoto et al. (2009) introduced MgO, CaO and SrO in the Ni/SDC anode and tested their use with dry methane. They lowered the maximum power density, but a positive effect on the reduced the extent of carbon deposition.

Kawano et al. (2007) prepared a Ni:SDC composite anode by spray pyrolysis and fed the cell with steam/ methane mixtures in the temperature range of 700-1000°C. The methane conversions at 1000°C were in the range of 30-40% , whereas those at 700 and 800°C were only 12% . Moreover, the performance at 700 and 800°C were much lower than that at 1000°C and the anode microstructures were destroyed significantly by deposited carbon. A Ni:SDC anode was synthesized by a urea-combustion technique in Chen et al. (2008). After reduction, they measured the open porosity, thermal expansion and mechanical properties with respect to the volume content of Ni. The optimum Ni contents were 50-60 vol.% Ni. These compositions provide an open porosity greater than 30% and electrical conductivities over 1000 S/cm at 600-800°C. Iido et al. (2007) evaluated the rates of carbon deposition on five different anodes. Among them, Ni/SDC showed the highest rate of carbon deposition followed by Ni/YSZ, Ni/ScSZ, Ni-Ru/YSZ, and Ru/YSZ, respectively. They concluded that the rate of carbon deposition depended on both the oxide species and the metal.

Another metal used in anodes is Cu. Gorte and co-workers have spent considerable effort to develop Cu/oxide cermet anodes using wet impregnation due to the low melting point of copper. They constructed a dual tape with the wafer layer being placed on the dense layer. A 50:50 mixture of LSM and YSZ was painted on the other side of the dense layer, then calcined to 1250°C to form the cathode. The wafer layer was then impregnated with an aqueous solution of $Ce(NO_3)_3{\cdot}H_2O$, then calcined at 500°C to form CeO_2 followed by impregnation of an aqueous solution of $Cu(NO_3)_2{\cdot}H_2O$ (and $Ni(NO_3)_2{\cdot}H_2O$ solution if needed) and calcined at the same temperature (Gorte and Vohs (2003)). CeO_2 must be present because Park et al. (2000) found that Cu/YSZ itself is close to inactive. A Cu-CeO_2-SDC anode cermet investigated by Lu et al. (2003), allowed butane to be used as a fuel. Ye et al. (2007) applied a similar technique for Cu-CeO_2-ScSZ and found no visible carbon formation; the performance was good enough for it to be considered as an alternative anode material for SOFC fuelled by ethanol. $Ni_{0.95}Cu_{0.05}$/SDC was compared with Ni/SDC and Cu-impregnated Ni/SDC in terms of their performance and the amount of deposited carbon (Wang et al., 2008). $Ni_{0.95}Cu_{0.05}$/SDC were synthesized by the glycine–nitrate process. Anode-supported cell was prepared by pressing the anode then co-pressing the electrolyte with the anode disc. The cathode was coated on

the disc at the final step. They found that Cu-impregnated Ni/SDC yielded the highest conductivity followed by $Ni_{0.95}Cu_{0.05}$/SDC and Ni/SDC, respectively. Moreover, Cu-impregnated Ni/SDC showed the maximum power density as high as 317 $mW.cm^{-2}$ at 600°C in dry methane with the lowest amount of carbon deposition.

In addition to single metals, Ni-Cu alloys, Cu-Co alloys, Ni-Fe alloys and Fe-Co-Ni alloys have also been investigated. Kim et al. (2002b) have examined the used of Ni-Cu alloys as anode for the direct oxidation of methane at 800°C. Weight gain upon exposure to CH_4 at 700°C was observed and the changes were larger on the sample having more Ni. In addition, two interesting results were obtained on the plots of cell potential and power density after completion of the 500 h test and the impedance spectra at different times. Maximum power densities of 440 $mW.cm^{-2}$ for H_2 and 330 $mW.cm^{-2}$ for CH_4 were reported, as well as reduction in diffusional resistance with carbon deposition. Consequently, coke must not block a substantial fraction of pore volume and fingers of YSZ electrolyte extend into the anode region during operation to increase the transfer of O^{2-} ion. The use of Cu, Co, Ni, Cu-Ni and Cu-Co, anode cermets, was assessed in SOFC fuelled separately by dry H_2 and by dry n-butane (Lee et al. (2004)). Cu-Ni is completely miscible, whereas Cu-Co should have a strong tendency for Cu to coat the surface of Co. The weight gain of anodes exposed in n-butane oxidation at 700°C for 10 minutes was found to be in the following order Cu <Cu-Co<Cu-Ni<Co<Ni.

With dry H_2, the performances of SOFC cell fabricated by bimetallic anodes were higher than those of a Cu anode and improved steadily with increasing Ni content. Unlike the case of Cu-Co alloys, the amount of added Co did not seem to make a significant difference. Nonetheless, in dry n-butane, the performances of the cells made from both bimetallic anodes Cu-Co and Cu-Ni were similar. Sin et al. (2007) have also investigated the performance of Ni-Cu alloy/CGO in terms of catalytic activity and tolerance to carbon deposition when exposed to dry and humidified CH_4. For both fuels, the power density of the cell after 120 h of operation was higher than that of the cell after 20 h while the resistance was lower; the reason was attributed to the modification of the anode porosity during the operation. Besides, the amount of CO_2 detected from dry CH_4 was significantly higher than that with humidified CH_4; however, these species were not found to degrade the cell performance during about 1300 h of operation. These implied that the material gave a good compromise between catalytic activity and carbon tolerance. Another type of bimetallic alloy tested in IT-SOFC operation is Ni-Fe (Yan et al. (2005)). It exhibited excellent performance when working with SDC interlayer/ LSGM but there was no mention about its stability. Hung et al. (2004) investigated the use of Me/SDC (Me= Cu-Ni, Cu-Fe and Cu-Co) in methane steam reforming. The experiments of methane steam reforming were carried out in a fixed-bed quartz tube reactor and the highest methane conversion was observed

on 80 wt%Cu- 20wt% Ni/SDC. $Fe_xCo_{0.5-x}Ni_{0.5}$/SDC anodes were also studied (Xie et al. (2006)); interfacial polarization resistances and I-V curves were measured and compared with Ni/SDC at temperatures between 450 and 600°C in humidified H_2. The trimetallic anodes possessed lower resistances with higher power density. Tavares et al. (2008) created a different process to prepare (Ni-CeO_2)-Cu/SDC anode. Cu/SDC was first deposited on the SDC to prepare an electrolyte-supported cell followed by impregnating $Ce(NO_3)$ and $Ni(NO_3)$ solution on the anode side. The cell was tested with humidified hydrogen and methane at 500-700°C. A maximum power density of 250 $mW.cm^{-2}$ was observed both at 600°C in humidified hydrogen and at 700°C in humidified methane at 700°C. With this cell type, the ohmic loss at the electrolyte membrane was the main contribution to the total voltage loss.

Barnett and co-workers are among the leading researchers on perovskite-based anode materials. They have developed anodes based on LSCV that also contained GDC and a small amount of NiO. The cells, fabricated with this anode showed reasonably good performance for a few hours with a variety of humidified alkanes including CH_4, C_2H_6, C_3H_8, and C_4H_{10} and exhibited overall stability for over 250 h (Madsen and Barnett (2005)). Although they observed slight degradation because of carbon deposition, the cell performance could be recovered by switching to H_2 fuel or by exposing the anode to air. Peña-Martínez et al. (2006) studied the performance of SOFCs made of perovskite materials for all components. They used four different cells with similar anode (LSCM) and electrolyte (LSGM), but different cathodes LSM or BSCF, noting that some had thin SDC as a buffer layer between electrolyte and anode. However, the use of the interlayer did not help to improve the electrochemical performance. Gong et al. (2010) used an electrolyte-supported cell with $LaSr_2Fe_2CrO_{9-\delta}$ (LSFeCr)-GDC anode for a phosphine-containing fuel. This cell degraded within 24 h due to the decomposition of LSFeCr. A triple layer of SDC/LSGM/SDC electrolyte film was fabricated with PBCO ($PrBaCo_2O_{5+\delta}$)/SDC cathode and NiO/SDC anode by Zhu et al. (2010). They concluded that a cathode with trilayer electrolyte membrane achieves excellent performance for IT-SOFCs yielding 741 $mW.cm^{-2}$ maximum power density at 800°C under dry hydrogen. Maximum power densities of some materials studied as anode in single planar cells for IT-SOFCs (temperatures between 400°C and 850°C) are summarized in Table 2-6.

Table 2-6 Maximum power densities of some SOFC single cells for IT-SOFCs.

Anode cermet	Fuel	Temp (°C)	Max power density ($mW.cm^{-2}$)	Reference
50wt%Ni-50wt%YSZ//YSZ// 50wt%LSM-50wt%YSZ[a]	H_2	650	100	Koh et al. (2002)
		750	300	
		850	500	
Ni-YSZ//YSZ//LSCu[a]	Humidified H_2	700	250	Yu et al. (2005)
		750	400	
		800	650	
Ni -YSZ//YSZ//$La_{0.6}Sr_{0.4}CoO_3$[m]	Humidified H_2	700	100	Zheng et al. (2005)
		750	160	
		800	250	
		850	390	
50wt%Ni-50wt%YSZ//(31μm)YSZ //60wt%LSM-40wt%YSZ[a]	Humidified H_2	650	180	Zhang et al. (2006)
		700	330	
		750	580	
		800	970	
		850	1300	
Ni-YSZ//YDC/YSZ/YDC//LSM[c]	Humidified CH_4	550	125	Murray et al. (1999)
		600	250	
		650	370	
Ni-SDC//SDC//SSC-10 wt%SDC[a]	Humidified H_2	450	128	Xia et al. (2001)
		500	188	
		550	240	
		600	397	
	Humidified CH_4	500	78	
		550	195	
		600	304	
Ni-SDC//SDC//LSCF[a]	Humidified H_2	600	400	Xia et al. (2004)
		650	580	
		700	750	
Ni-SDC//SDC//50 wt%CSCF-SDC[a]	H_2	600	209	Fang et al. (2004)
		650	306	
		700	388	

Anode cermet	Fuel	Temp (°C)	Max power density ($mW.cm^{-2}$)	Reference
Ni-SDC//SDC//SSC-30 wt%SDC[a]	Humidified H_2	600	360-571	Zhu et al. (2006)
	Humidified CH_4	600	254-353	
50wt%Ni-50wt%SDC //GDC(30μm)//SSC[a]	Humidified H_2	500	~200	Tomita et al. (2006)
		550	~400	
		600	593	
		650	~620	
		700	~700	
50wt%Ni-50wt%SDC //GDC/BCY/GDC//SSC[a]	Humidified H_2	500	~260	
		550	~480	
		600	731	
		650	~950	
		700	~1040	
Ni-SDC (50wt%: 50wt%) //GDC/BCY/GDC//SSC[a]	CH_4	500	~180	
		550	~350	
		600	611	
		650	~780	
Ni-SDC (60wt%:40%) //SDC(20μm)//BSCF[a]	Humidified H_2	600	1010	Shao and Haile (2004)
Ni-SDC (65wt%:35%) //GDC(10μm)//LSCF[a]	Humidified H_2	600	578	Leng et al.(2004)
Ni-SDC (65wt%:35%) //GDC(20μm)//SSC[a]	Humidified H_2	600	602	Zha et al.(2004)
Ni-SDC (65wt%:35%) //GDC(26μm)//SSC[a]	Humidified H_2	600	270	Xai and Lui (2001)
Ni-SDC (65wt%:35%) //YDC(15μm)//SSC[a]	Humidified H_2		230	Peng et al.(2002)
Ni-SDC (50:50 wt %) //SDC//SSC-30 wt% SDC[a]	Humidified H_2	600	491	Yin et al. (2006)
		550	370	
		500	130	
		450	50	
Ni-SDC //SDC//SSC-SDC[a]	Dry CH_4	600	240	Wang et al. (2008)
Cu impregnated Ni-SDC //SDC//SSC-SDC[a]			338	
$Ni_{0.95}Cu_{0.05}$/SDC//SDC//SSC-SDC[a]			317	

Anode cermet	Fuel	Temp (°C)	Max power density ($mW.cm^{-2}$)	Reference
Ni-SDC//GDC//SSC-30 wt%SDC [a]	Humidified H_2	600	540	Xie et al. (2006)
		550	250	
		500	100	
		450	30	
Ni-GDC (40wt%:60%) //YDC-LiCl//$LiNiO_2$	Humidified H_2	525	200	Meng et al. (2002)
		575	240	
Ni-GDC (40wt%:60%) //GDC-LiCl-$SrCl_2$//$LiNiO_2$	Humidified H_2	525	200	
		575	260	
		600	310	
		650	380	
Ni-SDC//ScCSZ//Pt[e]	Dry CH_4	700	40.3	Asamoto et al. (2009)
Ni-CaO-SDC//ScCSZ//Pt[e]			35.6	
Ni-SrO-SDC//ScCSZ//Pt[e]			21.7	
Ni-MgO-SDC//ScCSZ//Pt[e]			14.3	
(Ni-CeO_2)Cu-SDC//ScCSZ//Pt-PrO_{2-x}[e]	Humidified H_2	600	~250	Tavares et al. (2008)
		550	~170	
		500	~70	
	Humidified CH_4	700	~250	
		650	~190	
		600	~140	
Cu-CeO_2-SDC (anode)[a]	C_4H_{10}	600	~40	Lu et al. (2003)
		650	~75	
		700	~175	
	Humidified H_2	600	~70	
		650	~120	
		700	~250	
21.5 wt%Cu-8.5 wt%CeO_2-ScSZ//ScSZ//$(Pr_{0.7}Ca_{0.3})_{0.9}MnO_3$[a]	Humidified H_2	700	130	Ye et al. (2007)
		750	234	
		800	372	
	Humidified C_2H_5OH	700	94	
		750	139	
		800	222	

Anode cermet	Fuel	Temp (°C)	Max power density ($mW.cm^{-2}$)	Reference
20 wt%Cu-10 wt%CeO_2-ScSZ//ScSZ//$(Pr_{0.7}Ca_{0.3})_{0.9}MnO_3$[a]	Humidified C_2H_5OH	700	122	Ye et al. (2007)
		750	220	
		800	322	
18 wt%Cu-12 wt%CeO_2-ScSZ//ScSZ//$(Pr_{0.7}Ca_{0.3})_{0.9}MnO_3$[a]	Humidified C_2H_5OH	700	122	
		750	205	
		800	310	
15 wt%Cu-15 wt%CeO_2-ScSZ//ScSZ//$(Pr_{0.7}Ca_{0.3})_{0.9}MnO_3$[a]	Humidified C_2H_5OH	700	122	
		750	220	
		800	322	
20 wt% Cu-CeO_2-YSZ[a]	H_2	700	220	Lee et al. (2004)
20 wt% $Cu_{0.95}Ni_{0.05}$-CeO_2-YSZ[a]			275	
20 wt% $Cu_{0.8}Ni_{0.2}$-CeO_2-YSZ[a]			300	
20 wt% $Cu_{0.7}Ni_{0.3}$-CeO_2-YSZ[a]			340	
20 wt% $Cu_{0.9}Co_{0.1}$-CeO_2-YSZ[a]			310	
20 wt% $Cu_{0.8}Co_{0.2}$-CeO_2-YSZ[a]			320	
20 wt% $Cu_{0.5}Co_{0.5}$-CeO_2-YSZ[a]			330	
20 wt% $Cu_{0.95}Ni_{0.05}$-CeO_2-YSZ[a]	n-butane	700	125	
20 wt% $Cu_{0.8}Ni_{0.2}$-CeO_2-YSZ[a]			130	
20 wt% $Cu_{0.7}Ni_{0.3}$-CeO_2-YSZ[a]			140	
20 wt% $Cu_{0.9}Co_{0.1}$-CeO_2-YSZ[a]			110	
20 wt% $Cu_{0.8}Co_{0.2}$-CeO_2-YSZ[a]			130	
20 wt% $Cu_{0.5}Co_{0.5}$-CeO_2-YSZ[a]			140	
20 wt% Cu-CeO_2-YSZ[a]	H_2	800	420	
20 wt% $Cu_{0.5}Co_{0.5}$-CeO_2-YSZ[a]			570	
20 wt% Cu-CeO_2-YSZ[a]	n-butane	800	300	
20 wt% $Cu_{0.5}Co_{0.5}$-CeO_2-YSZ[a]			360	
10 wt% $Cu_{0.6}Ni_{0.4}$-CeO_2-YSZ[a]	H_2 (500h)	800	440	Kim et al. (2002)
	CH_4 (500h)	800	330	
50wt%NiCu alloy-50wt%GDC //GDC//LSFCO[e]	CH_4 (500h)	650	~90	Sin et al.(2007)
		700	~180	
		750	~230	
		800	~320	
60 wt% (9:1 Ni:Fe) -SDC // SDC / LSGM (0.4/5μm)//SSC[a]	H_2	400	80	Yan et al. (2005)
		500	112	
		600	1951	
		700	3270	

Anode cermet	Fuel	Temp (°C)	Max power density ($mW.cm^{-2}$)	Reference
$Fe_{0.2}Co_{0.3}Ni_{0.5}$-SDC //GDC//SSC-30 wt%SDC [a]	Humidified H_2	600	600	Xie et al. (2006)
$Fe_{0.3}Co_{0.2}Ni_{0.5}$-SDC //GDC//SSC-30 wt%SDC [a]			490	
$Fe_{0.1}$ $Co_{0.4}Ni_{0.5}$-SDC //GDC//SSC-30 wt%SDC [a]			400	
$Fe_{0.4}$ $Co_{0.1}Ni_{0.5}$-SDC //GDC//SSC-30 wt%SDC [a]			385	
$Fe_{0.25}Co_{0.25}Ni_{0.5}$-SDC //GDC//SSC-30 wt%SDC [a]			750	
$Fe_{0.25}Co_{0.25}Ni_{0.5}$-SDC //GDC//SSC-30 wt%SDC [a]		550	350	
$Fe_{0.25}Co_{0.25}Ni_{0.5}$-SDC //GDC//SSC-30 wt%SDC [a]		500	150	
$Fe_{0.25}Co_{0.25}Ni_{0.5}$-SDC //GDC//SSC-30 wt%SDC [a]		450	50	
47.5 wt% LSCV- 47.5 wt%GDC- 5 wt% NiO//GDC//LSCF[e]	Humidified H_2	600	96.8	Madsen and Barnett (2005)
		650	124	
		700	114	
		750	144	
	Humidified CH_4	700	107	
	Humidified C_2H_6	700	105	
	Humidified C_3H_8	700	128	
	Humidified C_4H_{10}	700	85	
LSCM//LSGM//BSCF[e]	H_2	600	34	Peña-Martínez et al. (2006)
LSCM//LSGM//LSM[e]			20	
LSCM//SDC(interlayer)/LSGM //LSM[e]			7	
LSCM//LSGM//LSM-LSGM[e]			5	
LSCM//LSGM//BSCF[e]		800	160	
LSCM//LSGM//LSM[e]			133	
LSCM//SDC(interlayer)/LSGM //LSM[e]			60	
LSCM//LSGM//LSM-LSGM[e]			35	

Anode cermet	Fuel	Temp (°C)	Max power density ($mW.cm^{-2}$)	Reference
LSFeCr-GDC//LSGM//LSCF-GDC[e]	Dry H_2	800	355	Gong et al. (2010)
	Humidified H_2		341	
PBCO-30SDC//SDC/LSGM/SDC//Ni-SDC[a]	Dry H_2	600	130	Zhu et al. (2010)
		650	231	
		700	364	
		750	521	
		800	741	

e Electrolyte supported cell

c Cathode supported cell

m Metal supported cell

2.7.3 Interesting properties of Ni-Cu-MgO

Ni-Cu/SDC was examined as a catalyst for methane reforming by Huang and Jhao (2006). They reported that methane dissociated only on Ni and the copper led to a higher active surface area with higher reactivity for CO_2 dissociation. Although methane steam reforming is not active over Cu/SDC, H_2O dissociation activity over Cu/SDC is better than over Ni/SDC because of enhanced water-gas shift activity. Gac et al. (2009) introduced MgO into Ni-Al_2O_3 by co-precipitation. This additional magnesium oxide yielded smaller and strongly dispersed nickel crystallites. MgO-rich catalysts acted as stronger adsorption sites than catalyst without MgO. This effect increased the rate of methane decomposition and caused carbon to deposit with different structures. Normally, carbon filaments form on NiO catalysts but the addition of MgO generated more densely packed graphite layers or thinner walls. In the case of slow removal rate, this catalyst could be deactivated rapidly. Li et al. (2004) showed that Ni-Mg-Cu alloy is a better hydrogen storage system than Mg_2Ni systems.

Chapter 3
Experimental

For clarification, the tests in this study are categorized into three different types: methane steam reforming (SMR), electrochemical measurements, and material characterizations. However, they are closely related and reflect the simultaneous phenomena of chemical reactions, electrochemical reactions and transport phenomena (gas and charge transport) occurring at the anode, especially for the CH_4-fueled SOFC (Figure 2-1). The requirements of the anode in this case are that it must catalyze CH_4 to produce H_2 and CO without depositing carbon, be a good electronic conductor to minimize the inhibition of electromotive force, and also be stable to maintain its desired composition and microstructure. The SMR tests are used to determine the catalytic activity of the alternative anode. The electrochemical measurements evaluate the performance of button cells made using the alternative anode. Finally, the material compositions/phases/structures are identified before and after SMR by material characterization. The combination of all the information may reveal the correlation of the material to the catalytic activity and the cell performance.

3.1 Methane Steam Reforming and Water Gas Shift Reaction

Methane steam reforming is the most common process to generate hydrogen. It involves the catalytic conversion of methane into a hydrogen-rich gas. Methane steam reforming (global reaction shown in Equation 3-1) is a highly endothermic reaction that requires a large amount of steam in the presence of a suitable catalyst. In addition to the steam reforming reaction, the water-gas shift reforming reaction (Equation 3-2) is inevitable.

Methane steam reforming (SMR) $CH_{4(g)} + H_2O_{(g)} \leftrightarrow CO_{(g)} + 3H_{2(g)}$ $\Delta H°$=206 kJ/mol (3-1)

Water gas shift reaction (WGS) $CO_{(g)} + H_2O_{(g)} \leftrightarrow CO_{2(g)} + H_{2(g)}$ $\Delta H°$=-41 kJ/mol (3-2)

Methane steam reforming is usually carried out at 700-800°C over nickel-containing catalysts in a greater-than-stoichiometric amount of steam (two- to four- fold). Methane steam reforming is affected by operating pressure, temperature and the ratio of steam to carbon (S/C) in the feed gas. Thermodynamically, methane steam reforming is favoured at low pressure, high temperature and high S/C ratio. Under these conditions, the water-gas shift (WGS) reaction takes place simultaneously, converting CO and H_2O to CO_2 and H_2. Typically, the catalyst is deactivated via deposition of carbon; nonetheless, the catalytic deactivation can be prevented by elevating the pressure and increasing the steam content (hence the high S/C ratio in practical reforming operations).

The most likely reactions leading to the formation of carbon/coke deposition are the following:

Methane cracking $$CH_{4(g)} \leftrightarrow C_{(s)} + 2H_{2(g)} \quad (3\text{-}3)$$

Boudouard $$2CO_{(g)} \leftrightarrow C_{(s)} + CO_{2(g)} \quad (3\text{-}4)$$

CO hydrogenation $$CO_{(g)} + H_{2(g)} \leftrightarrow C_{(s)} + H_2O_{(g)} \quad (3\text{-}5)$$

The formation of carbon is a serious problem in solid oxide fuel cells. Carbon deposition results in anode deactivation because deposited carbon can plug the gas flow and block active sites which lead to a loss of cell performance and poor durability. Even worse, carbon deposition (e.g. in the form of carbon whisker) can cause fracturing and permanent damage to the cell.

Several 50wt% $Ni_{1-x-y}Cu_xMg_yO$/ 50wt% SDC samples are tested at different S/C ratios. The conditions of S/C ratio is first chosen to be 3 (the most favourable situation to prevent coking) at 750°C and 650°C. Then, S/C is progressively decreased to 2, 1 and 0.

The SMR reactions are characterized in terms of methane conversion, species yield and selectivity, described in equations (3-6), (3-7) and (3-8), respectively.

$$\%conversion = \frac{\left(Molar\ flow\ rate\ of\ CH_{4(in)} - Molar\ flow\ rate\ of\ CH_{4(out)}\right)}{Molar\ flow\ rate\ of\ CH_{4(in)}} \times 100 \quad (3\text{-}6)$$

$$species\ i\ yield = \frac{Molar\ flow\ rate\ of\ species\ i}{\left(Molar\ flow\ rate\ of\ CH_{4(in)} - Molar\ flow\ rate\ of\ CH_{4(out)}\right)} \quad (3\text{-}7)$$

$$species\ i\ selectivity = \frac{Molar\ flow\ rate\ of\ species\ i}{Total\ molar\ flow\ rate\ of\ all\ product\ species} \quad (3\text{-}8)$$

The activity and stability of the developed anode material for the SMR and WGS reactions were evaluated using a fully automated catalytic fixed-bed reactor, developed in our laboratory are capable of handling both gas and liquid feeds. The catalyst is placed in a downflow quartz reactor. The exiting gases are analyzed online by a gas chromatograph (GC), Varian 3800 GC. A schematic of the fixed-bed reactor is illustrated in Figure 3-1. As seen in Figure 3-1, the fixed-bed reactor consists of:

- gas manifold and liquid water flow-evaporator system to create the desired S/C ratio,
- pre- and post heating sections to prevent any condensation between the evaporator and the reactor inlet, and between the reactor outlet and GC. Note that all the product gas is analyzed in the gas phase (no prior separation between condensable and non condensable gases),

- furnace,
- quartz tube fixed-bed reactor,
- data acquisition and control system to connect LabVIEW program with all electronic devices. The LabVIEW program is used to enter set points and monitor parameters (e.g. furnace temperature, pre-heater temperature, gas flow rates, pressure drop through the reactor, etc.),
- GC for product gas analysis.

The schematic of the reactor is drawn in Figure 3-2. The top and bottom of the reactor is connected to the pre-heater and post-heaters using Swagelok Ultra-Torr vacuum fittings and tees. The half inch tee female fittings are connected to the vacuum fittings. One path in each tee is used for gas flow and the other for inserting a sheathed K-type thermocouple to pass through and be placed close to the catalyst bed. The catalyst bed is seats on a quartz frit located in the isothermal zone of the furnace. The maximum operating temperature in this fixed-bed setup is 850°C.

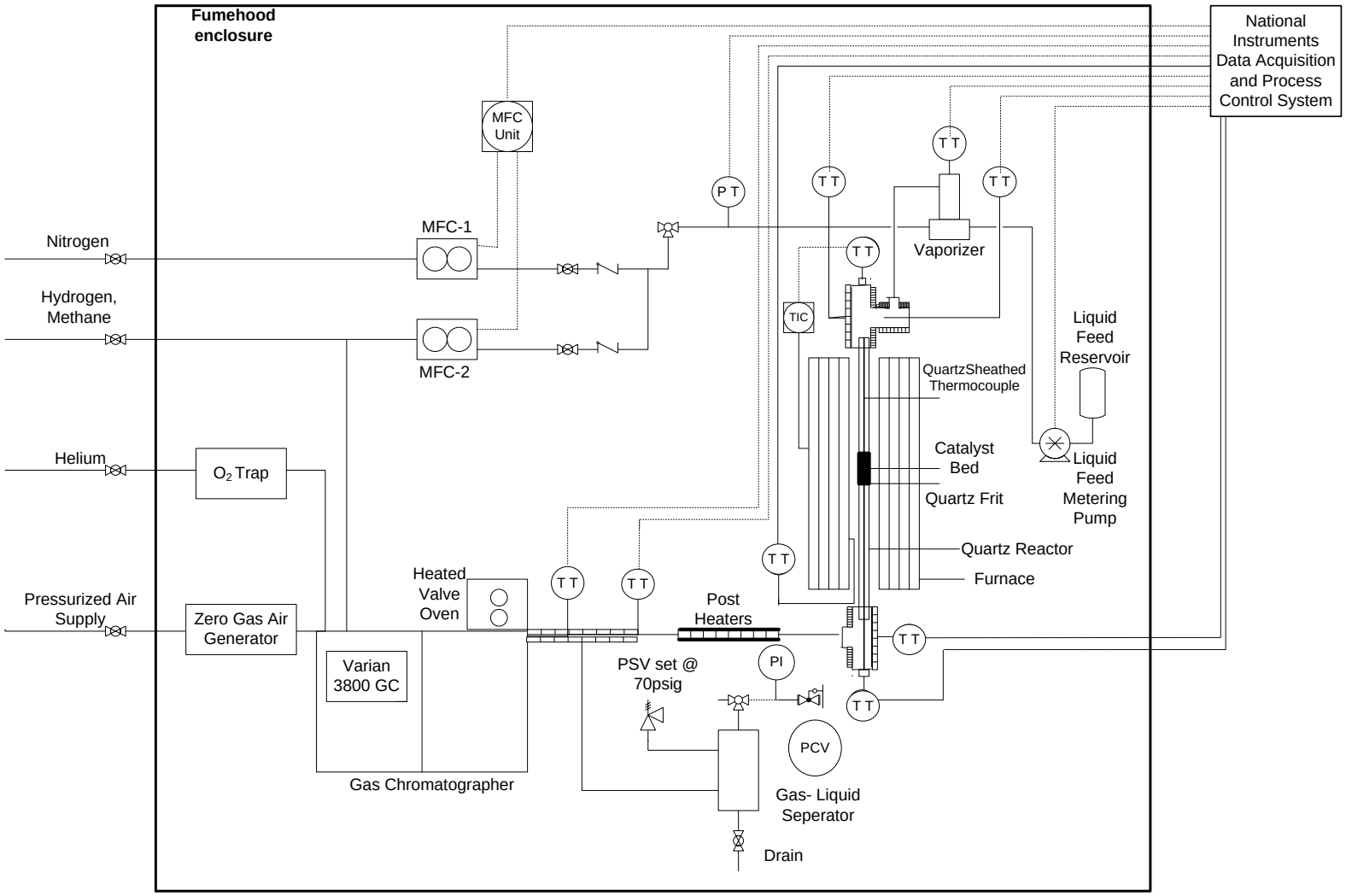

Figure 3-1 Experimental setup for SMR-WGS

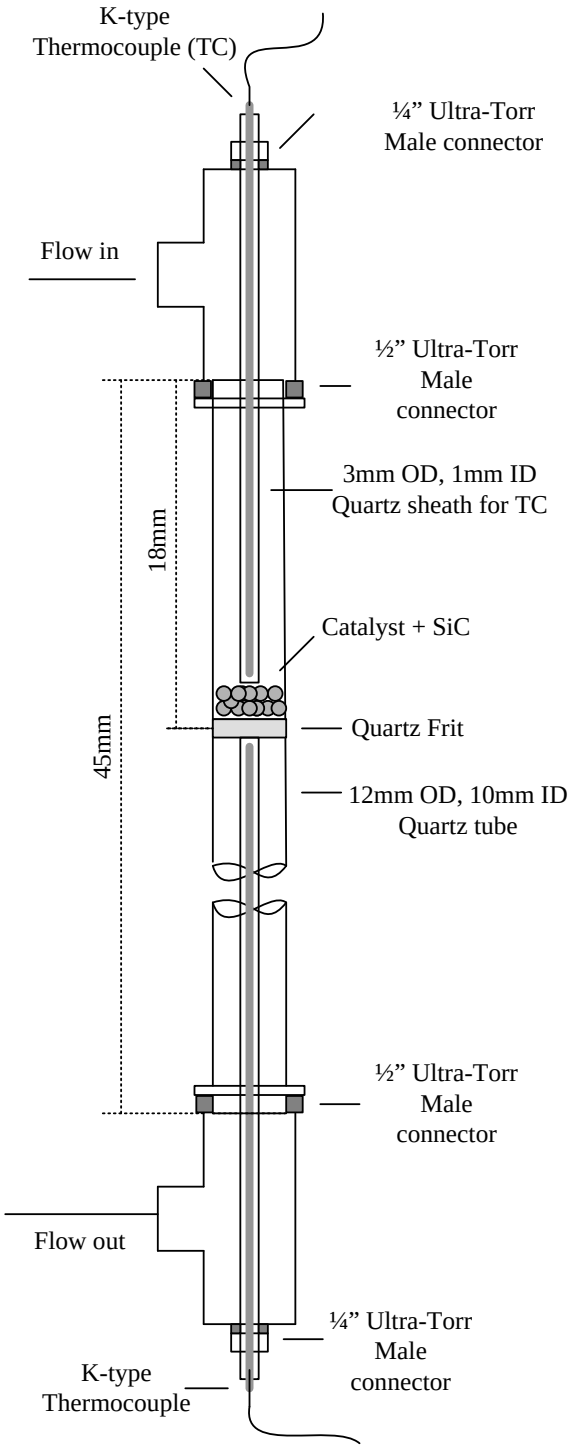

Figure 3-2 Quartz tube reactor

3.2 Electrochemical Measurements

The electrochemical tests are carried out in a SOFC button-cell test station. The parameters that have been mostly used to evaluate the performance of fuel cells are the maximum power density (P_{max}), the limiting current density (i_L) and the electrochemical impedance of the cell. These parameters are characteristics of each cell depending on the testing conditions, the material and bonding between layers.

The test station consists of six primary parts: SOFC cell, test rig, gas conditioning and fuel-humidifier (i.e., controlled evaporator and mixer, CEM), furnace, control system and measurement equipment. A schematic diagram and photographs of the setup are shown in Figure 3-3. Details of each part are given in the following sections, followed by information about the electrochemical techniques used to investigate the cell performance. However, details on the fabrication of the cell and procedures to run this test station are presented in Chapter 4 and Chapter 6, respectively.

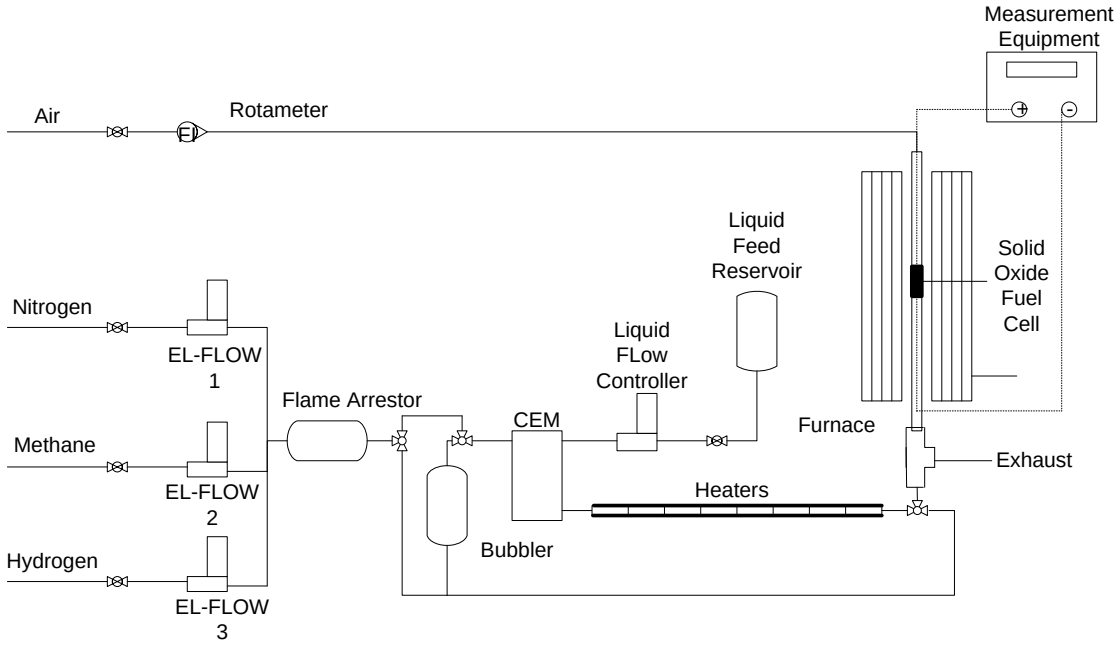

(a)

(b)

Rotameter

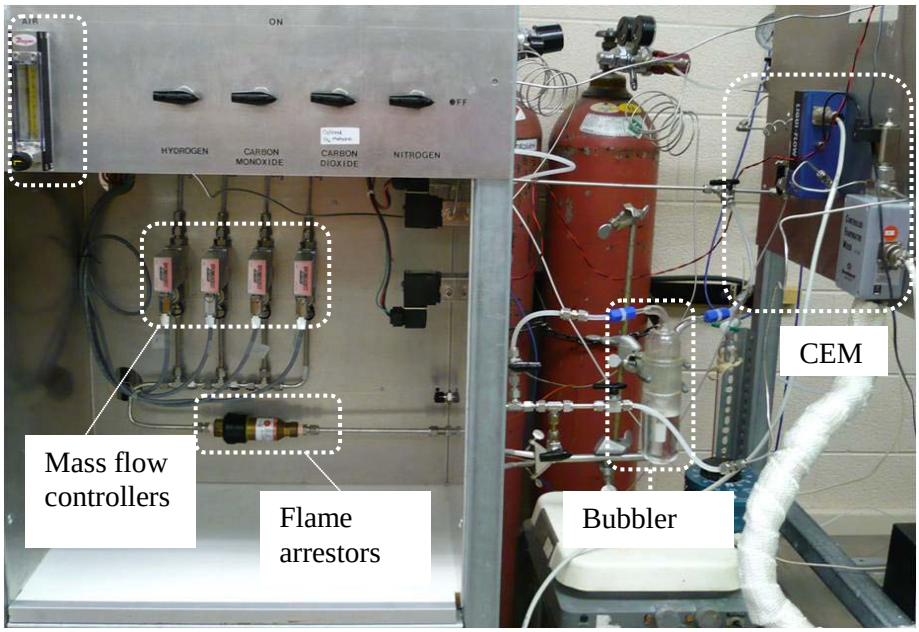

(c)

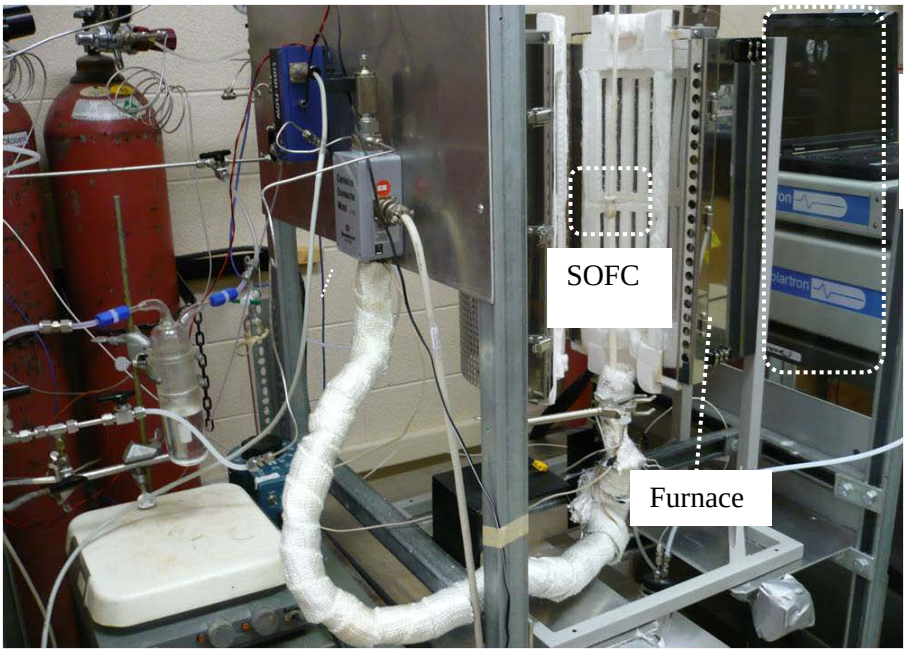

(d)

Figure 3-3 The SOFC button cell setup a) schematic diagram b) overall feature c) fuel conditioning system and d) SOFC located in the furnace and the measurement equipment

3.2.1 Button Cell

The performance of the SOFC materials is tested using a so-called single-button cell which is a disc-like with 14 mm diameter. Most tests were performed on an electrolyte-supported cell. The anode material is coated at the centre on one side of the electrolyte disc with a 6 mm diameter. On the other side of the disc, the cathode is deposited, to cover the same area as the anode. A schematic of the button cell is shown in Figure 3-4. Detailed description of the button cell fabrication procedure is given in Chapter 4. The button cell is installed in the test rig located in a tube furnace.

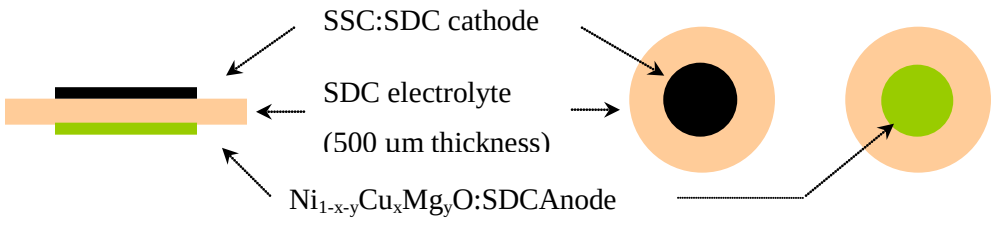

Figure 3-4 Schematic of the button cell

3.2.2 Test Rig

A drawing of the assembly for the fuel cell housing is presented in Figure 3-5. On the anode side, the rig consists of two co-axial tubes. The larger tube is made from 3 cm long 15 mm OD alumina tube seal on top of 35 cm length of 13mm OD alumina tube. The double tube is needed because the top must have diameter equal or slightly larger than the cell in order to make a perfect seal (using ceramic sealant, detail is presented in Chapter 6) mostly to prevent the fuel gas to enter into contact with the surrounding air. However, the standard tube is also required to be able to use a standard size fitting. The smaller co-axial tube (diameter 3 mm) works as a fuel pathway to bring the fuel closely to the electrode to supply the fuel to the cell. This tube can stay at the center of the 15 mm OD tube because of the balance of three small alumina rods (Top view is drawn in the up-right side in Figure 3-5). The anode deposited at the centre of the disc sits on three alumina rods and smaller tube with a silver current collector inserted in-between. Note that the current collector consists of silver wire and silver paste. The other end of the 13mm OD alumina tube connects to a half-inch stainless steel tee. The tee fitting is bored-through to allow for greater penetration of a quarter inch stainless steel tube connected (using ceramic seal) underneath the 3 mm OD alumina tube. The different type tube is required as the operating temperatures at the top are from 600°C -750°C but the bottom side is connected to a three-way valve. The three-way valve assembly allows the user to switch between high percentage humidified fuel and 3% humidified fuel or dry fuel. A stainless steel tube is needed here since an alumina tube might break during switching process. Note that the other path of the tee is for the exhaust. During the experiments, the fuel flows upward through the inner co-axial alumina tube on the anode side and leaves the system by flowing downward, through the annulus space between the two tubes, to the outlet hooked at the side next to the end of the larger tube. The cathode (upper side) also contacts directly the silver current collector which is located underneath the alumina tube. The alumina tube on the cathode side acts as a light weight to press upon the current collector.

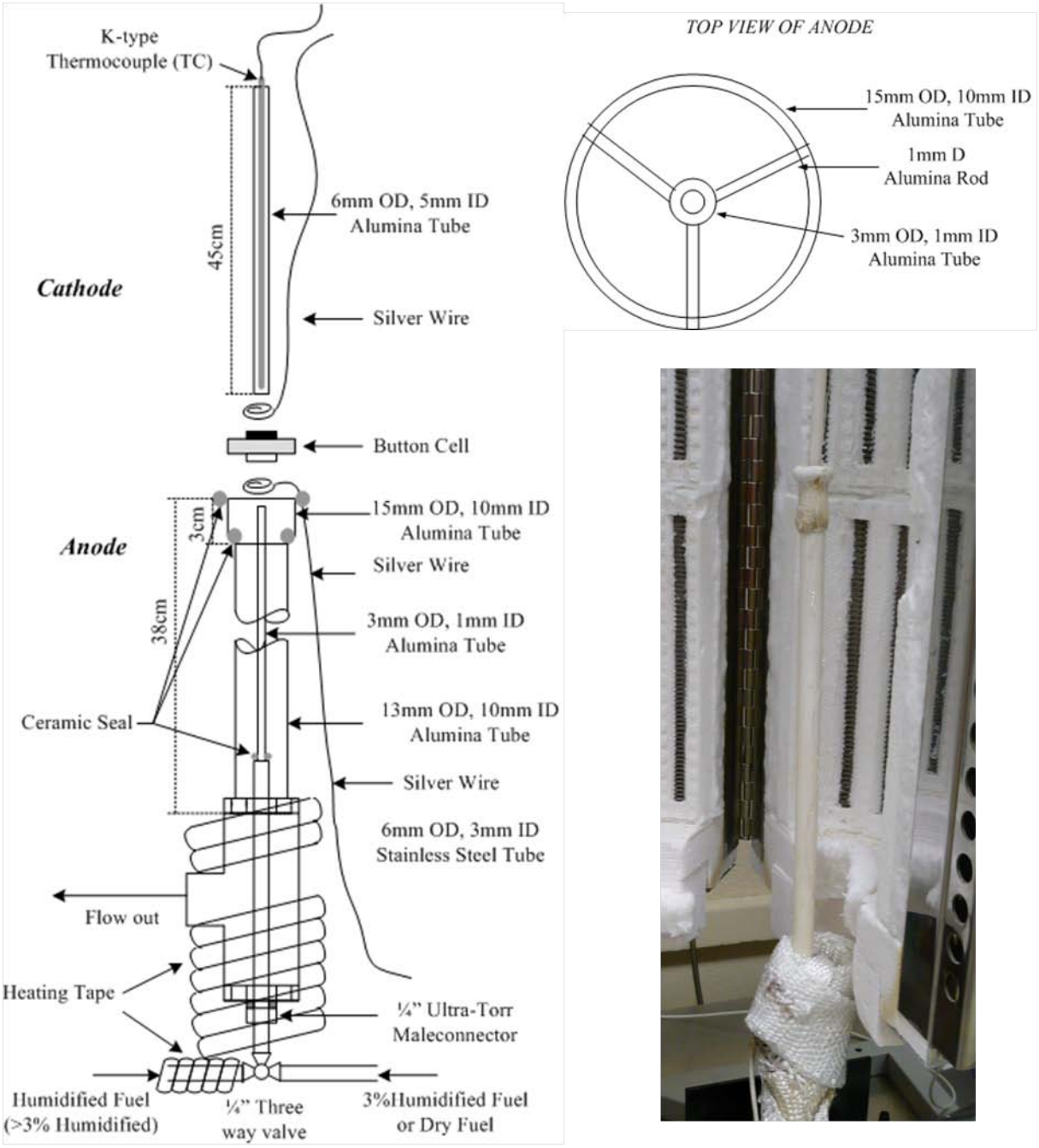

Figure 3-5 Schematic of the rig design.

3.2.3 Control System

LabVIEW–field point is used in this setup in order to communicate with the electronic instruments. It controls, monitors and records the conditions and the results in every test. Only the air flow rate to the cathode side is adjusted manually, using a rotameter (0-2000mL/min). The control panel was developed in-house using LabVIEW and is shown in Figure 3-6. Figure 3-7 shows the field-point used for SOFC setup. All mass flow controllers accept input from the control panel and send the signal corresponding to the real flow rate to the program at the same time (lower part). As a result, the real flow rate is constantly checked during operation. Because hydrogen is one of the fuels in the test, an online hydrogen detector is necessary for safety reasons. In case the rig leaks, the online detector sends a 15V signal to LabVIEW when it detects hydrogen (middle left hand side). That causes the panel to show a message with the red alarm, and turns off all mass flow controllers, except the one for nitrogen. In this situation, the flow of nitrogen is set to the maximum flow rate of 500 ml/min to flush the system. Likewise, the program written here can receive the data of the temperature from thermocouples located close to the cell. When the temperature in the furnace exceeds the limit defined by the operator, the gas flows are also shut down. Moreover, all investigated conditions are automatically recorded in an electronic file.

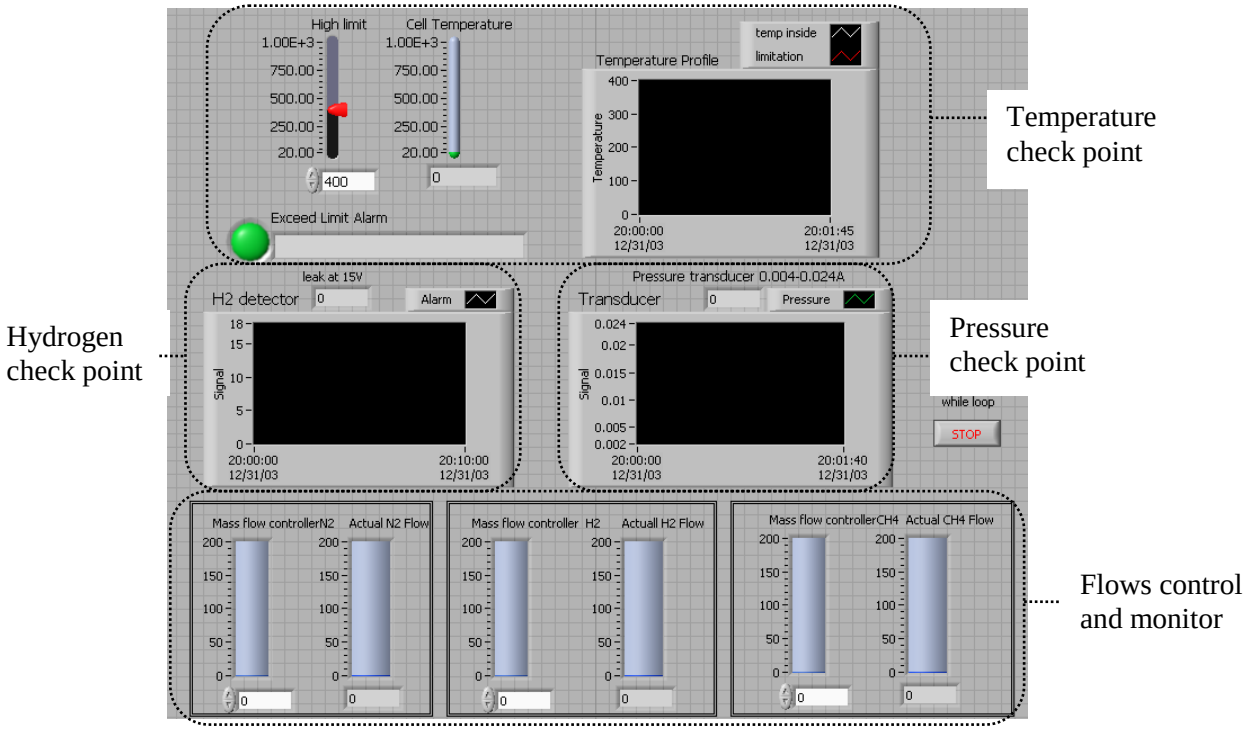

Figure 3-6 Control panel of LabVIEW program

Figure 3-7 Field-point used as an interface of the electronic devices and LabVIEW program.

3.2.4 Gas Conditioning System and Fuel Humidifier

Gases in a fuel cell are classified into two main types: reduction gas and oxidation gas. As known from chapter 2, the oxidation gas is oxygen which commonly comes from air while the reduction gas is the fuel (it can be a gas mixture or hydrogen). Fuel gas composition is set using mass flow controllers which receive the command directly from a LABVIEW program. Figure 3-8 shows the flow controllers next to the computer in the experimental setup.

Figure 3-8 Flow controllers placed next to the computer in the real set up.

Fuel can be dry or humidified (Figure 3-9). In this work, fuel is humidified using two different methods depending on the desired percentage of water in the gas stream. The first technique is to simply bubble the gas through water and the second technique is a Control Evaporator and Mixer (CEM). Both are described next.

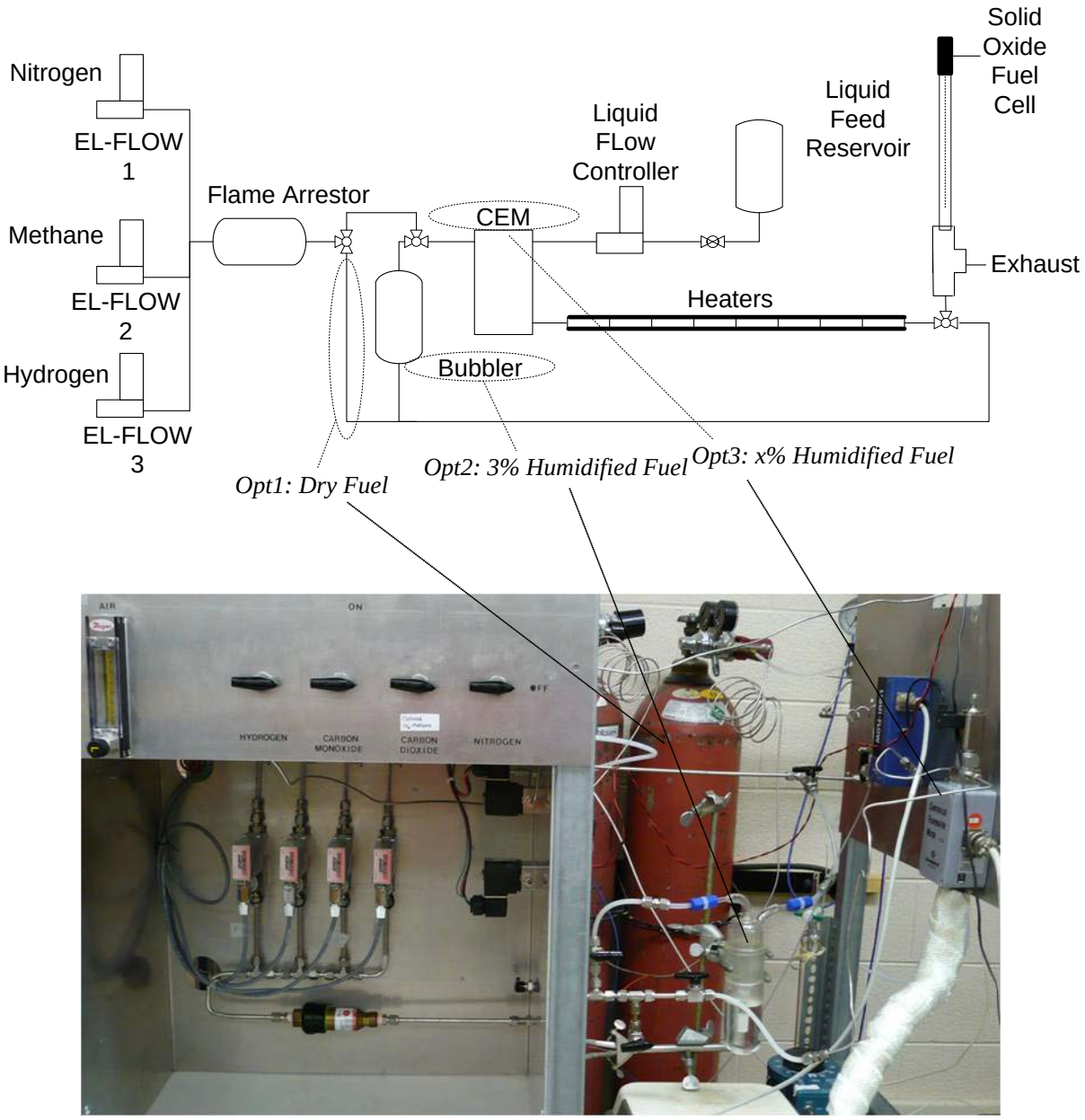

Figure 3-9 Three options of fuel conditioning system.

Bubbler:

This method is the easiest way to produce 3% humidified gas at room temperature. The bubbler is made from glass which has gas come into water on one side. Gas flows in the water through the porous nozzle and diffuses to the gas zone above the water. Then, 3% humidified gas leaves the bubbler from the other side to the anode of the cell.

Control Evaporator and Mixer (CEM):

The CEM includes three parts: a control valve, a mixing device and a heat exchanger. It is a combination of liquid flow controller, mixing chamber and heat exchanger functioning as an evaporator to make steam and to mix steam with the gaseous fuel. The control valve is used to control the liquid flow rate in order to achieve the desired concentration of water. The liquid flow meets with the gas flow at the mixing point. Then, the mixture goes to the heat exchanger for vaporization.

3.2.5 Furnace

The button cell is located in a vertical-tubular furnace (Carbolite Co. Ltd., VST 12/400, 1200°C maximum) controlled by an eight-segment controller which means that the system can be heated up (or cooled down) and maintained at eight different temperatures. This option is helpful for fuel cell tests as many temperature segments are needed. The test starts from curing the seal in two steps: 1) ramp up and maintain at 98°C for 2h and 2) 212°C for 2h. Then, the temperature is changed to 750°C at 80°C/h for the anode reduction step. After reduction, the electrochemical measurements are performed at the desired temperature (here 750, 700, 650 and 600°C)

3.2.6 Measurement Equipment

The main approaches to electrochemical measurements in this research are to evaluate the performance of the button cells made from our alternative anode material and also to compare with those of traditional materials. Cell performance is defined by current-voltage-power (IVP) characterization, so-called polarization measurement, and by Electrochemical Impedance Spectroscopy (EIS). Polarization measurements identify the open circuit voltage, the power density, the overpotential, and the limiting current density, whereas EIS is used here essentially to determine the total and polarization resistances. The polarization and the impedance reflect the electrochemical properties for all materials and the interface bonding within the cell. Because the electrochemical properties refer to a whole circuit, unfortunately, it contains the information of the connection between the current collector and the cell, as

well. Figure 3-10 illustrates the actual view of the connection between the SOFC setup and the measurement equipment.

The measurements are performed using the electrochemical interface SI-1287 and SI-1260 impedance analyzer (Solartron Instrument). The IVP characterizations are carried out using potentiodynamic. The voltage is imposed and the current is measured. The measured current is converted into current density by dividing the current by the electrode surface area. The electrochemical power density (P in $mW.cm^{-2}$) is calculated by the cell voltage (E_{cell}, in V) times the corresponding current density (i in $A.cm^{-2}$) as indicated in equation (3-9):

$$P = E_{cell} \cdot i \tag{3-9}$$

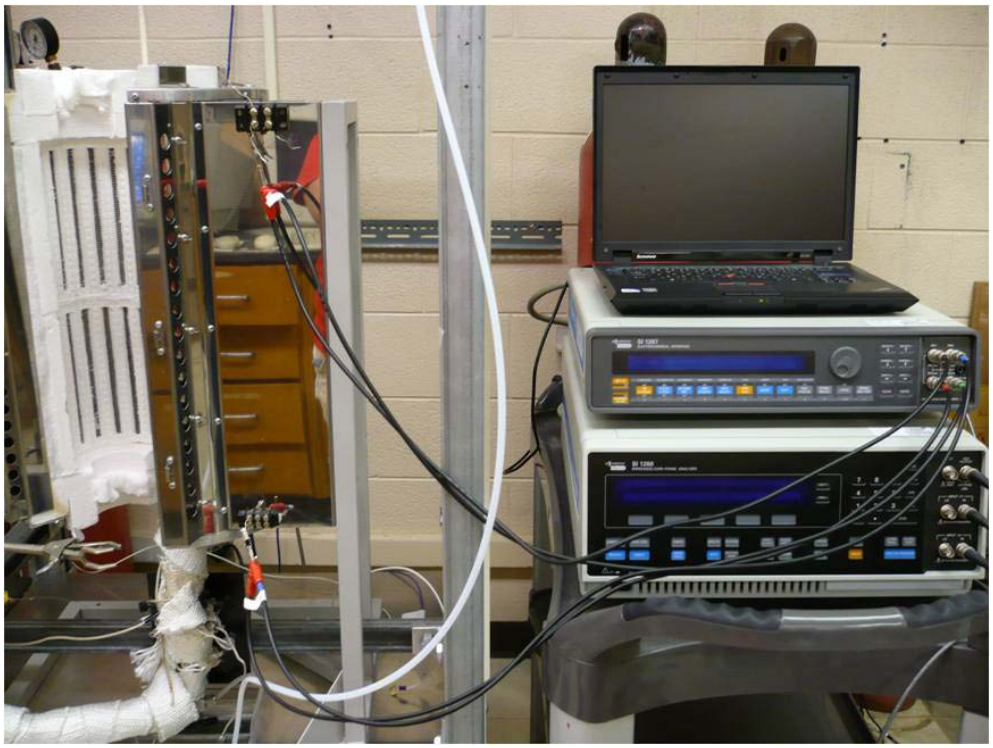

Figure 3-10 The connection between the SOFC setup and the measurement equipment

An example of a polarization measurement was shown in Figure 2-2. For an ideal case, the cell voltage should remain constant (horizontal dash line in Figure 2-2). In reality, as soon as some current is drawn some types of overpotential, mentioned in chapter 2, take place, thereby lowering the cell voltage. These overpotentials can be interpreted/characterized from the results of the button cell tests. In this work, two electrode measurements were employed for EIS, where the anode is the working electrode and the cathode is the counter electrode connected to the cathode. EIS is performed by applying a small amplitude sinusoidal voltage to the working electrode and then measuring the resulting current density. The resulting current density usually also has a sinusoidal shape characterized by its amplitude and phase angle shift between applied voltage and current response as a function of the frequency. The sinusoidal voltage (E) has the thus the following form:

$$E = E_{max}\, sin(\omega t) \tag{3-10}$$

where E_{max} is the amplitude and ω is the angular frequency. Usually, the current response, I, will also be a sinusoidal with the same frequency but different phase. Its expression is given by equation (3-11).

$$I = I_{\max} \sin(\omega t + \varphi) \tag{3-11}$$

where I_{max} is the current amplitude and φ represents the phase angle shift.

It should be noted that in the case of a resistor, the current response is in-phase (φ is equal zero). In contrast, for a capacitor and an inductor, the responses are out-of-phase and φ equals π/2 and -π/2, respectively. Similar to Ohm's law, the voltage drop across two electrodes is represented by equation (3-12)

$$E = iZ \tag{3-12}$$

where Z is the impedance. Impedance is a general term for all forms of opposition to electron flow, resistance from the resistor and reactance from the capacitor and/or the inductor. Impedance is represented by complex numbers as in equation (3-13), including a real component Z_{real} and an imaginary component Z_{im}. The resistance is represented by Z_{real} while the reactance is pointed by Z_{im}.

$$Z = Z_{real} + jZ_{im} \tag{3-13}$$

This technique can be applied to analyze impedances involved within a cell. The impedance spectra, in most cases, are presented as Nyquist plots (Figure 3-11). In the simplest case, the real part, the horizontal axis, associated with this plot is attributed to resistance and the imaginary part, the vertical axis, is attributed to the capacitance. Therefore, the highest value of the real part accounts for the total resistance

(R_t). The first intercept at the real part (R_s) is the sum of resistances used to transfer charges from one electrode to the other, and represents the resistance of the electrolyte and electrodes. The resistance of the semicircle is the potential resistance used to drive the reactions (R_p). Accordingly, in Figure 3-11, the high frequency intercept on the real axis is R_s and the low frequency intercept is R_t. In a real SOFC operation, in addition, the impedance at the low frequency increases with the amount of deposited carbon (Souththampton Electrochemistry Group, 1985, Adler, 2004)

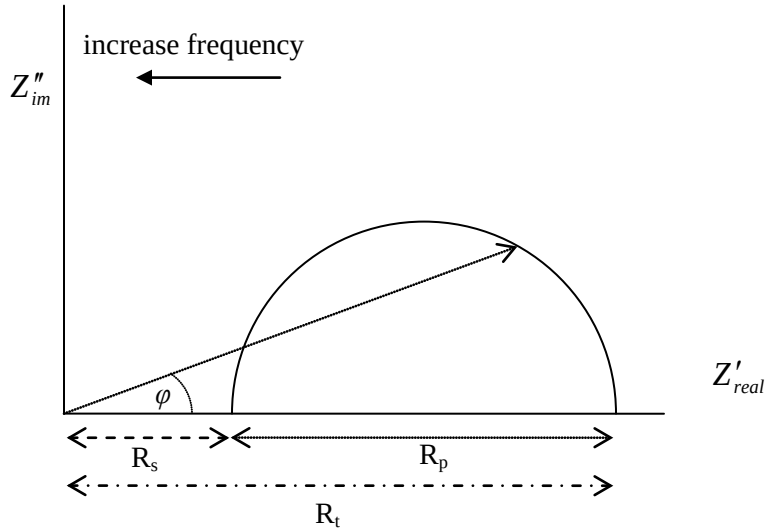

Figure 3-11 Idealization of the impedance spectra in the Nyquist plot

3.3 Material Characterization Techniques

The chemical and physical properties of fresh and spent alternative materials are characterized by different techniques to determine various properties, as illustrated in Table 3-1. The properties of the new materials have guided the experimental conditions and also clarified the initial state of the material. The materials are characterized before and after steam reforming and electrochemical tests. The benefit is to follow up the composition and the arrangement related to the activity, performance and stability. More details about the instruments and techniques employed are discussed in the following sections.

Table 3-1 Properties and the corresponding material characterization techniques used in this work

Properties	**Techniques**
Calcination-Oxidation Properties	Temperature-programmed oxidation (TPO) with air using temperature gravimetric analyser (TGA)
Reduction Properties	Temperature-programmed reduction (TPR) with H_2/N_2 using temperature gravimetric analyser
Crystalline Phase identification	Power X-ray diffraction, XRD
Surface Area Analysis	BET N_2 physisorption
Microstructure and Particle Size	Scanning electron microscopy (SEM)
Carbonaceous Deposits	Scanning electron microscopy
Conductivity	Conductivity measurement

3.3.1 Temperature Programmed Analysis (TPO and TPR)

Two temperature programmed techniques (TP) have been used to determine the calcination temperature and the reduction conditions: temperature-programmed oxidation (TPO) and temperature-programmed reduction (TPR), respectively. TPO is carried out by heating up materials at a constant heating rate in air. In this process, materials will be transformed into oxide form and will lose weight. Their weight becomes stable once they have completely changed to the oxide phase. The temperature at which the sample weight remains constant thus represents the minimum calcination temperature. TPR is a similar technique where the materials are exposed to hydrogen in order to reduce a metal oxide into a metal. Again, the materials are deemed entirely reduced when the weight no longer changes with temperature. The TPR

results allow the determination of the minimum reduction temperature for a given reducing gas. The TPO and TPR ($5\%H_2/N_2$) of powder materials have been utilized in a thermogravimetric analyzer (Cahn TG-2151 thermobalance), depicted in Figure 3-12.

In the Cahn TG-2151 thermobalance, one side of the balance holds the reference basket that has been used for calibrating the system with the empty sample basket and the other side carries a sample basket. The analyzer works following the principle of equilibrium, keeping the balance in null position. It means that the electronic balance will give the equivalent response to weight gains or weight losses during the reaction to maintain the equilibrium state. Those signals are sent to a computer and converted to the corresponding weight changes (Rahman, 2004).

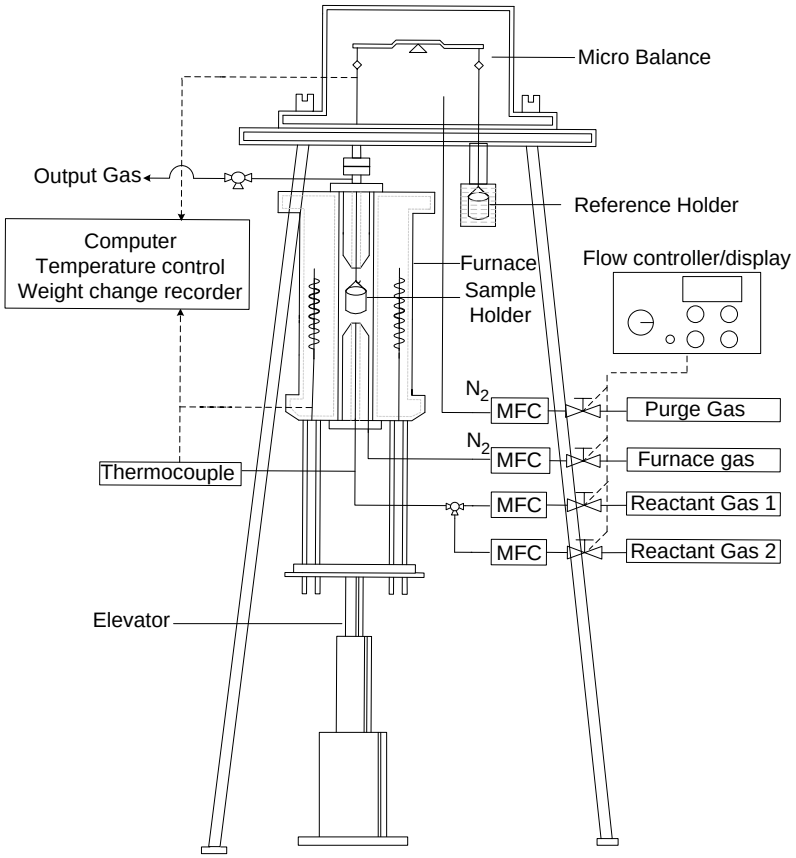

Figure 3-12 Schematic of Cahn TG-2151 thermobalance.

3.3.2 Phase Identification

Using XRD, crystalline phases can be identified using Bragg's law (equation (3-14) and Figure 3-13)

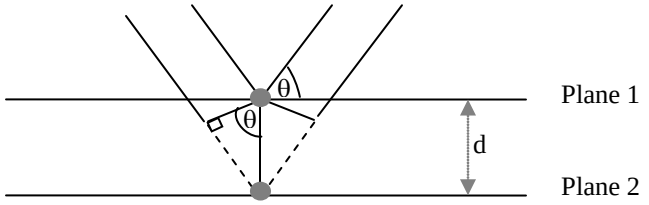

Figure 3-13 Schematic showing the principle behind XRD

$$n\lambda = 2d_{hkl}\sin\theta \tag{3-14}$$

where λ is the wavelength of the x-ray (λ =1.5425Å for CuK_α), n is the integral number of wavelength called order of the reflection, d is the interplanar spacing of the crystal planes of indices (hkl) and θ is the angle of incidence. Once x-rays of known wavelength λ are applied and θ are measured, d of various planes in a crystal can be determined by equation (3-14). As a result, the structure can be defined. In this work, x-ray diffraction patterns have been measured using a Bruker D8 FOCUS for 2θ of 30 to 80° using a step size of 0.02° and a count time of 0.5 s.

3.3.3 Surface Area Analysis

The Brunaure, Emmet and Teller (BET) method is a common technique applied for determining the surface area of a catalyst. The BET isotherm represents an extension of the Langmuir isotherm (monolayer adsorption) to multilayer adsorption.

The BET model can be expressed by equation (3-15).

$$\frac{P}{V_a(P_0 - P)} = \frac{1}{V_m C} + \frac{(C-1)}{V_m C}\frac{P}{P_0} \tag{3-15}$$

where P is the partial pressure of adsorbate, P_0 is the saturated vapour pressure of the adsorbing gas (normally N_2) at the temperature of the measurement, V_a is the volume of gas adsorbed per unit mass of catalyst, V_m is the volume required to cover the surface with a monolayer of nitrogen and C is a constant. V_m and C can be determined when considering the linear region of the plot of $P/(V_a(P_0-P))$ versus P/P_0,

P/P_0 existing from 0.05 to 0.3, where the slope is $(C-1)/(V_mC)$ and the intercept is $1/(V_mC)$. This range is adequate for a monolayer adsorption to be directly related to the surface area. By knowing the number of N_2 adsorbed at the monolayer, the total area is the summation area of all those N_2 molecules.

Consequently, the BET surface area per gram of the sample is calculated using equation (3-16)

$$BET\ S.A. = \frac{V_m \rho N_A a_{CS}}{MW_{N2} M_{sample}} \tag{3-16}$$

where ρ is the density of liquid nitrogen at the boiling point, N_A is the Avogadro's number, and a_{CS} is the cross-sectional area of nitrogen molecule. MW_{N2} is the molecular weight of nitrogen, and M_{sample} is the mass of the sample.

Here, samples have been pre-treated in N_2 at 573 K for one hour to remove any physisorbed moisture. The BET surface has been measured over the range $0.05 \leq P/P_0 \leq 0.3$ using a Micromeritics Gemini™ V-Series surface analyzer.

3.3.4 Scanning electron microscopy (SEM)

Scanning electron microscopy is a straightforward tool for observing the size of particles and the surface morphology. It is achieved by raster scanning a narrow electron beam onto the specific surface. It yields either secondary electrons or backscattered electrons. Detection of the secondary electron is the most common mode of the SEM. The contrast of the SEM micrographs depends on the position count from the detector. The part facing the detector appears brighter than the part located away from the detector. The backscattered electrons are emitted from a deeper surface than the secondary electrons and are more effective on heavy elements. Therefore, a micrograph obtained from the backscattered electrons illustrates the arrangement at that area because the heavier element will appear brighter. This research has used a LEO 1530 SEM (5-kV electron beam) with a backscattered electron detector to collect the information.

3.3.5 Conductivity test equipment

Good conductivity is a requirement for an anode material because electron from the electrochemical reaction must be able to move from the TPB through the anode area to the other end of the anode connected to the current collector. The setup used to measure the conductivity is shown in Figure 3-14. The sample is placed in-between two copper terminal blocks and the whole assembly sits on a plastic housing. The specific current is passed through the sample of known cross-sectional area and the voltage drop is measured for a particular distance. The conductivity (σ) is determined using equation (3-17)

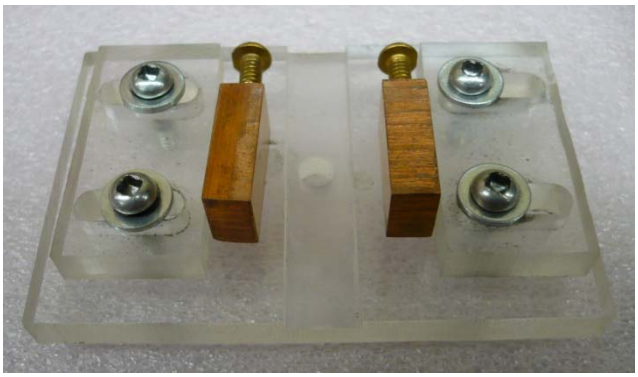

(a)

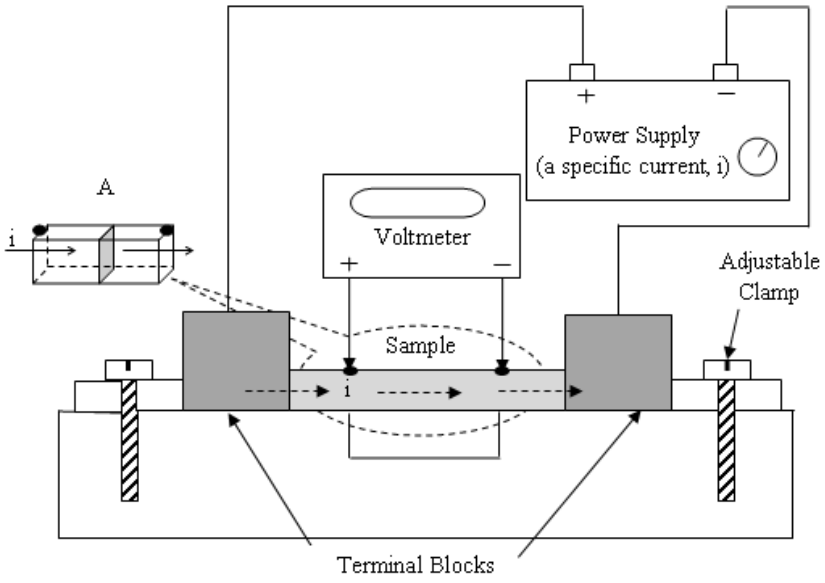

(b)

Figure 3-14 The setup designed for conductivity measurement a) Actual setup b) Schematic view and the flow of current.

$$\sigma = \frac{l}{R \times A} \tag{3-17}$$

where σ is the electrical conductivity normally reported in siemens per centimeter (S/cm), l is the distance of the measured interval, R is the resistance, and A is the cross-sectional area of the sample through which the current flows. In addition, when Ohm's law is used in for the resistance, then the equation becomes

$$\sigma = \frac{l \times i}{V \times A} \tag{3-18}$$

Note that when fabricating the anode material, it is initially in its oxide form and thus is not conductive. The sample must thus be reduced in order for the metal to be in pure metal form. The weights of sample before reduction (w_0) and after reduction ($w_{experimental}$) were measured. The weight after reduction determined experimentally is compared to the one that can be determined theoretically to come up with a percentage reduction, as indicated in equation 3-19. The percentage reduction is an important parameter to know when determining the conductivity, since it directly depends on this percentage reduction. If the percentage of reduction is not high enough, the material will not become conductive. For the conductivity measurements, the samples were reduced at 750°C in a vacuum furnace for two hours.

$$\%\,reduction = \frac{w_0 - w_{experimental}}{w_0 - w_{theoretical}} \times 100 \tag{3-19}$$

Chapter 4
Material Preparation and Properties

This chapter describes two material preparation methods and presents the properties of those materials when they are oxidized or reduced. The detailed procedures for button cell fabrication are presented, as well. Finally, the conductivity of the anode material is discussed in the last section.

4.1 Material Preparation

The $Ni_{1-x-y}Cu_xMg_yO$ samples were prepared using two different methods: a one-step co-precipitation method and a two-step co-precipitation/impregnation method. These two methods are similar to processes used for catalyst preparation. All metal nitrates (nickel nitrate, copper nitrate and magnesium nitrate) are synthesized by co-precipitation for the one-step method. However, with the two-step method, $Ni_{0.9}Mg_{0.1}O$ is first prepared from co-precipitation, followed by impregnation of copper nitrate. Detailed descriptions of the two methods are presented next.

4.1.1 One-Step Co-precipitation Method

For the first method, $Ni_{1-x-y}Cu_xMg_yO$ is synthesized by co-precipitation of Ni, Mg and Cu. To begin with, a metal nitrate aqueous mixed solution containing 0.2M $Ni(NO_3)_2.6H_2O$, 0.2M $Mg(NO_3)_2.6H_2O$ and 0.2M $Cu(NO_3)_2.3H_2O$ is prepared to yield a desired concentration of Ni, Cu and Mg. This mixture is then added drop wise with a 30% ammonium hydroxide solution to a vessel maintained at pH 9. The solution is then stirred for 30 minutes in a closed system and aged for 24 hours. The resulting solid cake is washed and filtered with distilled water, and dried at 115ºC overnight to produce a precipitate. Finally, the powder is transformed into a metal oxide form by calcination in air at 750ºC for 4 hours. The calcination temperature is limited because of the presence of Cu because Cu in the form of CuO has a melting point as low as 1201ºC. The entire procedure is summarized Figure 4-1.

4.1.2 Two-Step Co-precipitation/Impregnation Method

In the two-step method (Figure 4-2), $Ni_{0.9}Mg_{0.1}O$ is first prepared by co-precipitation of Ni and Mg, similar to the one-step preparation above but then calcined at 800ºC, and finally by addition of copper to $Ni_{0.9}Mg_{0.1}O$ by impregnation. The impregnation starts by predetermining the volume of an aqueous 0.2 M $Cu(NO_3)_2.6H_2O$ solution required depending on the amount of $Ni_{0.9}Mg_{0.1}O$. The copper solution is then applied uniformly drop by drop in a suitable amount to just cover $Ni_{0.9}Mg_{0.1}O$. The material is heated in the oven at 115°C for 15 minutes. The procedure for drop by drop application

followed by drying is repeated until the copper solution has been completely used. Finally, the coated $Ni_{0.9}Mg_{0.1}O$ is calcined at the desired temperature for 4 hours.

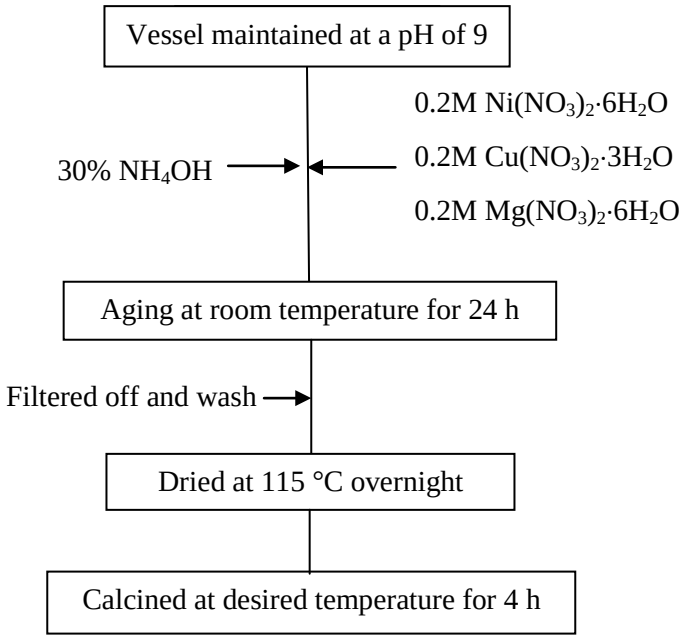

Figure 4-1 Procedure for preparing $Ni_{1-x-y}Cu_xMg_yO$ powder by one-step co-precipitation.

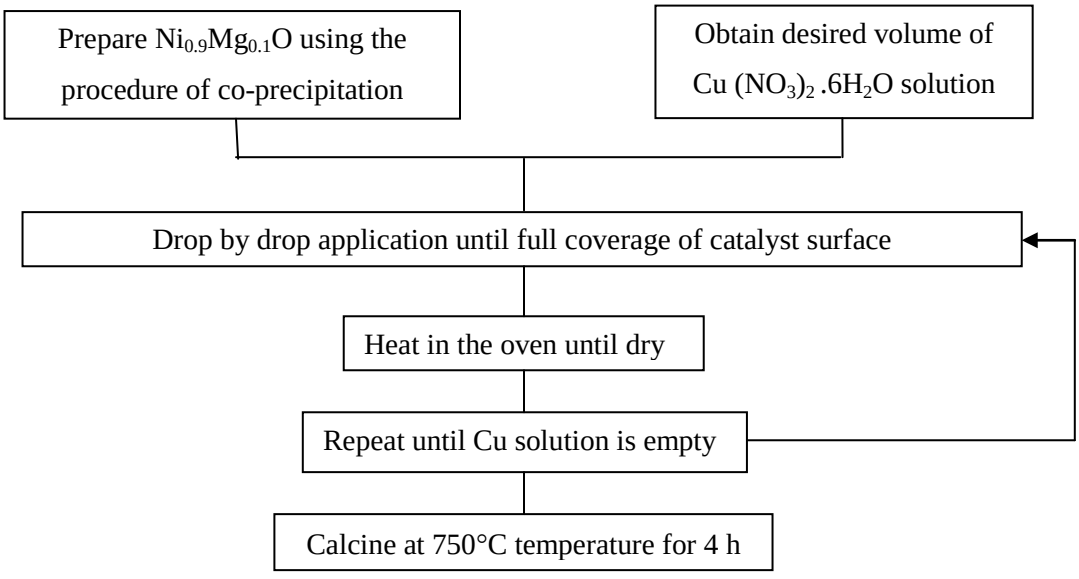

Figure 4-2 Process of wet impregnation of Cu on Ni-based catalyst (two-step method).

4.2 Material Properties

In order to maintain the samples stable, they are transformed from metal hydroxide or metal nitrate to metal oxide by calcinations (equation (4-1)). Ultimately, they must be activated by reduction into metal form of the active metal (here Ni and Cu as seen in equation (4-2)). The properties of the materials prepared in these two steps (calcinations and reduction) are reported in this thesis, including calcination temperature, reduction temperature, phase of the material (XRD), surface area analysis (BET), calcination properties (TPO) and reduction properties (TPR).

$$Ni_{1-x-y}Cu_xMg_y(OH)_2 \rightarrow Ni_{1-x-y}Cu_xMg_yO + H_2O \quad (4\text{-}1)$$

$$Ni_{1-x-y}Cu_xMg_yO + (1\text{-}y)H_2 \rightarrow Ni_{1-x-y}Cu_xMg_yO_y + (1\text{-}y)H_2O \quad (4\text{-}2)$$

4.2.1 Calcination Temperatures

The TPO results, following the TPO procedure explained in Chapter 3 to determine the calcination temperature, are presented in Figure 4-3. For the one-step co-precipitation method, the peak of the weight loss rate for the un-calcined sample occurs at approximately 270°C for $Cu_{0.9}Mg_{0.1}(OH)_2$, whereas it occurs at 350°C for $Ni_{0.9}Mg_{0.1}(OH)_2$. The results also show that no further weight loss happens after 400°C for $Cu_{0.9}Mg_{0.1}(OH)_2$ and after 600°C for $Ni_{0.9}Mg_{0.1}(OH)_2$. For copper content up to 10 mol%, the TPO profiles are similar to that of $Ni_{0.9}Mg_{0.1}(OH)_2$. For 15% and more Cu, the peak is shifted to lower temperatures; for example for $Ni_{0.75}Cu_{0.15}Mg_{0.1}(OH)_2$, the peak occurs at about 310°C. The sample with 15% Cu also exhibits a peak for CuO in the XRD pattern (as seen later in this chapter). For the two-step method, the $Ni_{0.9}Mg_{0.1}(OH)_2$ was first prepared and calcined at 800°C, before impregnating Cu. Therefore, Ni and Mg were already oxidized before impregnation of Cu. The TPO profiles, thus, represents mostly the oxidation of the impregnated Cu. Figure 4-3(b) shows that the more copper is impregnated the larger is the weight loss. However, for 3% Cu almost no change in the weight is observed. The TPO profiles of the un-calcined Cu-impregnated samples from the two-step method indicate that above 400°C, the samples are completely oxidized. Experimental and theoretical weight losses (based on Equations 4.1) are reported in Table 4-1. For TPO, the experimental weight loss is almost always greater than the theoretical weight loss, which is attributed to the initial water content in the sample that vaporizes during the TPO analysis or water molecules remaining in the solid cake within a complex compound as (Grgicak et al. (2006)).

4.2.2 Reduction Temperatures

The reduction properties of the oxide materials were analysed at a ramping rate of 10ºC min^{-1} up to 800ºC and held for 30 min in 5% hydrogen balanced with nitrogen (TPR procedure). From equation (4-2), the theoretical weight loss can be determined. Comparison between the observed and theoretical weight loss indicates agreement within 3%, as shown in Table 4-2. Note that when calculating the theoretical weight loss, it is assumed that MgO is not reduced and remains in its oxide form (Choudhary et al. (1998) and Shiratori et al. (2006)). Figure 4-4 represents the rate of weight change as a function of temperature for different compositions of the oxide material. The oxygen in $Ni_{0.9}Mg_{0.1}O$ begins to be released at approximately 350°C, and by 750°C the Ni oxide is completely reduced into metallic Ni. Complete reduction can be checked by comparing the experimental percentage weight loss after the test to the theoretical percentage weight loss. The experimental weight loss is 21% which is very close to the theoretical calculation (21.4%). Therefore, we conclude that the metals are fully reduced. $Cu_{0.9}Mg_{0.1}O$ released oxygen at 200°C and Cu oxide was fully reduced at 430°C (19.5% for experimental weight loss and 19.0% for theoretical weight loss). As seen in Figure 4-4, $Ni_{0.9}Mg_{0.1}O$ shows two peaks; the first one at about 500°C and the second one at about 650°C, which is attributed to the reduction of Ni in NiO and in Ni-Mg-O solid solution, respectively. In the present work the amount of Mg is small compared to that of Ni (10 mol% Mg vs. 90% Ni) resulting in MgO being dissolved in the NiO matrix. Comparing the TPR results for the 5% Cu prepared from the two different methods reveals that when Cu is co-precipitated with Mg and Ni, much higher temperatures are required to fully reduce the sample; when 5% Cu is impregnated, the sample is fully reduced at temperatures close to 700°C, whereas when it is co-precipitated, it requires temperatures close to 800°C as seen in Figure 4-4 (a) where the rate of weight loss for $Ni_{0.85}Cu_{0.05}Mg_{0.1}O$ is almost zero at 800°C. This implies that $Ni_{0.9-x}Cu_xMg_{0.1}O$ made from the one-step method is more difficult to reduce than when prepared using the two-step method.

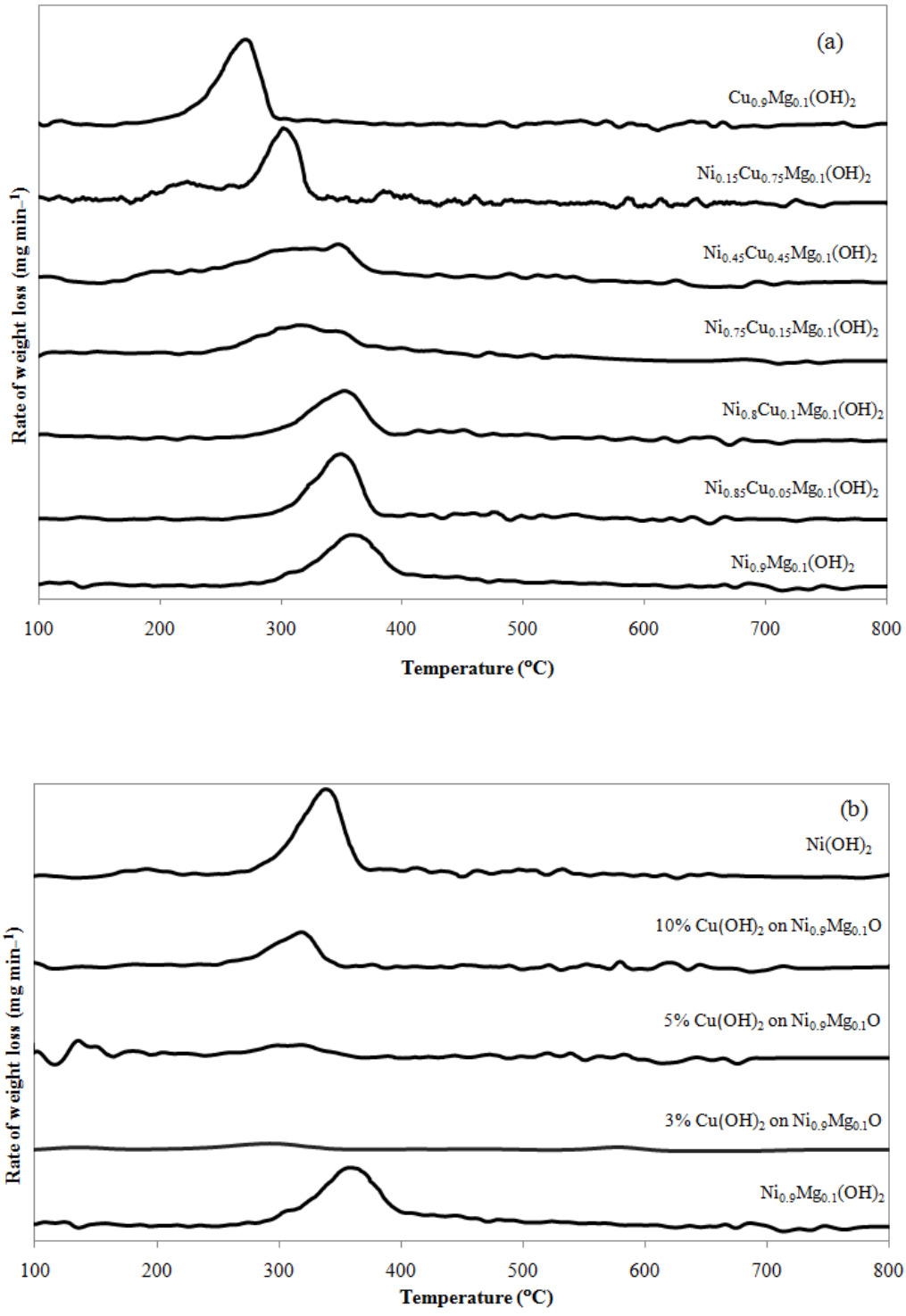

Figure 4-3 Rate of weight loss in TPO test for different $Ni_{1-x-y}Cu_xMg_yO$ materials. a) Materials fabricated using one-step co-precipitation, b) materials prepared using two-step method (Cu impregnation).

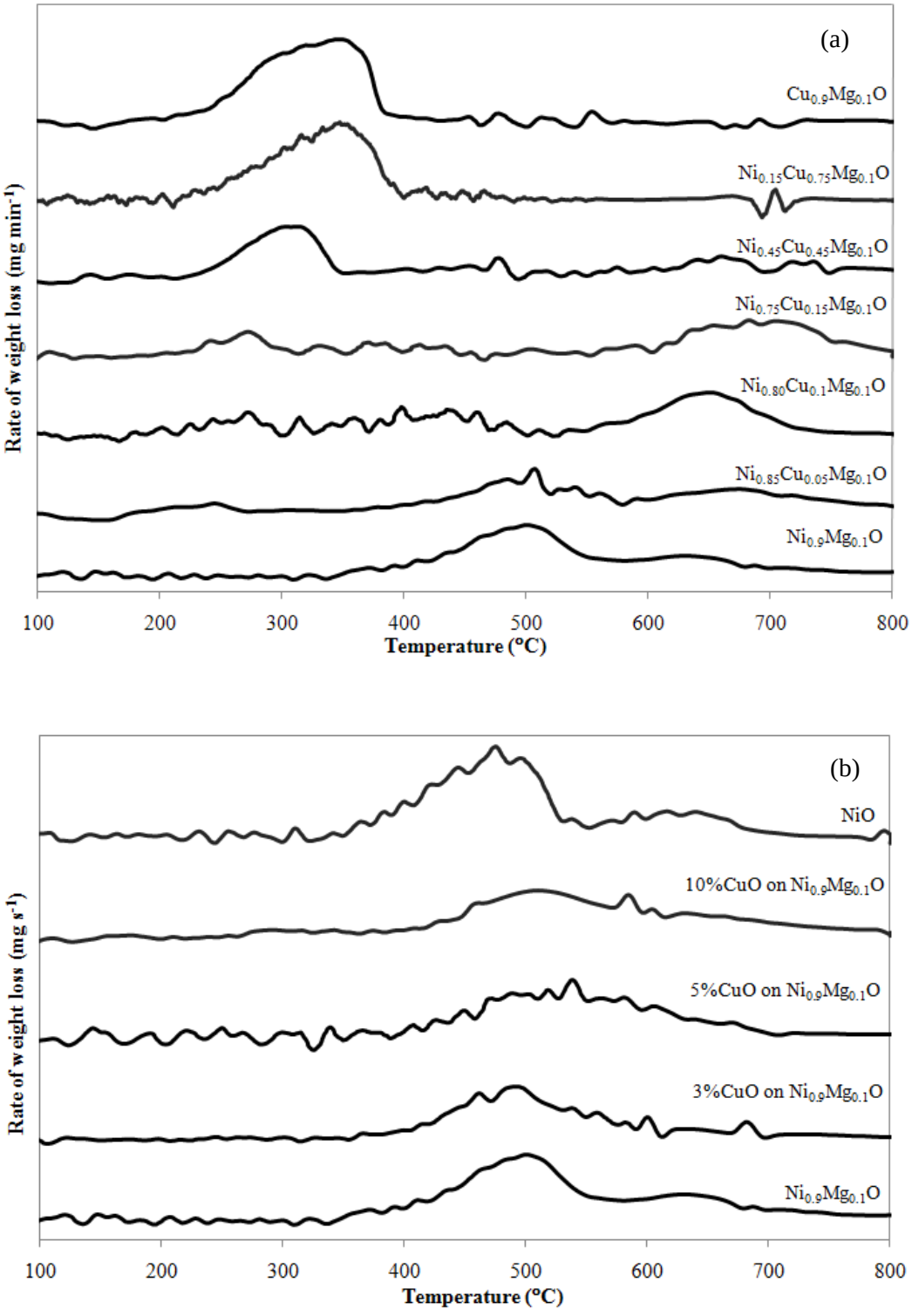

Figure 4-4 Rate of weight loss in TPR test for different $Ni_{1-x-y}Cu_xMg_yO$ materials. a) Materials fabricated using one-step co-precipitation, b) materials prepared using two-step method (Cu impregnation).

Table 4-1 Results for TPO analysis.

Sample	TPO weight loss	
	Experimental	**Theoretical**
$Ni(OH)_2$	19.5%	19.4%
$Ni_{0.90}Mg_{0.10}(OH)_2$	25.4%	20.2%
$Ni_{0.85}Cu_{0.05}Mg_{0.1}(OH)_2$	19.5%	20.1%
$Ni_{0.8}Cu_{0.1}Mg_{0.1}(OH)_2$	24.6%	20.1%
$Ni_{0.75}Cu_{0.15}Mg_{0.1}(OH)_2$	28.1%	20.0%
$Ni_{0.45}Cu_{0.45}Mg_{0.1}(OH)_2$	27.7%	19.7%
$Ni_{0.15}Cu_{0.45}Mg_{0.1}(OH)_2$	24.4%	19.4%
$Cu_{0.90}Mg_{0.10}(OH)_2$	20.6%	19.2%
3%$Cu(OH)_2$ impregnated on $Ni_{0.90}Mg_{0.10}O$	1.7%	-
5% $Cu(OH)_2$ impregnated on $Ni_{0.90}Mg_{0.10}O$	5.3%	-
10% $Cu(OH)_2$ impregnated on $Ni_{0.90}Mg_{0.10}O$	8.5%	-

Note Experimental weight losses represent weight losses at the end of TPO (i.e. when temperature reached 800°C).

Table 4-2 Results for TPR analysis

Sample	TPR weight loss	
	Experimental	**Theoretical**
NiO	21.0%	21.4%
$Ni_{0.90}Mg_{0.10}O$	20.8%	20.2%
$Ni_{0.85}Cu_{0.05}Mg_{0.1}O$	20.7%	20.1%
$Ni_{0.8}Cu_{0.1}Mg_{0.1}O$	20.1%	20.1%
$Ni_{0.75}Cu_{0.15}Mg_{0.1}O$	20.0%	20.0%
$Ni_{0.45}Cu_{0.45}Mg_{0.1}O$	19.5%	19.6%
$Ni_{0.15}Cu_{0.45}Mg_{0.1}O$	18.8%	19.2%
$Cu_{0.90}Mg_{0.10}O$	19.5%	19.0%
3%CuO impregnated on $Ni_{0.90}Mg_{0.10}O$	19.8%	20.2%
5% CuO impregnated on $Ni_{0.90}Mg_{0.10}O$	19.8%	20.2%
10% CuO impregnated on $Ni_{0.90}Mg_{0.10}O$	20.0%	20.2%

Note Experimental weight losses represent weight losses at the end of the TPR analysis (i.e. when temperature reached 800°C).

4.2.3 Material Phase

Figure 4-5 shows the effect of calcination temperature on the crystalline phases (XRD patterns) in the case of $Ni_{0.45}Cu_{0.45}Mg_{0.1}O$ prepared using the one-step co-precipitation method. This figure shows that the higher the calcination temperature, the higher the crytallinity. Figure 4-6 shows the presence of Ni and Mg solid solution, as reported previously in the literature (Zinkevich et al. (2005)). The XRD peaks for NiO and MgO are very closed to each other and hardly distinguishable. Figure 4-7 are the patterns obtained from samples prepared by the one-step method for different compositions. The results reveal that the XRD pattern of pure NiO and that of the mixture $Ni_{0.9}Mg_{0.1}O$ are similar, as shown in the literature, for example, by Moon and Ryu (2003). However, the XRD patterns of samples containing more than 15 mol% copper have distinct peaks associated with CuO. The same patterns were also obtained for $Ni_{0.9x-}Cu_xMg_{0.1}O$ when Cu is less than 10 mol% ($x \leq 0.1$). The XRD patterns of the samples prepared by the two-step method are similar to those obtained from the one-step method when Cu-content is equal to or less than 10% (Figure 4-8). These patterns are matched with the patterns of $Ni_{1-x}Cu_xO$ when $x \leq 0.25$ (interpreted by the EVA software). However, the XRD pattern of 3% Cu-content sample is similar to $Ni_{1-x}Cu_xO$ when $x \leq 0.20$. Although the XRD patterns of $Ni_{0.9-x}Cu_xMg_{0.1}O$ ($x \leq 0.10$) are similar to that of NiO, the TPR results (see Figure 4-4) indicated the presence of multi-phases in $Ni_{0.9-x}Cu_xMg_{0.1}O$. For example, $Ni_{0.9}Mg_{0.1}O$ and $Ni_{0.85}Cu_{0.05}Mg_{0.1}O$ have the fingerprints of NiO and Ni-Mg-O solid solutions, as illustrated in Figure 4-4 by the rate of reduction at higher temperatures. It implies that, in these cases, the Ni-Mg-O solid solution is dispersed into the NiO matrix and that Ni-Mg-O (and also CuO) pattern were hidden because of their significant lower amount compared to that of NiO.

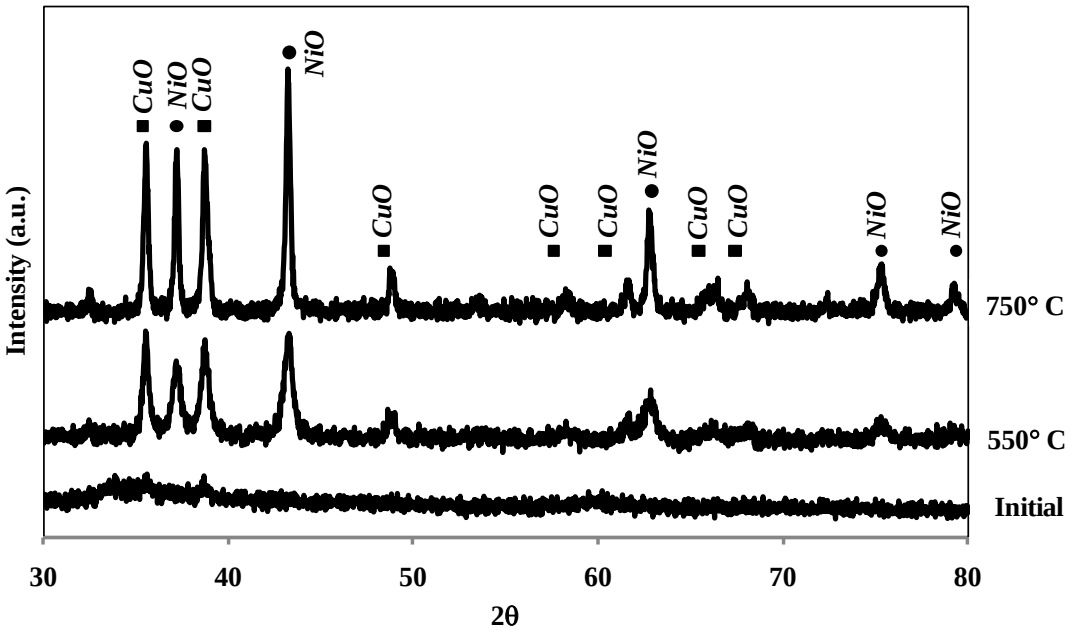

Figure 4-5 XRD patterns of $Ni_{0.45}Cu_{0.45}Mg_{0.1}O$ from the one-step method at the initial state and after calcination at 550ºC and 750ºC for 4h.

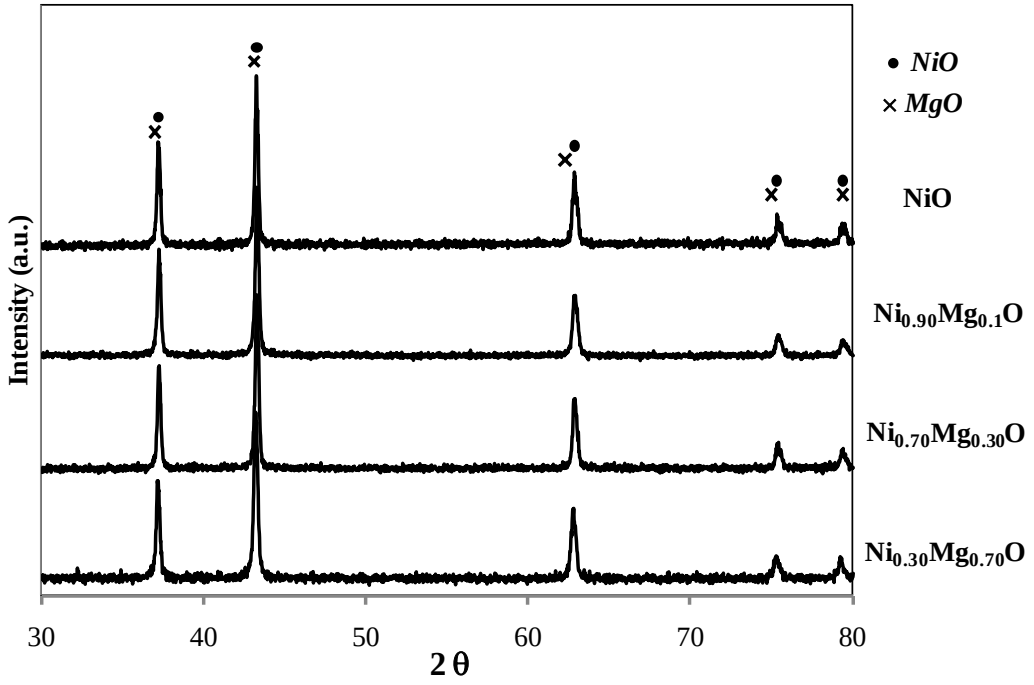

Figure 4-6 XRD patterns of $Ni_{1-y}Mg_yO$ calcined at 750ºC for 4h.

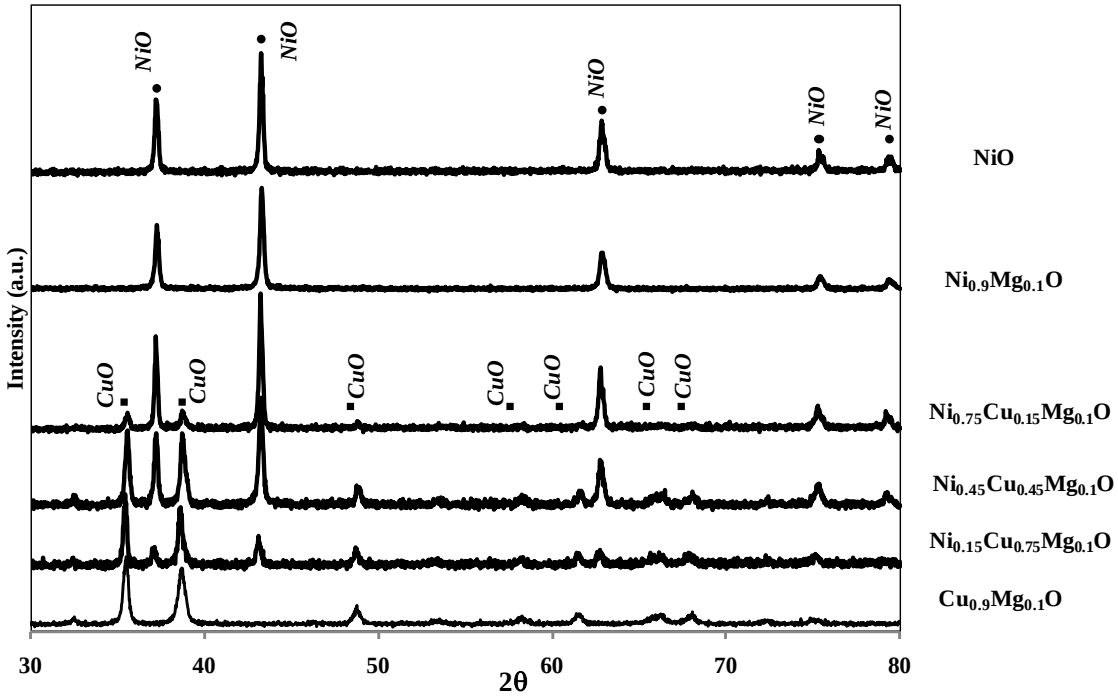

Figure 4-7 XRD patterns of $Ni_{1-x-y}Cu_xMg_yO$ from the one-step method after calcination at 750ºC for 4h.

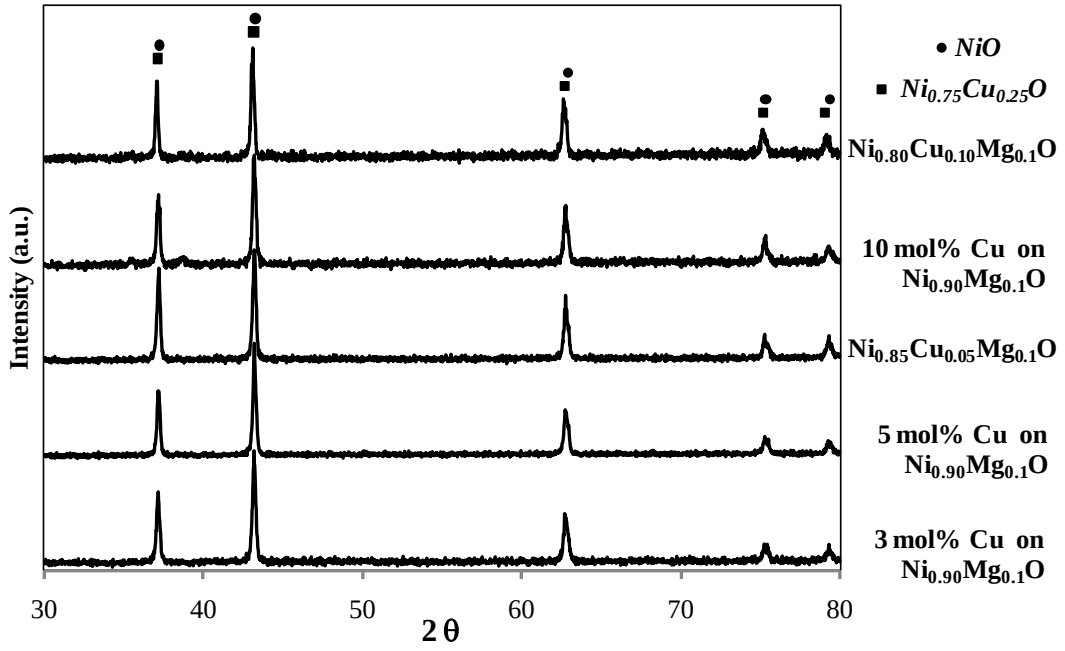

Figure 4-8 XRD patterns of 3, 5 and 10 mol% Cu impregnated on $Ni_{0.9}Mg_{0.1}O$ made from the two-step method after calcination at 750ºC for 4h compared with $Ni_{0.85}Cu_{0.05}Mg_{0.10}O$ and $Ni_{0.80}Cu_{0.10}Mg_{0.10}O$ made from the one-step method.

4.2.4 Surface Area

Total surface areas of the samples analysed by the BET technique are reported in Table 4-3. The comparison between the samples containing 10% of Mg indicates that the surface area of the samples decreases somewhat when the copper content increases; from 9.6 m^2/g for $Ni_{0.85}Cu_{0.05}Mg_{0.1}O$ down to 8.1 m^2/g for $Ni_{0.45}Cu_{0.45}Mg_{0.1}O$. The samples prepared from a two-step co-precipitation/impregnation method have similar, or slightly lower, surface area than those prepared using the one-step method.

Table 4-3 Single point and BET surface areas of $Ni_{1-x-y}Cu_xMg_yO$ (note: every sample contains 50 wt% of SDC).

Sample	BET surface area (m^2/g)
SDC	11.4
NiO	11.8
$Ni_{0.90}Mg_{0.10}O$	10.7
$Ni_{0.85}Cu_{0.05}Mg_{0.1}O$	9.6
$Ni_{0.8}Cu_{0.1}Mg_{0.1}O$	8.9
$Ni_{0.75}Cu_{0.15}Mg_{0.1}O$	8.5
$Ni_{0.45}Cu_{0.45}Mg_{0.1}O$	8.1
$Ni_{0.15}Cu_{0.75}Mg_{0.1}O$	7.2
$Cu_{0.90}Mg_{0.10}O$	6.8
3%CuO impregnated on $Ni_{0.90}Mg_{0.10}O$	10.5
5% CuO impregnated on $Ni_{0.90}Mg_{0.10}O$	9.2
10% CuO impregnated on $Ni_{0.90}Mg_{0.10}O$	8.4

4.3 Button Cell Fabrication Using Alternative Anode Material

Electrolyte-supported cells are fabricated using a dry pressing technique. To make the dense SDC electrolyte pellets, 0.73 g of SDC powder are pressed and sintered at 1450ºC for 5 hours using a heating rate of 5 ºC/min. The thickness of the pellet starts from 600 µm approximately. To reduce the thickness, the pellet is polished by sand paper no.600. Then, the anode (without Cu), is fabricated by drop-and-dry of the suspension on one side of the electrolyte disc. The suspension material consists of 50wt% Ni-Mg-O: 50wt% SDC in ethanol (0.5g solid in 30g suspension). The anode is then sintered at 1300ºC for 3 hours with a ramping rate of 5 ºC/min. The cathode is deposited using the same drop-and-dry method as for the anode: the suspension consists of 70wt% SSC: 30wt% SDC in ethanol (0.5g solid in 30g suspension). The cathode is finally sintered at 950ºC (heating rate of 5ºC/min) and

stay for 3 hours. For anodes containing Cu, the desired amount of 0.01M Cu nitrate solution is impregnated. The anode is then calcined at 750 ºC for 4 hours. The entire procedure is illustrated in Figure 4-9.

The actual cell is shown in Figure 4-10 which shows (a) the size of the cell and the electrode, (b) SEM micrograph of the anode/electrolyte interface microstructure of 50wt% $Ni_{0.9}Mg_{0.1}O$: 50wt% SDC anode/SDC electrolyte (after sintering) (c) SEM micrograph of 50wt% $Ni_{0.9}Mg_{0.1}O$: 50wt% SDC on the anode side after reduction. The button cell and the electrodes have 14 and 6 mm diameters, respectively and the anode is firmly bonded to the electrolyte as well as a porous structure at the anode/electrolyte interface. After the anode is reduced, it contains small particles (dark spots in Figure 4-10(c)) dispersed on large particles (light spots Figure 4-10(c)). The small particles are $Ni_{0.9}Mg_{0.1}O_{0.1}$, while the large particles are SDC.

To evaluate elemental distribution in the anode material, the 5%Cu on 50wt% $Ni_{0.9}Mg_{0.1}O$: 50wt% SDC powder was prepared and analyzed via SEM/energy-dispersive X-ray spectroscopy (EDX). Figure 4-11 displays the results of the final product after reduction. Figure 4-11(a) is the original SEM image, whereas Figure 4-11 (b), (c), (d) and (e) show the EDX mapping of cerium, samarium, nickel and copper, respectively. The EDX mappings demonstrate that all elements including copper are distributed uniformly.

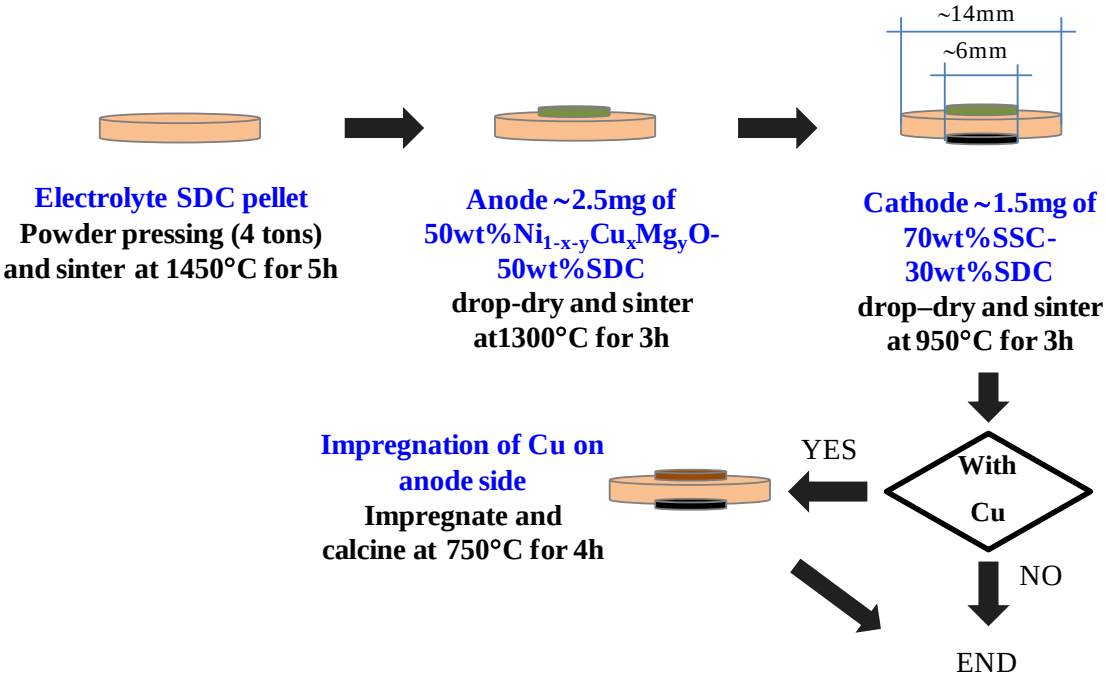

Figure 4-9 Process of button cell preparation.

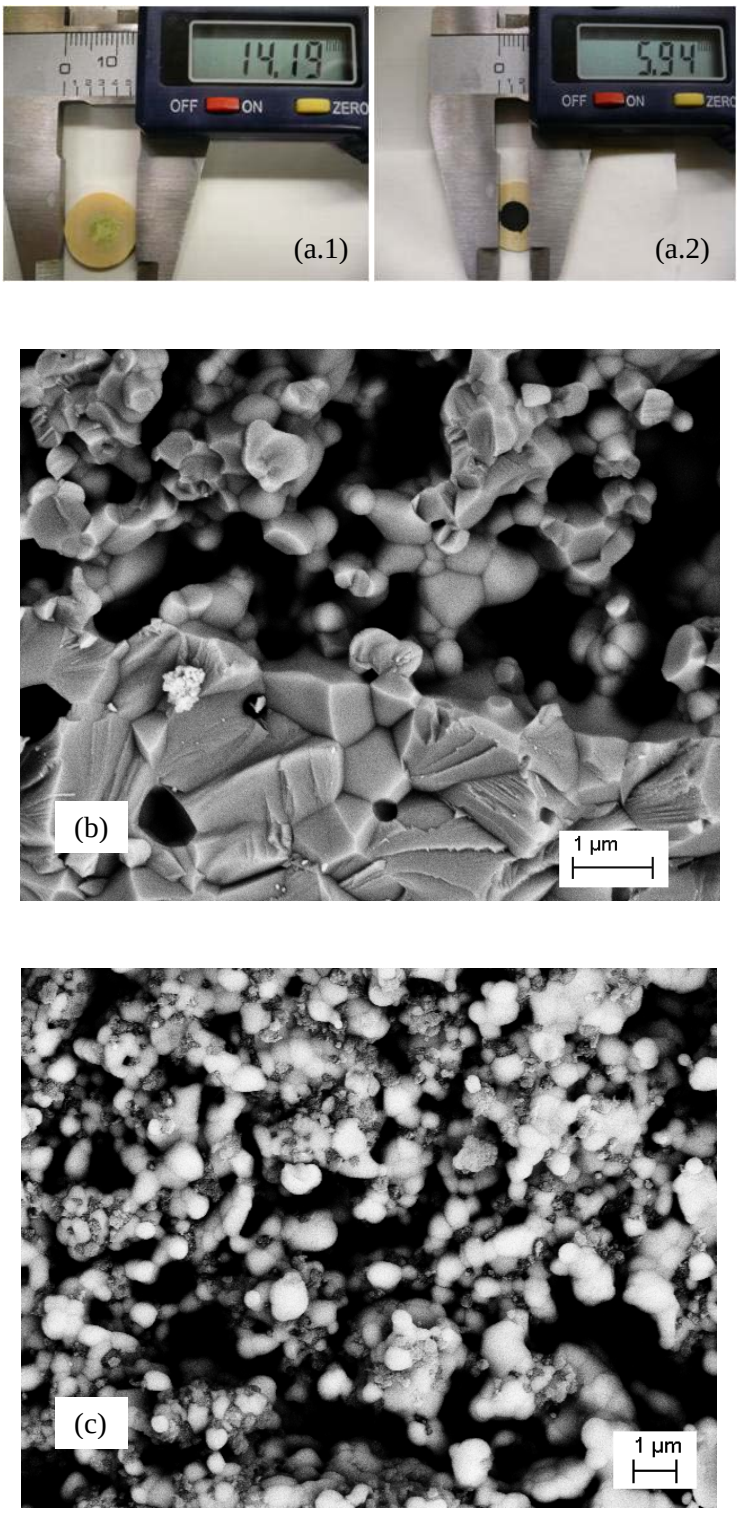

Figure 4-10 Button cell a) actual feature b) SEM backscattered electron micrograph of the anode/electrolyte interface (after sintering) c) SEM backscattered electron micrograph of the anode surface (after reduction).

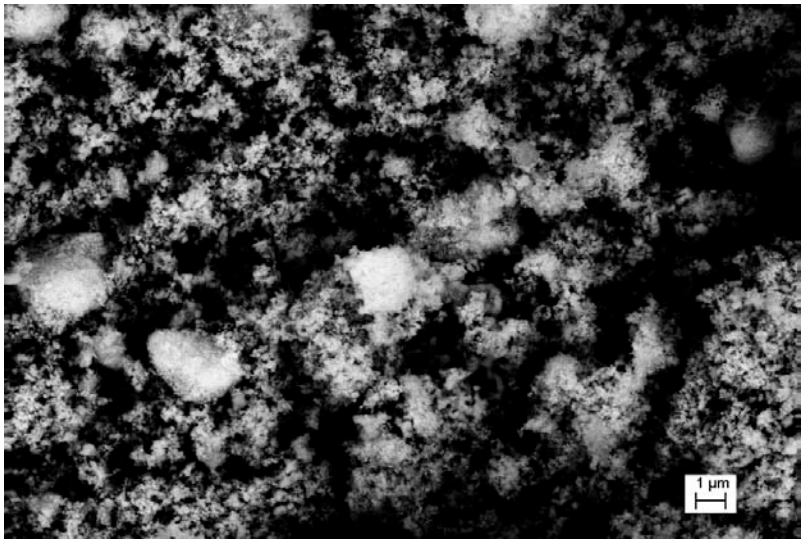

(a)

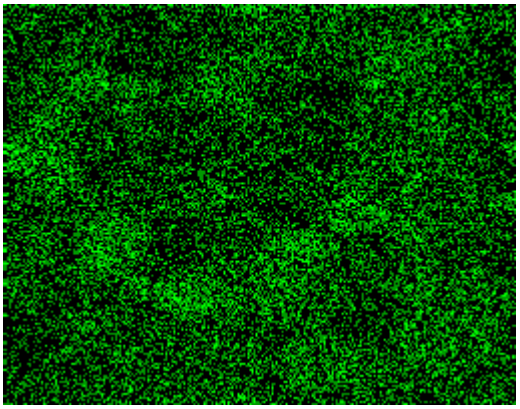

(b) Ce

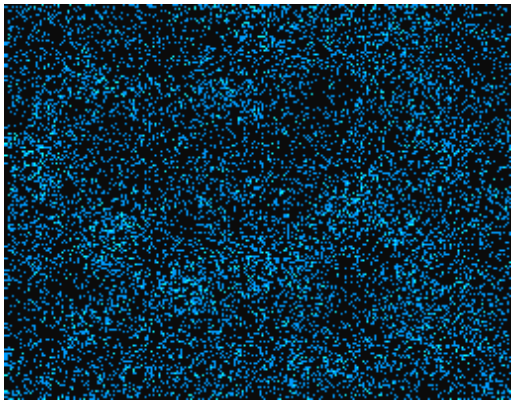

(c) Sm

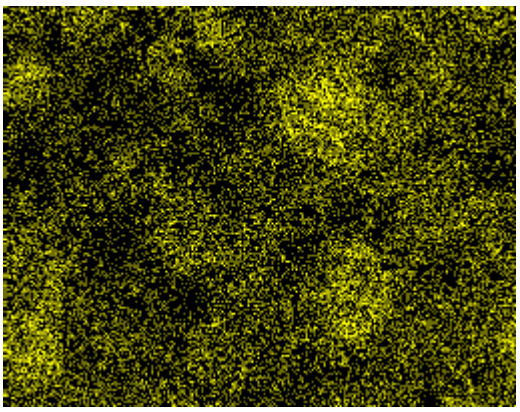

(d) Ni

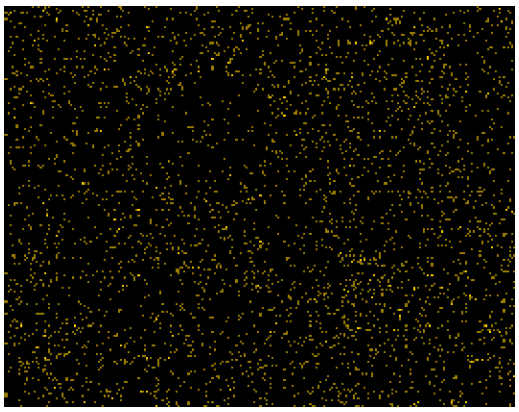

(e) Cu

Figure 4-11 SEM-EDX image and elemental distribution of a 50wt% $Ni_{0.9}Mg_{0.1}O$: 50wt% SDC impregnated with Cu to make 50wt% 5%Cu on $Ni_{0.9}Mg_{0.1}O$: 50wt% SDC a) SEM backscattered electron image for overall determination b) cerium c) samarium d) nickel and e) copper.

4.4 Conductivity

A critical property of an electrode is its electronic conductivity because the electrons must be transported through the cermet from the TPB as easily as possible to the other side of the anode and to the external circuit. To determine the conductivity (at room temperature under air), the alternative anodes have been pelletized and formed into a rectangular piece.

The sample preparation begins with blending 50wt% Ni-Mg-O: 50wt% SDC via traditional ball milling. The product is pressed using a hydraulic press. Since the sample is still fragile, sintering at the sintering temperature of the actual anode is necessary. Copper is added by impregnation after sintering at high temperature. To this point in the process, the sample is not conductive because all metals are in oxide form. To activate the sample, it must be reduced in H_2 atmosphere. The treated sample is then ready for the measuring the conductivity which was carried out at room temperature. A flow sheet of this procedure and image of specimen after sintering are shown in Figure 4-12and Figure 4-13, respectively.

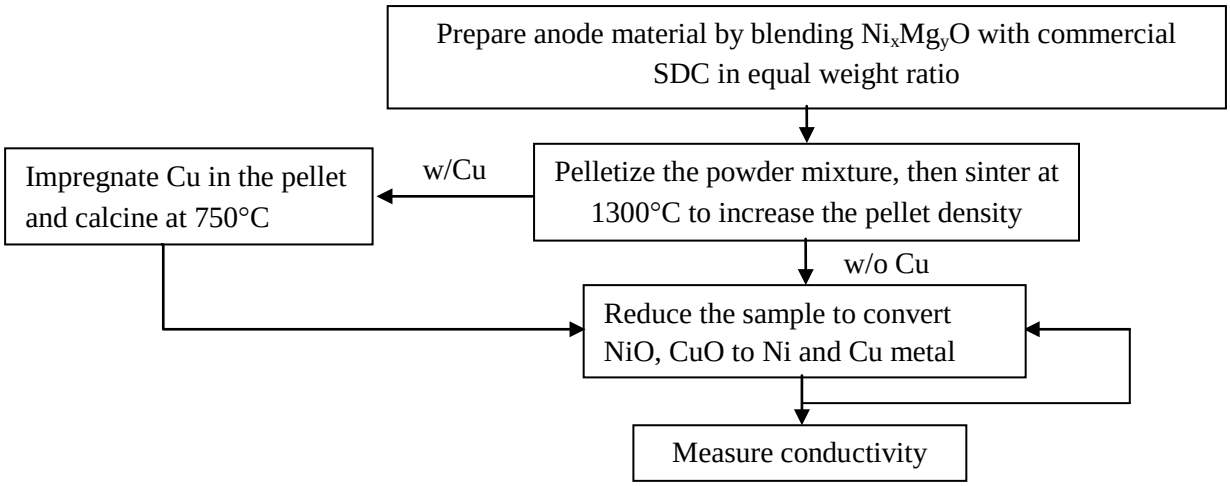

Figure 4-12 Procedure of sample preparation for the conductivity measurement.

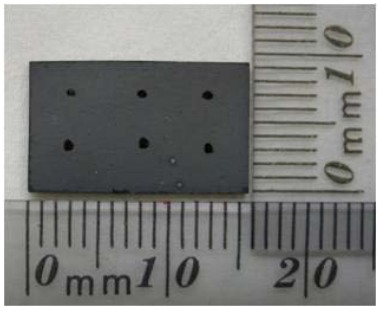

Figure 4-13 $Ni_{0.9}Mg_{0.1}O$ sample after sintering.

The 5mm intervals are marked on the sample as two sets of dots. A constant current of 1A is supplied along the sample, the voltage difference between the dots is measured, from which the conductivity is computed (see chapter 3 for more details). Closely related to conductivity is the percentage of reduction, which is determined by the method described in Chapter 3. The percentage of reduction and the conductivities are given in Table 4.2. The reduction of $Ni_{0.7}Mg_{0.3}O$ is 42%, indicating that at least half of NiO is dissolved in the MgO and remains in solid solution and so cannot be reduced. Therefore, a completely conductive path cannot be formed in this sample. Among all compositions, $Ni_{0.9}Mg_{0.1}O$ has the highest conductivity (~136 S/cm). Impregnation of Cu reduces the conductivity, although no differences in conductivity of 3% Cu impregnation and 5% Cu impregnation on $Ni_{0.9}Mg_{0.1}O$ (~100 S/cm) were observed. NiO:SDC had the lowest conductivity (~70 S/cm). The above results can be explained as follows, using percolation theory:

- Ni-based anodes with some amounts of magnesium oxide ($Ni_{0.9}Mg_{0.1}O$, 3% Cu on $Ni_{0.9}Mg_{0.1}O$, 5% Cu on $Ni_{0.9}Mg_{0.1}O$) prevent the nickel metal from agglomerating. They also better distribute the small nickel metal particles throughout the entire sample resulting in better conductance. Figure 4-14 shows the microstructure of two types of powder (a) Ni:SDC, (b) reduced $Ni_{0.9}Mg_{0.1}O$:SDC and (c) reduced 5% Cu on $Ni_{0.9}Mg_{0.1}O$. The middle image confirms better dispersion of particles than in the Ni:SDC structure. Shiratori et al. (2006) and Gac et al. (2009) also presented similar results.
- However, excessive magnesium oxide keeps Ni in a Ni-Mg-O form which is a non-conductive form. This is illustrated by the very poor conductivity obtained with 30% Mg, whereas 10% Mg did improve the conductivity over NiO:SDC, as also found by Choi et al. (1984).
- 3% Cu on $Ni_{0.9}Mg_{0.1}O$ and 5% Cu on $Ni_{0.9}Mg_{0.1}O$ have lower conductivity than the $Ni_{0.9}Mg_{0.1}O$, even though their reduced form has similar structure to the reduced $Ni_{0.9}Mg_{0.1}O$ (Figure 4-14(c)). It is speculated that Ni-Cu bond and Cu-Cu bond are not as strong as Ni-Ni bond in these samples. Although the sample was already calcined, the reduction time (1 h at 750°C)was not long enough to make a Ni-Cu alloy

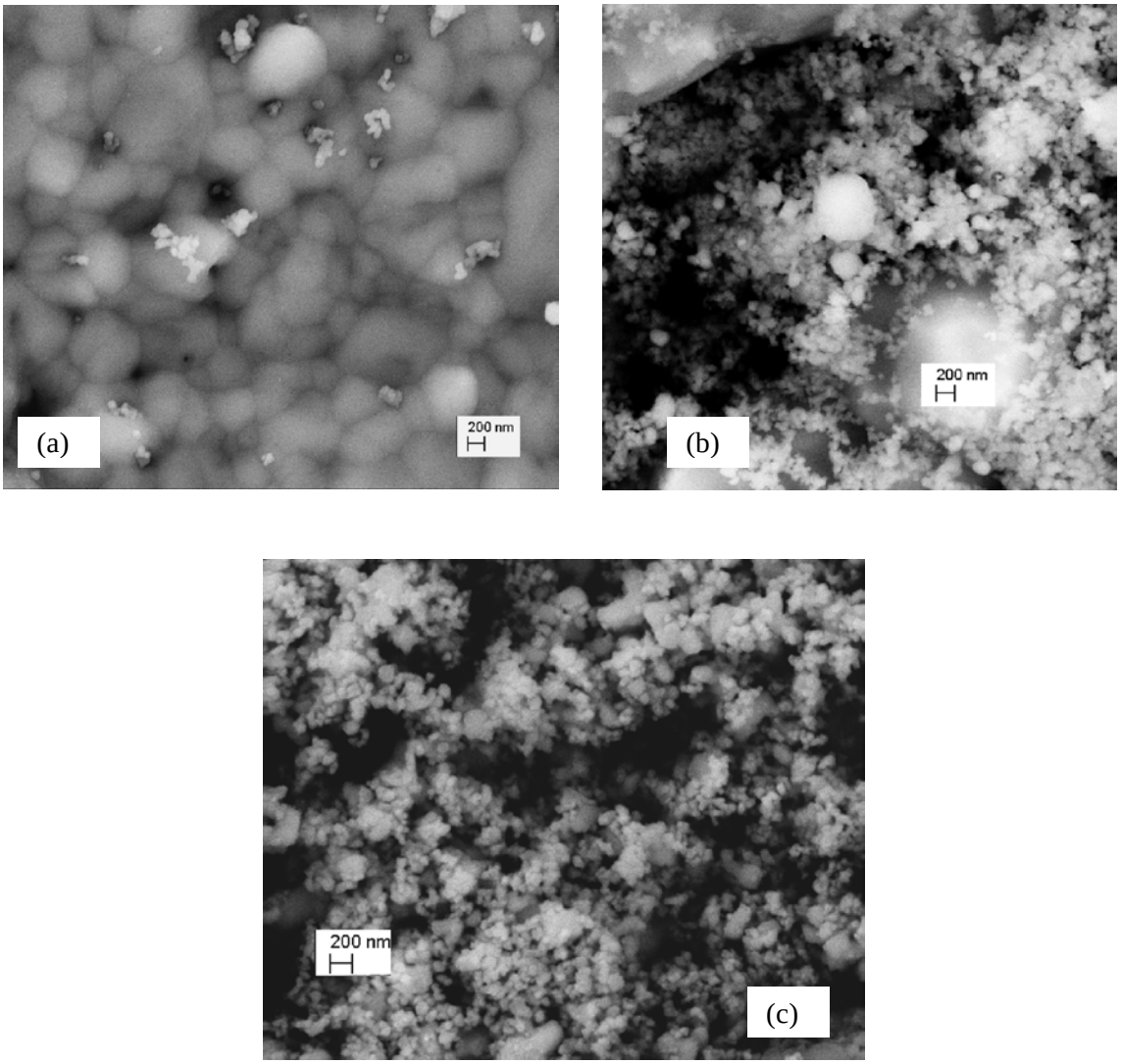

Figure 4-14 SEM backscattered electron micrographs of a) Ni:SDC and b) $Ni_{0.9}(MgO)_{0.1}$:SDC c) 5%Cu impregnated on $Ni_{0.9}(MgO)_{0.1}$:SDC.

Table 4-4 Percentage of reduction and conductivity

Sample	%Reduction	Conductivity ($S.cm^{-1}$)
NiO:SDC	97.1	69.8
$Ni_{0.7}Mg_{0.3}O$:SDC	42.4	n/a
$Ni_{0.9}Mg_{0.1}O$:SDC	94.1	135.8
3%Cu on $Ni_{0.9}Mg_{0.1}O$:SDC	94.9	101.6
5%Cu on $Ni_{0.9}Mg_{0.1}O$:SDC	95.3	101.4

n/a : non applicable

Chapter 5

Methane Steam Reforming Activity over $Ni_{0.9-x}Cu_xMg_{0.1}O$/SDC

Because internal methane steam reforming (SMR) is of great benefit to SOFCs, it is important to study the SMR performance of the alternative anodes developed in this work. To evaluate the anode performance (characterized here by its activity, selectivity and stability), several 50wt% $Ni_{0.9-x}Cu_xMg_{0.1}O$/ 50wt% SDC samples were tested at S/C ratios of 3, 2, 1 and 0, and at 750ºC and 650ºC, in a fixed-bed reactor using GC for product analysis.

5.1 Experimental Procedure

To perform methane steam reforming tests, the reactor, containing the catalyst bed, is placed inside a tube furnace. Before carrying out any experiments, a leak test must be done first to confirm that no leak occurs in the system. Then, the catalyst is reduced in-situ under 10%H_2/N_2 atmosphere for one hour. Finally, the temperature and the flow rate of each reactant are set to their desired values. The first sample is collected approximately 5 min after introducing the reactant gas (i.e. $CH_4/H_2O/N_2$ mixture) and repeated every 33 min until finishing the experiment. The procedure is summarized in Figure 5-1.

The activity, selectivity and stability depend not only on the test conditions (e.g., S/C ratio, temperature), but also on the 50wt% $Ni_{0.9-x}Cu_xMg_{0.1}O$/ 50wt% SDC composition. Before determining the effect of all the parameters using experimental data, a thermodynamic analysis is reported.

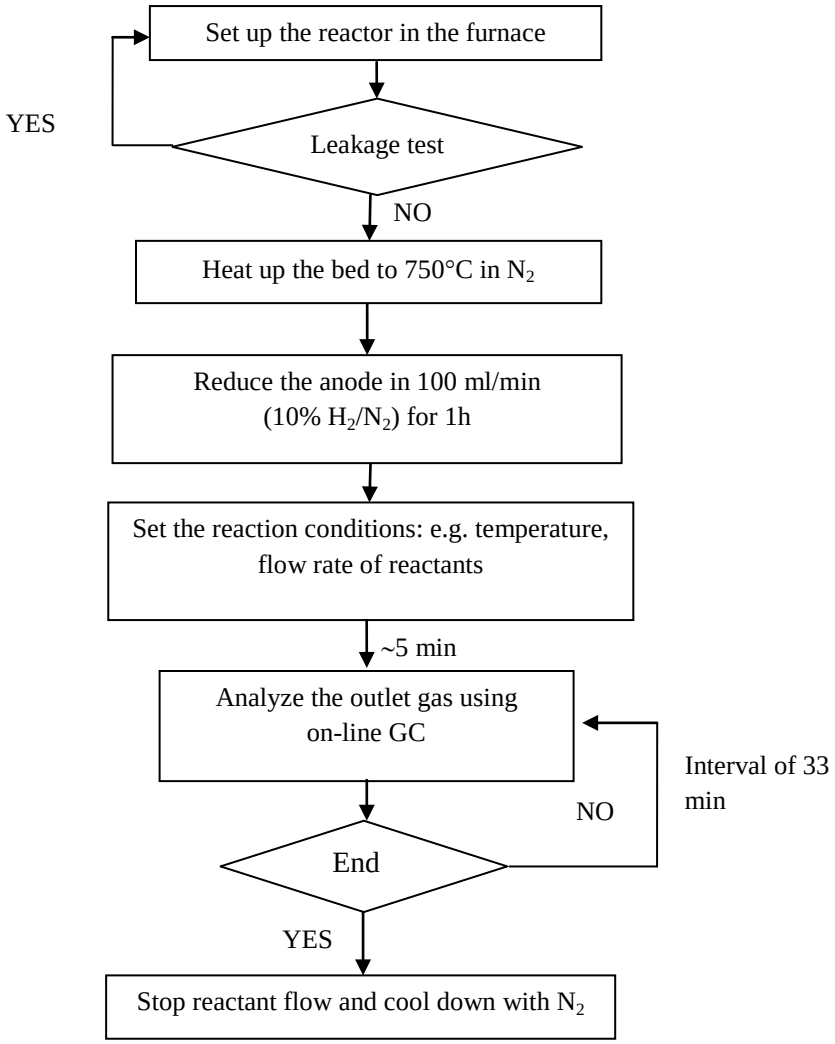

Figure 5-1 Procedure of SMR test.

5.2 Thermodynamic Simulation Results: Effect of Temperature and S/C on Methane Conversion, Carbon Yield, Hydrogen Yield and $CO_2/(CO+ CO_2)$ Ratio

Thermodynamic calculations were performed using the Gibb's equilibrium reactor utility in Aspen 12.1. The results were generated by the minimization of Gibb's free energy method. The objective of this thermodynamic study was to assess the effects of temperature and S/C ratio on SMR. The possible formation of carbon was also considered in this simulation. Figure 5-2 shows the equilibrium methane conversion and carbon yield as a function of S/C for temperatures of 650 and 750°C. Figure 5-3 shows the equilibrium hydrogen yield and $CO_2/(CO+CO_2)$ ratio as function of S/C, again at temperatures of 650 and 750°C.

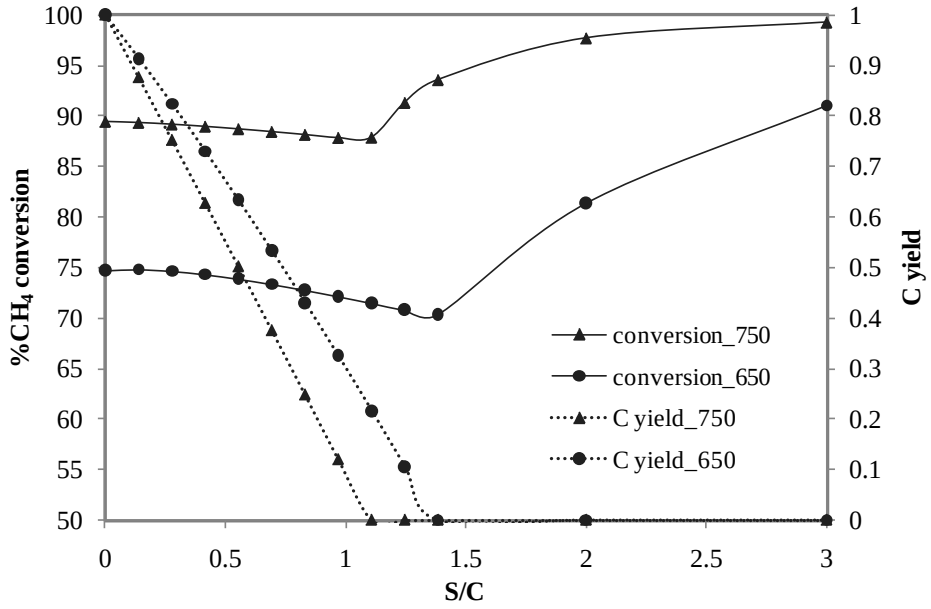

Figure 5-2 Effect of temperature and S/C on equilibrium CH_4 conversion and C yield.

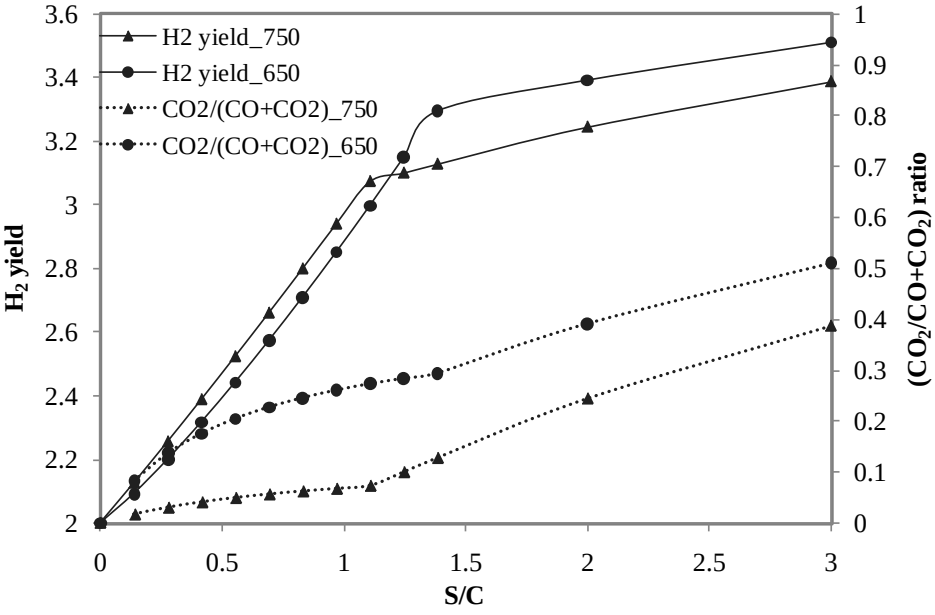

Figure 5-3 Effect of temperature and S/C on equilibrium H_2 yield and $CO_2/(CO+ CO_2)$ ratio.

In Figure 5-2, the predicted equilibrium CH_4 conversion at 650°C is always lower than that at 750°C because both SMR and methane cracking are endothermic reactions.

From Figure 5-2 (carbon yield), it is seen that the methane cracking reaction contributes to the overall reaction for S/C in the range 0 - 1.1 at 750°C and for S/C in the range 0 - 1.4 at 650°C. In those ranges the CH_4 conversion decreases slightly with increasing S/C. As expected, the maximum carbon yield appears at the dry condition. When carbon is not produced (carbon yield of zero), the conversion increases significantly as S/C increases, because SMR/WGS become the dominating reactions.

Recall that the SMR reaction and WGS are:

$$CH_{4(g)} + H_2O_{(g)} \leftrightarrow CO_{(g)} + 3H_{2(g)} \quad (\text{CH}_4 \text{ steam reforming}) \qquad (5\text{-}1)$$

$$CO_{(g)} + H_2O_{(g)} \leftrightarrow CO_{2(g)} + H_{2(g)} \quad (\text{water-gas shift}) \qquad (5\text{-}2)$$

We can therefore conclude that for these two reactions, the H_2 yield should be between 3 (if only reaction (2-4) takes place) and 4 (if all CO is converted via WGS).

The methane cracking reaction is:

$$CH_{4(g)} \leftrightarrow C_{(s)} + 2H_{2(g)} \qquad (5\text{-}3)$$

From Figure 5-3, it can be seen that the equilibrium H_2 yield is between 2 and 3 for S/C less than 1,which is related to the contribution of the cracking reaction at these low S/C ratios. Figure 5-3, H_2 yield is a little higher at 750°C than those at 650°C for S/C <1.3. However, for S/C $\geq$ 1.3, the opposite is predicted: equilibrium H_2 yield greater at 650°C than at 750ºC. The simulation indicates that the equilibrium $CO_2/(CO+ CO_2)$ ratio is always greater at 650°C than at 750°C because low temperature is more favourable than high temperature for the WGS reaction. It should be noted that most of the equilibrium $CO_2/(CO+ CO_2)$ ratio are lower than 0.5. In the experiment, the gas hourly space velocity (GHSV) of about 200,000 $L.g^{-1}.h^{-1}$ was used at S/C at 3 and 2 while GHSV of about 150,000 was used for S/C at 1. N_2 dilution was used to control the value of GHSV. However, in order to make the condition close to fuel cell feed, N_2 should be kept low because diluting the feed with N_2 decreases the fuel cell performance. This is why the GHSV was lower at S/C of 1, compare to that at S/C of 2 and 3.

5.3 No Cu Addition: NiO:SDC and $Ni_{0.9}Mg_{0.1}O$:SDC

Effect of S/C

Figure 5-4(a), (b) and (c) show, the effect of S/C at 750°C, on CH_4 conversion, H_2 yield and $CO_2/(CO+CO_2)$ ratio, respectively for NiO:SDC and $Ni_{0.9}Mg_{0.1}O$:SDC. Figure 5-4(a) shows that, at a given S/C ratio, the material composition has no effect on CH_4 conversion. In other words, addition of 10 mol% Mg has no impact on the conversion at 750°C. Figure 5-4(a) clearly shows that CH_4 conversion decreases as S/C decreases. Methane conversion is about 85% for S/C of 3. The conversion reduces to about 70% and 50% for S/C of 2 and 1, respectively. With dry methane, the conversion started at just above 20%, but rapidly decreases to almost zero after five hours due to coke deposition from methane cracking.

As seen in Figure 5-4(b), the H_2 yield exhibits many fluctuations, in particular for $Ni_{0.9}Mg_{0.1}O$:SDC. Although it is difficult to draw a conclusion as to the effect of the material on H_2 yield, it is apparent that the H_2 yield decreases as S/C decreases. The situation is clearer for the $CO_2/(CO+ CO_2)$ ratio, as indicated in Figure 5-4(c). The $CO_2/(CO+ CO_2)$ ratio does not seem to be much affected by the nature of the material. However, it is clear that the $CO_2/(CO+ CO_2)$ ratio increases as S/C increases. Combined with the fact that H_2 yield increases with increasing S/C, it is logical to attribute the changes in H_2 and CO yields to the water-gas shift (WGS) reaction. Indeed, because steam is a reactant for methane steam reforming, the methane conversion increases with a greater S/C. Because steam is also a reactant for the WGS reaction, as the amount of water is increased, this will displace the WGS to the right and form more H_2 and CO_2, at the expense of CO.

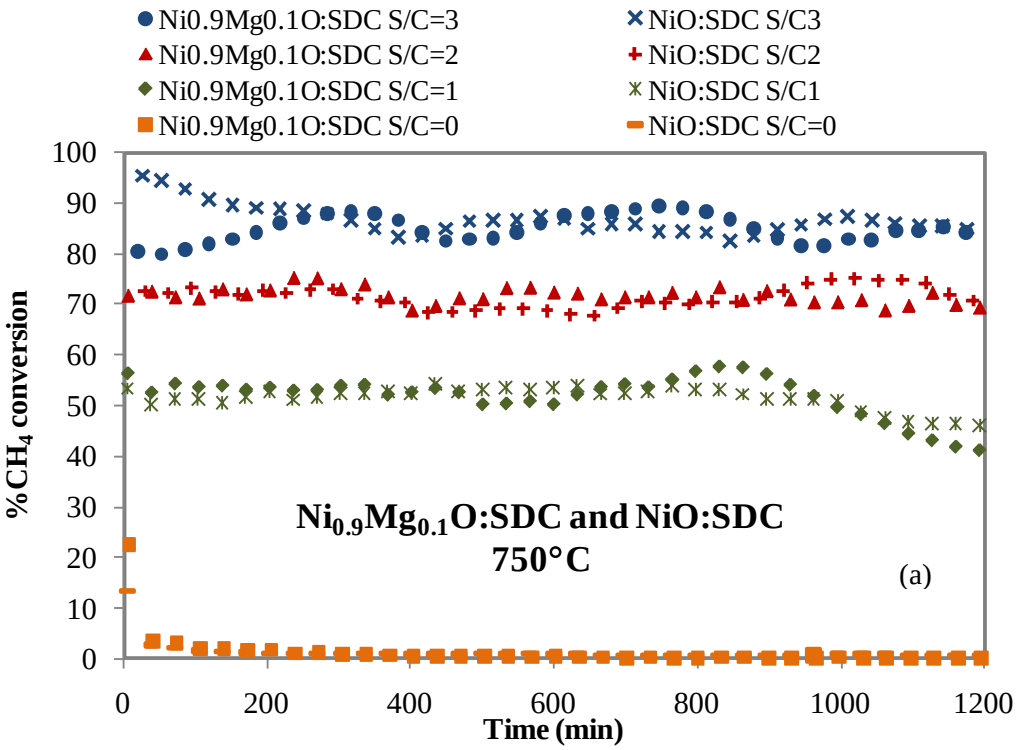
Ni0.9Mg0.1O:SDC S/C=3
NiO:SDC S/C3
Ni0.9Mg0.1O:SDC S/C=2
NiO:SDC S/C2
Ni0.9Mg0.1O:SDC S/C=1
NiO:SDC S/C1
Ni0.9Mg0.1O:SDC S/C=0
NiO:SDC S/C=0
% CH4 conversion
Ni0.9Mg0.1O:SDC and NiO:SDC
750°C
(a)
Time (min)

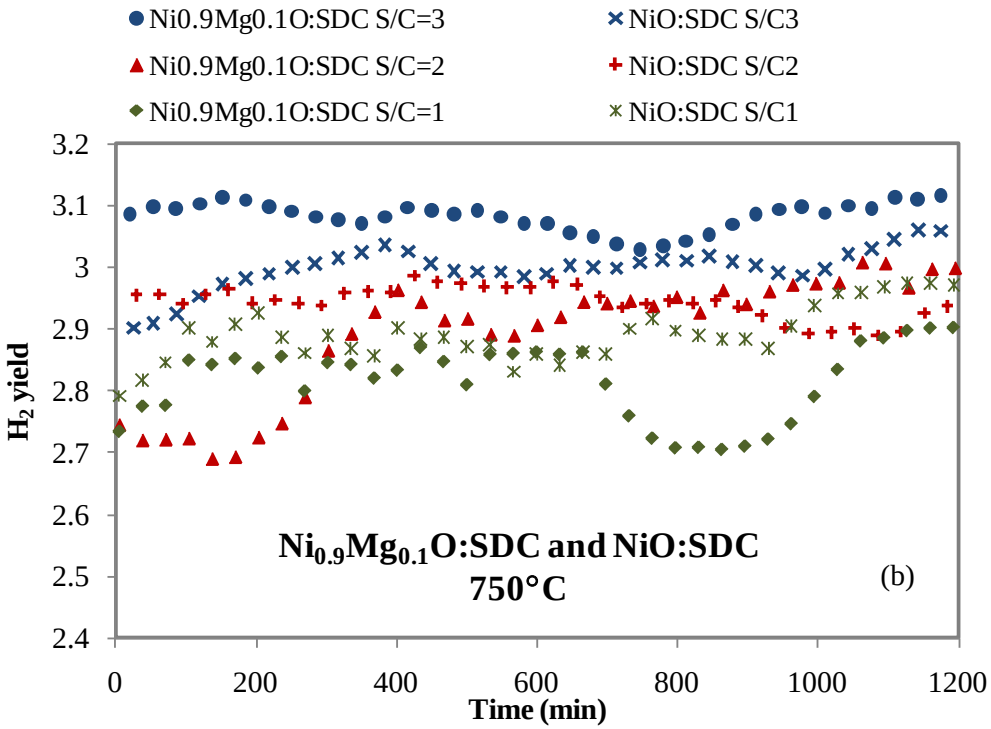
Ni0.9Mg0.1O:SDC S/C=3
NiO:SDC S/C3
Ni0.9Mg0.1O:SDC S/C=2
NiO:SDC S/C2
Ni0.9Mg0.1O:SDC S/C=1
NiO:SDC S/C1
H2 yield
Ni0.9Mg0.1O:SDC and NiO:SDC
750°C
(b)
Time (min)

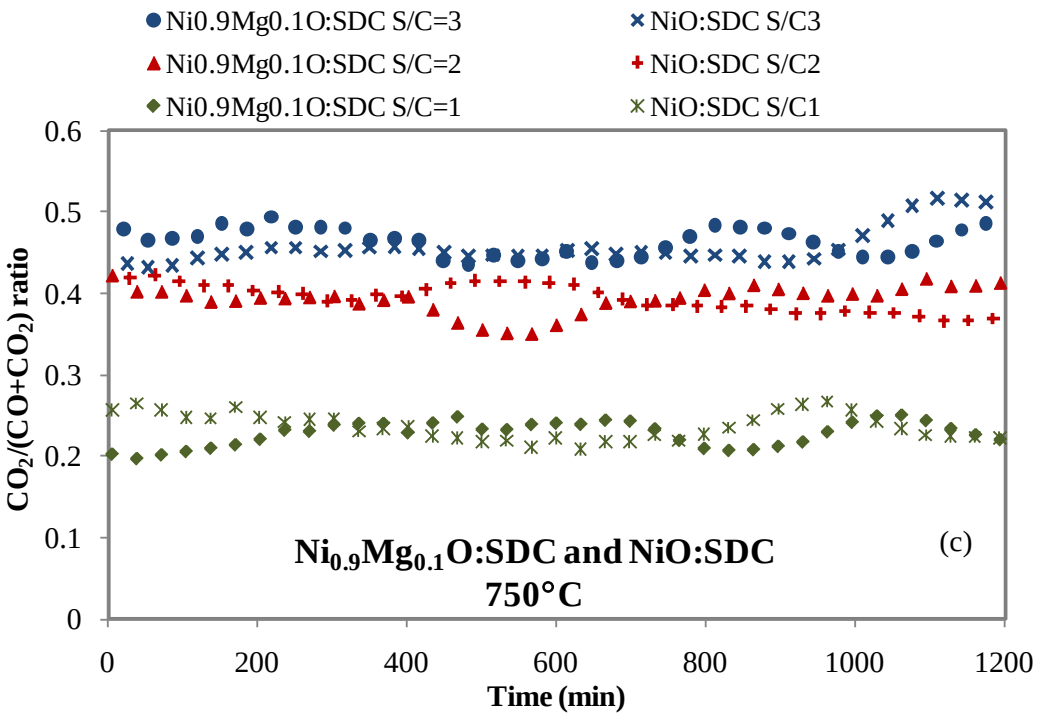

Figure 5-4 Results for NiO:SDC and $Ni_{0.9}Mg_{0.1}O$:SDC for S/C of 1, 2 and 3 at 750°C over 1200 min a) CH_4 conversion, b) H_2 yield, and c) $CO_2/(CO+ CO_2)$ ratio.

Effect of Temperature

Figure 5-5 shows the CH_4 conversion of NiO:SDC and $Ni_{0.9}Mg_{0.1}O$:SDC at temperatures of 650 and 750°C. Figure 5-5(a) represents the result for NiO:SDC, while Figure 5-5(b) is for $Ni_{0.9}Mg_{0.1}O$:SDC. Figure 5-5 shows that, for both materials, the conversion remains stable over 1200 minutes. As expected, the conversion increases as the temperature increases, which is in agreement with the expected trend. Nonetheless, the conversions obtained experimentally are systematically lower than the equilibrium conversions using thermodynamic calculation at both 650 and 750°C. A likely reason is that kinetics of the reaction and transport may be limiting under the conditions used here. In addition, the nature of the material composition can affect the conversion. With a NiO:SDC methane, conversion at 750°C is about 85, 70 and 50% for S/C values of 3, 2 and, respectively and decreases to about 60%, 50% and 13% in the same order of S/C at 650°C. Although $Ni_{0.9}Mg_{0.1}O$:SDC yields similar methane conversions as NiO:SDC at 750°C, the conversions differ at 650°C, down to about 55%, 43%, and up to 28% for S/C = 3, 2 and 1, respectively.

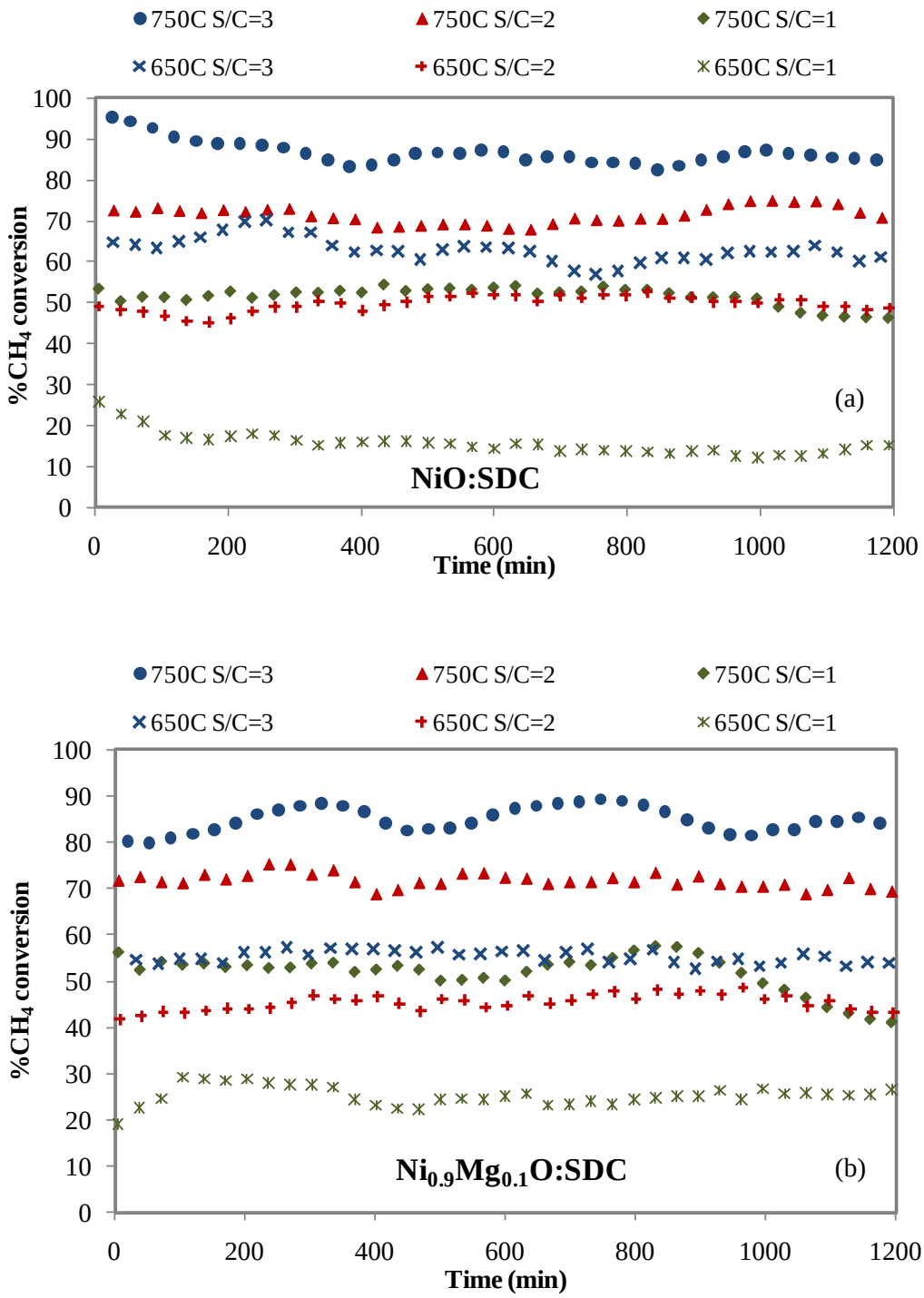

Figure 5-5 CH_4 conversion for S/C of 1 2 and 3 at 750°C and 650°C over 1200 min for a) NiO:SDC, b) $Ni_{0.9}Mg_{0.1}O$:SDC.

Figure 5-6 presents the H_2 yield as a function of temperature, S/C and material composition. The H_2 yield is higher at the lower temperature. This is in agreement with the equilibrium H_2 yield for S/C greater than 1.3 (see Figure 5-3). However, at S/C of 1, the experiments show the highest difference in H_2 yield between 650 and 750°C, whereas from thermodynamics the difference should be small. The discrepancy between the experimental results and the thermodynamic analysis at S/C of 1, may be attributed to errors in thermodynamic prediction at low S/C ratios. Indeed, at low S/C ratios, methane cracking plays an important role. It is known (Nielson and Trimm, 1977) that thermodynamic prediction of methane cracking, assuming carbon to be graphite (as we did here in section 5.2) shows deviation from experimental data which can have carbon in the other forms such as film or fiber.

The effect of S/C on H_2 yield for Ni:SDC, is small at 750°C and 650°C for S/C of 3 and 2. For $Ni_{0.9}Mg_{0.1}O$:SDC, the H_2 yield fluctuates more over time. However, the average H_2 yields of $Ni_{0.9}Mg_{0.1}O$:SDC at 650°C for the three S/C ratio were similar at about 3.2-3.5, whereas the average H_2 yields at 750°C were similar for S/C of 2 and 1 (about 2.7-2.9). The results at S/C =1 are more dependent on temperature than S/C ratio. In Figure 5-6 (a), NiO:SDC shows average H_2 yields in the range of 2.8-3.0 at 750°C for three different S/C. However, H_2 yields of around 3.2-3.3 were observed for S/C of 3 and 2 at 650°C while H_2 yield for S/C of 1 fluctuated around 3.4-3.6. A contributing reason for the high H_2 yield observed with S/C of 1 on Ni:SDC at 650°C can be related to the corresponding very low conversion (13%), far from the equilibrium conversion. In this case, the system still contained enough amount of steam to drive the water-gas shift reaction leading to high H_2 production.

Considering the $CO_2/(CO+CO_2)$ ratio, with both materials and at 750°C, this ratio increases as S/C increases. At 650°C, the trend with S/C is the same for $Ni_{0.9}Mg_{0.1}O$:SDC, but for NiO:SDC the S/C ratio has no effect on $CO_2/(CO+CO_2)$. The $CO_2/(CO+CO_2)$ ratio increases when the temperature is reduced, which is the same trend as for the H_2 yield and as expected from thermodynamics (Figure 5-3). The observation that the $CO_2/(CO+CO_2)$ follows similar trend as the H_2 yield is expected, as long as the CO_2 produced is generated mostly from the WGS reaction. In conclusion, for S/C of 2 and 3, the effects of temperature and S/C on H_2 yield and $CO_2/(CO+CO_2)$ are very similar. The main difference occurs for S/C of 1, at which condition methane cracking is likely to play an important role. Combined with uncertainty concerning methane cracking thermodynamic calculations, it is, presently, more difficult to explain the SMR results for S/C of 1.

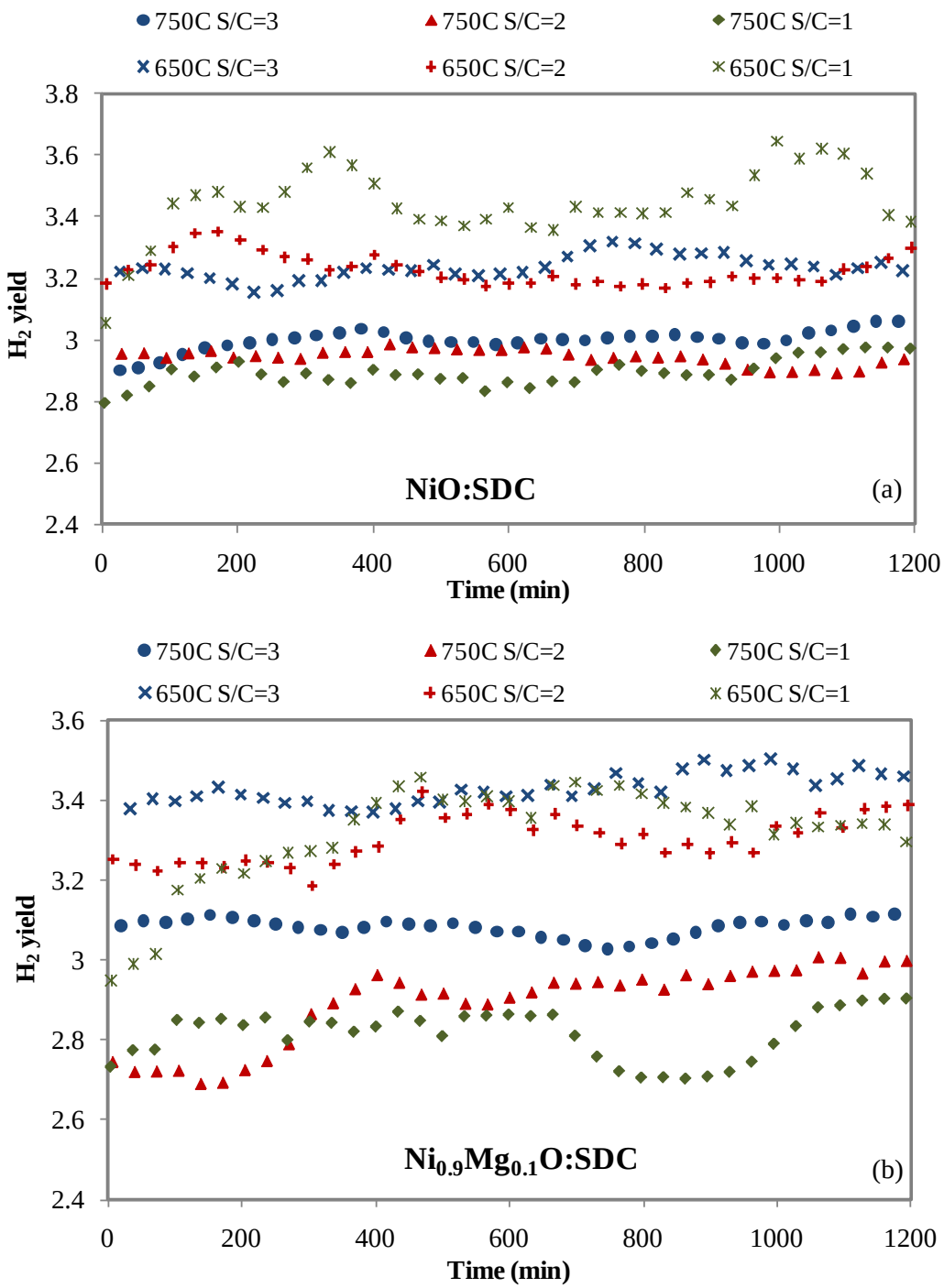

Figure 5-6 H_2 yield for S/C of 1 2 and 3 at 750°C and 650°C over 1200 min for a) NiO:SDC, b) $Ni_{0.9}Mg_{0.1}O$:SDC.

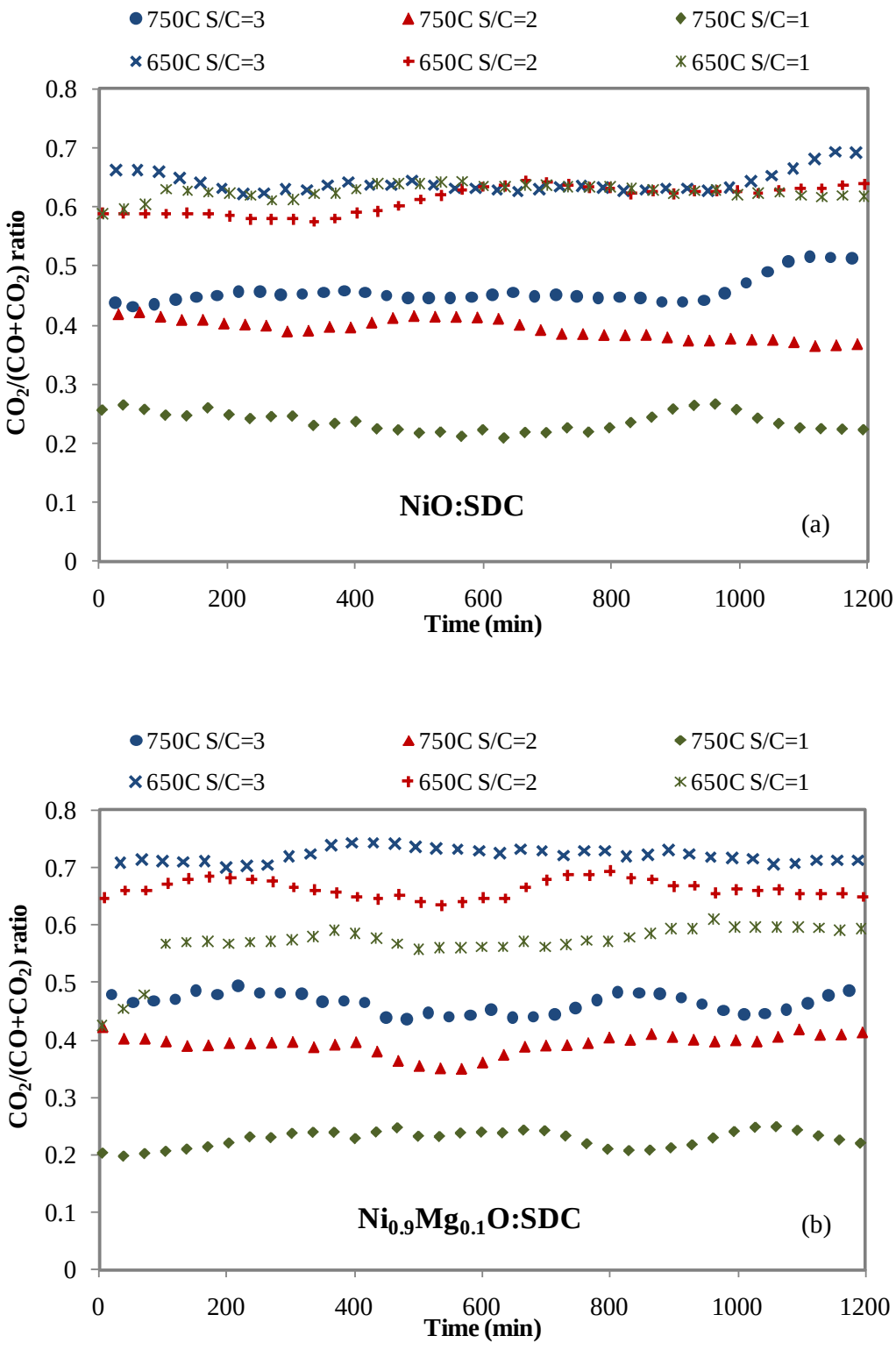

Figure 5-7 $CO_2/(CO+CO_2)$ ratio for S/C of 1 2 and 3 at 750°C and 650°C over 1200 min for a) NiO:SDC, b) $Ni_{0.9}Mg_{0.1}O$:SDC.

5.4 Cu Addition

To evaluate the activity of materials containing copper, the one-step and two-step methods were applied to add copper to Ni-Mg-O. Procedures for these two methods were explained in Chapter 4. The one-step method co-precipitates nickel, copper and magnesium oxide together in one-step. The two-step approach, adds copper by impregnation in a second step after preparing $Ni_{0.9}Mg_{0.1}O$. This section shows the effect of temperature, steam to carbon ratio, copper content and preparation method on SMR performance. Section 5.4 is separated into two sub-sections: section 5.4.1 presents the results obtained with material prepared using the one-step method, while section 5.4.2 discusses results obtained using the two-step method.

5.4.1 Addition of Copper via One-step Co-precipitation Method

Effect of S/C

Experiments with $Ni_{0.85}Cu_{0.05}Mg_{0.1}O$:SDC were conducted for S/C ratios of 1, 2 and 3 650 and 750°C. Figure 5-8 presents the conversion, H_2 yield and $CO_2/(CO+CO_2)$ ratios as a function of S/C and temperature for $Ni_{0.85}Cu_{0.05}Mg_{0.1}O$:SDC. Focusing on the result at 750ºC, methane conversion oscillates about 55% for S/C of 3. The conversion decreases to ~40% and 25% for S/C ratios of 2 and 1, respectively. Note that these conversions are lower than those with no additional copper material ($Ni_{0.9}Mg_{0.1}O$:SDC and NiO:SDC); recall that the conversions without Cu addition were 85, 70 and 50% for S/C ratios of 3, 2 and 1, respectively. This is not unexpected because Cu is known to be quite inactive for SMR (Huang and Jhao (2006)).

As seen in Figure 5-8(b), for the one-step method at 750°C, the S/C ratio between 1 and 3 does not appear to affect the H_2 yield, oscillating between 3.1 and 3.2 at 750ºC. Note, however this H_2 yield is greater than what was observed without Cu addition. This may be attributed to the fact that Cu is a good catalyst for the WGS reaction. Therefore, we should also expect higher $CO_2/(CO+CO_2)$ when Cu is added, which is indeed the case, as shown in Figure 5-8(c). For example, this ratio increases from 0.2 for $Ni_{0.9}Mg_{0.1}O$:SDC to 0.4 for $Ni_{0.85}Cu_{0.05}Mg_{0.1}O$:SDC (S/C = 1, T = 750°C). As seen in Figure 5-8 (c), the trend is clearer in that the $CO_2/(CO+CO_2)$ ratio improves with increasing S/C.

At 650°C, the effect of S/C is similar as at 750°C, i.e., when S/C increases, conversion and $CO_2/(CO+CO_2)$ ratio increase, but H_2 yield is not affected by S/C.

Effect of Temperature

Figure 5-8 also shows that, at a given S/C, lowering the temperature lower the conversion. The conversion reduced to 17%, 12%, and 6% for S/C of 3, 2 and 1, respectively. These values are significantly lower than those obtained with $Ni_{0.9}Mg_{0.1}O$:SDC (recall 55%, 43% and 28% for S/C of 3, 2 and 1). Similar to what is observed for no Cu addition, the H_2 yield and $CO_2/(CO+CO_2)$ ratio increase when the temperature decreases. At 750°C, the addition of copper increases the H_2 yield and $CO_2/(CO+CO_2)$ ratio. It is still true at 650°C, but the increase is not as pronounced.

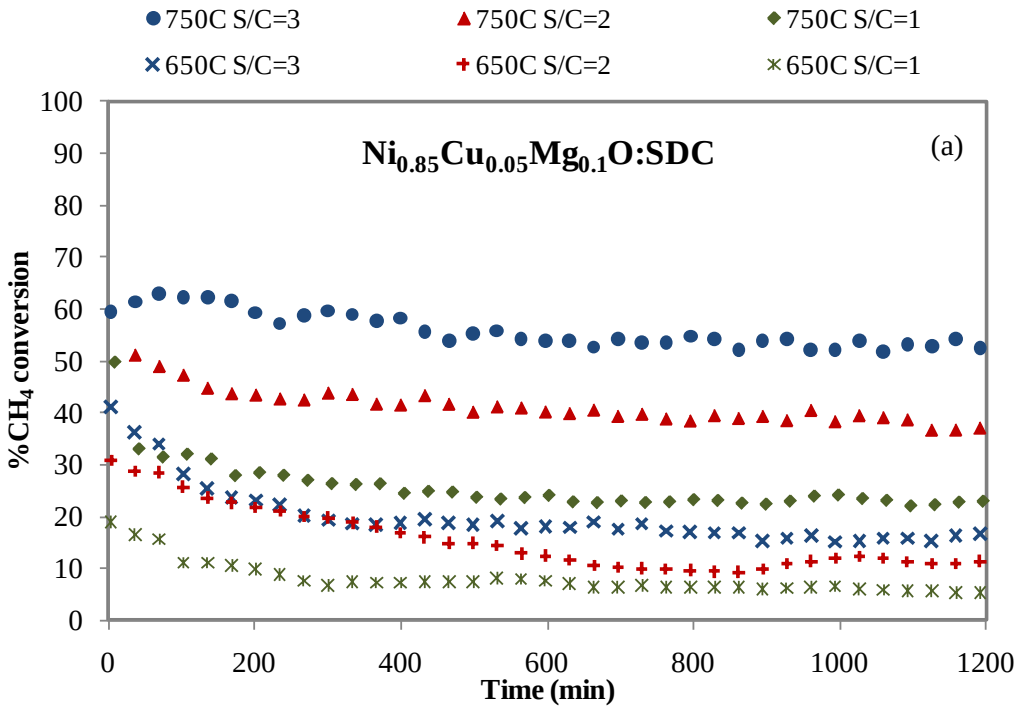

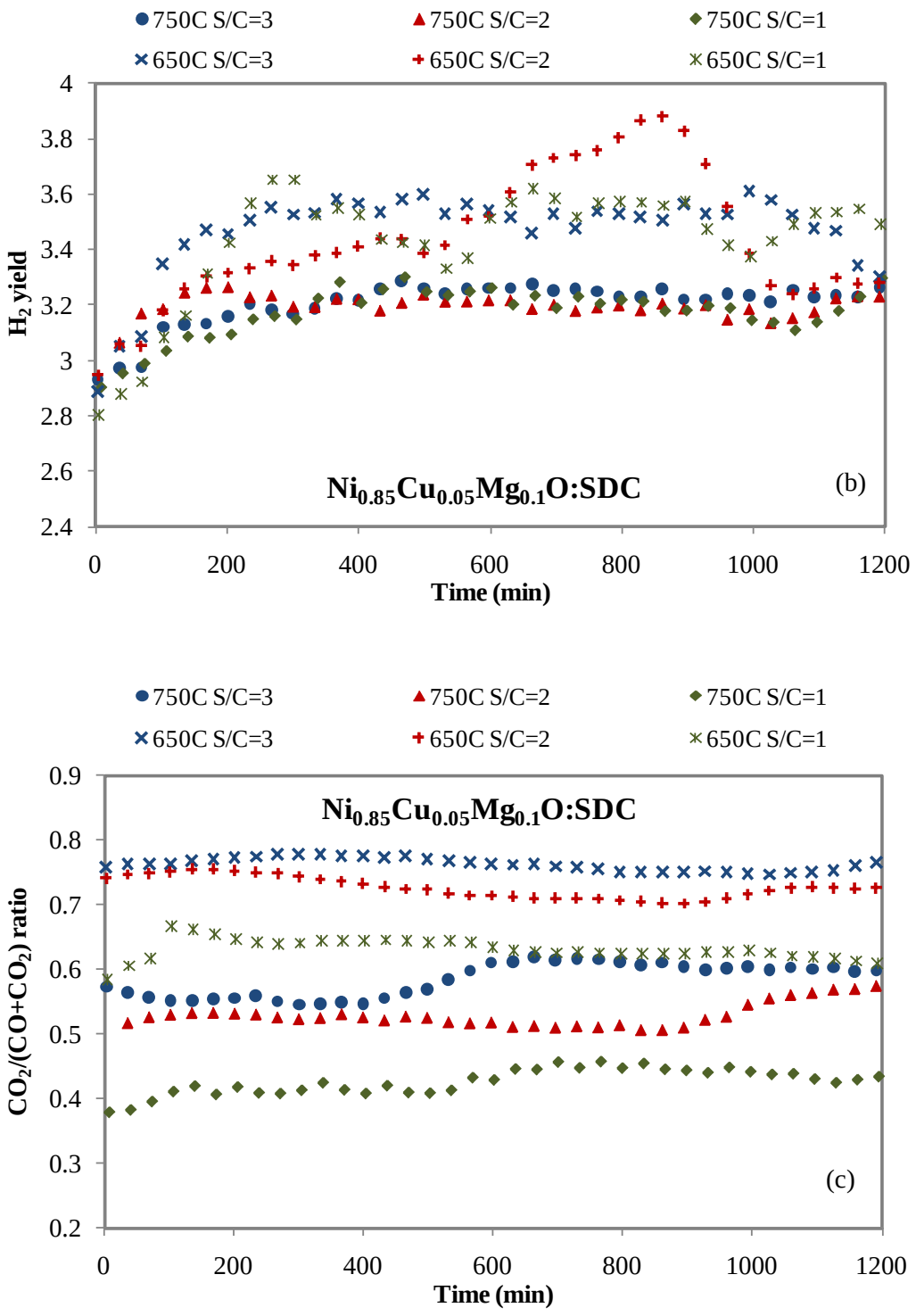

Figure 5-8 Results for $Ni_{0.85}Cu_{0.05}Mg_{0.1}O$:SDC for S/C of 1, 2 and 3 at 750°C and 650°C over 1200 min a) CH_4 conversion, b) H_2 yield, and c) $CO_2/(CO+ CO_2)$ ratio.

Effect of Cu content

Figure 5-9 presents the conversion, H_2 yield and $CO_2/(CO+CO_2)$ ratio for $Ni_{0.85}Cu_{0.05}Mg_{0.1}O$:SDC and $Ni_{0.8}Cu_{0.1}Mg_{0.1}O$:SDC (5% and 10% Cu) at 750°C and S/C of 1, 2 and 3. Figure 5-9(a) shows that the conversion decreases with increasing Cu content. For example, we obtained a conversion of ~25% for S/C of 3 with 10% Cu compared to ~55% with 5% Cu. Note that the decrease in conversion due to the Cu content becomes smaller as the S/C ratio decreases. Figure 5-9(b) and Figure 5-9(c) indicate that the H_2 yield and $CO_2/(CO+CO_2)$ ratio increase with higher copper content, indicative of higher activity of the water-gas shift reaction. Since Cu is a good WGS catalyst.

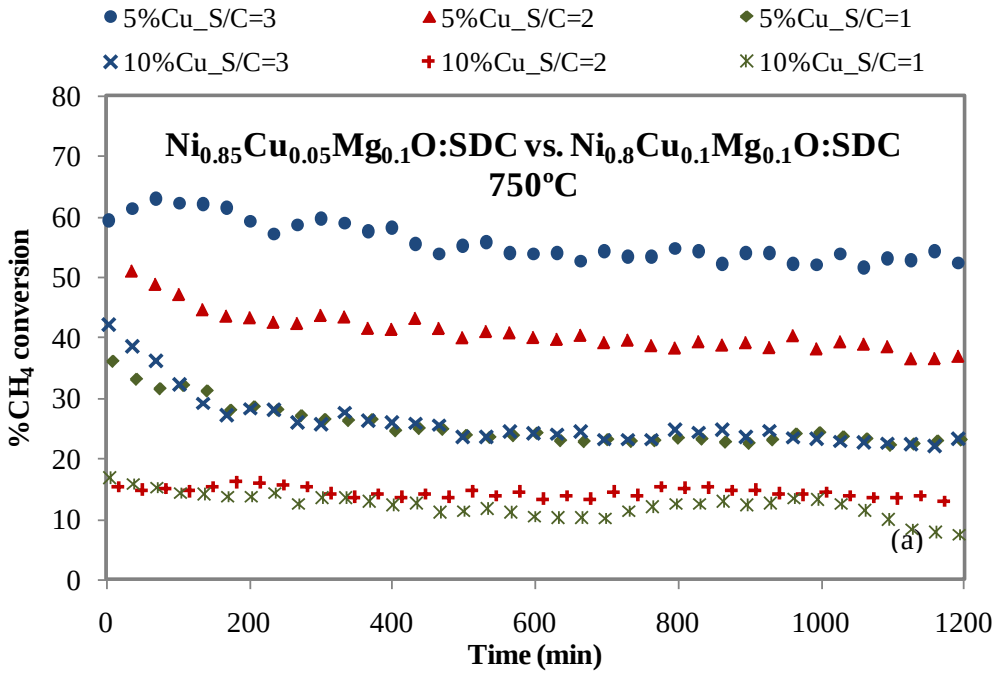

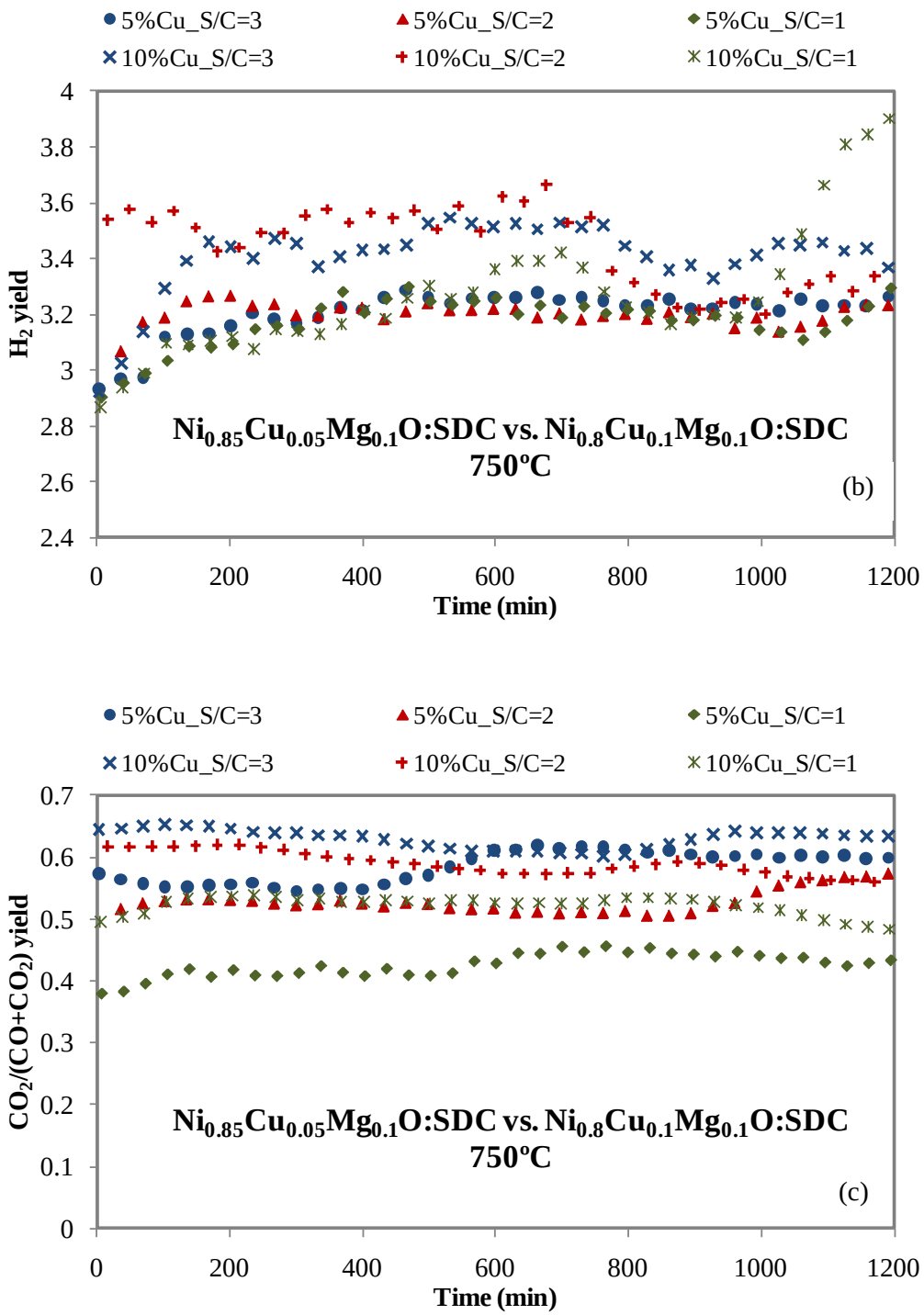

Figure 5-9 Results for $Ni_{0.85}Cu_{0.05}Mg_{0.1}O$:SDC and $Ni_{0.8}Cu_{0.1}Mg_{0.1}O$:SDC for S/C of 1, 2 and 3 at 750°C over 1200 min a) CH_4 conversion, b) H_2 yield, and c) $CO_2/(CO+ CO_2)$ ratio.

5.4.2 Addition of Copper via Two-step Co-precipitation/Impregnation Method

Effect of S/C

Figure 5-10 presents the conversion, H_2 yield and $CO_2/(CO+CO_2)$ ratios as a function of S/C and temperature for 5% Cu impregnated on $Ni_{0.9}Mg_{0.1}O$:SDC. Figure 5-10(a) shows that the conversion increases when S/C increases at both 650 and 750°C. This behaviour is very close to most of the other material compositions studies, but is particularly similar to that of $Ni_{0.9}Mg_{0.1}O$:SDC (compare Figure 5-10(a) with Figure 5-5(b)). The H_2 yield fluctuates quite a bit and it is difficult to make a definitive conclusion for the effect of S/C on H_2 yield here. However, the trend is more clear for the effect of S/C on the $CO_2/(CO+ CO_2)$ ratio: as in most cases seen previously, $CO_2/(CO+ CO_2)$ ratio increases when S/C increases.

Closer comparison with the other materials shows that the material preparation method has a significance impact on methane conversion, which is exacerbated as the S/C ratio decreases. Considering the case of 5% Cu content at 750ºC (Figure 5-10(a) vs. Figure 5-8(a)), the two-step method consistently produces higher methane conversion than the one-step method. At S/C of 3, methane conversion fluctuates around 62% for the two-step method, while it is about 55% for the one-step method. At S/C of 2, we obtained ~55% vs. 40% for the two-step and one-step methods, respectively. At S/C of 1, the difference is even greater: i.e., after 1200 minutes, values of ~43% vs. 25% are obtained for the two-step and one-step methods, respectively. Comparison with Figure 5-5(a) at 750ºC shows that the addition of 5% impregnated on $Ni_{0.9}Mg_{0.1}O$:SDC decreases the methane conversion from 85% down to ~62% for S/C of 3. The same trend is observed for S/C of 2 and 1. For the $CO_2/(CO+ CO_2)$ ratio, as seen in Figure 5-8(c) vs. Figure 5-10(c), the trend is clearer. The one-step method always results in higher $CO_2/(CO+ CO_2)$ ratios than the two-step method. Also, comparison with $CO_2/(CO+ CO_2)$ ratio without Cu addition, indicates that the $CO_2/(CO+ CO_2)$ ratio is greater when Cu is added (irrespective of the method).

Effect of Temperature

As seen in Figure 5-10(a), for 5%Cu on $Ni_{0.9}Mg_{0.1}O$:SDC, the methane conversion increases and the H_2 yield and $CO_2/(CO+CO_2)$ ratio decrease, as the temperature increases, which is the same trend as with all previously studied materials.

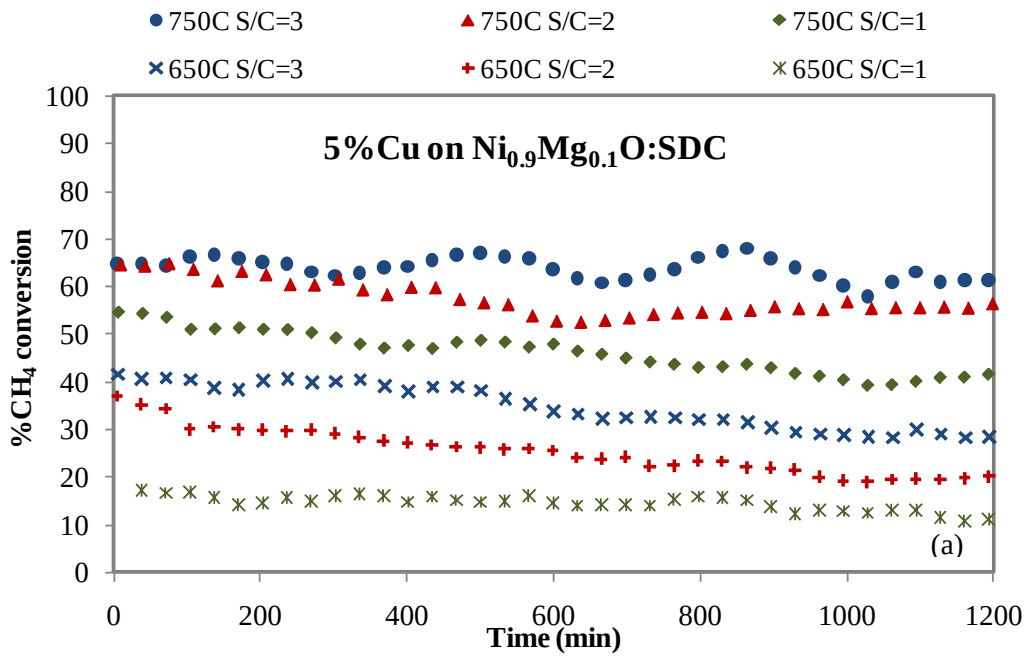
750C S/C=3
750C S/C=2
750C S/C=1
650C S/C=3
650C S/C=2
650C S/C=1
5%Cu on Ni0.9Mg0.1O:SDC
%CH4 conversion
Time (min)
(a)

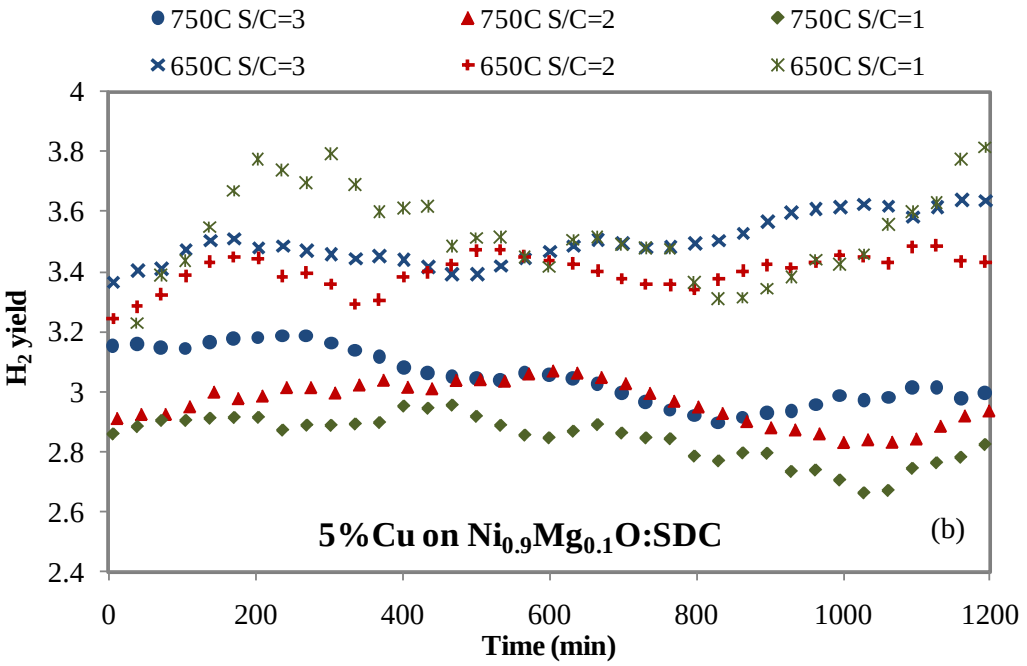
750C S/C=3
750C S/C=2
750C S/C=1
650C S/C=3
650C S/C=2
650C S/C=1
5%Cu on Ni0.9Mg0.1O:SDC
H2 yield
Time (min)
(b)

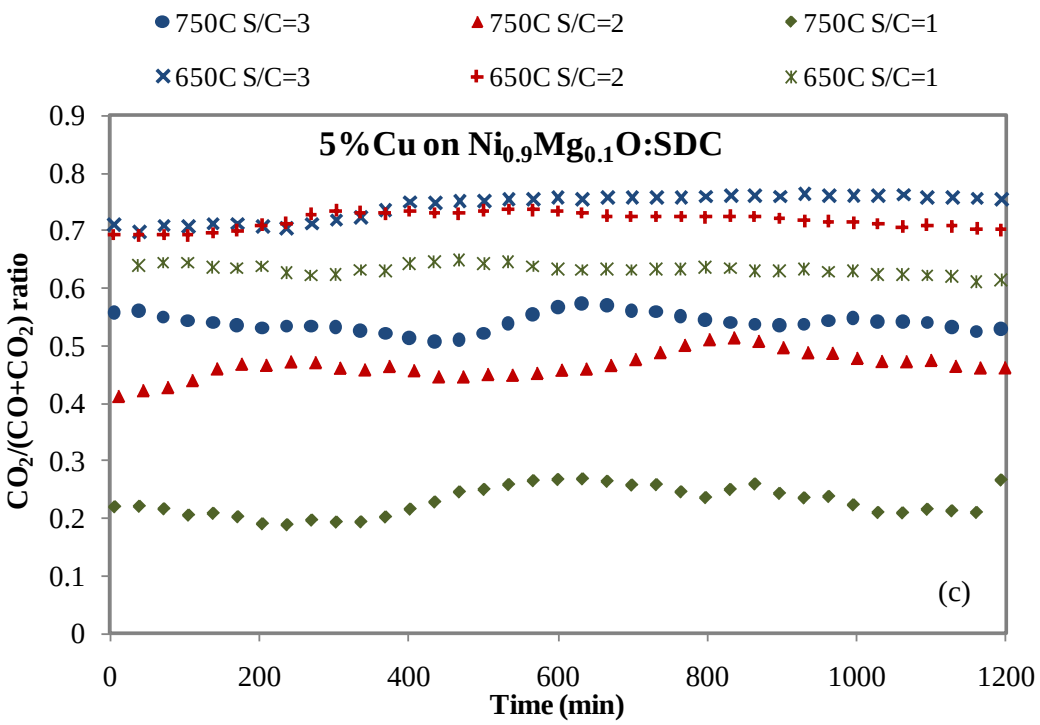

Figure 5-10 Results for 5%Cu impregnated on $Ni_{0.9}Mg_{0.1}O$:SDC for S/C of 1, 2 and 3 at 750°C and 650°C over 1200 min a) CH_4 conversion, b) H_2 yield, and c) $CO_2/(CO+ CO_2)$ ratio.

Effect of Cu content

For the impregnation method, the averages of CH_4 conversion, H_2 yield, and $CO_2/(CO+ CO_2)$ ratio from three different copper contents (3, 5 and 10 mol%) at 750°C are displayed in Figure 5-11. Those averages were calculated using the data over the time-on-steam between 10 to 20 h. Since the data were quite stable over the period considered, the standard deviation reported in the form error bars were small. Using average values help to illustrate clearly the results from many samples. At all S/C ratios, the conversion decreases when the Cu content increases. For example, after 1200 minutes and for S/C of 3, methane conversion is ~ 70% for 3%Cu, ~ 62% for 5%Cu and ~48% for 10%Cu. Recall that for similar conditions, the conversion was ~85% for $Ni_{0.9}Mg_{0.1}O$:SDC. The same trend is observed for S/C of 2 and 1. The effect of Cu content (impregnated) on conversion follows a similar trend as that for the material prepared by the one-step method and the explanation is that Cu is not an active metal for SMR. Figures 5-11(b) and (c) suggest that the H_2 yield and $CO_2/(CO+ CO_2)$ ratio of 3%Cu and 5%Cu impregnated on $Ni_{0.9}Mg_{0.1}O$:SDC are in the same range. Figure 5.11 (a) and (b) show that the H_2 yield and $CO_2/(CO+ CO_2)$ ratio obtained from the 10%Cu-content are greater than

those of 3 and 5% Cu content. This is because copper is a catalyst for WGS, and thus, additional copper enhances the WGS activity.

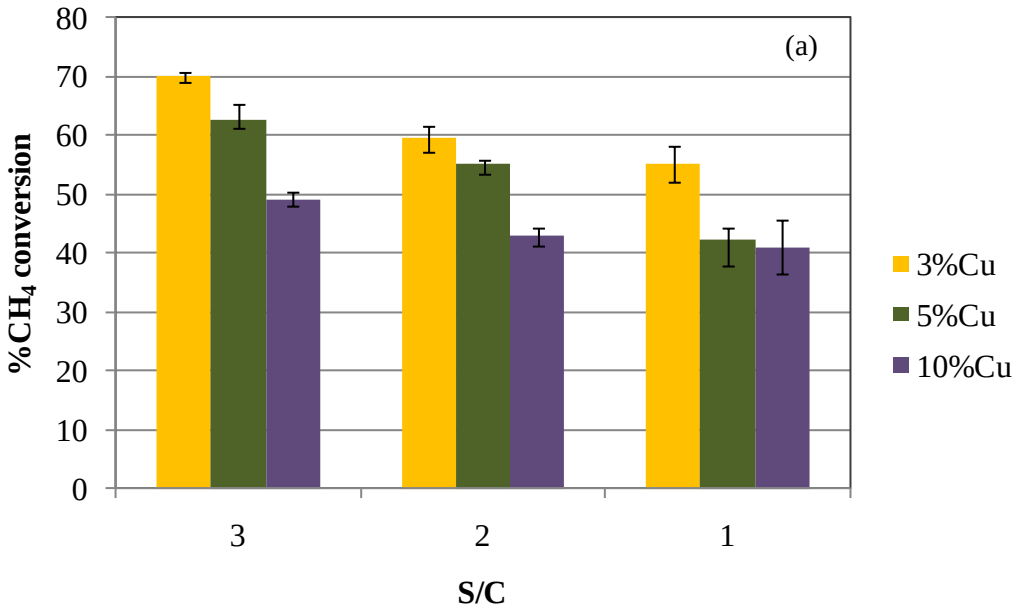

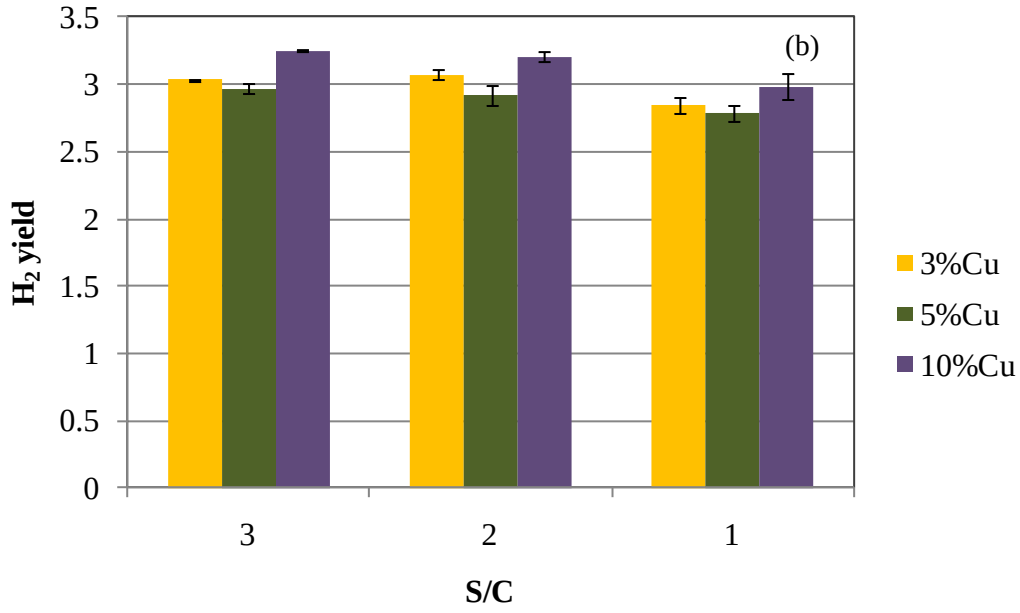

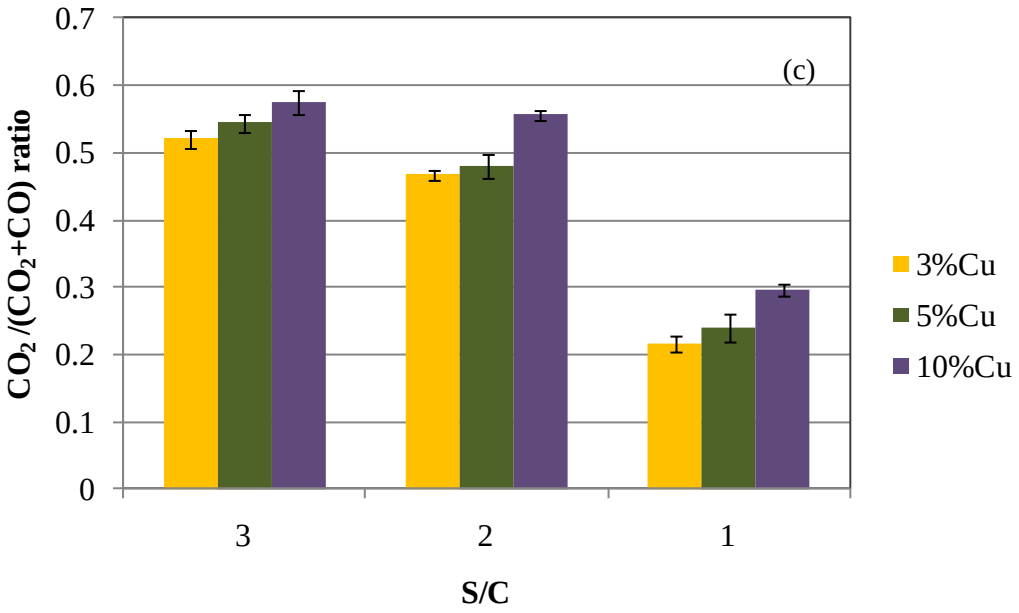

Figure 5-11 Average results for 3% 5% and 10% Cu impregnated on $Ni_{0.9}Mg_{0.1}O$:SDC for S/C of 1, 2 and 3 at 750°C (average data for time-on-steam between 10 and 20 h)
a) CH_4 conversion, b) H_2 yield, and c) $CO_2/(CO+ CO_2)$ ratio.

5.4.3 Summary of Effect of Material Preparation on SMR Activity

Figure 5-12 summarizes, for different material compositions, the average methane conversion and $CO_2/(CO+CO_2)$ ratios over the duration between 10 and 20 hours, at S/C of 2 and 3 and temperatures of 650 and 750ºC. The material compositions represented in Figure 5-12 are: $Ni_{0.9}Mg_{0.1}O$:SDC representing no copper addition, $Ni_{0.85}Cu_{0.05}Mg_{0.1}O$:SDC representing 5% Cu added via one-step co-precipitation method, 5% Cu on $Ni_{0.9}Mg_{0.1}O$:SDC representing 5% Cu added via impregnation, and 10% Cu on $Ni_{0.9}Mg_{0.1}O$:SDC representing 10% Cu added via impregnation.

The conclusions for methane conversion that can be drawn from Figure 5-12(a) are:

- The catalyst without Cu ($Ni_{0.9}Mg_{0.1}O$:SDC) provides the highest methane conversion,
- The more the additional copper, the lower the conversion (compare 5% Cu and 10% Cu on $Ni_{0.9}Mg_{0.1}O$:SDC, green and blue bars),
- For the same Cu content, the catalyst prepared via the one-step method has lower activity than the catalyst prepared via the two-step method (compare 5% Cu on $Ni_{0.9}Mg_{0.1}O$:SDC and $Ni_{0.85}Cu_{0.05}Mg_{0.1}O$:SDC, green and purple bars),
- All materials show higher conversion at higher temperature than at lower temperature,
- All materials also give a higher conversion at higher S/C than at lower S/C.

The conclusions for $CO_2/(CO+CO_2)$ ratio referring to the activity on WGS that can be drawn from Figure 5-12(b) are:

- The catalyst without Cu ($Ni_{0.9}Mg_{0.1}O$:SDC) provides the lowest $CO_2/(CO+CO_2)$ ratio,
- At 650ºC, the more the additional copper, the higher the $CO_2/(CO+CO_2)$ ratio. However, at 750ºC, the $CO_2/(CO+CO_2)$ ratio does not change much when varying the Cu content (5 and 10% Cu), but this ratio is greater than without addition of Cu.
- For same Cu content, the material synthesized using the one-step method yields higher $CO_2/(CO+CO_2)$ ratio than that synthesized by two-step method,
- For all materials, the $CO_2/(CO+CO_2)$ ratio increases when decreasing temperature.
- Higher $CO_2/(CO+CO_2)$ ratios are also observed at higher S/C than at lower S/C.

In conclusion of this section, the catalyst with copper improves the WGS activity but lowers SMR activity. As discussed earlier, copper is considered to be an inactive metallic species for SMR. We also found that the addition of 5% Cu decreases the methane conversion and this decrease was more pronounced for the one-step method than the two-step method. The lower activity obtained with the one-step method may be due to the decrease in reducibility as seen from the TPR results (Chapter 4). The TPR results indicated that the materials obtained from the one-step method is more difficult tobe to change into the active form during the reduction than that from two-step method; consequently, the material from the one-step method is less active. Another point that should be made is that the one-step method co-precipitates all metallic species (Ni, Cu and Mg) at once, while the two-step method coat Cu onto $Ni_{0.9}Mg_{0.1}O$. Consequently, the interaction between the three metals should be stronger due to the one-step method. Thus, the material prepared from the one-step method is more difficult to reduce than that fabricated from the two-step method, which was observed in the TPR results (see section 4.2.2). Because the interaction is stronger, the effect of copper addition on the conversion is more pronounced in the material fabricated from the one-step method than from the two-step method.

In addition, copper is active for WGS reaction. Huang and Jhao (2006) explained that copper provides higher activity on H_2O dissociation than Ni; therefore, it promotes WGS reaction on its site. The promoting effect of Cu addition for the WGS reaction (as represented by the $CO_2/(CO+CO_2)$ ratio) is more pronounced at lower temperature (650°C here). At 750°C, the amount of Cu (5 and 10%) or the preparation method, has no noticeable effect on the $CO_2/(CO+CO_2)$ ratio. This could be attributed to the fact that the WGS reaction is a fast reaction that reaches equilibrium rapidly as the temperature increases. It has been very common in the SOFC modelling literature to assume the WGS to be at equilibrium for temperatures above 800°C. In this case, the effect observed at 650°C indicates

that the WGS has not reached equilibrium in our setup. Furthermore, at 650°C, the addition of Cu using the one-step method resulted in higher $CO_2/(CO+CO_2)$ ratio, which is attributed to higher activity toward the WGS reaction. It can be concluded that Cu addition, via the one-step method, enhances the water-gas shift reaction.

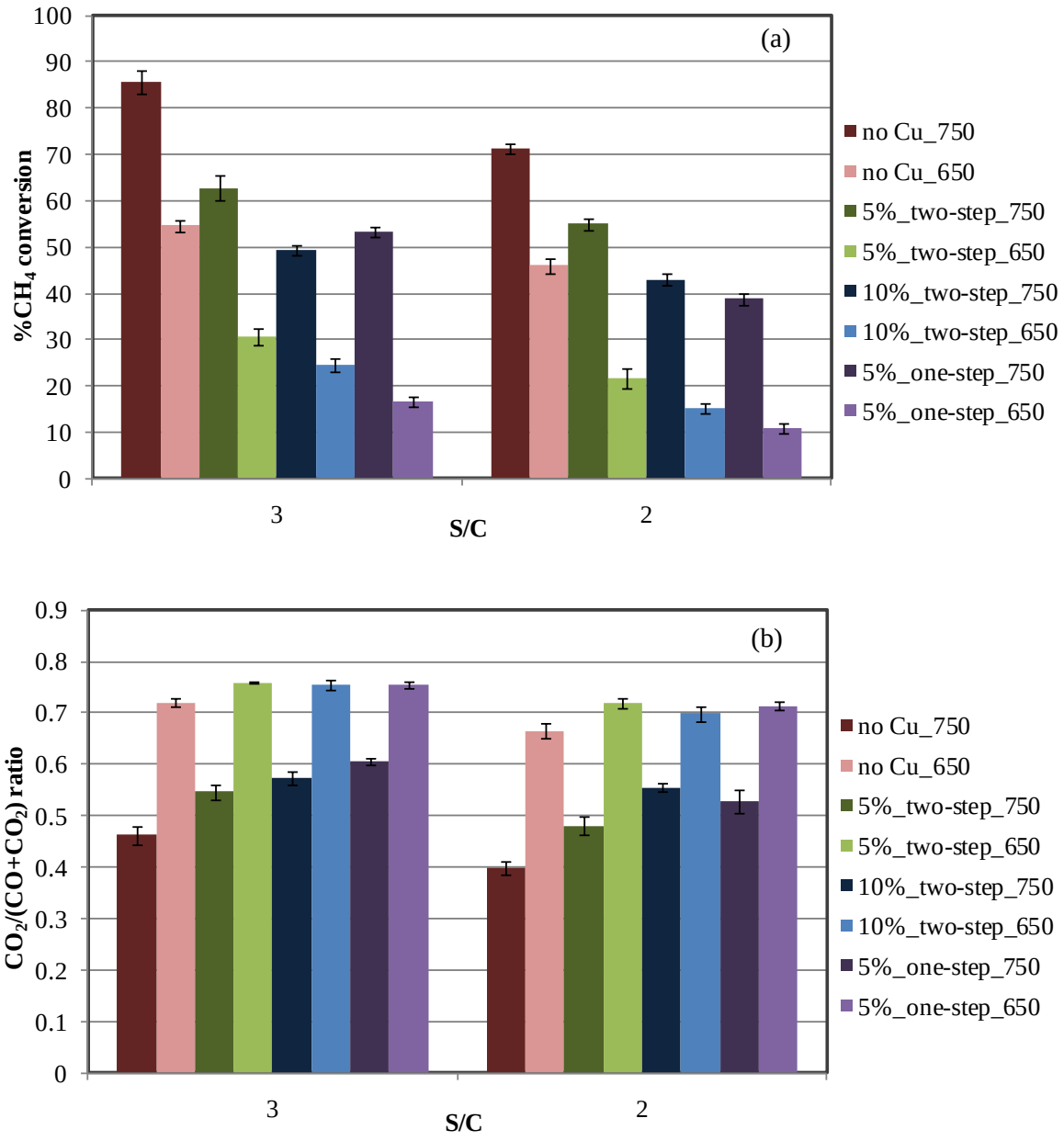

Figure 5-12 Average results for $Ni_{0.9}Mg_{0.1}O$:SDC (no_Cu), $Ni_{0.85}Cu_{0.05}Mg_{0.1}O$:SDC (5%_one-step), 5% Cu on $Ni_{0.9}Mg_{0.1}O$:SDC (5%_two-step), and 10% Cu on $Ni_{0.9}Mg_{0.1}O$:SDC (10%_two-step) for S/C of 2 and 3 at 650 and 750°C (average data for time-on-stream between 10 and 20 hrs) a) CH_4 conversion and b) $CO_2/(CO+ CO_2)$ ratio.

5.5 Carbon Deposition Analysis

5.5.1 Type of Carbon Deposited

Effect of S/C

SEM and TEM micrographs of spent $Ni_{0.9}Mg_{0.1}O$:SDC exposed to S/C ratios of 1 and 2 at 750ºC are shown in Figure 5-13. As seen in this figure, carbon whiskers were not found on the spent $Ni_{0.9}Mg_{0.1}O$:SDC from S/C of 2 (Figure 5-13(b) high magnification), but small amounts of carbon were found for S/C of 1, as circled in Figure 5-13(a). This is expected (from thermodynamics and from literature) as the amount of carbon deposited decreases as S/C increases. S/C plays a vital role in preventing carbon deposition in methane steam reforming processes. The recommended S/C ratio reported in the literature is about 3-5 (Ahmed and Foger, (2000)). Here, a S/C of 2 appen to be sufficient.

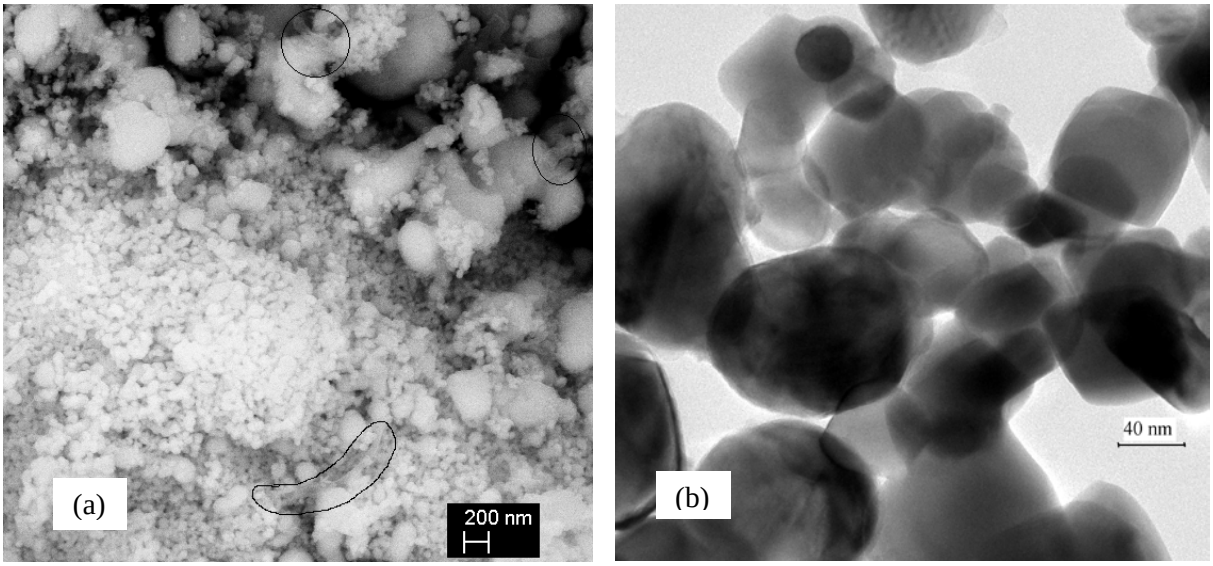

Figure 5-13 a) SEM micrograph of $Ni_{0.9}Mg_{0.1}O$:SDC after S/C=1 at 750°C b) TEM image of $Ni_{0.9}Mg_{0.1}O$:SDC after S/C=2 at 750°C.

Effects of Mg addition and Temperature

Figure 5-14 shows SEM images of fresh $Ni_{0.9}Mg_{0.1}O$:SDC (after reduction), spent $Ni_{0.9}Mg_{0.1}O$:SDC from S/C of 1 at 750°C, and spent $Ni_{0.9}Mg_{0.1}O$:SDC from S/C of 1 at 650°C. Figure 5-15 displays SEM images of reduced NiO:SDC, spent NiO:SDC from S/C of 1 at 750°C, and spent NiO:SDC from S/C of 1 at 650°C. Some carbon fibers were found on the spent $Ni_{0.9}Mg_{0.1}O$:SDC for S/C of 1 at 750°C (Figure 5-14(b)) but as a film over the material at 650°C. Note, however, that the amount of carbon at 650°C (Figure 5-14(c)) seems larger than at 750°C (Figure 5-14(b)). The greater amount of carbon at lower temperature can be seen more clearly in Figure 5-15 (case if NiO:SDC), but this time in the form of carbon filaments. Indeed, Figure 5-15(c), taken from the spent NiO:SDC with S/C of 1 at 650°C, showed many carbon fibers than the spent NiO:SDC with S/C of 1 at 750°C (Figure 5-15(b)). A comparison between Figure 5-14(c) and Figure 5-15(c) reveals that the addition of MgO changes the type of carbon deposited, from carbon filament (no MgO addition) to a thin graphite layer (with MgO addition). Although no carbon filaments were observed in Figure 5-14(c), EDX measurements indicated the presence of carbon. This result can be explained by the fact that the presence of MgO enhances carbon adsorption onto catalyst. Therefore, the presence of Mg limits the detachment of Ni particles that occurs at the onset of the carbon filament growth (Gac et al., 2009).

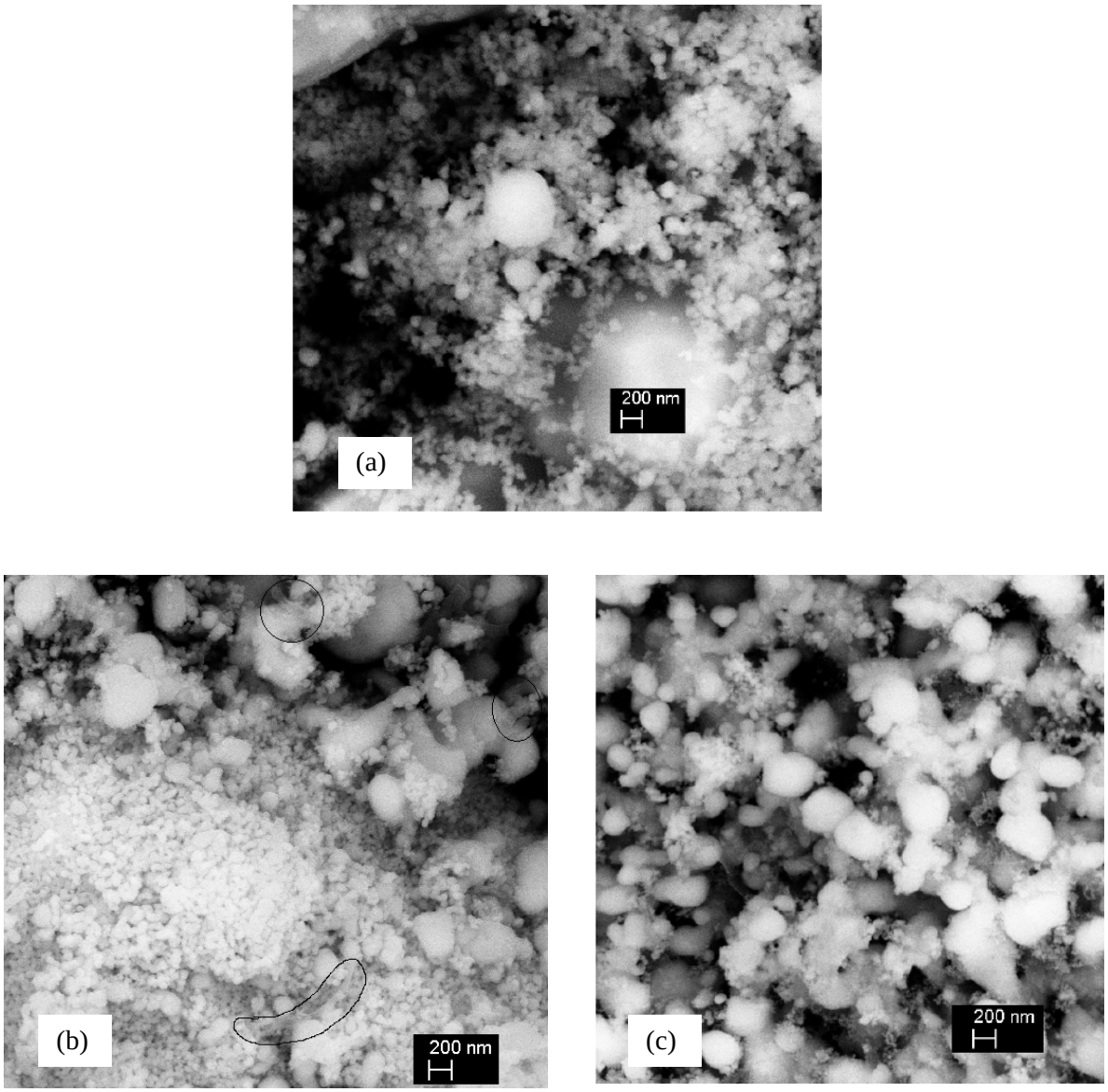

Figure 5-14 SEM backscattered electron micrographs of $Ni_{0.9}Mg_{0.1}O$:SDC a) freshly reduced, b) spent, S/C=1 at 750°C and c) spent, S/C=1 at 650°C.

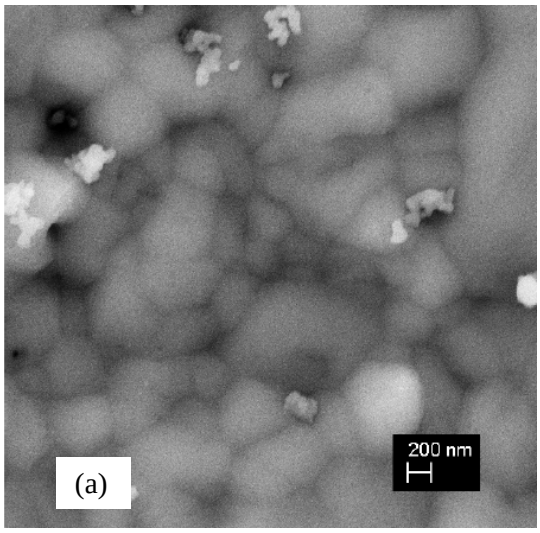

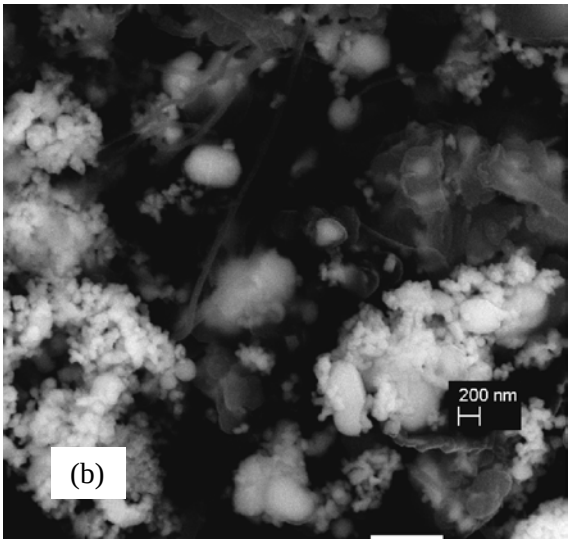

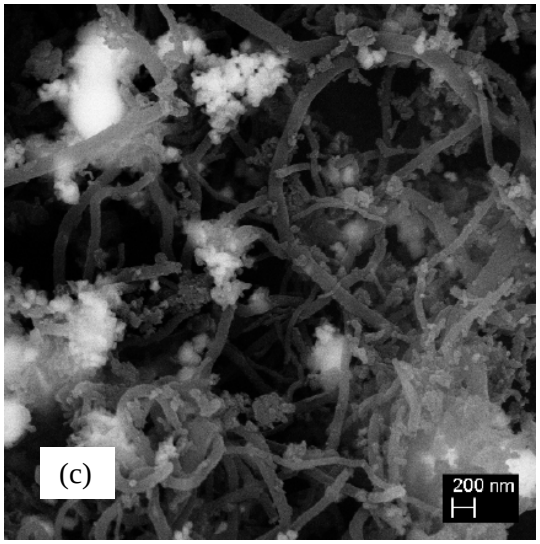

Figure 5-15 SEM backscattered electron micrographs of NiO:SDC a) freshly reduced, b) spent, S/C=1 at 750°C and c) spent, S/C=1 at 650°C.

Effect of Preparation Method

Figure 5-16 presents $Ni_{0.85}Cu_{0.05}Mg_{0.1}O$:SDC that is a) fresh reduced, b) spent after exposure to S/C of 1 at 750°C with S/C of 1 at 750°C, and spent $Ni_{0.85}Cu_{0.05}Mg_{0.1}O$:SDC with S/C of 1 at 650°C, while Figure 5-17 exhibites the corresponding images for 5%Cu impregnated on $Ni_{0.9}Mg_{0.1}O$:SDC. Spent $Ni_{0.85}Cu_{0.05}Mg_{0.1}O$:SDC shows very small amounts of filament carbon at 750ºC. At 650ºC, the SEM micrograph is similar to that for $Ni_{0.9}Mg_{0.1}O$:SDC obtained under same operating conditions. In

Figure 5-17 (b), spent 5% Cu on $Ni_{0.9}Mg_{0.1}O$:SDC at 750ºC contains some short carbon filaments, but the spent 5%Cu on $Ni_{0.9}Mg_{0.1}O$:SDC at 650ºC are free of filamentous carbon Figure 5-17 (c). However, it contains carbon in the form of layer as a thin film.

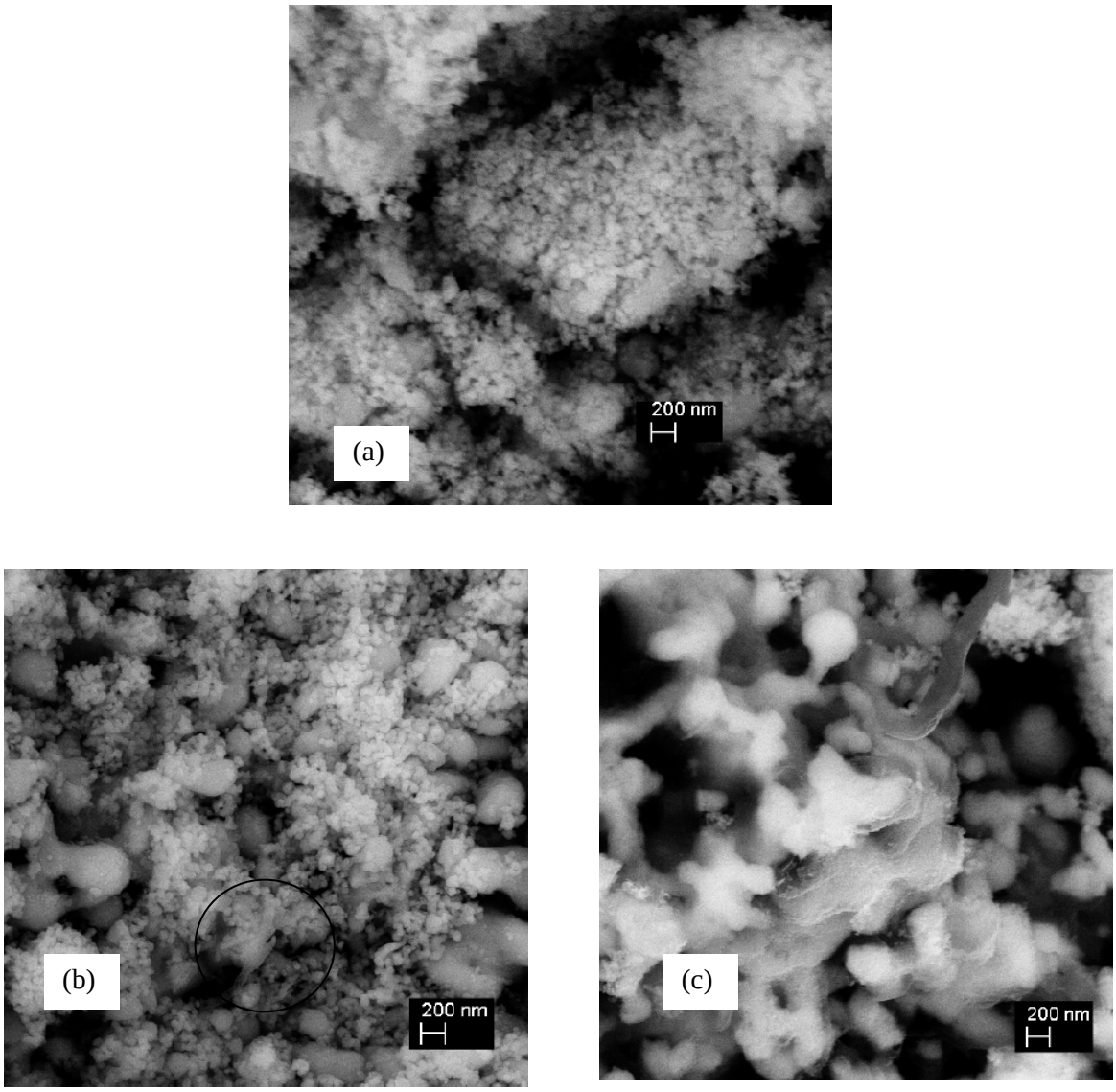

Figure 5-16 SEM backscattered electron micrographs of $Ni_{0.85}Cu_{0.05}Mg_{0.1}O$:SDC a) freshly reduced, b) spent, S/C=1 at 750°C and c) spent, S/C=1 at 650°C.

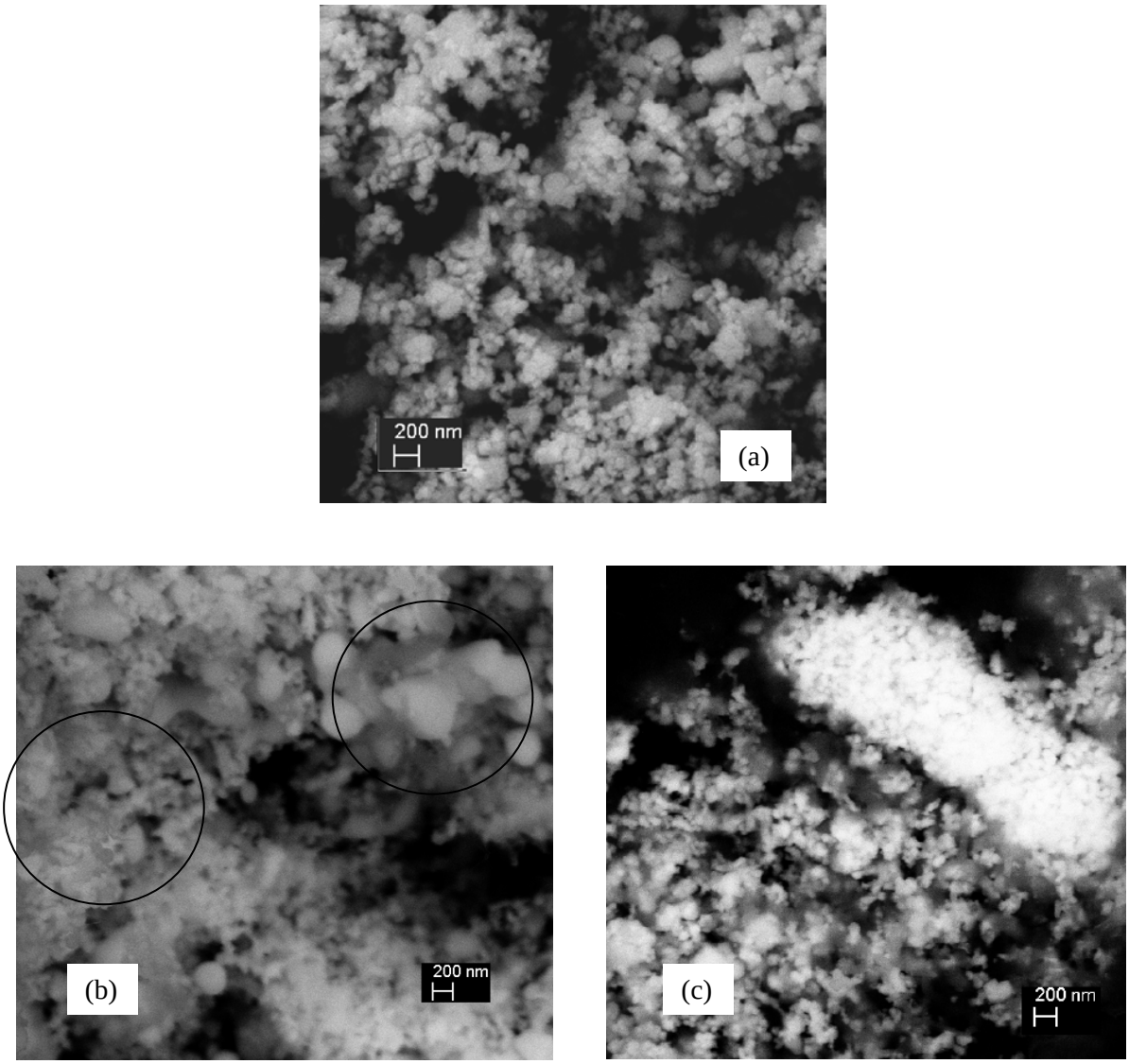

Figure 5-17 SEM backscattered electron micrographs of 5%Cu on $Ni_{0.9}Mg_{0.1}O$:SDC a) freshly reduced, b) spent, S/C=1 at 750°C and c) spent, S/C=1 at 650°C.

5.5.2 Amount of Carbon Deposition on Methane Cracking Using Copper-Free Material and Copper-Containing Material Prepared via Two-Step Co-precipitation/impregnation Method

The most extreme conditions of methane utilization occur when pure methane is fed. In this condition, methane cracking is the primary reaction potentially leading to carbon filament formation. This last section investigates methane cracking under pure methane feed. The objective is to

determine how the different materials behave under methane cracking conditions, which could arise at the entrance of a SOFC fed with dry natural gas. The cracking reaction was studied using thermogravimetry analysis (TGA) where the weight change due to carbon deposition was monitored. Four different samples were used as anode materials here: $Ni_{0.9}Mg_{0.1}O$:SDC, 3%Cu on $Ni_{0.9}Mg_{0.1}O$:SDC, and 5%Cu on $Ni_{0.9}Mg_{0.1}O$:SDC. It should be noted that the samples made from the one-step method were not included because only the two-step method is practical for fuel cell fabrication. With the two-step preparation method, the anode can be sintered, prior to Cu impregnation, at temperatures higher than the melting point of CuO in order to to form a well connected anode/electrolyte interface.

The procdure for the TGA experiments was simple: 10 mg samples were reduced in-situ (within the thermobalance) at 750°C and then exposed to dry methane for 20 hours at 750°C. The resulting profiles of percentage weight gain are plotted in Figure 5-18.

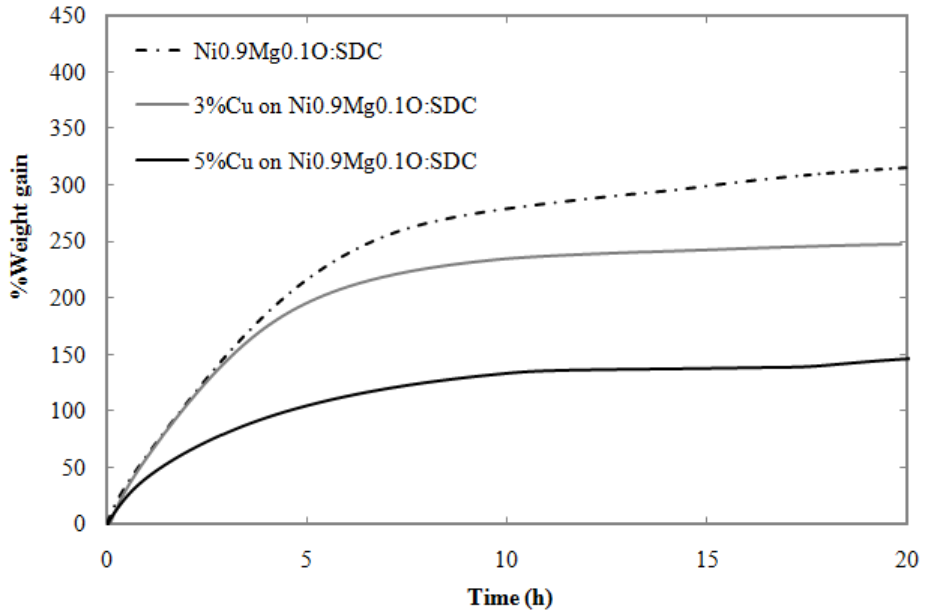

Figure 5-18 Percentage weight gain for $Ni_{0.9}Mg_{0.1}$OSDC, 3%Cu on $Ni_{0.9}Mg_{0.1}O$:SDC, and 5%Cu on $Ni_{0.9}Mg_{0.1}O$:SDC at 750°C.

The three materials have similar initial rates of methane cracking, although the cracking rate in the presence of the 5% Cu on $Ni_{0.9}Mg_{0.1}O$:SDC clearly decreases much more rapidly over time. The deactivation rate follows the order: 5% Cu impregnated, 3% Cu impregnated, no Cu impregnated. Therefore, the more the amount of Cu, the faster the cracking reaction deactivates. As far as

resistance to carbon deposition concerned, addition of Cu appears to be beneficial according to the TGA results.

All in all, comparison between 750°C and 650°C indicates that more carbon was formed at 650°C than at 750°C and the carbon was of a different type when Mg-containing catalyst is used. Here, the longest filamentous carbon was found with NiO:SDC at 650°C. Addition of Mg significantly reduced the amount of carbon deposited in the form of filament, especially at 650°C. Addition of 5% Cu by co-precipiation on $Ni_{0.9}Mg_{0.1}O$:SDC did not appear to have much effect on carbon deposition compared to $Ni_{0.9}Mg_{0.1}O$:SDC. However, addition of 5% Cu by impregnation had more of an effect in preventing carbon deposition, as revealed by the SEM micrographs.

From those results, we can conclude that at low S/C ratio, where carbon deposition is more of an issue, addition of Cu should help in reducing the amount of carbon deposited. However, addition of Cu should be done only via impregnation to maintain good SMR activity. In addition, even with Cu impregnation, the amount of copper should remain small: at S/C 1, 3% Cu impregnation yields SMR activity very close to that achieved without carbon deposition (50% vs. 53% conversion).

Chapter 6
Electrochemical Test

This chapter focuses on the analysis of electrochemical performance and impedance when NiO:SDC, $Ni_{0.9}Mg_{0.1}O$:SDC, 3%Cu on $Ni_{0.9}Mg_{0.1}O$:SDC, and 5%Cu on $Ni_{0.9}Mg_{0.1}O$:SDC are used as an anode in a SOFC button cell. This chapter starts with a section describing the electrochemical performance of the full cell under hydrogen is presented, which represents the bulk of chapter 6. Finally, the last section presents some preliminary results obtained with methane as fuel.

6.1 Evaluation of Cell Performance with Hydrogen Fuel

The procedure for fuel cell testing begins with sealing the button cell on the 15 mm diameter alumina tube as shown in Chapter 3, and assembled in the tube furnace. Ceramic paste (Aremco product) is applied as a sealant for this work. To achieve a perfect seal, the cell must remain at room temperature for two hours once the paste is applied, then heated up at 98°C for 2-4 hours, and finally heated up at 212°C for 2-4 hours. In each step, additives in the paste are burned off and stronger bonds are formed in the ceramic. All the sealing process takes place in the button cell furnace. Once the sealing processes completed (i.e. temperature of 212°C for 2-4 hours), the temperature is raised up to 750°C for the reduction step. It should be mentioned that nitrogen flows on the anode side during this heating process. Once the temperature system reaches 750°C, the anode atmosphere is controlled in 20%H_2/N_2 at a total flow rate of 100mL/min in order to slowly reduce the anode material in-situ for 30 min. The next step is to gently change the anode atmosphere to 3% humidified hydrogen at a total flow rate of 90 $mL.min^{-1}$. Note that this humidification is produced via a bubbler. Before the polarization measurements start, the cell is checked to ensure that the current can be drawn and that the anode is fully reduced. To do so, a current density of 0.250 $A.cm^{-2}$ is employed and the resulting cell voltage monitored over 30 minutes. If a stable cell voltage is obtained, we assumed that the reduction reaction is complete and thus the performance test can proceed. At a given temperature, two techniques are used to evaluate the cell performance. First, polarization measurements are performed by a potentiodynamic technique with a sweep rate of 1 mV/s. Then, EIS measurements are performed over a frequency range from 0.01Hz to 1 MHz with polarization amplitude of 10mV. The temperature is then adjusted to the next value, in the following order: 750°C, 700°C, 650°C, and 600°C. When the system is stable at a given temperature for 30 min, the polarization test is started, followed by the EIS test. After that, the temperature decreases again to determine the performance at this temperature. When finishing the test with humidified hydrogen, the system is then purged with dry hydrogen and

re-heated to 750°C for standard electrochemical tests in dry hydrogen. The procedure is summarized in Figure 6-1. However, it should be informed that the potentiostat was recently arrived. An electronic load boxed has been used to perform a polarization measurement in that time and EIS is not available with the electronic load box.

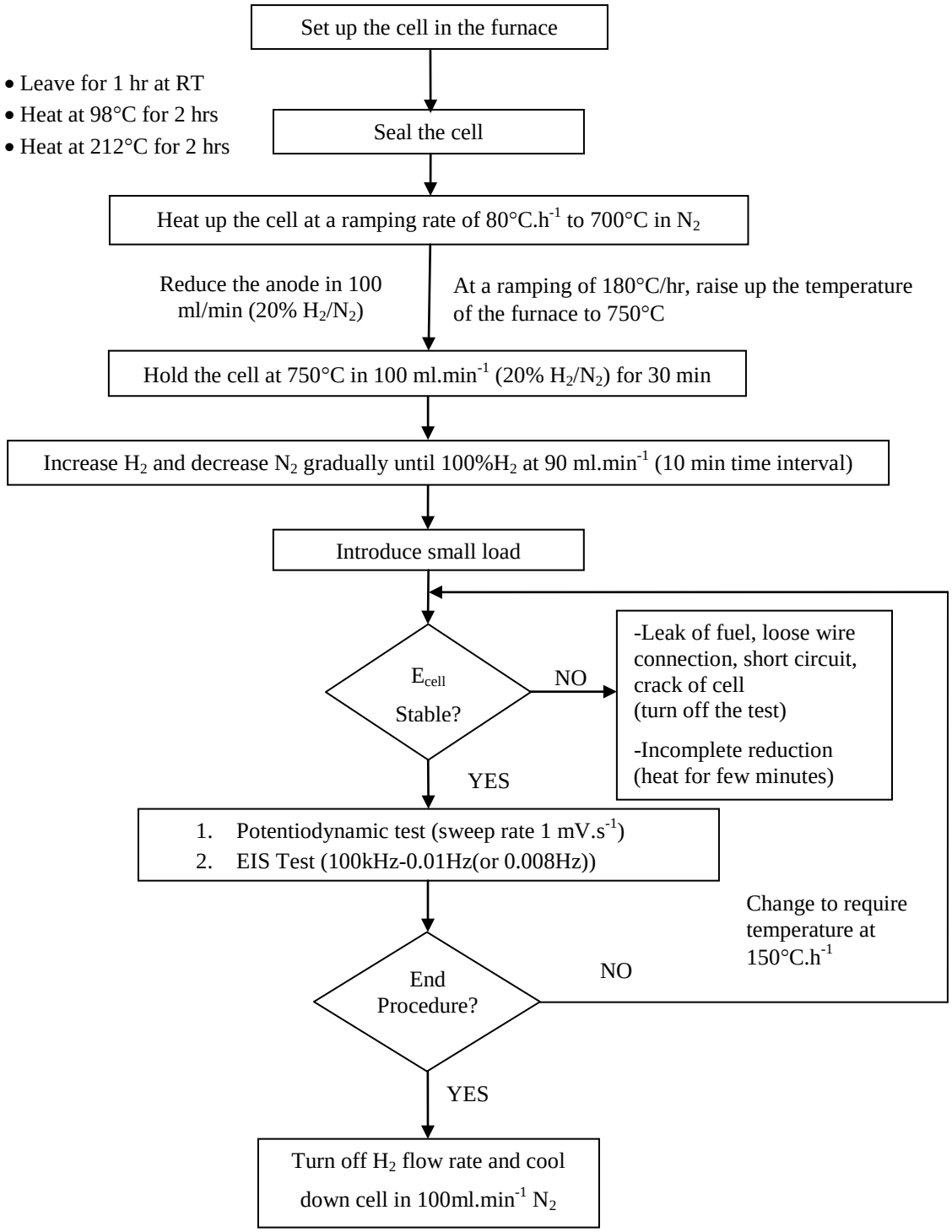

Figure 6-1 Procedure for fuel cell testing with hydrogen.

6.1.1 Polarization Test

This section focuses on obtaining maximum power density and the limiting current density from polarization tests. An example of results demonstrated from the same cell at different temperatures for dry hydrogen fueled SOFC is shown in Figure 6-2: All curves are similar in two repeats: cell voltage decreases with increasing current density and the maximum power density decreases as temperature is lowered. The results in Figure 6-2 were obtained with a button cell fabricated using $Ni_{0.9}Mg_{0.1}O$:SDC in dry hydrogen. The maximum power densities were 360, 245, 150, and 79 $mW.cm^{-2}$ at 750, 700, 650, and 600°C, respectively. The current densities at the maximum power density showed the same trend: 0.72, 0.43, 0.26, and 0.13 $A.cm^{-2}$ at 750, 700, 650, and 600°C, respectively.

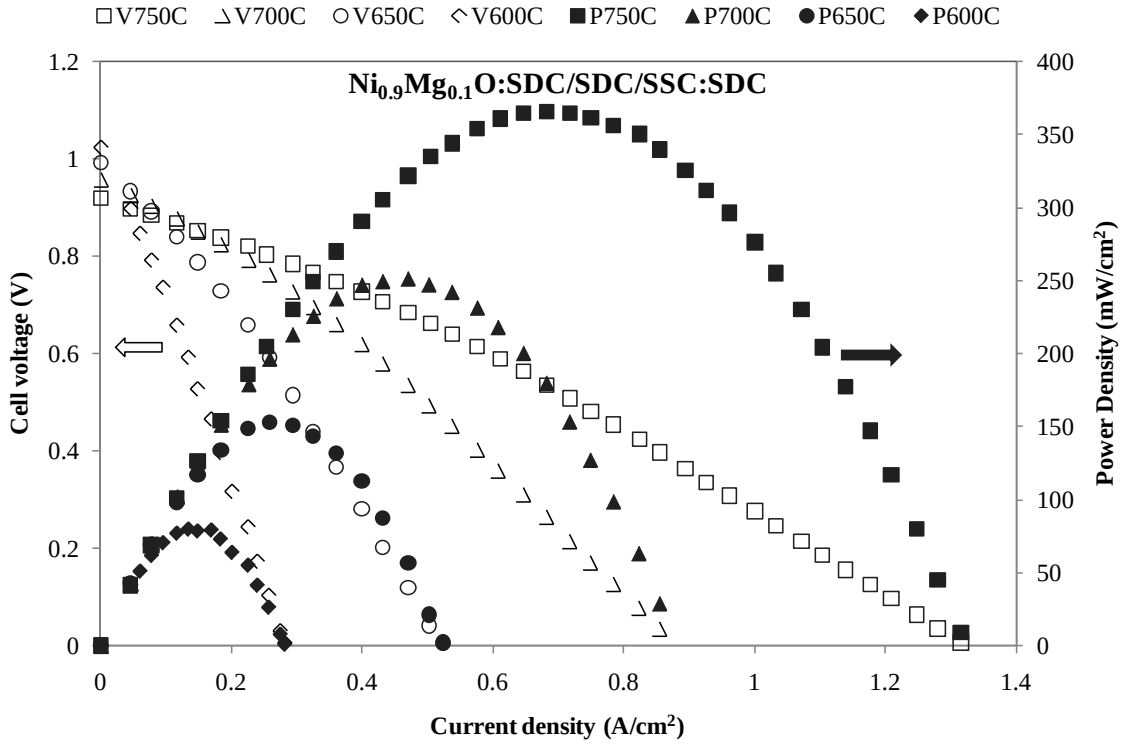

Figure 6-2 Voltage and power density vs. current density with dry H_2 on $Ni_{0.9}Mg_{0.1}O$:SDC/SDC/SSC:SDC

The flow rates of the feed gases are important parameters that can influence the performance of the cell, which can be seen in Figure 6-3. The measurements Figure 6-3 in were taken from $Ni_{0.9}Mg_{0.1}O$:SDC/SDC/SSC:SDC after finishing the routine experiments. The temperature was re-heated to 700°C with 90 $mL.min^{-1}$ of pure hydrogen. Once isothermal condition was reached, the polarization test for that flow rate was performed. Then, the hydrogen flow rate was reduced to 50 $mL.min^{-1}$. The system was sustained under this condition for 15 min before the second polarization

test began. The process was repeated for a hydrogen flow rate of 20 mL.min^{-1} and also another at 90 mL.min^{-1}. The last 90 mL.min^{-1} was to check whether the cell performance changed significantly from the initial state. The results show that the flow rate does not affect the polarization much as long as it is high enough. In the present case, a flow rate of 20 mL.min^{-1} n gave the lowest polarization, but for flow rates of 50 and 90 mL.min^{-1} the polarization curves were almost the same. The maximum power density at a H_2 flow rate of 90 mL.min^{-1} was about 230 mW.cm^{-2}, which is slightly lower than 225 mW.cm^{-2} obtained at 50 mL.min^{-1}. When hydrogen was set to a flow rate of 20 mL.min^{-1}, the maximum power density was much lower (205 mW.cm^{-2}) than at the two previous flow rates. Once the H_2 flow rate was readjusted to 90 mL.min^{-1}, the maximum power was similar to the previous test at 90 mL.min^{-1}.

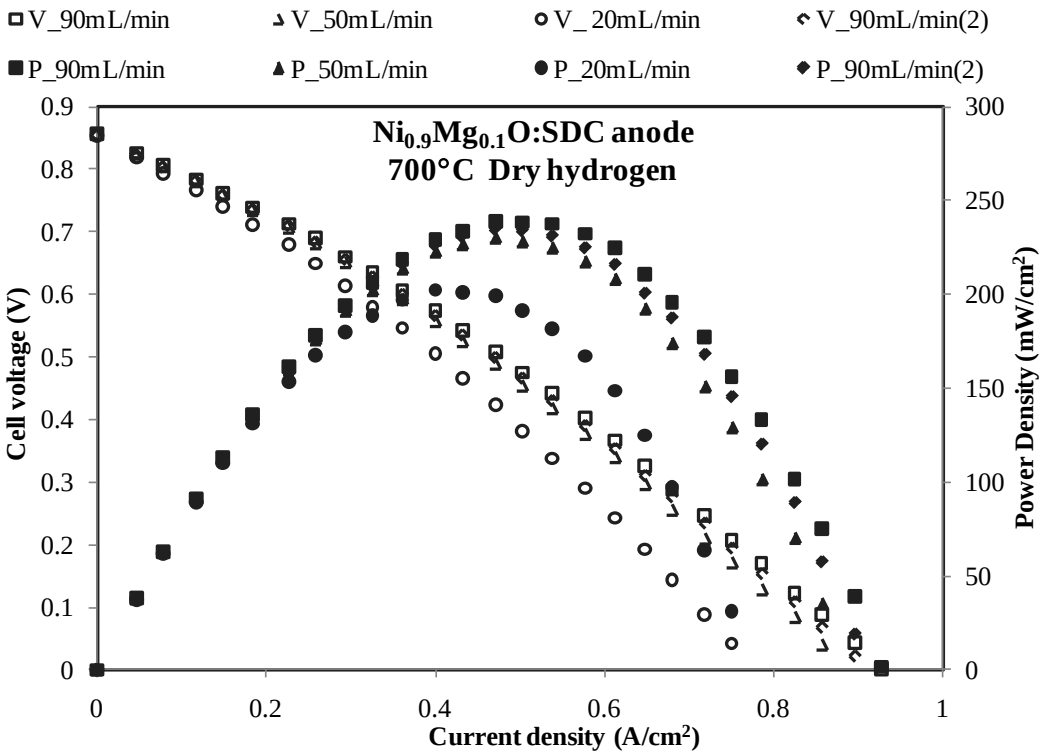

Figure 6-3 Voltage and power density vs. current density at different flow rates of dry H_2 on $Ni_{0.9}Mg_{0.1}O$:SDC/SDC/SSC:SDC at 700°C.

Figure 6-4 and 6-5 show the polarization curves with humidified and dry H_2, respectively, for four different anodes: NiO:SDC, $Ni_{0.9}Mg_{0.1}O$:SDC, 3%Cu on $Ni_{0.9}Mg_{0.1}O$:SDC, and 5%Cu on $Ni_{0.9}Mg_{0.1}O$:SDC. The maximum power density (P_{max}) and the limiting current density (i_L) for all samples in each condition are reported in Table 6-1. Figure 6-4 (a) (b) (c), and (d) are the set of polarization measurements taken when dry hydrogen was used as a fuel at 750°C 700°C 650°C and 600°C, respectively. At each temperature, the same conclusion can be drawn: $Ni_{0.9}Mg_{0.1}O$:SDC

provides the highest power density followed by NiO:SDC, 3%Cu on $Ni_{0.9}Mg_{0.1}O$:SDC, and 5%Cu on $Ni_{0.9}Mg_{0.1}O$:SDC anode. For example, at 750°C, the maximum power density decreased from 369 $mW.cm^{-2}$, with $Ni_{0.9}Mg_{0.1}O$:SDC, to 356 $mW.cm^{-2}$ with NiO:SDC. Adding copper resulted in a decrease in power density compared to $Ni_{0.9}Mg_{0.1}O$. At 750°C, 3%Cu on $Ni_{0.9}Mg_{0.1}O$:SDC and 5%Cu on $Ni_{0.9}Mg_{0.1}O$:SDC reduced the maximum power density to 325 $mW.cm^{-2}$ and 303 $mW.cm^{-2}$, respectively. The limiting current densities also followed the same order as the power densities. At 750°C the limiting current densities were 1.43, 1.41, 1.23 and 1.16 $A.cm^{-2}$ for $Ni_{0.9}Mg_{0.1}O$:SDC, NiO:SDC, 3%Cu on $Ni_{0.9}Mg_{0.1}O$:SDC, and 5%Cu on $Ni_{0.9}Mg_{0.1}O$:SDC, respectively. The reason for these results is given later on the base of the polarization resistance obtained from EIS spectra.

With the same sample set, similar trends for maximum power densities and limiting current densities were obtained with 3% humidified hydrogen fuel (Figure 6-5) at 650°C and 600°C. That is the highest maximum density was observed with $Ni_{0.9}Mg_{0.1}O$:SDC, followed by NiO:SDC, 3%Cu on $Ni_{0.9}Mg_{0.1}O$:SDC, and 5%Cu on $Ni_{0.9}Mg_{0.1}O$:SDC anode. However, at 750°C and 700°C, the cells fabricated with $Ni_{0.9}Mg_{0.1}O$:SDC and NiO:SDC still yielded higher power densities and higher limiting current densities than the cells containing Cu. However, the cell with 5%Cu on $Ni_{0.9}Mg_{0.1}O$:SDC produced greater values than the cell with 3%Cu on $Ni_{0.9}Mg_{0.1}O$:SDC at 750°C and 700°C. At 750°C, the maximum power density and limiting current density obtained with $Ni_{0.9}Mg_{0.1}O$:SDC anode were 362 $mW.cm^{-2}$ and 1.43 $A.cm^{-2}$. An equal power density of 317 $mW.cm^{-2}$ with NiO:SDC anode and 5%Cu on $Ni_{0.9}Mg_{0.1}O$:SDC anode was obtained, but the limiting current density decreased from 1.31 $A.cm^{-2}$ for NiO:SDC to 1.21 $A.cm^{-2}$ for 5%Cu on $Ni_{0.9}Mg_{0.1}O$:SDC. With 3%Cu on $Ni_{0.9}Mg_{0.1}O$:SDC, the maximum power density was 298 $mW.cm^{-2}$ and the limiting current density was 1.15 $A.cm^{-2}$. As seen in Table 6-1, results at 700°C indicate that P_{max} and i_L are both higher with 5% Cu than with 3% Cu, similar to the results at 750°C. However, at the lower temperatures (600 and 650°C), the opposite was observed: 3% Cu yielded higher P_{max} and i_L than 5% Cu. Nonetheless, at all temperatures, addition of Cu decreased P_{max} and i_L, when compared to NiO:SDC and NiMgO:SDC.

These results can be compared to the results observed from conventional electrode (NiO:YSZ) in 50wt%Ni-50wt%YSZ//YSZ//50wt%LSM-50wt%YSZ (anode-supported cell) reported by Koh et al. (2002) tested with dry hydrogen. A maximum power density of 300 and 100 $mW.cm^{-2}$ were obtained at 750 and 650°C, respectively. At 750°C, NiO:SDC, $Ni_{0.9}Mg_{0.1}O$:SDC and 3%Cu on $Ni_{0.9}Mg_{0.1}O$:SDC anode provide higher P_{max} than that of conventional anode, as reported in the literature, while 5%Cu on $Ni_{0.9}Mg_{0.1}O$:SDC yields a similar P_{max} as NiO/YSZ. All of the anode

samples in this thesis give a higher P_{max} than that of NiO/YSZ at 650°C In addition, all samples reported in this thesis are for electrolyte supported cells. It is expected that anode supported cell would result in even higher performance.

Table 6-1 Maximum power densities and limiting current density with dry H_2 and 3% humidified H_2 on NiO:SDC, $Ni_{0.9}Mg_{0.1}O$:SDC, 3%Cu on $Ni_{0.9}Mg_{0.1}O$:SDC, and 5%Cu on $Ni_{0.9}Mg_{0.1}O$:SDC

Anode	Feed	Temp (°C)	P_{max} (mW/cm^2)	i_L (A/cm^2)
NiO:SDC	Humidified H_2	750	317	1.31
		700	214	0.89
		650	130	0.52
		600	71	0.26
	Dry H_2	750	356	1.41
		700	236	0.91
		650	142	0.56
		600	78	0.29
NiMgO:SDC	Humidified H_2	750	362	1.43
		700	251	0.96
		650	158	0.60
		600	90	0.33
	Dry H_2	750	369	1.43
		700	257	0.97
		650	161	0.59
		600	94	0.34
3%Cu on NiMgO:SDC	Humidified H_2	750	298	1.15
		700	200	0.74
		650	120	0.43
		600	65	0.22
	Dry H_2	750	325	1.23
		700	225	0.8
		650	114	0.38
		600	63	0.21
5%Cu on NiMgO:SDC	Humidified H_2	750	317	1.21
		700	208	0.75
		650	114	0.39
		600	57	0.18
	Dry H_2	750	303	1.16
		700	195	0.68
		650	112	0.36
		600	58	0.18

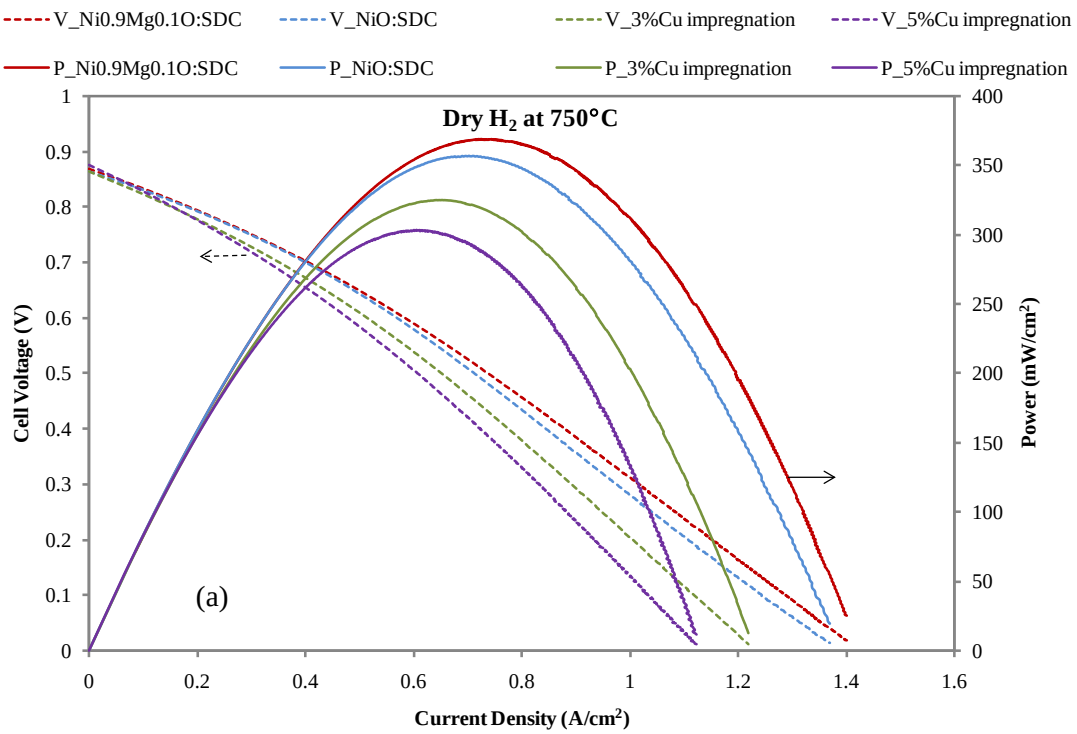
V_Ni0.9Mg0.1O:SDC
V_NiO:SDC
V_3%Cu impregnation
V_5%Cu impregnation
P_Ni0.9Mg0.1O:SDC
P_NiO:SDC
P_3%Cu impregnation
P_5%Cu impregnation
Dry H2 at 750°C
(a)
Cell Voltage (V)
Power (mW/cm2)
Current Density (A/cm2)
0
0.1
0.2
0.3
0.4
0.5
0.6
0.7
0.8
0.9
1
0
50
100
150
200
250
300
350
400
0
0.2
0.4
0.6
0.8
1
1.2
1.4
1.6

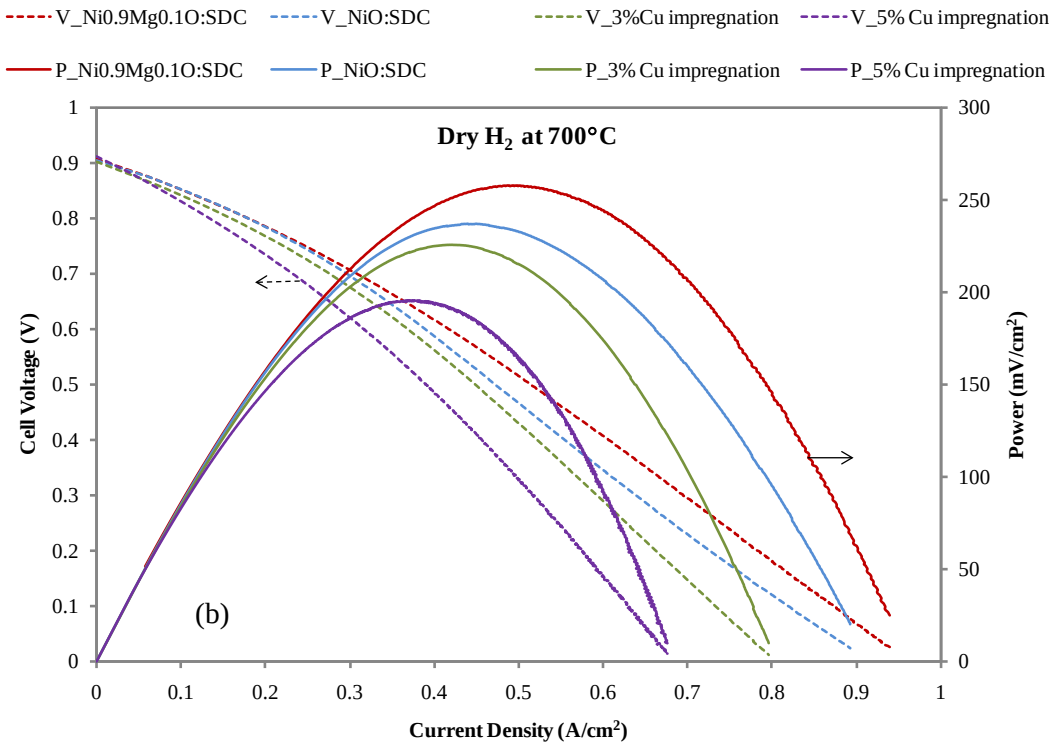
V_Ni0.9Mg0.1O:SDC
V_NiO:SDC
V_3%Cu impregnation
V_5% Cu impregnation
P_Ni0.9Mg0.1O:SDC
P_NiO:SDC
P_3% Cu impregnation
P_5% Cu impregnation
Dry H2 at 700°C
(b)
Cell Voltage (V)
Power (mV/cm2)
Current Density (A/cm2)
0
0.1
0.2
0.3
0.4
0.5
0.6
0.7
0.8
0.9
1
0
50
100
150
200
250
300
0
0.1
0.2
0.3
0.4
0.5
0.6
0.7
0.8
0.9
1

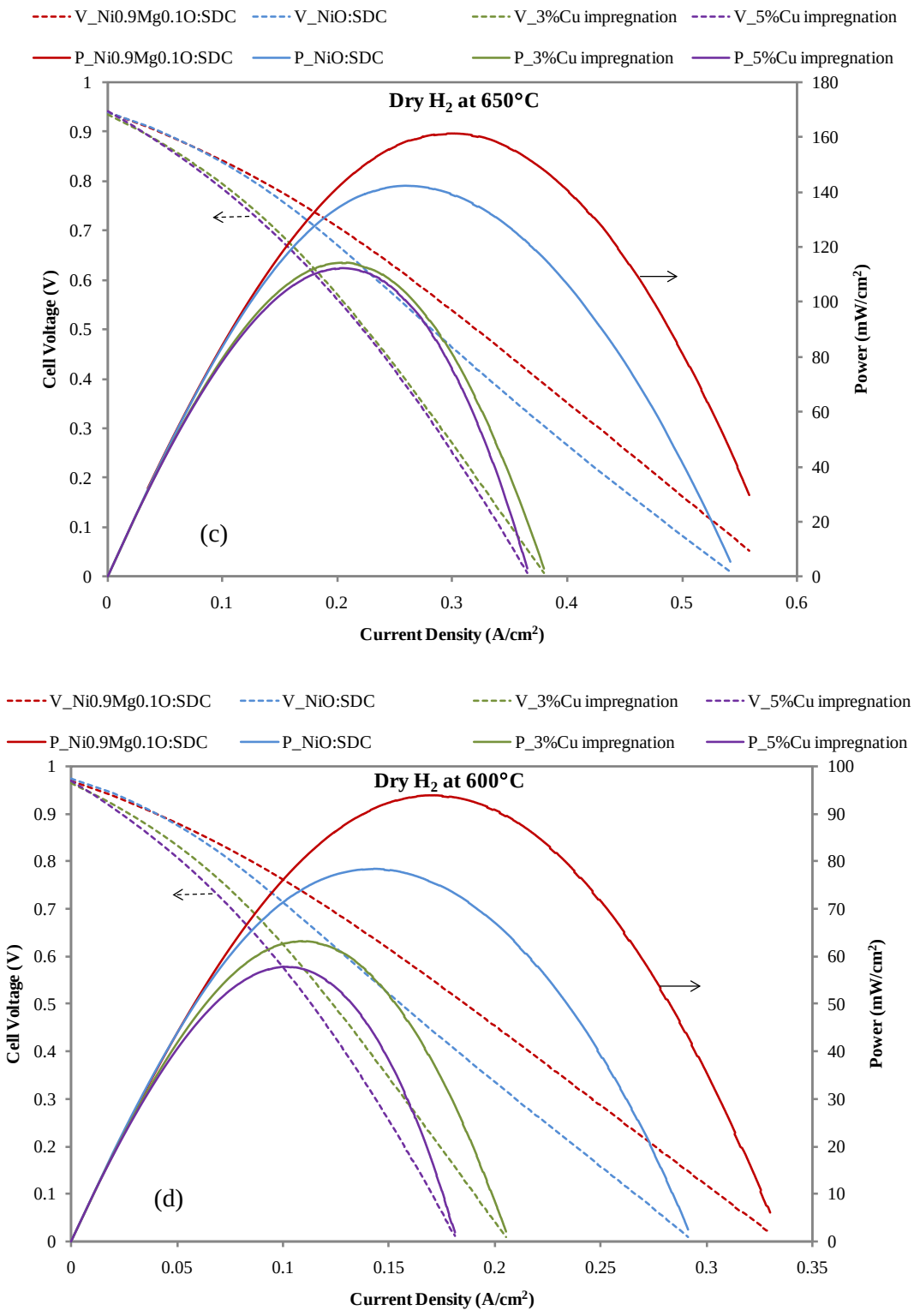

Figure 6-4 Voltage and power density vs. current density with dry H_2 on NiO:SDC, $Ni_{0.9}Mg_{0.1}O$:SDC, 3%Cu on $Ni_{0.9}Mg_{0.1}O$:SDC, and 5%Cu on $Ni_{0.9}Mg_{0.1}O$:SDC anodes at a)750°C, b) 700°C, c) 650°C, and d) 600°C.

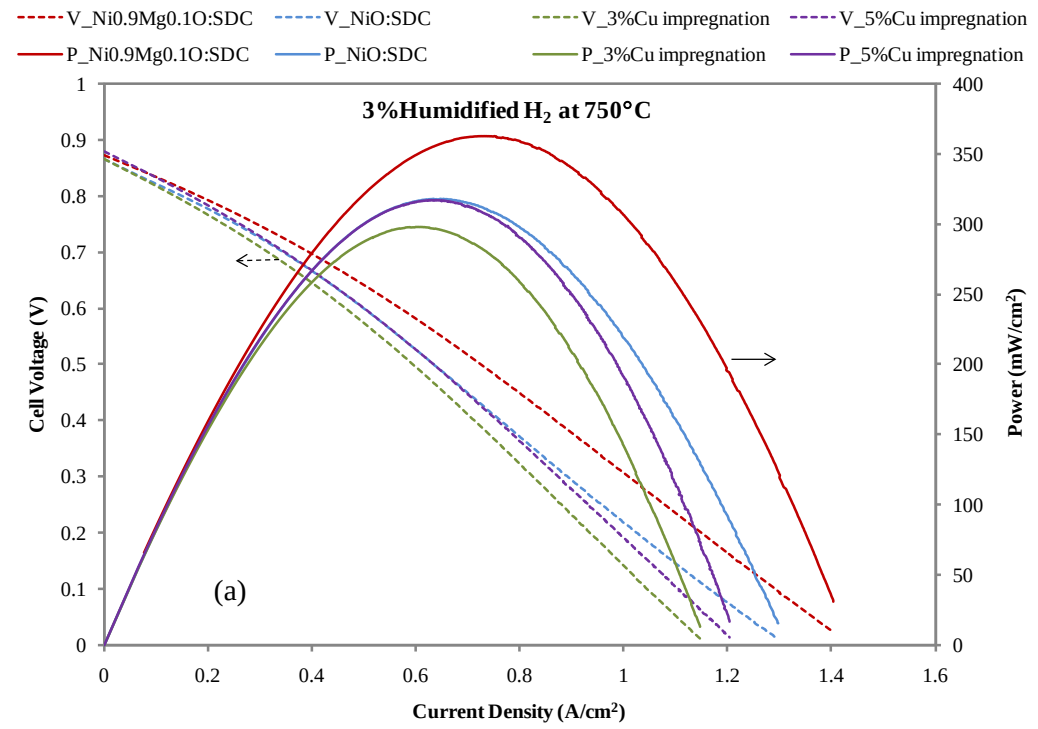
V_Ni0.9Mg0.1O:SDC
V_NiO:SDC
V_3%Cu impregnation
V_5%Cu impregnation
P_Ni0.9Mg0.1O:SDC
P_NiO:SDC
P_3%Cu impregnation
P_5%Cu impregnation
3%Humidified H2 at 750°C
(a)
Cell Voltage (V)
Power (mW/cm2)
Current Density (A/cm2)

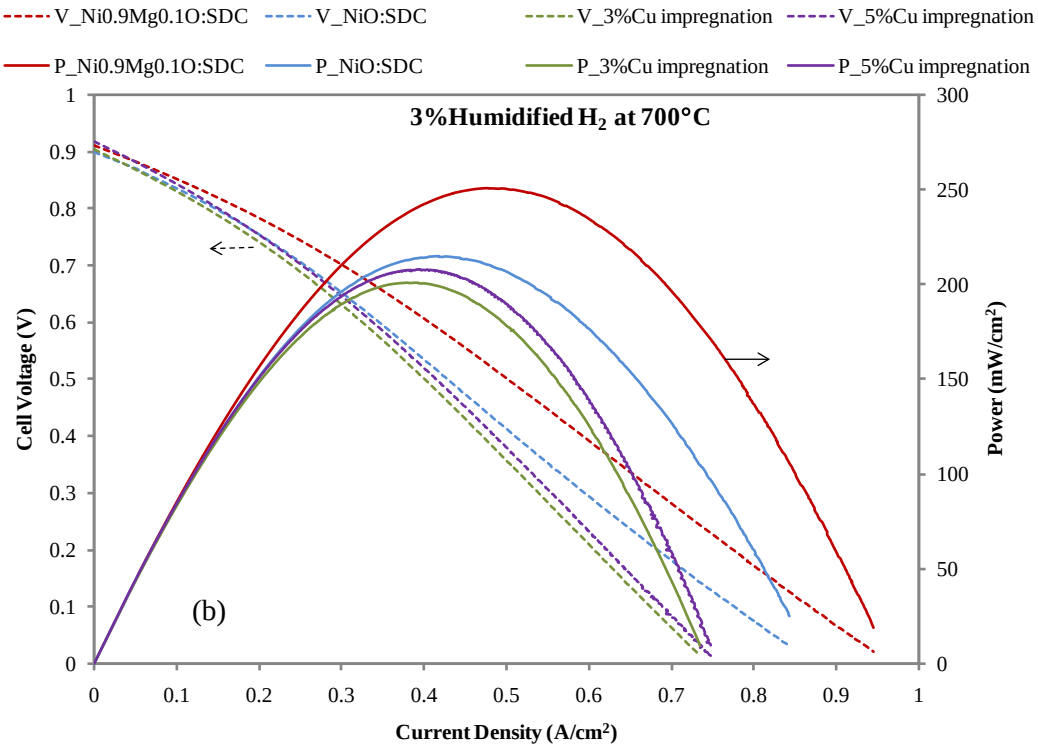
V_Ni0.9Mg0.1O:SDC
V_NiO:SDC
V_3%Cu impregnation
V_5%Cu impregnation
P_Ni0.9Mg0.1O:SDC
P_NiO:SDC
P_3%Cu impregnation
P_5%Cu impregnation
3%Humidified H2 at 700°C
(b)
Cell Voltage (V)
Power (mW/cm2)
Current Density (A/cm2)

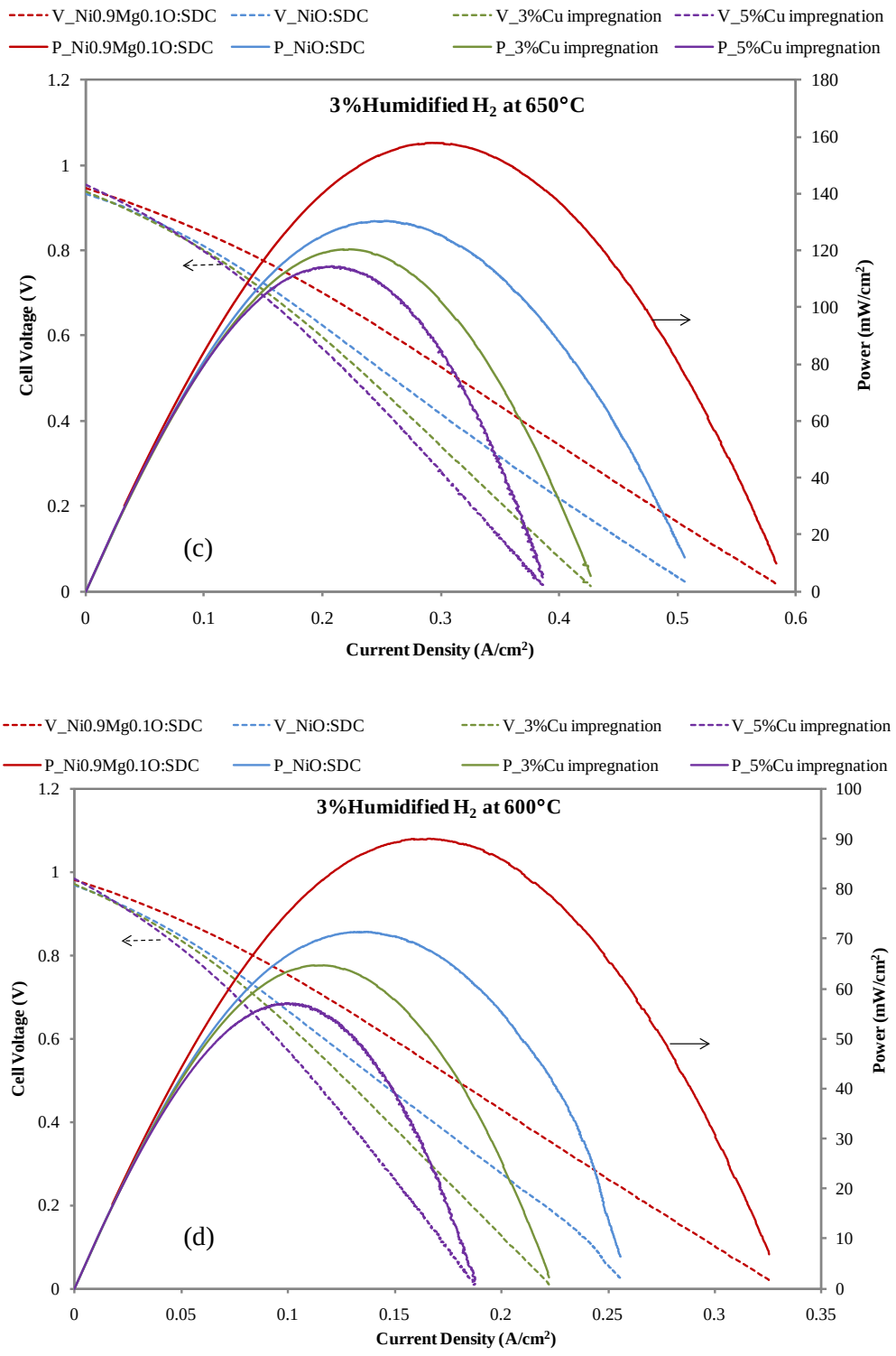

Figure 6-5 Voltage and power density vs. current density with 3%humidified H_2 on NiO:SDC, $Ni_{0.9}Mg_{0.1}O$:SDC, 3%Cu on $Ni_{0.9}Mg_{0.1}O$:SDC, and 5%Cu on $Ni_{0.9}Mg_{0.1}O$:SDC anodes at a)750°C, b) 700°C, c) 650°C, and d) 600°C.

Repeating each test three times, average values of power densities and limiting current densities, along with confidence interval were obtained. Those values are summarized in Figure 6-6 for the maximum power density and in Figure 6-7 for the limiting current density. Similar to the previous discussion on the polarization curves, results in Figure 6-6 and 6-7 reinforce the conclusion that both the average power density and average limiting current density obtained with $Ni_{0.9}Mg_{0.1}O$:SDC anode had the highest values, followed by samples with NiO:SDC anode, followed by samples with 3%Cu on $Ni_{0.9}Mg_{0.1}O$:SDC anode, and the lowest values were found from cells with 5%Cu on $Ni_{0.9}Mg_{0.1}O$:SDC anode. Nonetheless, when standard deviations are considered (drawn as error bars in figures), it was not possible to distinguish much difference between the results obtained with NiO:SDC, 3%Cu on $Ni_{0.9}Mg_{0.1}O$:SDC and 5%Cu on $Ni_{0.9}Mg_{0.1}O$:SDC. Possible reasons for why the best results were obtained with $Ni_{0.9}Mg_{0.1}O$:SDC are that $Ni_{0.9}Mg_{0.1}O$:SDC has a high activity, as well as a high Ni dispersion. Therefore, it provides a larger TPB than NiO:SDC . In addition, it provides a better performance than Cu-containing material because it gives a higher conductivity compared to Cu-containing material as reported in Chapter 4.

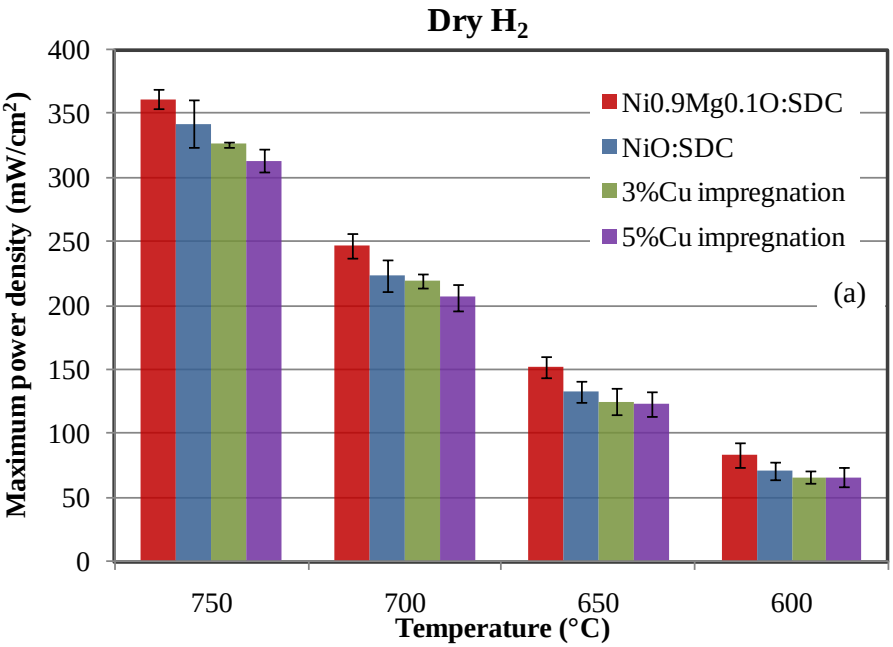

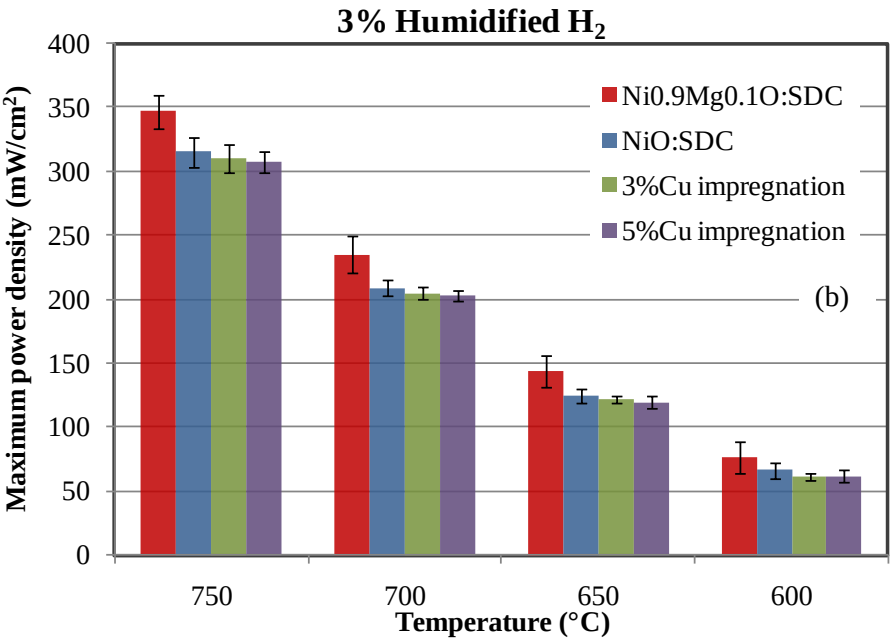

Figure 6-6 Average maximum power density vs. temperature to NiO:SDC, $Ni_{0.9}Mg_{0.1}O$:SDC, 3%Cu on $Ni_{0.9}Mg_{0.1}O$:SDC, and 5%Cu on $Ni_{0.9}Mg_{0.1}O$:SDC anodes with a) dry H_2 b) 3% humidified H_2.

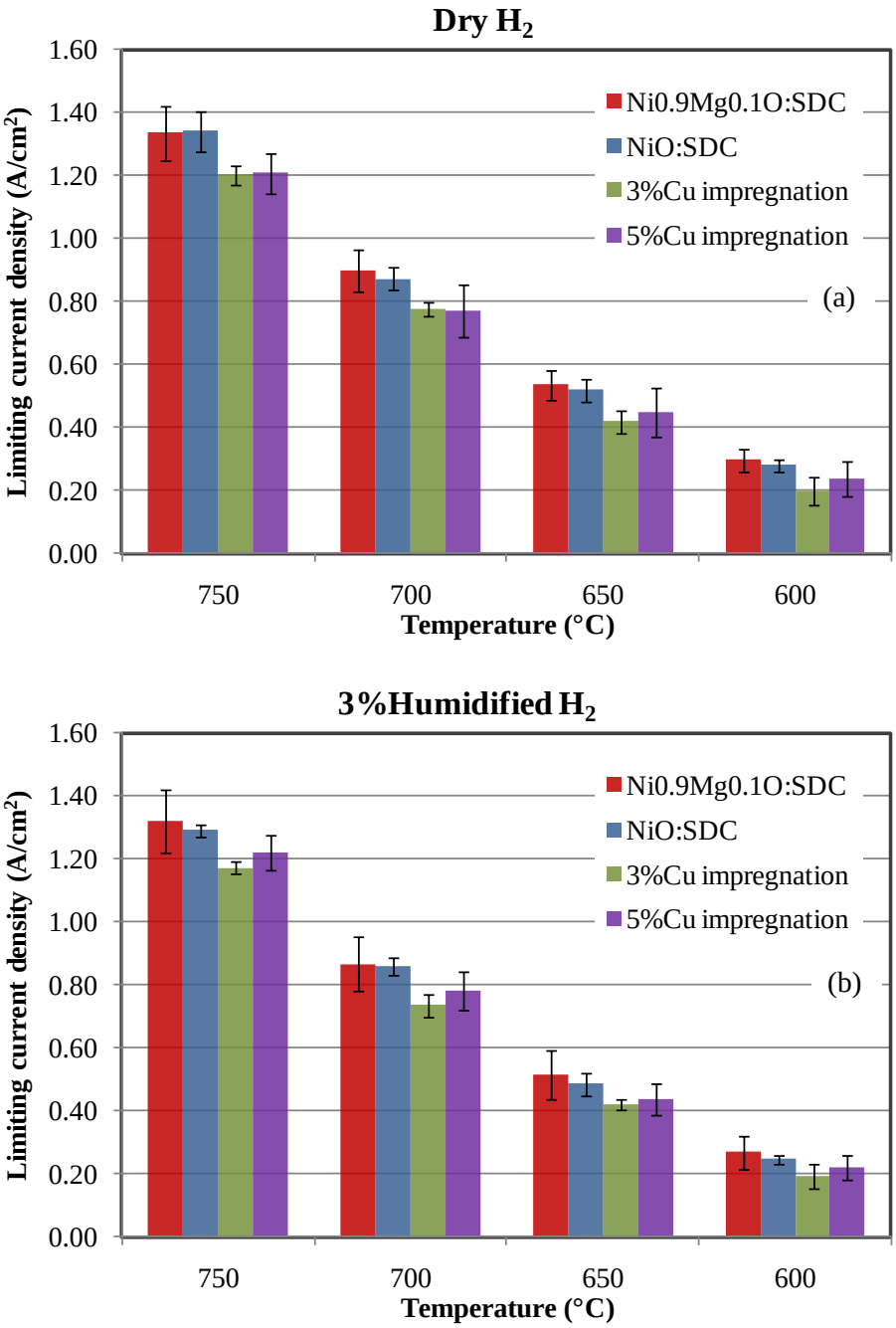

Figure 6-7 Average limiting current density vs. temperature to NiO:SDC, $Ni_{0.9}Mg_{0.1}O$:SDC, 3%Cu on $Ni_{0.9}Mg_{0.1}O$:SDC, and 5%Cu on $Ni_{0.9}Mg_{0.1}O$:SDC anodes with a) dry H_2 b) 3% humidified H_2.

6.1.2 Electrical Impedance Spectra (EIS)

The impedance spectra are shown in Figure 6-8 using the same sample set as those presented in Figure 6-4 and Figure 6-5. All EIS measurements were carried out with base potential at the open circuit voltage (OCV) with a voltage amplitude of 10 mV. As explained in Chapter 3, the high frequency intercept refers to the ohmic resistance (R_s) and the difference between the intercept of the data at low and high frequency is the so-called polarization resistance (R_p). Here, R_s for NiO:SDC is the lowest but the maximum power density was obtained for $Ni_{0.9}Mg_{0.1}O$:SDC. The maximum power density may be related to R_p more than R_s. To verify this assumption, values of R_p were calculated and presented in Table 6-2. It should be noted that the R_p reported here are only the values determined from the first arc. The first arc for R_p is attributed to activation polarization resistance (Kawano et al. (2008)). All values agreed with the polarization measurement in that the lower the R_p, the higher the maximum power density. Table 6-2 shows that $Ni_{0.9}Mg_{0.1}O$:SDC exhibited the lowest value of R_p (0.0266 ohm.cm^2), followed by NiO:SDC (0.0272 ohm.cm^2), 3% Cu on $Ni_{0.9}Mg_{0.1}O$:SDC (0.041 ohm.cm^2) and finally 5% Cu on $Ni_{0.9}Mg_{0.1}O$:SDC (0.047 ohm.cm^2). As expected, R_p became larger as the temperature decreased, as seen in Table 6-2, where the values were about 0.059, 0.135 and 0.315 ohm×cm^2 for $Ni_{0.9}Mg_{0.1}O$:SDC at 700, 650 and 600°C, respectively. It should note that the EIS measurement had a little noisy as appearing in the spectra.

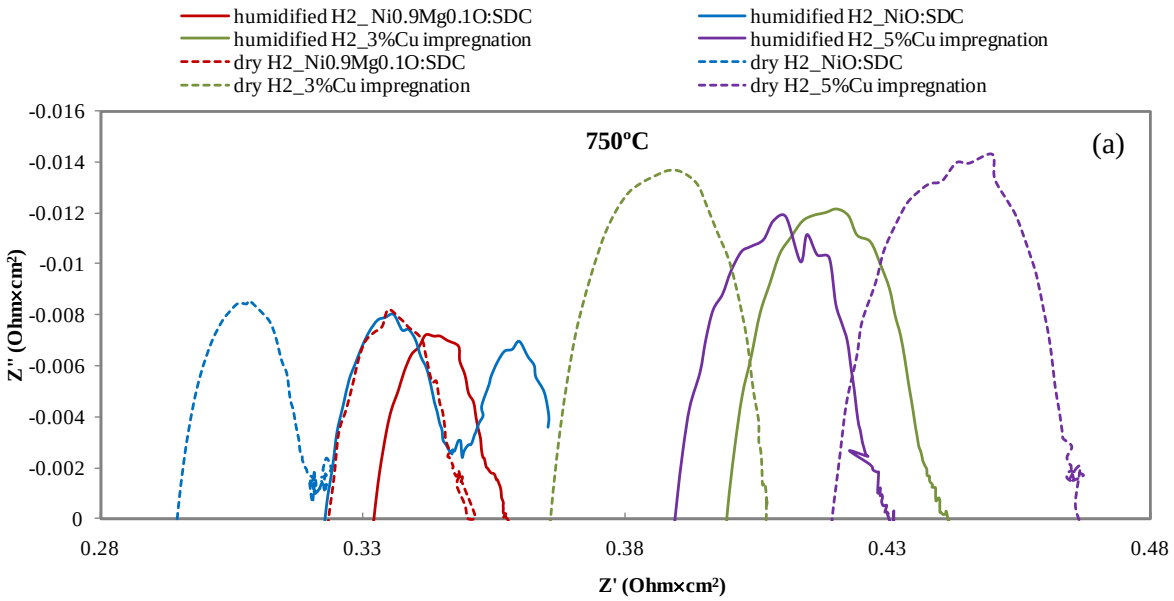

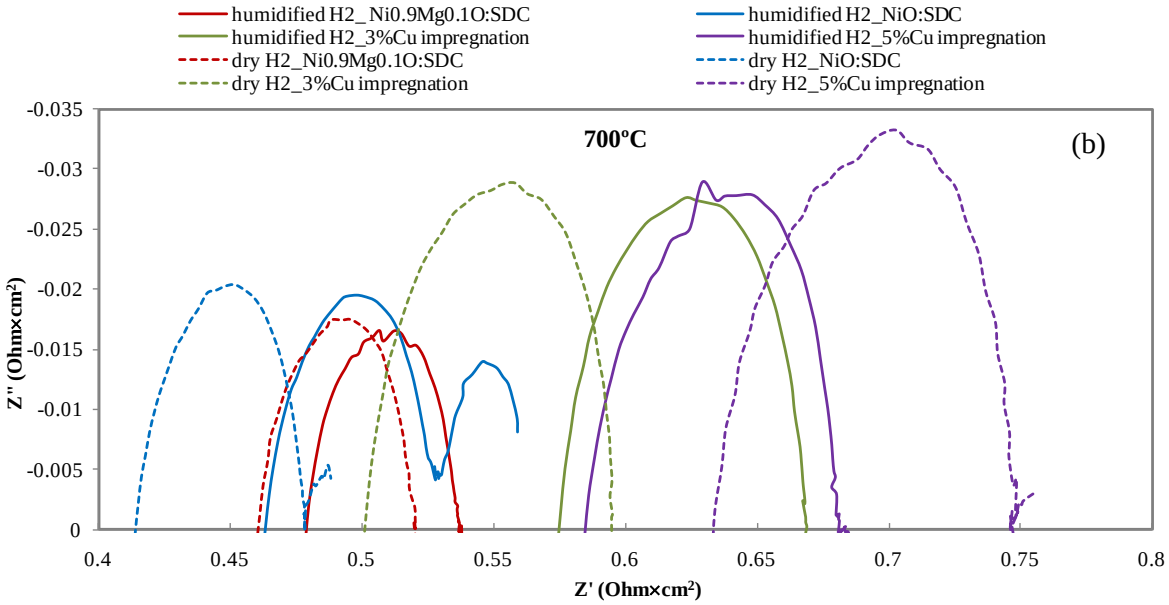
humidified H2_Ni0.9Mg0.1O:SDC
humidified H2_NiO:SDC
humidified H2_3%Cu impregnation
humidified H2_5%Cu impregnation
dry H2_Ni0.9Mg0.1O:SDC
dry H2_NiO:SDC
dry H2_3%Cu impregnation
dry H2_5%Cu impregnation
700°C
(b)
-0.035
-0.03
-0.025
-0.02
-0.015
-0.01
-0.005
0
0.4
0.45
0.5
0.55
0.6
0.65
0.7
0.75
0.8
Z'' (Ohm×cm²)
Z' (Ohm×cm²)

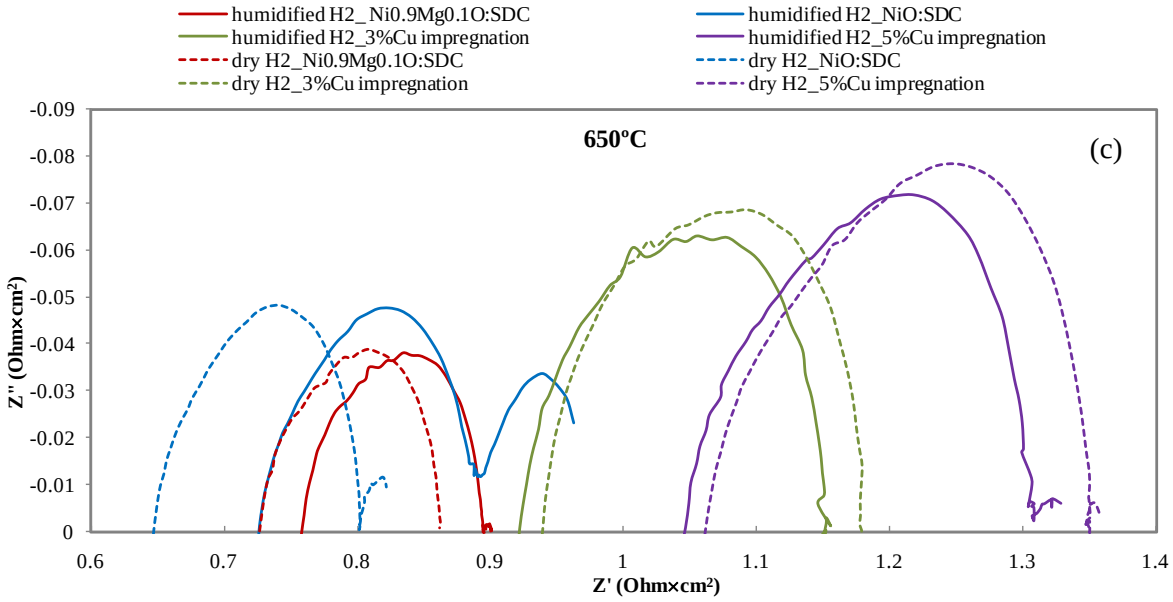
humidified H2_Ni0.9Mg0.1O:SDC
humidified H2_NiO:SDC
humidified H2_3%Cu impregnation
humidified H2_5%Cu impregnation
dry H2_Ni0.9Mg0.1O:SDC
dry H2_NiO:SDC
dry H2_3%Cu impregnation
dry H2_5%Cu impregnation
650°C
(c)
-0.09
-0.08
-0.07
-0.06
-0.05
-0.04
-0.03
-0.02
-0.01
0
0.6
0.7
0.8
0.9
1
1.1
1.2
1.3
1.4
Z'' (Ohm×cm²)
Z' (Ohm×cm²)

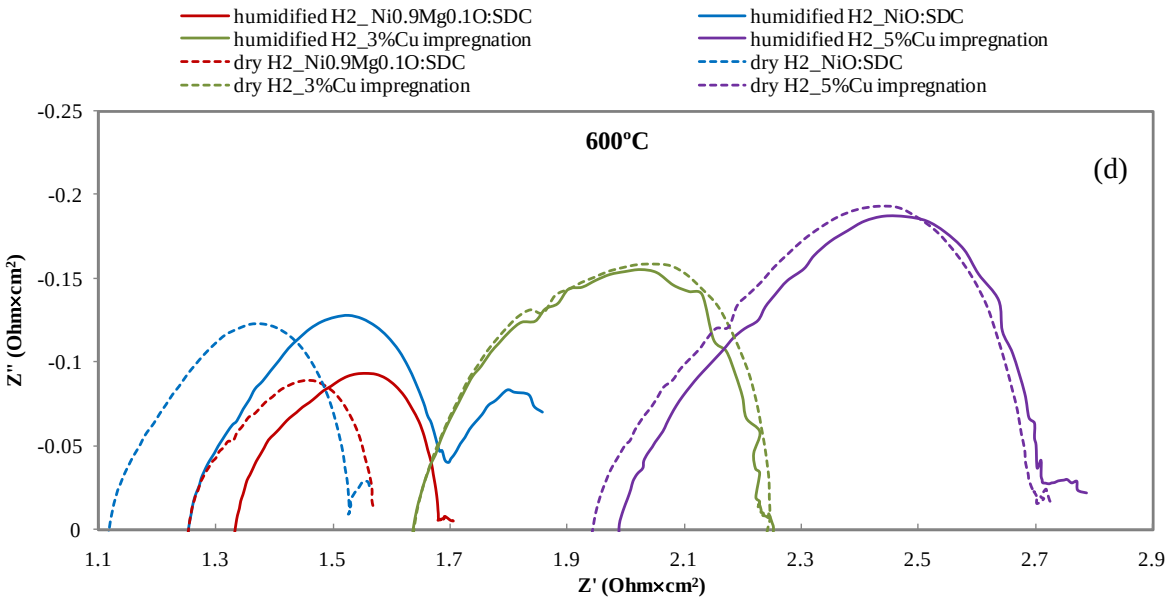

Figure 6-8 EIS spectra with dry H_2 (dotted lines) and 3% humidified H_2 (solid lines) on NiO:SDC, $Ni_{0.9}Mg_{0.1}O$:SDC, 3%Cu on $Ni_{0.9}Mg_{0.1}O$:SDC, and 5%Cu on $Ni_{0.9}Mg_{0.1}O$:SDC anodes at a) 750°C, b) 700°C, c) 650°C, and d) 600°C

Table 6-2 Polarization resistance with dry H_2 and 3% humidified H_2 on NiO:SDC, $Ni_{0.9}Mg_{0.1}O$:SDC, 3%Cu on $Ni_{0.9}Mg_{0.1}O$:SDC, and 5%Cu on $Ni_{0.9}Mg_{0.1}O$:SDC

Anode	Temp (ºC)	R_p (ohm.cm^2)	
		Dry H_2	Humidified H_2
NiO:SDC	750	0.0272	0.026
	700	0.064	0.064
	650	0.155	0.165
	600	0.411	0.438
NiMgO:SDC	750	0.0266	0.025
	700	0.059	0.058
	650	0.135	0.136
	600	0.315	0.351
3%Cu on NiMgO:SDC	750	0.041	0.041
	700	0.091	0.095
	650	0.239	0.234
	600	0.607	0.613
5%Cu on NiMgO:SDC	750	0.047	0.040
	700	0.113	0.097
	650	0.287	0.262
	600	0.758	0.722

The values of R_p with 3% humidified H_2 follows the same order as that with dry H_2. At 750°C, the smallest value of R_p was obtained with $Ni_{0.9}Mg_{0.1}O$:SDC (0.025 ohm.cm^2) followed very closely by NiO:SDC (0.026 ohm.cm^2). Then 0.040 and 0.041 ohm.cm^2 from 5% Cu and 3% Cu on $Ni_{0.9}Mg_{0.1}O$:SDC, respectively (Figure 6-8(a)). This R_p order is similar to the P_{max} order in the polarization test. At lower temperature such as 700°C, the order of R_p was changed to 0.058, 0.064, 0.095, and 0.097 ohm×cm^2 for $Ni_{0.9}Mg_{0.1}O$:SDC, NiO:SDC, 3%Cu on $Ni_{0.9}Mg_{0.1}O$:SDC, and 5%Cu on $Ni_{0.9}Mg_{0.1}O$:SDC (Figure 6-8(b)). R_p values of 0.136, 0.165, 0.234 and 0.262 ohm×cm^2 were observed at 650°C (Figure 6-8 (c)) whereas R_p of 0.351, 0.438, 0.613 and 0.722 ohm×cm^2 were investigated at 600 °C (Figure 6-8 (d)).

Therefore, it can be concluded $Ni_{0.9}Mg_{0.1}O$:SDC is the most active anode for hydrogen fuel. The results also suggests that NiO:SDC is more active than 3% and 5%Cu on $Ni_{0.9}Mg_{0.1}O$:SDC, but the performance of 3% and 5%Cu on $Ni_{0.9}Mg_{0.1}O$:SDC anode are very similar to each other.

6.2 Preliminary Test with Methane

In this work, two preliminary tests in direct methane-fuelled SOFC, dry methane and methane/ steam =6/1, were carried out to investigate the behavior of $Ni_{0.9}Mg_{0.1}O$:SDC anode.

6.2.1 Dry Methane

The testing procedure is a modification of the procedure described previously for hydrogen, but taking into account recommendations from Lin et al. (2005). The procedure starts with sealing the cell (as described in section 6.1)), then ramping the temperature to 750°C, reducing the anode material, feeding humidified hydrogen and finally drawing 0.250 $A.cm^{-2}$ current density from the cell. First, stability/sealing of the cell is checked by monitoring the cell voltage (still under humidified H_2) and ensuring that it remains constant for 30 minutes. If the stability/sealing test is successful, a standard polarization curve is produced to make sure that the cell performance with humidified H_2 is reproducible (e.g. indicating no problem with contact resistance). If the performance of the cell with hydrogen reproduces past performance, cell testing under methane can proceed. The feed on the anode side is slowly adjusted to 30 $mL.min^{-1}$ of pure methane while continuously drawing a current density of 0.10 $A.cm^{-2}$ to minimize methane cracking causing carbon deposition. The cell voltage is expected to become stable again within 2 hours under pure methane. The cell is then maintained under this condition and cell voltage measurements can be done as long as no evidence of cell degradation is observed. The procedure is summarized in Figure 6-9.

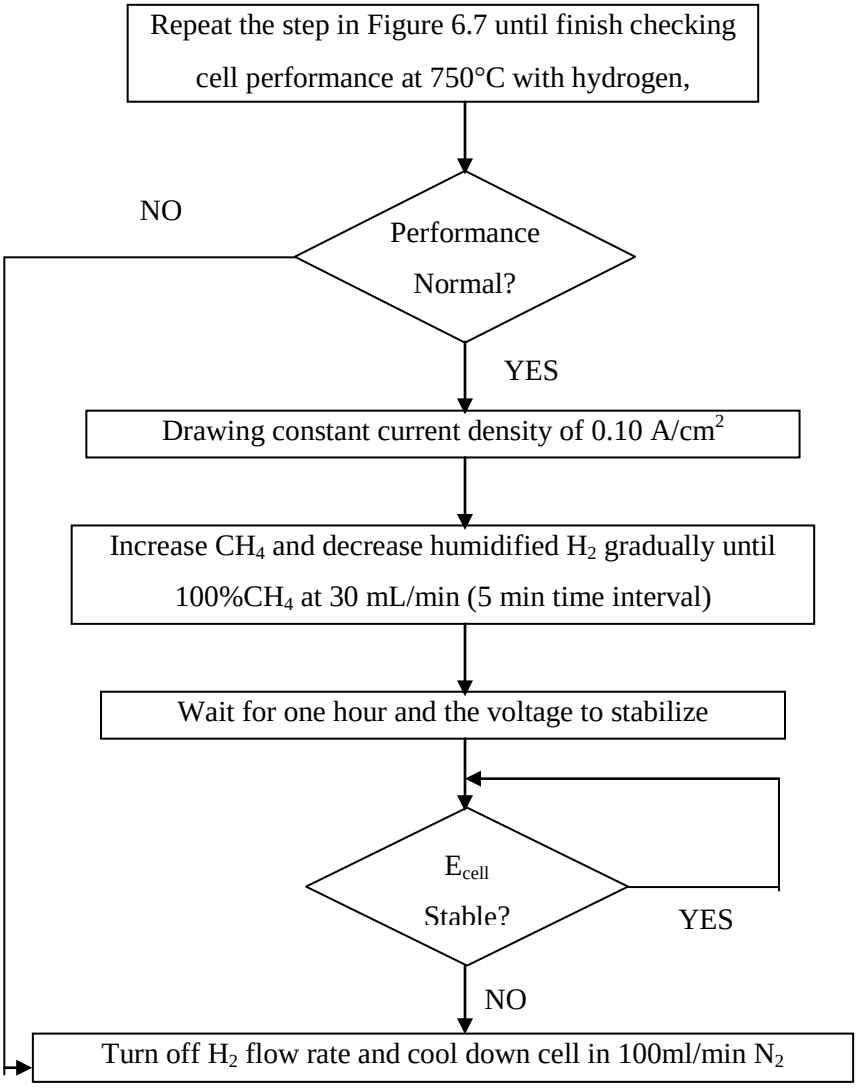

Figure 6-9 Procedure of fuel cell test with pure methane

Although the button cell fabricated following the procedure described in Chapter 3 operated well under a hydrogen atmosphere, it was not working properly under pure methane atmosphere. In the original fabrication procedure, a small amount of anode was used (2.5 mg resulting in 20μm anode thickness), thus eliminating (or at least significantly minimizing) concentration polarization. However, such thin anode was problematic since the anode weight deposited on the cell was too low to show enough activity for methane oxidation or SMR. Indeed, the voltage dropped to zero as soon as some current was drawn from the cell. To remediate this problem, a double of the amount of anode (5.0 mg) helped in sustaining a cell voltage when drawing current, but this voltage was very small, and

dropped to nearly zero after a couple of hours. It was then decided to test a cell with 10 times the original amount of anode amount (25 mg, providing an anode thickness of 180 µm). Note that the area of the cell was increased as well, from 28.3 mm^2 to 38.5 mm^2. With this new cell ($Ni_{0.9}Mg_{0.1}O$:SDC), the test in pure methane test succeeded for ten hours(see Figure 6-11). The detail is discussed next.

This cell was first checked with humidified hydrogen. The polarization curve for humidified H_2 is shown in Figure 6-10 whereas Figure 6-11 shows the corresponding EIS results. In both figures, results for thin (20µm) and thick (180µm) anodes show the effect of anode thickness. For the thick anode, the power density decreases compared to the original cell; from a maximum power density with humidified H_2 of 362 $mW.cm^{-2}$ to 327 $mW.cm^{-2}$. As expected, the polarization resistance is larger with the thick anode than with the thin one: The R_p increases from 0.025 $ohm.cm^2$ to 0.055 $ohm.cm^2$. Note that the ohmic resistance R_s increases as the thickness of the anode increases (from 0.33 to 0.38 $ohm.cm^2$).

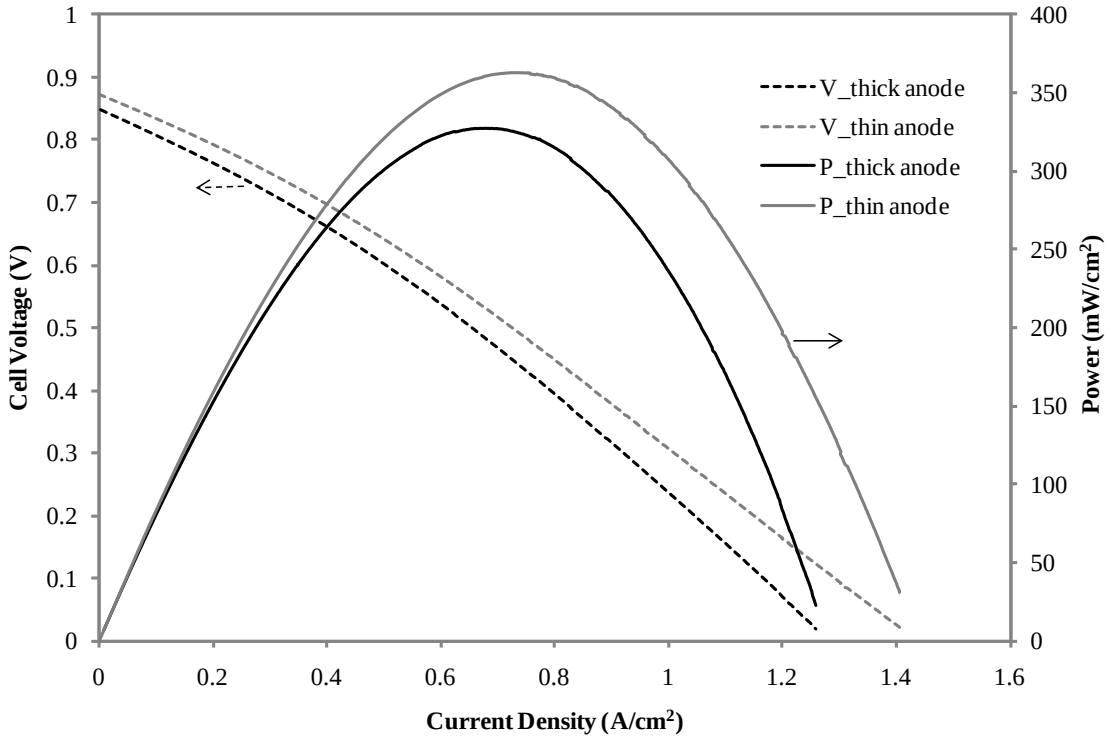

Figure 6-10 Voltage and power density vs. current density with humidified H_2 on $Ni_{0.9}Mg_{0.1}O$:SDC anode. Thick anode: 180µm; thin anode: 20µm.

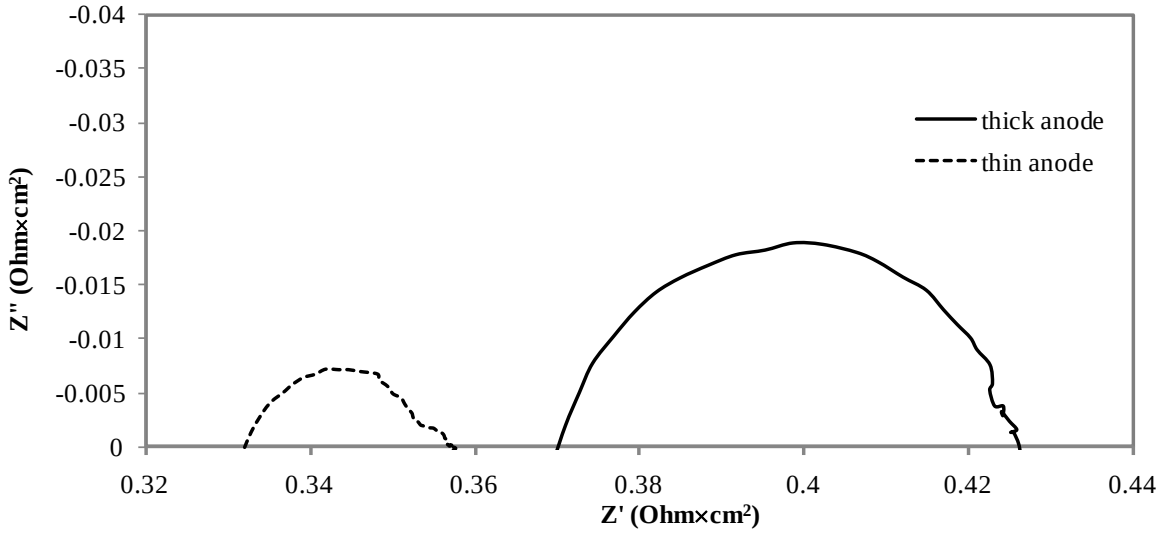

Figure 6-11 EIS spectra with humidified H_2 to $Ni_{0.9}Mg_{0.1}O$:SDC anode cell. Thick anode: 180µm; thin anode: 20µm.

Figure 6-12 shows the voltage over more than 10 hours under a constant load of 0.10 $mA.cm^{-2}$ (galvanostatic) at 750°C for the $Ni_{0.9}Mg_{0.1}O$:SDC anode material. Once the galvanostatic started, the fuel was switched from H_2 to CH_4 (60 mL H_2 to 10mL CH_4 for 5 min, 30 mL H_2 to 20mL CH_4 for 5 min and 0 mL H_2 to 30mL CH_4 for 5 min). The cell voltage was high and almost stable when the hydrogen was still flowed in the system. Then, the voltage dropped significantly in the pure methane compare to hydrogen. After a drop in voltage during the first hour, stable voltage for 10 hours can be attained with under pure methane. However, the voltage started decreasing after 10 hours. After cooling down, the spent cell still remained as one piece but cracks appeared all over the cell. These cracks may be indicative of leaks with carbon deposition that could explain the spikes observed. These spikes are similar to the patter of galvanostatic obtained from the cell degraded by carbon deposition and this cell was tested under the mixture of air, carbon dioxide and iso-octane (Zhan and Barnett (2005)). It can be explained by that the cell voltage is low when the amount of oxygen increases (the oxygen from small leaks). When the amount of oxygen and hydrocarbon (or depositing carbon) is enough, the combustion takes place quickly. Suddenly, the amount of oxygen become normal (as low as no leak) and the cell voltage rises up. Then, the amount of oxygen builds up again and the cell voltage lower down. When the system has this cycle, the spikes exist along the test.

Some experiments were also performed under dry methane before this experiment with similar cells (thick anode), but without drawing any current. In those experiments, the OCV dropped very fast and the cell was covered with carbon (black color). In the experiments with 0.1 $A.cm^{-2}$, the spent cell

remained grey, similar to what is observed when H_2 is the fuel, which means that the amount of carbon in this experiment was less than the pervious.

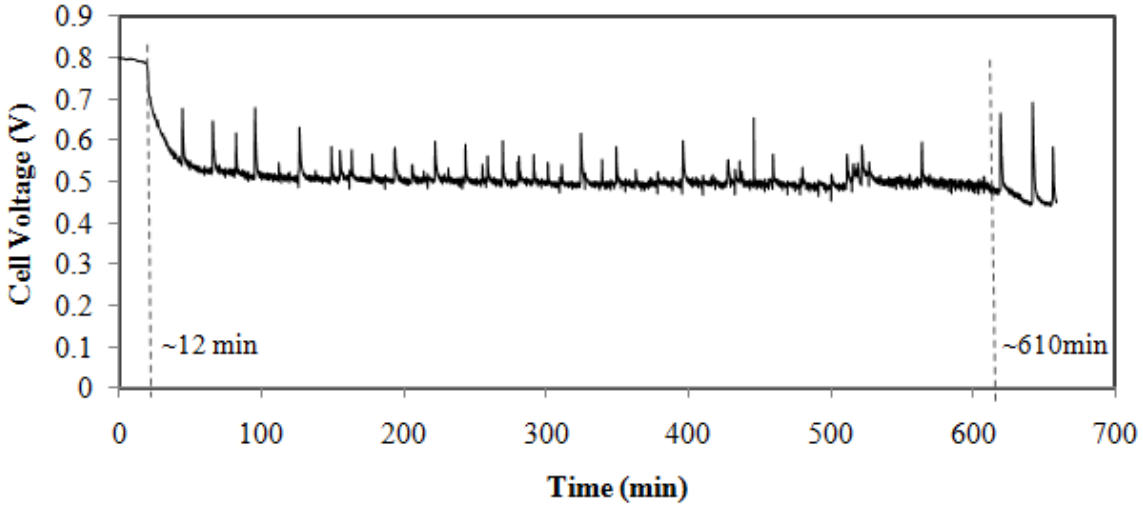

Figure 6-12 Cell voltage vs. time at constant current density of 0.10A/cm^2 to $Ni_{0.9}Mg_{0.1}O$:SDC anode cell operated in dry methane at 750°C

6.2.2 Humidified Methane (H_2O/CH_4= 1/6)

Mixtures of methane and steam were also used as a fuel in order to perform polarization tests at different temperatures. To test the resistance to carbon deposition, it was attempted to use as little steam as possible. In this work, the lowest ratio for which a polarization test can be successfully performed is H_2O/CH_4=1/6 without drawing current while switching from hydrogen fuel to methane/steam fuel mixture. The procedure employed is represented in Figure 6-13 and is the following: hydrogen fuel is first replaced by H_2O/CH_4=1/1 for 30 min under OCV. This ratio is reduced to ½ for 30 min and adjusted to 1/6 for 2 h (at which point the cell voltage is stable here) before starting the polarization test.

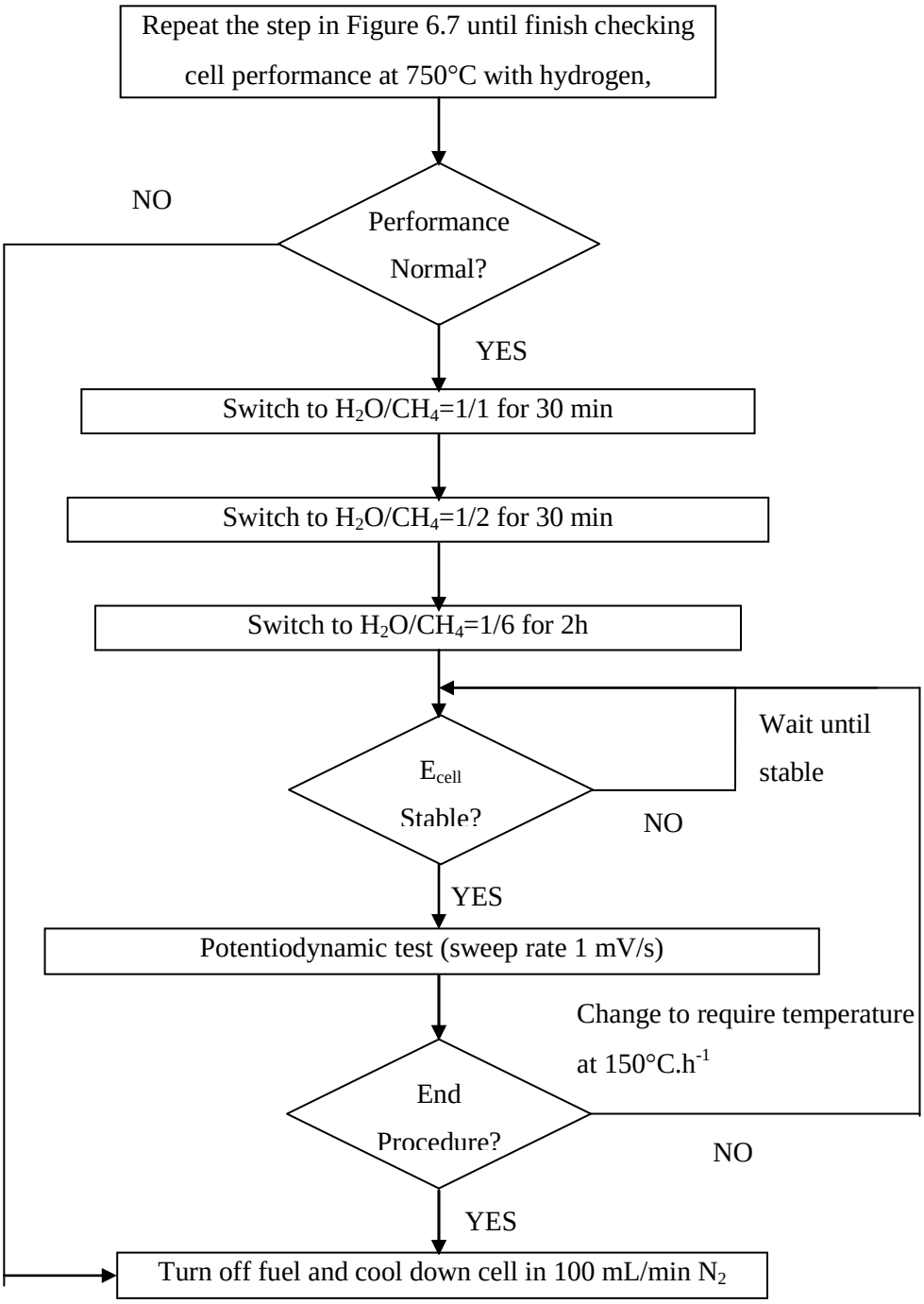

Figure 6-13 Procedure of fuel cell test with H_2O/CH_4=1/6

Results at 750, 700, 650, and 600°C are shown in Figure 6-14. The trends for the polarization curves with H_2O/CH_4 = 1/6 are similar to that of the tests with hydrogen in that the cell voltage lowers with increasing current density and the maximum power density reduces with decreasing temperature. The results in Figure 6-14 reveal that the maximum power densities are 226, 124, 65, and 43 $mW.cm^{-2}$ at 750, 700, 650, and 600°C, respectively. These maximum power densities are less than in the case of humidified H_2 fuel (362, 251, 158, and 90 $mW.cm^{-2}$ at 750, 700, 650, and 600°C, respectively). One would also notice that the curve is not as smooth as with the test in hydrogen, which may be due to small leaks as evidenced by some cracks observed on the cell after the test.

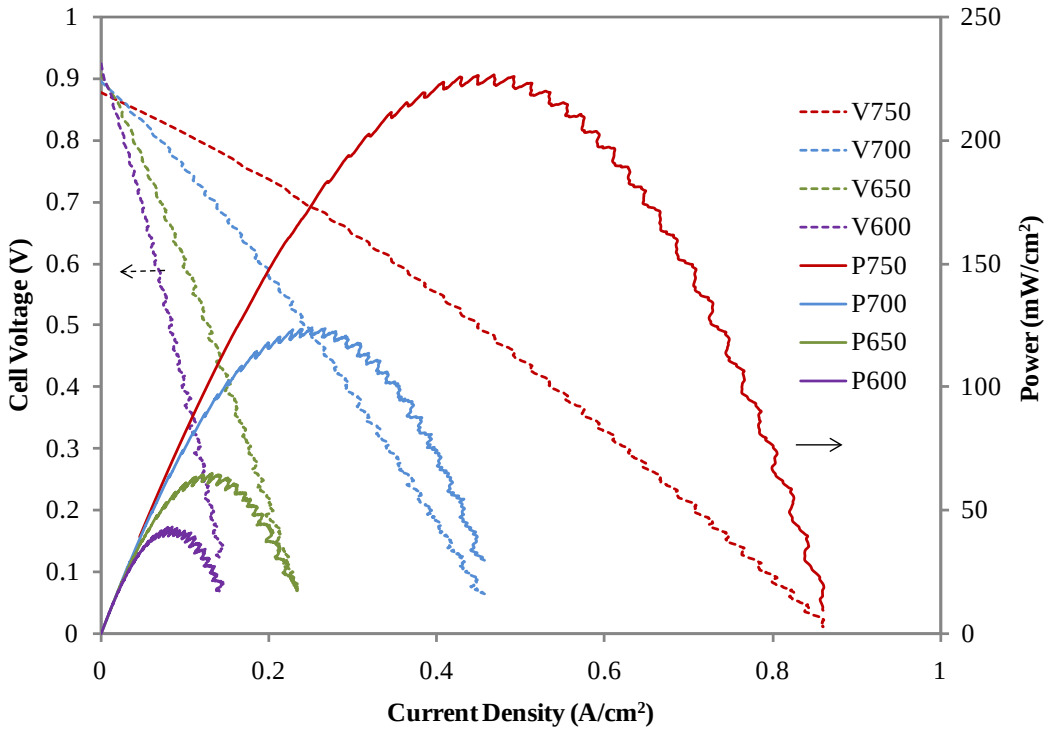

Figure 6-14 Voltage and power density vs. current density with H_2O/CH_4=1/6 on $Ni_{0.9}Mg_{0.1}O$:SDC anodes at 750°C, 700°C, 650°C and 600°C.

Chapter 7
Conclusions and Recommendations

7.1 Conclusions

7.1.1 Material Preparation and Properties

- A procedure for preparing $Ni_{1-x-y}Cu_xMg_yO$ anode materials has been developed. Without addition of Cu, the anode materials were prepared by co-precipitation. Cu was added using two different methods: one-step co-precipitation method and two-step co-precipitation/impregnation method. In the two-step method, various amounts of Cu were impregnated in $Ni_{0.9}Mg_{0.1}O$.
- For SOFC applications, the one-step co-precipitation with Cu is not suitable because the firing temperature is limited by the melting point of CuO. Thus, if Cu is to be added to the anode, only the two-step method is practical. Therefore, the following conclusions/recommendations are relevant only to the materials prepared via two-step methods.
- Reduction properties were determined via TPR. Addition of Mg lowers the reducibility of anode. Anode materials containing up to 5% Cu were fully reduced at temperatures just below 700°C, similar to $Ni_{0.9}Mg_{0.1}O$. When %Cu increases (e.g. 10% Cu), the reduction temperature increases. The reason for lower reducibility when Mg is added (and also at high Cu content) is the formation of Ni-Mg-O (and also CuO) solid solution where MgO (and CuO) disperses into the NiO matrix. However, for all materials considered here, 750°C is sufficient for complete reduction.
- BET surface area of the oxide materials decreases when adding Mg: from 11.5 m^2/g for NiO to 10.4 m^2/g for $Ni_{0.9}Mg_{0.1}O$. The surface area is further reduced as more Cu is impregnated $Ni_{0.9}Mg_{0.1}O$ (down to 8.2 m^2/g for 10% Cu).

7.1.2 Button Cell Fabrication

- A procedure for fabricating a full SDC electrolyte-supported button cell based on $Ni_{1-x-y}Cu_xMg_yO$ anode materials was developed. The general formulation of this button cell is:
  SSC:SDC//SDC// $Ni_{1-x-y}Cu_xMg_yO$:SDC

- For the cathode, it was found that a SSC:SDC ratio 7:3 is most appropriate here. This ratio has been kept constant in all electrochemical tests.
- The electrolyte-supported cell was prepared by first making the electrolyte by a pressing technique and sintering at 1450ºC. Then, the anode was deposited via drop-dry process and sintering at 1300ºC. Using drop-dry process again, a cathode was fabricated and sintered at 950ºC. Good bonding at both electrolyte/porous electrode interfaces was demonstrated by SEM.

7.1.3 Material Activity on SMR

A comprehensive set of experiments was carried out in a fixed bed reactor to evaluate the steam reforming activity of the various anode materials at temperatures of 650 and 750°C, and S/C ratios of 1, 2 and 3. To better mimic the SOFC conditions, SDC was mixed with the $Ni_{1-x-y}Cu_xMg_yO$ materials in a 50:50 ratio. The reforming activities were characterized by methane conversion, H_2 yield and $CO_2/(CO+CO_2)$ ratio. For all experiments, the catalyst was first reduced at 750°C under 10% H_2/N_2 for 1 hour and the reforming experiments were carried out over 20 hours.

Methane conversion:

- As expected because SMR is an endothermic reaction, methane conversion was higher at 750°C than at 650°C for all materials considered. Note, however, that the experimental conversions were always lower than those predicted from thermodynamic calculations.
- For all materials, methane conversion increases as the S/C ratio increases, as expected from thermodynamics.
- Methane conversion over NiO:SDC and $Ni_{0.9}Mg_{0.1}O$:SDC is greater than over material impregnated with copper. The conversion decreases as the amount of Cu impregnated increases because Cu is considered inactive for SMR.

H_2 yield and $CO_2/(CO+CO_2)$ ratio:

- For most experiments, H_2 yield and $CO_2/(CO+CO_2)$ ratio follow the same trends: they decrease as the temperature rises and the S/C ratio is ruduced. Similar trends are expected because both H_2 yield and $CO_2/(CO+CO_2)$ ratio can be linked to the extent of the WGS reaction since it produces proceeds both H_2 and CO_2 (while the total $CO+CO_2$ remains constant).

- When performing SMR on 50wt% Ni-Cu-Mg-O: 50wt% SDC catalyst, the following expected results were found: the methane conversion is higher at 750°C than at 650ºC and it also increases with rising S/C. The activity of WGS was studied using $CO_2/(CO+CO_2)$ ratio. The activity of WGS decreases at higher reaction temperature because WGS is a moderately exothermic reaction.
- Adding 10% Mg does not affect the $CO_2/(CO+CO_2)$ ratio, compared to NiO:SDC. This means that the WGS activity on $Ni_{0.9}Mg_{0.1}O$:SDC and NiO:SDC are similar.
- At 650°C, increasing copper content increases the $CO_2/(CO+CO_2)$ ratio. However, at 750°C, the $CO_2/(CO+CO_2)$ ratio does not change much with Cu content between 5 and 10%. However, this ratio remains greater than that obtained without Cu addition. Cu is a known active metal for the WGS reaction. The observed difference in the trend between 650 and 750°C may be attributed to the fact that the WGS reaction is a fast reaction that reaches equilibrium rapidly as the temperature increases; the effect of Cu content observed at 650°C indicates that the WGS reaction has not reached equilibrium.

Carbon deposition:

- The analyses for carbon deposition were done only for S/C of 1, the lowes ratio, which represents the conditions where carbon deposition is more likely to occur.
- For all anode materials, more carbon is deposited at 650°C than at 750°C. At 750ºC, the carbon deposited is mostly in the form of filaments. Athough in carbon filaments still forms in some situations at 650°C, the carbon deposited is primarily in the form of a thin graphite layer.
- The longest filaments are found on NiO:SDC at both 650°C and 750°C. Addition of Mg considerably reduced the amount of carbon filaments at 750°C. At 650°C, carbon is deposited as a thin graphite layer in the presence of Mg with no evidence of carbon filament.
- Impregnation of 5% Cu on $Ni_{0.9}Mg_{0.1}O$:SDC further reduces the amount of carbon deposited at 650°C. At 750°C, the carbon deposited on 5% Cu on $Ni_{0.9}Mg_{0.1}O$:SDC and $Ni_{0.9}Mg_{0.1}O$:SDC are similar.
- Thermogravimetric experiments for methane cracking revealed that the initial rate of cracking is not dependent on the amount of Cu deposited (0%, 3% and 5% Cu yielded similar initial rate),

but deactivated faster as the amount of Cu impregnated is increased. Therefore, the presence of Cu helps in reducing carbon filament growth.

7.1.4 Electrochemical Performance

- Four anode materials were tested in the button cell test station for their electrochemical performance; NiO:SDC, $Ni_{0.9}Mg_{0.1}O$:SDC, 3%Cu and 5% Cu on $Ni_{0.9}Mg_{0.1}O$:SDC. All those cells were tested under dry and humidified hydrogen at 600, 650, 700 and 750°C.
- The highest maximum power density and highest limiting current is achieved, at all operating conditions with $Ni_{0.9}Mg_{0.1}O$:SDC. For example, the maximum power density at 750°C under dry hydrogen is 369 $mW.cm^{-2}$, and 161 $mW.cm^{-2}$ at 650°C. Addition of Mg improves the cell performance compared to that of NiO:SDC, for which the maximum power density under dry hydrogen is 356 $mW.cm^{-2}$ at 750°C and 142 $mW.cm^{-2}$ at 650°C.
- Higher amount of Cu reduces the performance of the cell. The maximum power density under dry hydrogen using on $Ni_{0.9}Mg_{0.1}O$:SDC is 325 $mW.cm^{-2}$ at 750°C with 3%Cu and 303 $mW.cm^{-2}$ with 5% Cu. Despite the presence of Mg, addition of Cu as low as 3% results in a poorer performance than with NiO:SDC.
- EIS measurements were performed and ohmic (R_s) and polarization (R_p) resistances were determined. Compared to NiO:SDC, addition of Mg decreases the value of R_p; for example, at 650°C and under dry H_2, R_p changes from 0.155 $ohm.cm^2$ with NiO:SDC down to 0.135 $ohm.cm^2$ with $Ni_{0.9}Mg_{0.1}O$:SDC.
- Addition of Cu, on the other hand, increases R_p significantly. At 650°C and under dry H_2, R_p increased from 0.135 $ohm.cm^2$ with $Ni_{0.9}Mg_{0.1}O$:SDC to 0.239 $ohm.cm^2$ with 3% Cu on $Ni_{0.9}Mg_{0.1}O$:SDC.
- An experiment with dry methane was carried out after devising a proper experimental protocol for this type of experiments. The experiment with dry methane was performed over $Ni_{0.9}Mg_{0.1}O$:SDC under a load of 0.10 $A.cm^{-2}$. The voltage decreases during the first hour from 0.8 V down to about 0.5 V, but remains constant for the following 9 hours. After 10 hours of operation, a further decrease in the cell voltage is observed. In addition, voltage spikes are observed throughout the experiments. Those spikes may be attributed to small leaks. Indeed, at the end of the experiment, the cell shows small cracks.

- In H_2O/CH_4=1/6, the maximum power density at 750°C is 226 $mW.cm^{-2}$. However, under this condition, small cracks were observed after the polarization test.

7.2 Recommendations for Future Work

This thesis presents the first study to investigate $Ni_{1-x-y}Cu_xMg_yO$:SDC as an anode material for IT-SOFCs with internal reforming capabilities. Its main objective was primarily to evaluate overall steam reforming and electrochemical performance of the studied materials. Considerable time has been devoted to setup the electrochemical test station, develop produces to fabricate this type of electrolyte-supported button cells and develop procedures for cell testing under hydrogen and methane environments. As such, although a large number of experimental results are presented in this thesis, it was not possible to conduct all the experiments initially planned. In particular, few electrochemical tests with methane feed were conducted. Therefore, a considerable amount of research is still needed to be done to characterizing these materials. Below are suggested recommendations for future work.

7.2.1 Button Cell Fabrication

- Although all problems were resolved when fabricating the button cell for testing in hydrogen, the test with dry methane led to cracks in the cell. In addition, several anode thicknesses were studied for testing with dry methane. It was found that if the anode is too thin, tests with dry methane were unsuccessful. The successful test with dry methane was carried out with an anode thickness 10 times larger than for tests with H_2. It is recommended that the anode thickness be optimized for optimum performance while ensuring the cell remains intact.
- It is recommended that the button cell be fabricated using finer powder, which can be achieved using methods such as the glycine-nitrate process.
- This thesis found that SDC has poor mechanical strength resulting in cracking during the operation or fabrication. Gadolinia-doped ceria (CeO_2-Gb_2O_3; GDC) is the other doped-ceria that receives an interest as high as SDC. Therefore, some samples should use GDC to replace SDC and the electrochemical performance and the mechanical property should be compared.
- To achieve higher performance, fabrication of an anode-supported cell is recommended to create a larger active area on the same area of electrolyte/anode interface. In this type of cell, one has to find a good compromise between high enough porosity and mechanical strength. Another

possible problem may be the impregnation of Cu if the anode is too dense. To ensure good Cu impregnation, a vacuum system may be required.

- It has been proposed in the literature that a bi-layer anode be used when feeding a SOFC with hydrocarbon fuel. A bi-layer anode is composed of an active layer to maximize the electrochemical activity and a support layer for mechanical strength. With hydrocarbon fuels, it has been shown that carbon deposition is much less of an issue on the active layer because the carbon can be oxidized by the oxygen ions. However, carbon deposition is much more of a problem for the support layer. Thus, one should choose a support layer not active toward hydrocarbon reforming, thus minimizing carbon deposition. Since we have shown here that addition of Cu can considerably decrease the SMR activity (and consequently carbon deposition), one possibility is to design a support layer with Cu impregnated on $Ni_{0.9}Mg_{0.1}O$:SDC, in contact with an $Ni_{0.9}Mg_{0.1}O$:SDC active layer.
- Finally, it would also be worthwhile to consider this material for a metal supported cell, as well. It is, therefore, suggested to that metal-supported cell based on $Ni_{1-x-y}Cu_xMg_yO$:SDC anode be used in a button cell.

7.2.2 Material Activity on SMR

- Study of the amount of carbon deposited is critical, which is usually done via TPO. In our study, TPO was done using thermogravimetry analysis (TGA). The difficulty with TPO-TGA is that weight change is not only due to carbon removal in the form of CO and CO_2 (in which case only weight loss should be observed), but also due to oxidation of the reduced Ni (in which case weight gain is observed). A much better way is to carry out TPO using a mass spectrometer (MS), which unfortunately was not readily available at the time of this thesis. In any future work, it is highly recommended to perform TPO-MS systematically on the spent catalysts.

7.2.3 Electrochemical Performance

- This work used two electrodes for the electrochemical measurement. The maximum power densities and the EIS spectra (along with R_p) were used as overall cell properties to compare the performance of the various materials. To evaluate the electrode performance individually, it is required that three electrodes measurement be employed. Figure 7-1 shows the schematics of two- and three-electrode configurations.

(a) (b)

Figure 7-1 Schematic of a) two electrodes b) three electrodes

- More electrochemical measurements (polarization and EIS) must be carried out with methane over the electrolyte-supported button cell. All candidate materials must be tested, not only with dry methane, but also at various S/C ratios.
- The experiments described in the preceding recommendation should also be performed on an anode-supported cell (and eventually on metal supported cell).
- All anode materials should be thoroughly characterized after each electrochemical test, in particular those with methane, using SEM (EDX) and TPO with MS.
- The conductivity measurements for the anode material should be done at the actual operating conditions that are in the temperature range 600-750 º C and under reducing atmosphere.

Appendix A
Mass Flow Control Calibration

Prior to using mass flow controllers in the fuel cell test station, they were connected to the computer and calibrated using bubble-film flow meter. The volume flow rates for different signals from each mass flow controller are measured and a correlation between the signal and the flow rate is determined. The calibration results for N_2, H_2 and CH_4 flow controllers are reported in Table A-1 which reported the average and standard deviation from five repeats for each signal. The calibration curves for N_2, H_2 and CH_4 are plotted in Figure A-1. The error bars are indicated in Figure A-1 but they can barely be seen because the errors are small.

Table A-1 Average flow rate and standard deviation with different signals for each mass flow controller

Controller for	Signal	Average flow rate	Standard deviation
N_2	0.5	53.64	0.93
	0.7	75.10	0.45
	1.0	108.64	1.64
	1.5	162.82	0.27
	2.0	209.26	3.73
H_2	0.2	6.07	0.15
	0.5	20.13	0.39
	1.0	42.32	0.45
	2.0	80.70	0.96
	3.0	117.15	1.27
CH_4	0.2	9.91	0.13
	0.5	24.20	0.50
	1.0	47.35	0.34
	2.0	91.04	1.56
	3.0	136.78	2.78

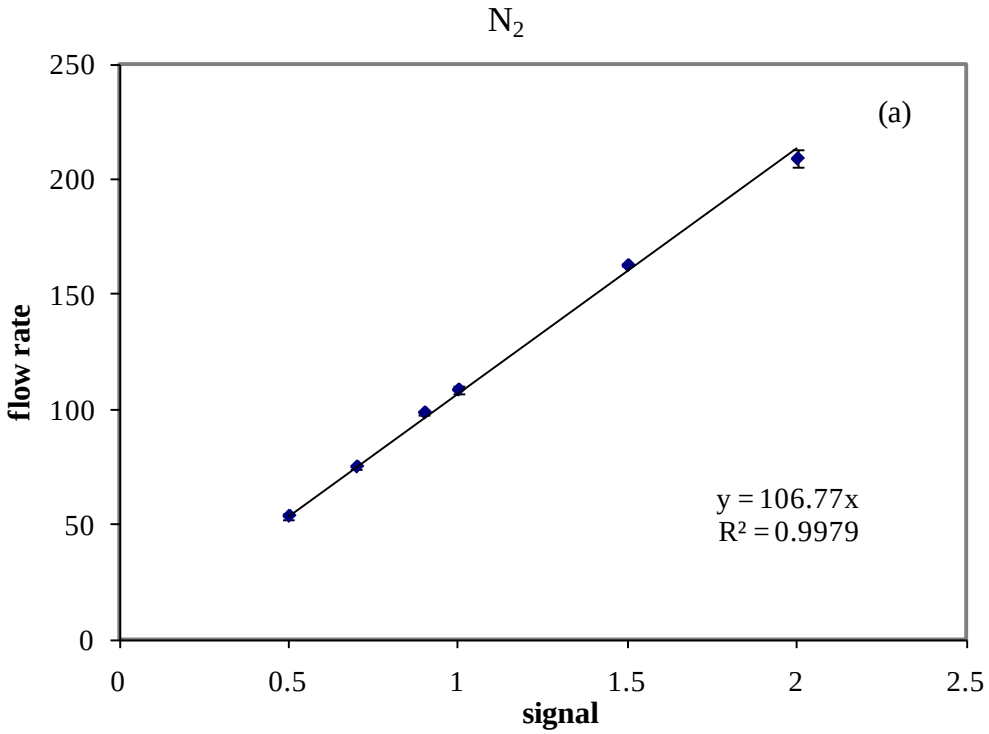
N_2
(a)
flow rate
signal
y = 106.77x
R² = 0.9979
0
50
100
150
200
250
0
0.5
1
1.5
2
2.5

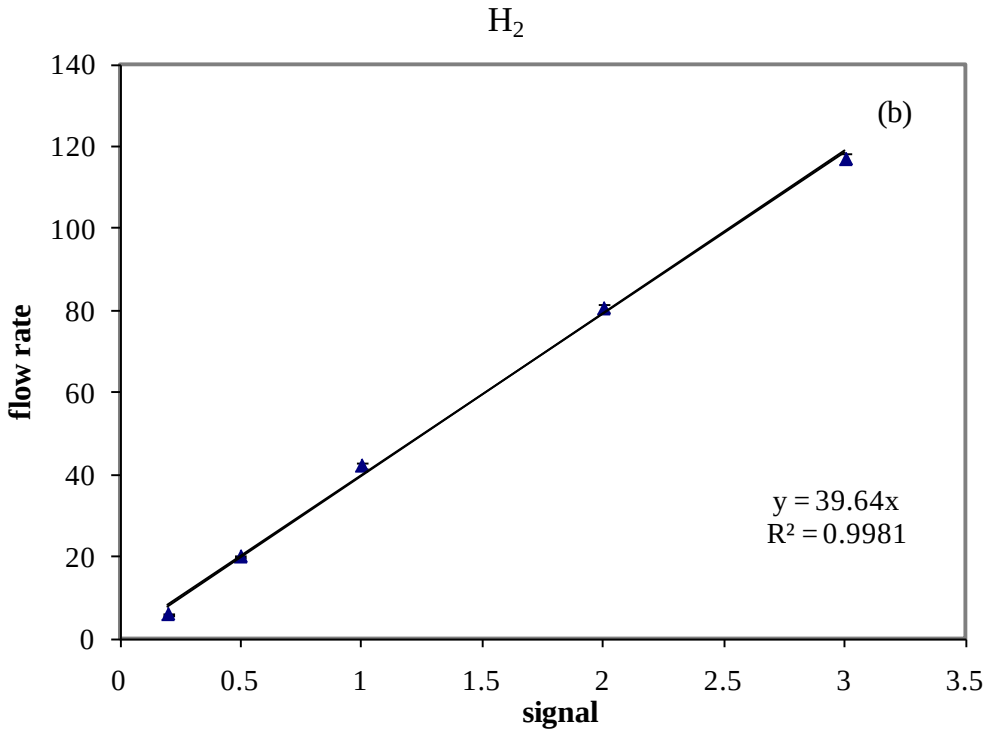
H_2
(b)
flow rate
signal
y = 39.64x
R² = 0.9981
0
20
40
60
80
100
120
140
0
0.5
1
1.5
2
2.5
3
3.5

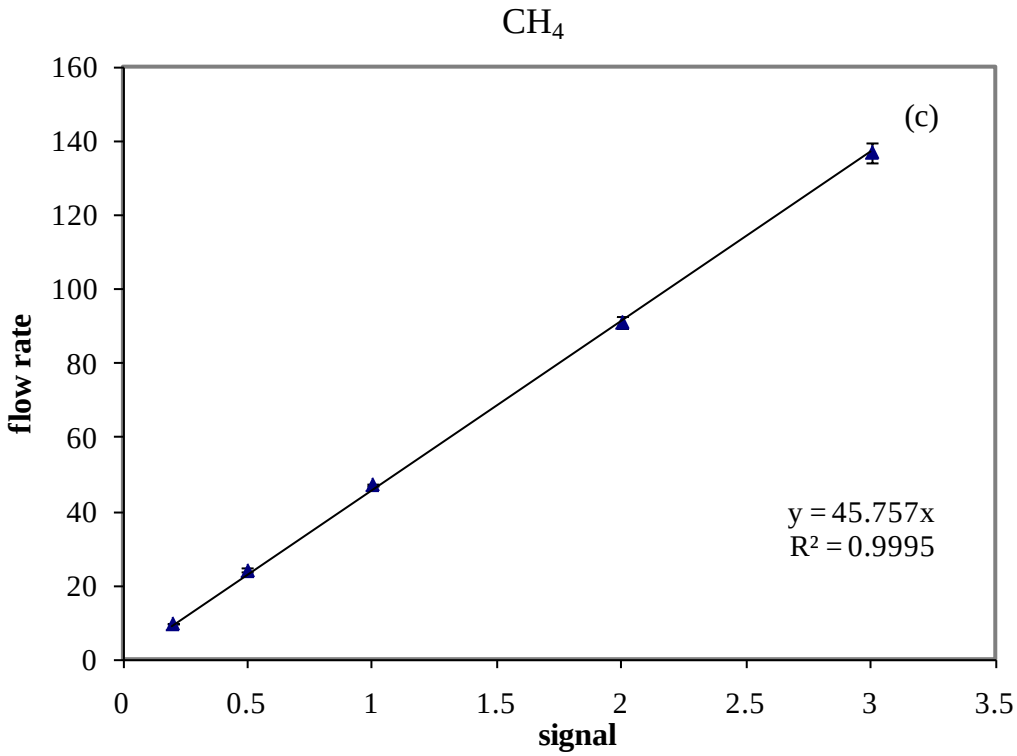

Figure A-1 Calibrations curve of the mass flow controller for a) nitrogen, b) hydrogen and c) methane.

Appendix B

Calculations for Control Evaporator and Mixer (CEM)

This appendix describes the calculation that was used when the mixture of methane and steam generated through the CEM. The CEM has a separate controller which requires the input the mass flow rate of water (in $g.h^{-1}$) and the temperature at the evaporator. This mass flow rate must correspond to the desired volume flow rate once the water is changed into steam. The calculation starts with finding the upper limit of the fraction of steam in the feed at standard pressure, which is determined from the saturated pressure of the steam at that temperature. If the amount of desired steam in the feed is not over the limit at the temperature of the evaporator, then the mixture can be achieved using the CEM. However, to ensure that the amount of steam in the feed is similar to the requirement, taking the efficiency of CEM that is less than 100% efficiency into account is recommend (i.e. 80% efficiency of CEM). The limiting volume fractions of steam in the feed at 100% efficiency and 80% efficiency are reported in Table B-1. In this work, the temperature of evaporator was set at 100°C and the limiting volume fraction of steam was considered at 80% efficiency of CEM.

Table B-1 Limiting volume fraction of steam in the feed

Temperature (°C)	Saturated pressure (atm)	Limiting percentage of steam in the feed (100% efficiency)	Limiting percentage of steam in the feed (80% efficiency)
0	0.006	0.6	0.5
10	0.012	1.2	1.0
20	0.023	2.3	1.8
30	0.042	4.2	3.3
40	0.073	7.3	5.8
50	0.121	12.1	9.7
60	0.196	19.6	15.7
70	0.307	30.7	24.5
80	0.466	46.6	37.3
90	0.691	69.1	55.3
100	0.997	99.7	79.8

The liquid water flow rate that corresponds to the demand is:

Mass water flow rate (g/h) = Volume flow rate of steam (mL/min) ×60×18/22.4

Appendix C

Phase diagrams for systems involved in the thesis

This appendix illustrates phase diagrams of phase diagram NiO-MgO system, CuO-MgO system, and Cu-Ni system in Figure C-1, C-2 and C-3, respectively.

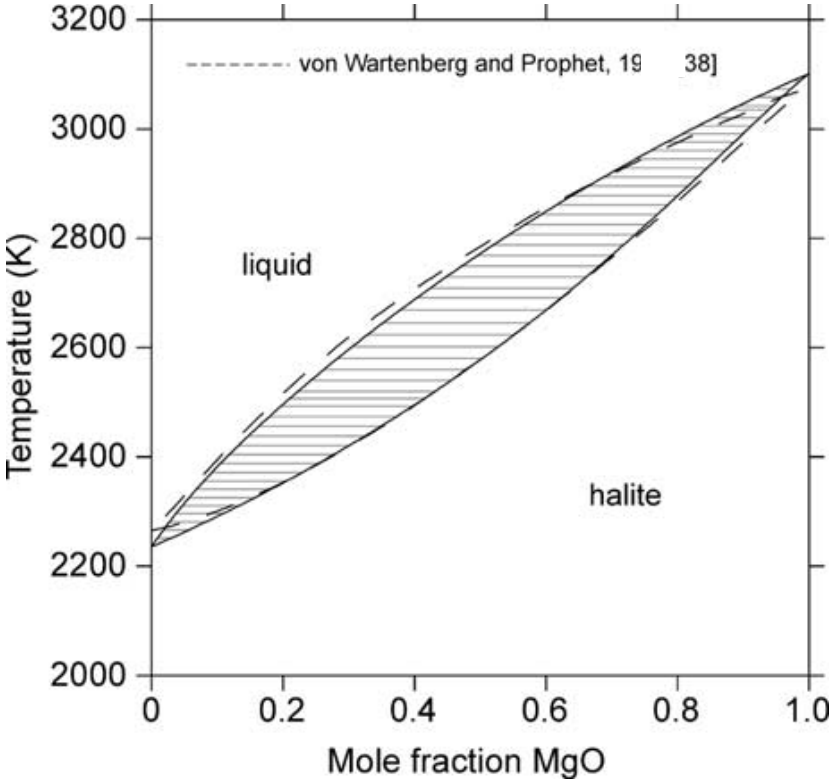

Figure C-1 Calculated quasibinary NiO–MgO phase diagram in air as compared with literature data Zinkevich et al. (2005).

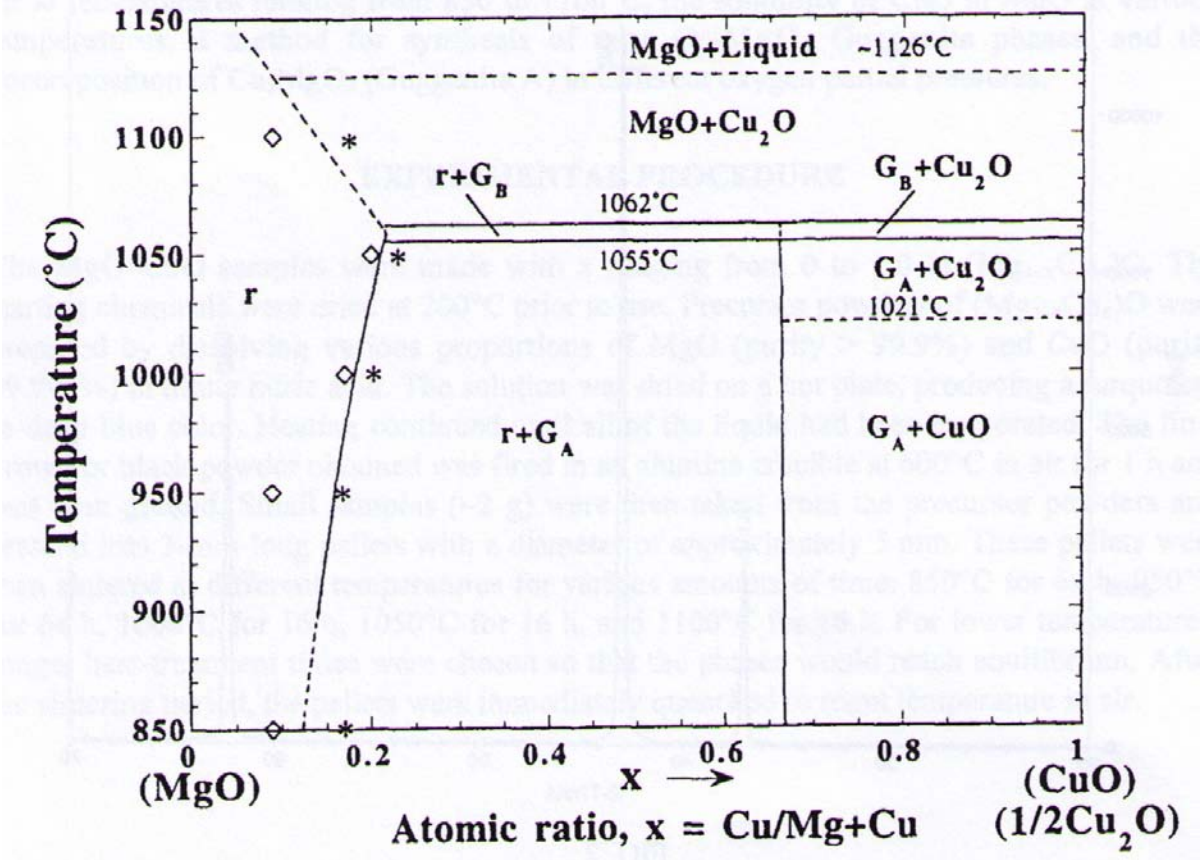

Figure C-2 The pseudo-binary phase diagram for the MgO-CuO system in air. r: cubic periclase phase; G_A: Guggenite A, Cu_2MgO_3, orthorhombic phase; G_B: Guggenite B, Cu_2MgO_3, orthorhombic phase; ◊ indicates single phase region; * indicates mixed phase region (Paranthaman et al. (1996)).

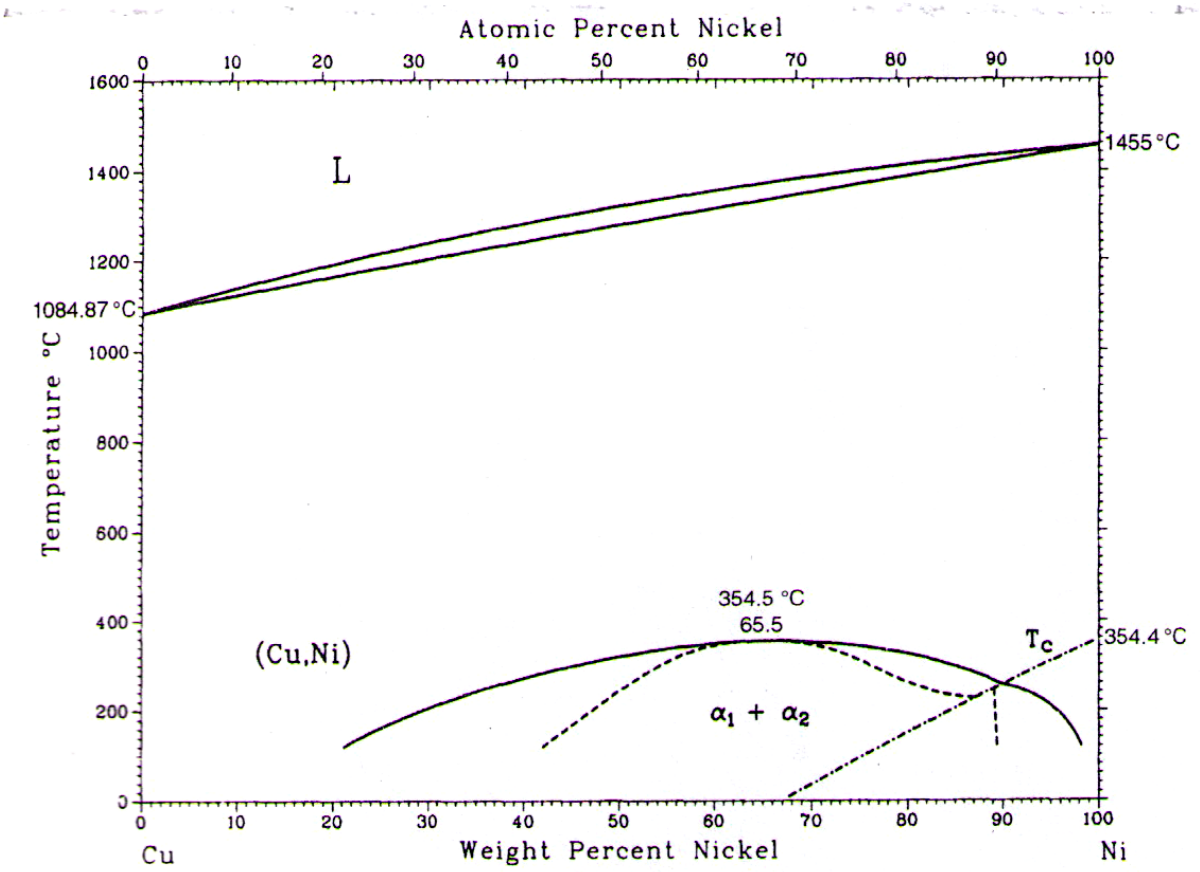

Figure C-3 The copper-nickel (Cu-Ni) binary phase diagram and crystal structure data **(**ASM International, the Materials Information Society**).**

Bibliography

Achenbach, E. and E. Riensche, *J. Power Sources,* 52 (1994) 283.

Adler, S.B., *Chem. Rev.*, 104 (2004) 4791.

Aguiar, P., Ph.D. Thesis, Imperial College of Science, Technology and Medicine, London , 2002.

Ahmed, K. and K, Foger, *Catalysis Today*, 63 (2000) 479.

Aruna, S.T., M. Muthuraman, and K.C. Patil, *Solid State Ionics*, 111(1998) 45.

Asomoto, M., S. Miyake, K. Sugihara, and H. Yahiro, *Electrochem. Communicat.*, 11(2009)1508

Asomoto, M., S. Miyake, Y. Itagaki, Y. Sadaoka, and H. Yahiro, *Catal. Today* 139(2008)71.

Badwal, S.P.S., *J.Mat. Sci.*, 18 (1983) 3230.

Badwal S.P.S. and K. Foger, *Ceram. International*, 22 (1996) 257.

Baker, R.T. and I.S. Metcalfe, *Ind. Eng. Chem. Res.*, 34 (1995) 1558.

Bansal, N.P. and Z. Zhong, *J. Power Sources*, 158 (2006) 148.

Barbir, F., *PEM Fuel Cell: Theory and Practice*, Elsevier Inc., London, 2005.

Bolmen, L. J. M. J. and M. N. Mugerwa, *Fuel Cell Systems*, Plenum Press, New York, 1993.

Boder, M. and R. Dittmeryer, *J. Power sources*, 155(2006)13.

Boer, B. Dr. Thesis, Universiteit Twente, Enschede, 1998.

Brown, M., S. Primdahl, and M. Mogensen, *J. Electrochem. Soc*., 147(2) (2000) 475.

Chan, S.H. and Z.T. Xia., *J. Appl. Electrochem.*, 32 (2002) 339.

Chen, M., B.H. Kim, Q.Xu, B.K. Ahn, W.J. Kang, and D.P. Huang, *Ceram. International*, 35(2009) 1335.

Chen, M., B.H. Kim, Q.Xu, O.J. Nam, and J.H. Ko, *J. Eur. Ceram. Soc.*, 28 (2008) 2947.

Chen, F. and M. Liu, *J. Mater. Chem***.,** 10 (2000) 2603.

Choi, S.C., K. Koumoto, and H. Yanagida, *J. Solid State Chem.*, 55 (1984) 150.

Choi, Y.M., C. Compson, M.C.Lin, Meilin Liu, *J. Alloys Compd.*, 427 (2007) 25.

Choudhary, V.R., A.M.Rajput, and A.S. Mamman, *J. Catal.*, 178 (1998) 576.

Clarke, S.H., A.L. Dicks, K. Roiton, T.A. Smith, and A. Swann, *Catalysis Today*, 38(1997) 411.

Clemmer, R.M.C., Ph.D. Thesis, University of Waterloo, Waterloo, 2006.

Dees, D.W., T.D. Claar, T.E. Easler, D.C. Fee, and F.C. Mrazek, *J. Electrochem. Soc*., 134 (1987) 2141.

Eguchi, K., *J. Alloys and Compounds*, 250 (1997) 486.

EG&G Technical Services, *Fuel Cell Handbook*, 6th Edition, US DOE, Morgantown, West Virginia, 2002.

Fang, X., G. Zhu, C. Xia, X. Liu, and G. Meng, *Solid State Ionics*, 168 (2004) 31.

Finnerty, C.M., N. J. Coe, R.H. Cunningham, and R.M. Ormerod, *Catalysis Today*, 46 (1998) 137.

Finnerty, C.M., R.M. Ormerod, *J. Power Source.* 86 (2000) 390.

Fukui, T., S. Ohara, M. Naito, and K. Nogi, *J. Power Sources*, 110 (2002) 91.

Gac, W., A. Denis, T. Borowiecki, and L. Kępiński. *Appl. Catal., A Gen.*, 357 (2009) 236.

Ganguli, D. and M. Chatterjee, *Ceramic Powder Preparation: a Handbook*, Kluwer Acadamic Publishers, Massachusetts, 1997.

Gao, J., X. Liu, D. Peng, and G. Meng, *Catalysis Today*, 82 (2003) 207.

Gong, M., D. Brechenk, J. Hagg, K.R. Poeppelmerer, S.A. Barnebb, C. Xu , J.W. Zondlo, and X. Liu, *J. Power Sources*, 195 (2010) 4013.

Gorte, R.T. and J.M. Vohs, *J. Catal.*, 216 (2003) 477.

Grgidak, C.M., R.G.Green, and J.B.Giorgi, *J. Mater. Chem.*, 16 (2006) 885.

Gubner, A., H. Landes, J. Metzger, H. Seeg, and R. Stubner, in "SOFC-V" edited by S.C Singhal and H. Tagawa (Electrochem. Soc., Pennington, NJ, 1997) Vol 97-40 p.844

Gunji, A., C. Wen, J. Otomo, T. Kobayashi, K. Ukai, Y. Mizutani, and H. Takahashi *J. Power Sources*, 131 (2004) 285.

He, H., R.J. Gorte, and John M. Vohs, Electrochem. *Solid-State Lett.*, 8(6) (2005a) A279.

He, H. and J.M. Hill, *Appl. Catal., A Gen.*, 317 (2007) 284.

He, H., J.M. Vohs, and R.J. Gorte, *J. Power Sources*, 144 (2005b) 135.

Huang, T.J. and S.Y. Jhao, *Appl, Catal., A Gen.*, 302(2006) 325.

Huebner W., D.M. Reed, and H.U. Anderson, in "SOFC-VI" edited by S.C. Singhal and M. Dokiya (Electrochem. Soc., Pennington, NJ, 1999) Vol 99-19 p.503

Huebner, W., H.U. Anderson, D.M. Reed, S.R. Sehlin, and X. Deng, in "SOFC-IV" edited by M. Dokiya , O. Yamamoto, H. Tagawa and S.C. Singhal (Electrochem. Soc., Pennington, NJ, 1995) Vol 95-01 p.696

Hung, I.M.,Y. Yoo, I. Davidson, and M.H. Hon, Proceedings of the 6th European Solid Oxide Fuel Cell Forum in Lucerne, Switzerland, pp.1387-1395, June 2004

Iida, T., M, Kawano, T. Matsui, R. Kikuchi, and K. Eguchi, *J. Electrochem. Soc.*, 154(2) (2007) B234

Irvine, J.T.S., D.I. Fagg, J. Labrinch, F.M.B. Marques, *Catal. Today*, 38 (1997) 467.

Iwasawa, C., M. Nagata, S. Yamaoka, Y. Seino, and M. Ono, in "SOFC-IV" edited by M. Dokiya , O. Yamamoto, H. Tagawa and S.C. Singhal (Electrochem. Soc., Pennington, NJ, 1995) Vol 95-01 p.686

Iwata, T., *J. Electrochem. Soc.*, 143(5) (1996) 1521.

Ivers-Tiffeé, E., A. Weber and D. Herbstritt, *J. Eur. Ceram. Soc.*, 21 (2001) 1805.

Jiang, S.P., *J. Electrochem. Soc.*, 150(11) (2003) E548.

Kawada, T., N. Sasaki, H. Yokokawa, M. Dokiya, M. Mori, and T. Iwata, *J. Electrochem. Soc.*, 137 (1990) 3042.

Kawano, M., T. Matsui, R. Kikuchi, H. Yoshida, T. Inagaki and K. Eguchi. J. *Electrochem. Soc.*, 154(5) (2007) B460.

Kim ,T., G. Liu, M. Boaro, S.-I. Lee, J.M. Vohs, R.J. Gorte, O.H. Al-Madhi, B.O. Dabbousi, *J. Power Sources*, 155 (2006) 231.

Kim, H., C. da Rosa, M. Boaro, J. M. Vohs, and R. J. Gorte, *J. Am. Ceram. Soc.*, 85 (2002a) 1473.

Kim, H., C. Lu, W. L. Worrell, J. M. Vohs, and R. J. Gorte, *J. Electrochem. Soc.*, 49(3) (2002b) A247.

Koh, J.H., Y.S. Yoo, J.W. Park, H.C. Lim, *Solid State Ionics*, 149 (2002) 157.

Lee, A.L., R.F. Zabransky, and W.J. Huber, *Ind. Eng. Chem. Res.*, 29 (1990) 766.

Lee, S.I., J.M. Vohs, R.J. Gorte, *J. Electrochem. Soc.*,151(9) (2004) A1319.

Leng, Y. J., S. H. Chan, S. P. Jiang, and K. A. Khor, *Solid State Ionics*, 170 (2004) 9.

Li, L., I. Saita, K. Saito, and T. Akiyama, *J. Alloys Compd.*, 327 (2004) 218.

Li, S., R. Guo, J. Li, Y. Chen, and W. Liu, *Ceram. International*, 29 (2003) 883.

Lin, Y., Z. Zhan, and S.A. Barnett, *J. Power Source*, 158 (2006) 1313.

Lin, Y., Z. Zhan, and S.A. Barnett, *Solid State Ionics*, 176 (2005) 1827.

Lu, C., W. L. Worrell, R. J. Gorte, and J. M. Vohs, *J. Electrochem. Soc*., 150(3) (2003) A354.

Madsen, B.D. and S.A. Barnett, *Solid State Ionics*, 176 (2005) 2545.

Meng, G.Y., Q.X. Fu, S.W. Zha, C.R. Xia, X.Q. Liu, D.K. Peng. *Solid State Ionics,* 148 (2002) 533.

Minh, N. Q. and T. Takahashi, *Science and Technology of Ceramic Fuel Cells*, Elsevier, Amsterdam, 1995.

Mizutani, Y., M. Tamura, M. Kawai, and O. Yamamoto, *Solid State Ionics*, 72 (1994) 271.

Moon. D.J. and J.W.Ryu, *Catalysis Today*, 87 (2003) 255.

Mori T. and H. Yamamura, *Journal of Materials Synthesis and Processing*, 6(3) (1998) 175.

Murray, E.P., T. Tsai, and S.A. Barnett, *Nature,* 400 (1999) 649.

Nielsen, J.R. and D.L. Trimm, *J. Catal*, 48 (1977) 155.

Naoumidis, A., A. Tsogo, P. Nikopoulos, and H. Grubmeier, , in "SOFC-IV" edited by M. Dokiya , O. Yamamoto, H. Tagawa and S.C. Singhal (Electrochem. Soc., Pennington, NJ, 1995) Vol 95-01 p.667

O'Hayre, R.P., S.-W. Cha, W. Colella, and F.B. Prinz, *Fuel Cell Fundamentals*, John Wiley & Sons, New York, 2006

Odegard, R., E. Johnsen, and H. Karoliussen, in "SOFC-IV" edited by edited by M. Dokiya , O. Yamamoto, H. Tagawa and S.C. Singhal (Electrochem. Soc., Pennington, NJ, 1995) Vol 95-01, p.810

Ogumi, Z., T. Ioroi, Y. Uchimoto, Z.I. Takehara, T. Ogawa, and K. Toyama. *J. Am. Chem. Soc.*, 78 (1995) 593.

Paranthaman, M., K. A. David and T. B. Lindemer, *Materials Research Bulletin*, 32 (1997) 165.

Park, S., R.J. Gorte, and J.M. Vohs, *Appl. Catal., A Gen.*, 200(2000) 55.

Peña-Martínez, J., D.Marrero-López, J.C. Ruiz-Morales, B.E.Buergler, P.Núñez and .J.Gauckler, *J. Power Sources*, 159 (2006) 914.

Peng, R., C. Xia, X. Liu, D. Peng, and G. Meng, *Solid State Ionics*, 152–153 (2002) 561.

Perednis, D. and L.J. Gauckler, *Solid State Ionics*, 166 (2004) 229.

Primdahl, S. and M. Mogensen, J. *Electrochem. Soc.*, 144(10) (1997) 3409.

Razpotnik , T. and J. Maček, *J. Euro. Ceram. Soc*., 27 (2007) 1405.

Ringuedé, A., D. P. Fagg, and J. R. Frade, *J. Euro. Ceram. Soc.*, 24 (2004) 1355.

Sammes, N. M., M.S. Brown, and R. Ratnaraj, *J. Mat. Sci. Lett*., 13 (1994) 1124.

Sasaki, H., M. Suzuki, S. Otoshi, A. Kajimura, and M. Ippommatsu, *J. Electrochem. Soc*., 139(1) (1992) L12.

Sato, K., Y. Ohmine, K.Ogasa, and S. Tsuji, in "SOFC-VIII" edited by S. C. Singhal and M. Dokiya (Electrochem. Soc., Pennington, NJ, 2003) Vol. 2003–07, p. 695

Sfeir, J., D.Sc. Thesis, École Polytechnique Fédérale de Lausanne, Lausanne, 2002.

Shao, Z. and S.M. Haile, *Nature*, 431 (2004) 170.

Shiratori, Y., Y. Teroka and K.Sasaki, *Solid State Ionics*, 177 (2006) 1371.

Shiratori, Y., and K. Sasaki, *J. Power Sources*, 180 (2008) 738.

Simwonis, D., F. Tietz, and D. Stöver, *Solid State Ionics*, 132 (2000) 241.

Sin, A., E. Kopnin, Y. Dubitsky, A. Zaopo, A.S. Aricò, D. La Rosa, L.R. Gullo, and V. Antonucci, *J. Power Sources*, 164 (2007) 300.

Signhal, S.C. and K. Kendal, *High Temperature Solid Oxide Fuel Cells: Fundamental, Design and Application*, Elsevier, New York, 2003.

Southampton Electrochemistry Group, *Instrument Methods in Electrochemistry*, Ellis Horwood Ltd., Chichester, 1985.

Steele, B.C.H., *Solid State Ionics*, 86-88 (1996) 1223.

Steele, B.C.H., *Solid State Ionics*, 95-100 (2000) 129.

Sumi, H., K. Ukai, Y. Mizutani, H. Mori, C.J. Wen, H. Takahashid, and O.Yamamoto, *Solid State Ionics*, 174 (2004) 151.

Suwanwarangkul, R., Ph.D. Thesis, University of Waterloo, Waterloo, 2005.

Takaduchi, T., R. Kikuchi, T. Yano, K. Eguchi, and K. Marata, *Catalysis Today*, 84 (2003) 217.

Takeguchi, T., Y. Kani, T. Yano, R. Kikuchi, K. Eguchi, K. Tsujimoto, Y. Uchida, A. Ueno, K. Omoshiki, and M. Aizawa, *J. Power Sources*, 112 (2002) 588.

Tavares, A.C., B.L. Kuzin, S.M. Beresnev, N.M. Bogdanovich, E.Kh. Kurumchin, Y.A. Dubitsky and A. Zaopo, *J. Power Sources*, 183 (2008) 20.

Tomishige, K., Y.-G. Chen, and K, Fujimoto, *J. Catal.*, 181 (1999) 91.

Tomita, A., S. Teranishi, M. Nagao, T. Hibino, and M. Sano, *J. Electrochem. Soc*., 153(6) (2006) A956.

Tsogo ,A., A. Naoumidis, and P. Nikolopoulos, *Acra mafer.*, 44 (1996) 3679.

Vernoux, P., J. Guihdet, E. Gehain, and M. Klieitz in "SOFC-V" edited by U. Stimming, S.C. Singhal, H. Tagawa and W. Lehnert (Electrochem. Soc., Pennington, NJ, 1997) Vol 97-40 p. 219

Wang, J.B., J.C. Jang, and T.J. Huang, *J. Power Sources*, 122 (2003) 122.

Wang, F.Y., S. Chen, S. Cheng. *Electrochem. Communicat.*, 6(2004) 743

Wang, Z., W. Weng, K. Cheng, P. Pu, G. Shen, and G. Han, *J. Power Sources*, 179(2008) 541.

Wilkenböner, R., TH. Kloidt , and W. Malléner, in "SOFC-V" edited by S.C. Singhal and H. Tagawa (Electrochem. Soc., Pennington, NJ, 1997) Vol 97-40 p.851

Xia, C. and M. Liu, *Solid State Ionics*, 144 (2001) 249.

Xia, C., F. Chen and M. Liu, *Electrochem. Solid-State Lett*., 4(5) (2001) A52.

Xia, C., R. William, F. Chen, and M. Liu, *Solid State Ionics*, 149 (2002) 11.

Xia, C., Y. Lang, and G. Meng, *Fuel Cells*, 4 (2004) 41.

Xie, Z., W. Zhu, B. Zhu, and C. Xia, *Electrochimica Acta*, 51 (2006) 3052.

Yamaji, K., H. Kishimoto, Y. Xiong, T. Horita, N. Sakai, M.E. Brito, and H. Yokokawa, *J. Power Sources*, 159 (2006) 885.

Yan, J., H. Matsumoto, M. Enoki, and T. Ishihara, Electrochem. *Solid-State Lett*., 8 (2005) A389.

Yin, Y., S. Li, C. Xia, and G. Meng, *Electrochimica Acta*, 51 (2006) 2594.

Ye, X.F., B. Huang, S.R. Wang, Z.R. Wang, L. Xiong, and T.L. Wen, *J. Power Sources*, 164 (2007) 203.

Yu, H.C., F. Zhao, A.V. Virkar, and K.Z. Fung, *J. Power Sources*, 152 (2005) 22.

Zha, S., A. Moore, H. Abernathy, and M. Liu, *J. Electrochem. Soc*., 151(8) (2004) A1128.

Zhan, Z. and S.A. Barnett, *Science*, 308 (2005) 844.

Zhan, Z. and S.A. Barnett, *J. Power Sources*, 155 (2006) 353.

Zhang, X., S. Ohara, R. Maric, K. Mukai, T. Fukui,H. Yoshida, M. Nishimura, T. Inagaki, and K. Miura, *J. Power Sources*, 83 (1999) 170.

Zhang, Y., X. Huang, Z. Lu, X. Ge, J. Xu, X. Xin, X. Sha, and W. Su, *Solid State Ionics*, 177 (2006) 281.

Zhao, H., L. Huo, L. Sun, L. Yu, S. Gao and J. Zhao, *Mater. Chem. Phys.*, 88 (2004) 160.

Zheng, R., X.M. Zhou, S.R. Wang, T.-L. Wen, C.X. Ding, *J. Power Sources*, 140 (2005) 217.

Zhu, B., *J. Power Sources*, 93 (2001) 82.

Zhu, B., X. Liu, M. Sun, S. Ji, J. Sun, *Solid State Ionics*, 5 (2003) 1127.

Zhu, C., X. Liu, C. Yi, L. Pei, D. Wang, D. Yan, K. Yao, T. Lu and W. Su. *J. Power Source* 195(2010) 3504.

Zhu, W., C. Xia, J. Fan, R. Peng, and G. Meng, *J. Power Sources.* 160 (2006) 897.

Zhuang, Q., Y. Qin, L. Chang, *Appl. Catal*., 70 (1991) 1.

Zinkevich, M., S. Geupel, and F. Aldinger, *J. Alloys Compd.*, 393 (2005) 154.

ASM International, the Materials Information Society

www.csa.com/discoveryguides/fuecel/overview.php

www.powergeneration.siemens.com/en/fuelcells/technology/tubular/index.cfm